

Development and Evaluation of Methods to Follow Microstructural Development of Cementitious Systems Including Slags

THÈSE N° 4523 (2009)

PRÉSENTÉE LE 30 OCTOBRE 2009

À LA FACULTÉ SCIENCES ET TECHNIQUES DE L'INGÉNIEUR
LABORATOIRE DES MATÉRIAUX DE CONSTRUCTION
PROGRAMME DOCTORAL EN SCIENCE ET GÉNIE DES MATÉRIAUX

ÉCOLE POLYTECHNIQUE FÉDÉRALE DE LAUSANNE

POUR L'OBTENTION DU GRADE DE DOCTEUR ÈS SCIENCES

PAR

Vanessa KOCABA

acceptée sur proposition du jury:

Prof. A. Mortensen, président du jury
Prof. K. Scrivener, directrice de thèse
Prof. H. Hofmann, rapporteur
Prof. D. E. Macphee, rapporteur
Dr W. Matthes, rapporteur



ÉCOLE POLYTECHNIQUE
FÉDÉRALE DE LAUSANNE

Suisse
2009

ABSTRACT

Production of cementitious materials causes the emission of CO₂ gas, which has detrimental impact on the environment augmenting the global warming process. Using by-products such as slags is a possible strategy to limit the environmental impact of cementitious materials. Consequently, there is an increasing use of supplementary cementitious materials (SCMs), either pre-blended with ground clinker or added during fabrication of concrete. However, it is well known that these SCMs generally react slower than cement clinker so the levels of substitution are limited. However, substitution by SCMs should not compromise the development of mechanical properties especially at early ages. In order to better understand the factors affecting the degree of reaction of SCMs it is essential to have an accurate method to evaluate the actual rate of reaction of these materials independent from the degree of reaction of the clinker component. To this end, the contribution of slag in blended cements can be monitored and characterised as a function of time.

In this thesis, methods of characterisation of anhydrous materials were initially improved and provided the starting point for the study of hydrated systems.

Secondly, the effect of slag on clinker phases was identified. It was found that slag does not significantly affect the overall hydration of aluminate phase. Although, the slag favoured the hydration of the ferrite phases and significantly retarded the hydration of belite and, consequently, the degree of reaction of cement.

It was also observed that the slag modified the composition of hydrates. Analyses of hydrated cements with and without slag have shown two major effects: a) no significant decrease in calcium hydroxide content (normalized to cement content) in blended systems, b) higher substitution of Al for Si and lower C/S ratio in outer C-S-H in blended systems.

To measure the reactivity of slag in blended pastes at later ages, five methods were studied. As selective dissolution and differential scanning calorimetry have shown to be unreliable, even if SEM-IA-mapping is time consuming, it appeared to be the only accurate method to quantify the degree of reaction of slag. The computation of difference in cumulative calorimetry and chemical shrinkage curves of slag and its comparison to inert filler allowed the reaction of the slag to be isolated. Calibration of these techniques using the SEM-IA-mapping results proved to be a promising method to understand and quantify the reactivity of slag.

Using the overall degree of reaction, it was established that increasing reaction in the slag corresponds to an increasing strength in blended mortars. Comparing the strength with calculated total porosity, it was concluded that the contribution of the slag seemed to be more than just filling the microstructural space by producing hydration products. Slag was observed to also enhance the strength by its interaction with other phases. The study will focus on differentiating the two effects to elicit the influence of slag on development of strength.

Key words: slag, cement, microstructure, reactivity, XRD-Rietveld refinement, SEM-Image analysis-mapping, calorimetry, chemical shrinkage.

RESUME

La production de matériaux cimentaires génère des émissions de CO₂, néfastes à l'environnement.

L'utilisation de sous-produits comme les laitiers est une stratégie possible pour limiter l'impact sur les matériaux entrant dans la composition du mélange. Par conséquent, on assiste à une utilisation croissante de matériaux cimentaires de substitution (SCMs), soit pré-mélangés et broyés avec le clinker, soit venant en supplément pendant la fabrication du ciment. Quoiqu'il en soit, il est bien connu que ces SCMs réagissent généralement plus lentement que le clinker limitant ainsi les niveaux de substitution, ceci étant provoqué par les besoins spécifiques inhérents aux propriétés à jeune âge.

Pour mieux comprendre les facteurs influents sur le degré de réaction des SCMs, il est essentiel d'avoir une méthode précise pour évaluer le taux réel de réaction de ces matériaux, indépendamment du degré de réaction du clinker. Ainsi, la contribution apportée par le laitier dans les ciments composés peut être suivie et caractérisée dans le temps.

Dans cette thèse, les méthodes de caractérisation des matériaux anhydres ont été initialement développées et ont fourni le point de départ de l'étude de systèmes hydratés.

Ensuite, les conséquences de l'apport de laitier sur des phases du clinker ont été identifiées. Concernant les phases aluminates, il n'y a aucune preuve de réaction du laitier lui-même. Cependant, le laitier a favorisé l'hydratation des phases ferrite, a retardé significativement l'hydratation de la bélite et par conséquent, a agi sur le degré de réaction du ciment.

Le laitier a aussi modifié la composition d'hydrates. Les analyses des ciments hydratés avec et sans laitier ont montré a) qu'aucune diminution significative de la portlandite (normalisée par la quantité de ciment) n'est observée avec l'addition de laitier b) que, en particulier le « outer C-S-H » montre une substitution plus forte du silicium par l'aluminium.

Pour mesurer la réactivité du laitier dans des pâtes mélangées à plus long terme, cinq méthodes ont été étudiées. La dissolution sélective et la calorimétrie différentielle se sont montrées peu fiables. Même si l'analyse d'images couplée à la cartographie par microscopie prend beaucoup de temps, elle s'avère être la seule méthode précise pour quantifier la réactivité du laitier. Le calcul de différence dans des courbes cumulées de calorimétrie et de retrait chimique du laitier et sa comparaison à un filler inerte ont permis d'isoler la réaction du laitier. La calibration utilisant les résultats de l'analyse d'images couplée à la cartographie par microscopie semble être une méthode prometteuse pour comprendre et quantifier la réactivité du laitier.

En utilisant le degré de réaction totale, il a été établi que l'augmentation de la réactivité du laitier correspond à une augmentation de compression dans les mortiers composés. En comparant la compression à la porosité totale calculée, la contribution apportée par le laitier semble être augmentée au-delà de celle à laquelle on pouvait s'attendre due au remplissage de l'espace par ses produits d'hydratation.

Mots clés : laitier, microstructure, réactivité, DX-affinement Rietveld, MEB-Analyse d'images, calorimétrie, retrait chimique.

REMERCIEMENTS

Mes premiers remerciements s'adressent à ma directrice de thèse, la Professeure Karen Scrivener qui avec son caractère « béton » m'a ouvert les portes du milieu cimentaire et m'a permis de travailler dans des conditions idéales de recherche en milieu académique non seulement en terme de qualité d'équipements scientifiques et mais aussi d'atmosphère propice au travail.

Cette thèse faisait partie d'un projet financé par Nanocem, un consortium européen de recherches sur le ciment et le béton. Ce regroupement de partenaires industriels et académiques m'a offert l'opportunité d'accéder à une vision globale de la recherche dans le milieu cimentaire, et il m'a également permis des collaborations scientifiques privilégiées au sein de mon travail de recherche. Je remercie ainsi sincèrement :

- l'équipe RMN de l'Université d'Aarhus au Danemark, Søren Poulsen et Jørgen Skibsted: "tak for dit samarbejde" ;
- Leon Black, Qiu Lu et Ian Richardson, l'équipe MET de l'Université de Leeds: "thanks a lot for your TEM collaboration";
- Mette Geiker de l'Université Technique du Danemark à Lyngby: "tak for din velkommen i Danmark".

Je souhaite remercier les membres du jury de ma soutenance privée de thèse: Winnie Matthes, les Professeurs Donald Macphee, Heinrich Hofmann et Andreas Mortensen (président du jury).

Cette section remerciements ne pouvait pas selon moi ne pas s'accompagner d'une partie dédiée à mes collègues du LMC qui m'ont offerts la chance de travailler dans une atmosphère dynamique, motivante et constructive pendant quatre ans. Ainsi, j'aimerais en particulier remercier les personnes suivantes :

- Gwenn : « merci pour ton aide sur la diffraction des rayons X et l'affinement Rietveld » ;
- Mercedes : “muchas gracias por tu estado de ánimo”;
- Alex: « merci pour le temps partagé notamment nos manip au PSI et le concert de Ben »;
- Carolina : “ gracias por tu alegría de vivir”;
- Shashank : “thanks to guide me on the way of understanding a part of your world of modelling approaches”;
- Rodrigo : « merci pour ton enthousiasme diplomatique permanent »;
- Manu : « ta collaboration et ton expertise sur l'analyse d'images microscopiques m'ont été très utiles et se sont avérées plus que centrales à ce travail de thèse, merci beaucoup pour tout ça et aussi pour les journées aux Portes du Soleil »;
- Cyrille : « merci pour les coups de pouce simulation. Ton subtil sens de l'humour suisse-anglais me manquera ! »;
- Aditya : “thank you very much for your efficient help in writing correction of this thesis”;
- Patrick : « nos nombreuses discussions scientifiques et notre cohabitation me manqueront »;
- Julien : « merci pour ta bonne humeur, ton enthousiasme à faire partager tes compétences, tu m'as beaucoup aidé à mon arrivée au labo...et qu'est-ce que tu m'as fait rire...un vrai bout-en-train au grand cœur ! »;
- Aude : « plus qu'une collègue tu es devenue une véritable amie, sur qui je peux compter...et tu l'as déjà prouvé ! Un énorme merci pour l'ensemble du temps que nous avons partagé au LMC, ton soutien surtout pendant ces derniers mois plus difficiles...mais aussi toutes nos discussions, nos journées sans fin au labo et nos manip nocturnes ! ».

J'aimerais dédier une partie de ce travail à ma famille :

- Tout d'abord mes parents, Annick et Serge, auprès de qui j'ai appris la rigueur et la persévérance du travail ;
- mes sœurs : Floriane à qui je dois de multiples et sincères encouragements et Viridiana qui comprend plus que n'importe qui ce que travailler dur pour réussir veut dire ;
- et mes grands-parents qui se sont toujours montrés très compréhensifs et encourageants face à mes choix.
- Je remercie aussi sincèrement Laurent pour sa compréhension et son soutien répété.

Et puis ce périple helvétique n'aurait pas été le même sans les moments passés avec mon amie Francine...nos séances aux bords du lac vont me manquer... mais aussi Sylvia, merci pour les instants de détente que tu m'as permis de partager avec Inch Allah.

Pardon à tous ceux que j'ai un peu délaissés au cours de ces derniers mois au profit de ma thèse, notamment mes amies Anne-Laure, Elodie, Lucie et Perrine, mais aussi Rachid que j'aimerais particulièrement remercier pour toute la patience et la compréhension dont il a fait preuve au cours de ces 4 années cimentaires.

Je dédie l'ensemble de ce travail de thèse à mon filleul Yanis avec un clin d'œil particulier au fait qu'il soit entré dans le cursus scolaire le jour où j'en ai fini avec le mien !

TABLE OF CONTENTS

<i>Abstract</i>	<i>III</i>
<i>Résumé</i>	<i>V</i>
<i>Remerciements</i>	<i>VII</i>
<i>List of Tables</i>	<i>XV</i>
<i>List of Figures</i>	<i>XVI</i>
<i>Glossary-Notation</i>	<i>XXIII</i>
CHAPTER I: INTRODUCTION	1
I.1. Background	1
I.2. Objectives and research scope	2
I.3. Choice of materials	3
I.4. Outline of the thesis	4
CHAPTER II: QUANTITATIVE ANALYSIS OF ANHYDROUS CEMENTITIOUS MATERIALS	5
II.1. Quantitative analysis on anhydrous cements	5
II.1.1. State of the art	5
II.1.2. X-ray diffraction analysis	8
II.1.3. SEM-Point counting	22
II.1.4. Comparison of XRD, NMR and SEM	31
II.1.5. Accuracy of X-ray fluorescence	32
II.1.6. Composition of the cement phases from EDS	33
II.1.7. Reverse Bogue calculation	37
II.1.8. Standard Bogue calculation procedure	39
II.1.9. Modified Bogue calculation procedure	39
II.1.10. Comparison of XRD, NMR, Bogue and modified Bogue	40
II.2. Characteristics of anhydrous slags	43
II.2.1. Mineralogy	44
II.2.2. Structure of the slag	45
II.2.3. Chemical composition of slag	47
II.2.4. Identification of structures of phases in the anhydrous slags	49
II.2.5. Measurement of the glass content	51
II.3. Conclusions and discussion on anhydrous cementitious materials	56

CHAPTER III: INVESTIGATION AND IMPROVEMENTS OF METHODS TO STUDY HYDRATED CEMENTITIOUS MATERIALS	59
III.1. Experimental conditions	60
III.1.1. Mix design	60
III.1.2. Sample preparation	61
III.2. Quantitative analysis by XRD-Rietveld	63
III.2.1. XRD experimental conditions	63
III.2.2. Scope of refinement for hydrated pastes	63
III.2.3. Known problems-Improvements	70
III.2.4. Reproducibility, repeatability and accuracy	75
III.3. Thermal analysis	77
III.3.1. TGA experimental conditions	77
III.3.2. Principle	77
III.3.3. Data treatment	79
III.3.4. Sampling effect	82
III.3.5. Repeatability and reproducibility	84
III.4. Scanning electron microscopy	85
III.4.1. Principle	85
III.4.2. Image analysis	85
III.4.3. Definition of degree of hydration of cement by SEM-IA	87
III.4.4. Repeatability and reproducibility	88
III.5. Isothermal calorimetry	89
III.5.1. Principle	89
III.5.2. Procedure	90
III.5.3. Optimisation of experimental conditions	91
III.6. Chemical shrinkage	93
III.6.1. Principle	93
III.6.2. Experimental conditions	95
III.7. Comparison of all techniques	96
III.7.1. Comparison of degree of hydration of cement by XRD and SEM	96
III.7.2. Degree of hydration of cement defined by calorimetry	99
III.8. Conclusions and discussions on hydrated cementitious materials	101
 CHAPTER IV: HOW THE SLAG AFFECTS THE REACTION OF CEMENT?	 105
IV.1. Influence of slag on heat released	105
IV.2. Effect of slag on silicate phases	108

IV.3. Contribution of slag on aluminate phases _____	110
IV.3.1. XRD data _____	110
IV.3.2. Effect of slag on peaks III and IV associated with aluminates _____	112
IV.3.3. Separation treatment to isolate aluminate reaction _____	112
IV.4. Influence of slag on belite phase _____	122
IV.5. Influence of slag on ferrite phase _____	124
IV.6. Influence of slag on the degree of reaction of cement _____	127
IV.7. Influence of slag on portlandite _____	129
IV.7.1. State of the art on portlandite content in slag systems _____	129
IV.7.2. Portlandite content of blends from TGA and XRD _____	130
IV.8. Influence of slag on the composition of C-S-H and other hydrates _____	132
IV.8.1. C-S-H _____	135
IV.8.2. Slag hydration rims _____	146
IV.8.3. AFm phases _____	148
IV.9. Conclusions and discussion on the effect of slag on reaction of cement _____	149
CHAPTER V: MEASURING THE DEGREE OF REACTION OF SLAGS IN BLENDED PASTES _____	151
V.1. State of the art _____	151
V.1.1. Measurement of bound water _____	151
V.1.2. Methods to measure reaction in blended cements _____	153
V.2. Selective dissolution _____	154
V.2.1. State of the art _____	154
V.2.2. Protocol of the dissolution technique _____	154
V.2.3. Materials investigated _____	156
V.2.4. Results from selective dissolution _____	156
V.3. Differential scanning calorimetry _____	162
V.3.1. State of the art _____	162
V.3.2. Protocol for DSC measurement _____	162
V.3.3. Results from DSC _____	163
V.4. SEM with BSE-image analysis and elemental mapping _____	170
V.4.1. Method _____	170
V.4.2. Results from image analysis-mapping _____	174
V.5. Cumulative heat evolution curves from isothermal calorimetry _____	178
V.5.1. Why use cumulative heat curves? _____	178
V.5.2. Results from isothermal calorimetry _____	179
V.6. Chemical shrinkage _____	186

V.7. Comparison of calorimetry and chemical shrinkage results _____	189
V.8. Conclusions and discussion on methods to measure the degree of reaction of slag _____	190
CHAPTER VI: MECHANICAL PROPERTIES OF BLENDED SYSTEMS _	195
VI.1. State of the art _____	195
VI.2. Experimental procedure _____	196
VI.2.1. Results of compressive strength _____	198
VI.2.2. Compressive strength versus reactivity _____	204
VI.2.3. Porosity and compressive strength _____	208
VI.3. Conclusion on mechanical properties _____	211
CHAPTER VII: DISCUSSION, CONCLUSIONS AND PERSPECTIVES __	213
VII.1. Methods _____	213
VII.2. Study of Slag _____	214
<i>Appendices</i> _____	219
Appendix 1: XRD patterns of anhydrous cements and clinker _____	219
Appendix 2: matlab file for background removal of DSC curves _____	220
Appendix 3: schematic representation of program for Bogue calculation _____	221
<i>References</i> _____	225
<i>Curriculum Vitae</i> _____	237

LIST OF TABLES

Table I-1: main characteristics of selected materials	3
Table II-1: structures of phases in the anhydrous samples.....	9
Table II-2: refined parameters as a function of phases taken into account.....	17
Table II-3: different XRD-Rietveld refinements for Anhydrous Cement A	18
Table II-4: different XRD-Rietveld refinements for Anhydrous Cement B	19
Table II-5: different XRD-Rietveld refinements for Anhydrous Cement C	19
Table II-6: different XRD-Rietveld refinements for Anhydrous Cement D	20
Table II-7: phases composition from XRD-Rietveld for the 4 anhydrous cements and the Clinker L..	21
Table II-8: density values from stoichiometric and actual formulas.....	30
Table II-9: oxides composition of the 4 cements from XRF analysis and CO ₂ content from TGA analysis.....	32
Table II-10: atomic ratio composition of the main anhydrous phases in cements A-D by EDS analyses (N' is the number of analyses) and average compositions given by Taylor in [55] (T ^l : table p 10, T ^e : formulas p 7-26)	35
Table II-11: atomic ratios for phases in Cement A to D and Clinker L calculated from EDS	36
Table II-12: mineral compositions of crystallised blastfurnace slags [61].....	45
Table II-13: oxides composition of two slags from XRF analysis.....	47
Table II-14: main characteristic moduli of slag [61,67-69].....	48
Table II-15: structures of phases in the anhydrous slag samples.....	49
Table II-16: EDS of anhydrous slags.....	50
Table II-17: phases composition from XRD-Rietveld for the 2 anhydrous slags	55
Table II-18: phases composition from XRD-Rietveld for the 8 anhydrous slag-cements mixes.....	55
Table III-1: main systems and their characteristics in pastes	60
Table III-2: structures of phases in the hydrated samples.....	63
Table III-3: results of sampling effect from Cement B-Slag 8 pastes hydrated for 28 days	83
Table III-4: enthalpy values for main reactions in cement.....	100
Table IV-1: results from separation treatment for systems B and C without additional gypsum	120
Table IV-2: comparative Ca/Si results from TEM and SEM EDS analyses	144
Table IV-3: comparative Al/Si results from TEM and SEM EDS analyses	145
Table IV-4: composition of C-S-H in blended cements [59,144,155,156]	145
Table IV-5: Mg/Al atomic ratio in rim and relicts of slag from SEM-EDS analyses.....	146
Table IV-6: composition of slag hydrates in blended cements from literature [112,144,149,153-157,160].....	147
Table V-1: undissolved materials and corresponding degree of reaction of slag after selective dissolution.....	157
Table V-2: results of analysis of residues after selective dissolution	158
Table V-3: DTA data of devitrification of glass of clinker [177].....	167
Table V-4: enthalpy of slag under different atmospheres	183
Table V-5: calibration factors to correlate cumulative heat and degree of reaction of slag.....	184
Table V-6: calibration factors to correlate chemical shrinkage and degree of reaction of slag	186
Table V-7: comparison between different methods used to calculate the degree of reaction of slag ..	191
Table VI-1: list of mortars studied.....	197

LIST OF FIGURES

Figure I-1: ternary diagram of $\text{CaO-Al}_2\text{O}_3\text{-SiO}_2$ representing the composition of cementitious materials.....	2
Figure II-1: XRD patterns with two angular windows (a) $31.5\text{-}33.5^\circ$, (b) $51\text{-}53^\circ$ that allow the M_3 alite polymorph (Cements A, B and D), M_3+M_1 (Cement C) and M_1 (Clinker L) to be identified.....	10
Figure II-2: dependence of the polymorphic modification of alite in clinkers on the MgO and SO_3 contents of the clinkers [46]	11
Figure II-3: identification of preferred orientation	16
Figure II-4: infiltration of metal under pressure.....	23
Figure II-5: SEM-BSE picture of Cement A impregnated in epoxy resin with lots of grain fracturing, edge poorly defined and accumulation of charges	24
Figure II-6: SEM-BSE picture of Cement A impregnated in metal alloy which reduces the border effects and does not allow accumulation of charges.....	24
Figure II-7: representative SEM-BSE image of anhydrous Cement A (White cement).....	25
Figure II-8: representative SEM-BSE image of anhydrous Cement B.....	25
Figure II-9: representative SEM-BSE image of anhydrous Cement C.....	26
Figure II-10: representative SEM-BSE image of anhydrous Cement D.....	26
Figure II-11: method of segmentation from the original SEM-BSE image to the final segmented images of alite and belite grains	28
Figure II-12: comparison of the results achieved by XRD-Rietveld and SEM-Point counting for the 4 main cements in weight and volume ratios	30
Figure II-13: comparison of the results achieved by XRD-Rietveld, SEM-Point counting and ^{29}Si NMR for the 4 main cements.....	31
Figure II-14: anhydrous phases contents for 4 cements achieved by reverse Bogue calculation and XRF elemental composition	38
Figure II-15: phases contents from ^{29}Si NMR analysis, Bogue and modified Bogue calculations versus XRD-Rietveld results.....	40
Figure II-16: comparison of the results achieved by Bogue, modified Bogue calculations and XRD-Rietveld quantification.....	41
Figure II-17: ternary diagram of $\text{CaO-Al}_2\text{O}_3\text{-SiO}_2$ with 10 wt% MgO representing the main field of chemical compositions of blast furnace slags [62]	44
Figure II-18: schematic structure of a glassy slag [64]	46
Figure II-19: SEM-BSE image of anhydrous Slag 1	49
Figure II-20: SEM-BSE image of anhydrous Slag 8 with crystalline phase	50
Figure II-21: SEM-BSE image of crystals of melilite in Slag 8	50
Figure II-22: DTA curves of three different anhydrous slags with recrystallisation peaks at high temperature [75]	52
Figure II-23: DSC curves of a powdered anhydrous glass samples [79]	52
Figure II-24: schematic calculation of the amorphous content using an external standard.....	54
Figure II-25: comparison between the actual weight and Rietveld analyzed amount of slag in cement-slag model mixtures [84]	54
Figure III-1: influence of refinement of ferrite occupancy in Cement C	64
Figure III-2: part of XRD pattern of Cement C hydrated for 14 days	65
Figure III-3: XRD pattern of Cement B hydrated for 28 days	66
Figure III-4: XRD patterns of Cement B hydrated for 28 days with and without manual fit of background.....	67

Figure III-5: XRD patterns of Cement B hydrated for 2 years with and without manual fit of background.....	67
Figure III-6: XRD pattern of Cement B-Slag 1 paste hydrated for 28 days.....	68
Figure III-7: XRD patterns of rutile standard with and without deviation.....	70
Figure III-8: evolution of amorphous and C_3S contents of Cement D with or without an instability of the diffractometer	71
Figure III-9: XRD patterns of Cement A with influence of isopropanol.....	72
Figure III-10: schematic description of a closed system based on calculations.....	73
Figure III-11: evolution of C_3S corrected or not by dilution effect in the 4 cements mixes.....	74
Figure III-12: evolution of C_2S corrected or not by dilution effect in the 4 cements mixes.....	74
Figure III-13: evolution of contents of clinker phases in Cement D.....	75
Figure III-14: evolution of portlandite, ettringite and degree of hydration of Cement D.....	75
Figure III-15: degree of reaction of alite and belite from XRD-Rietveld and ^{29}Si NMR for Cement A	76
Figure III-16: degree of reaction of alite and belite from XRD-Rietveld and ^{29}Si NMR for Cement C	77
Figure III-17: TGA and DTG curves for Cement B hydrated for 12 hours.....	78
Figure III-18: determination of portlandite and calcite contents by tangent method.....	80
Figure III-19: determination of portlandite and calcite contents by derivative method	81
Figure III-20: results of TGA measurements for Cement A-Slag 8	82
Figure III-21: TG curves with an apparent weight gain in case of problem of calibration or contamination	83
Figure III-22: repeatability tests of Portlandite content from TGA measurements of Cement A hydrated for 2 days	84
Figure III-23: Portlandite content in B-S8 pastes determined by TGA measurement in two different laboratories	84
Figure III-24: SEM-BSE picture of Cement A hydrated for 3 days.....	86
Figure III-25: corresponding grey level histogram.....	86
Figure III-26: different degrees of hydration of cement from SEM-IA as a function of different mixes	88
Figure III-27: rate of heat evolution during the hydration of cement.....	89
Figure III-28: heat flow of 3 cements with different experimental conditions.....	92
Figure III-29: heat release for 3 pastes mixed with 3 different quantities.....	93
Figure III-30: schematic description of chemical shrinkage	94
Figure III-31: picture of the mounting of chemical shrinkage	94
Figure III-32: degree of hydration of cement with dilution effect from XRD-Rietveld versus that from SEM-IA for 4 cements pastes.....	96
Figure III-33: degree of hydration of Cement A with dilution effect from XRD versus that from SEM-IA for all A systems	97
Figure III-34: degree of hydration of Cement B with dilution effect from XRD versus that from SEM-IA for all B systems	98
Figure III-35: degree of hydration of Cement C with dilution effect from XRD versus that from SEM-IA for all C systems	98
Figure III-36: evolution of C_3S in 4 cements.....	103
Figure III-37: evolution of C_2S in 4 cements.....	103
Figure III-38: evolution of C_3S in 3 cements blended with Slag 1.....	103
Figure III-39: evolution of C_2S in 3 cements blended with Slag 1.....	103
Figure III-40: evolution of C_3S in 3 cements blended with Slag 8.....	103

Figure III-41: evolution of C_2S in 3 cements blended with Slag 8.....	103
Figure III-42: evolution of C_3A in 4 cements.....	104
Figure III-43: evolution of C_4AF in 3 cements.....	104
Figure III-44: evolution of C_3A in 3 cements blended with Slag 1.....	104
Figure III-45: evolution of C_4AF in 2 cements blended with Slag 1.....	104
Figure III-46: evolution of C_3A in 3 cements blended with Slag 8.....	104
Figure III-47: evolution of C_4AF in 2 cements blended with Slag 8.....	104
Figure IV-1: particle size distribution of cements, slags and quartz obtained with Malvern mastersizer laser granulometer.....	106
Figure IV-2: heat flow of cementitious A pastes.....	107
Figure IV-3: heat flow of cementitious B pastes.....	107
Figure IV-4: heat flow of cementitious C pastes.....	107
Figure IV-5: evolution of C_3S content in cementitious A systems.....	109
Figure IV-6: evolution of C_3S content in cementitious B systems.....	109
Figure IV-7: evolution of C_3S content in cementitious C systems.....	109
Figure IV-8: rate of heat release of pastes with cement blended with different kinds of filler [138] ..	110
Figure IV-9: evolution of C_3A content in cementitious A systems.....	111
Figure IV-10: evolution of C_3A content in cementitious B systems.....	111
Figure IV-11: evolution of C_3A content in cementitious C systems.....	111
Figure IV-12: normalised heat evolution profiles for B-S1 blended pastes plus varying additional gypsum contents.....	112
Figure IV-13: illustration of contribution of silicate and aluminate phases.....	113
Figure IV-14: difference of normalised heat evolution for B-S1 blended pastes plus varying additional gypsum contents.....	113
Figure IV-15: difference of normalised heat evolution rescaled on time for B-S1 blended pastes plus varying additional gypsum contents.....	114
Figure IV-16: modified heat evolution rescaled on time for B-S1 blended pastes plus varying additional gypsum contents.....	116
Figure IV-17: initial heat curves from A pastes plus varying additional gypsum contents.....	117
Figure IV-18: initial heat curves from A-S1 pastes plus varying additional gypsum contents.....	117
Figure IV-19: initial heat curves from A-S8 pastes plus varying additional gypsum contents.....	117
Figure IV-20: initial and modified heat curves from separation treatment of B pastes plus varying additional gypsum contents.....	118
Figure IV-21: initial and modified heat curves from separation treatment of B-S1 pastes plus varying additional gypsum contents.....	118
Figure IV-22: initial and modified heat curves from separation treatment of B-S8 pastes plus varying additional gypsum contents.....	118
Figure IV-23: initial and modified heat curves from separation treatment of C pastes plus varying additional gypsum contents.....	119
Figure IV-24: initial and modified heat curves from separation treatment of C-S1 pastes plus varying additional gypsum contents.....	119
Figure IV-25: initial and modified heat curves from separation treatment of C-S8 pastes plus varying additional gypsum contents.....	119
Figure IV-26: all resulting B curves from separation treatment.....	121
Figure IV-27: all resulting C curves from separation treatment.....	121
Figure IV-28: evolution of C_2S content in cementitious A systems.....	123
Figure IV-29: evolution of C_2S content in cementitious B systems.....	123
Figure IV-30: evolution of C_2S content in cementitious C systems.....	123

Figure IV-31: evolution of ferrite content in cementitious B-S8 systems.....	124
Figure IV-32: evolution of ferrite content in cementitious B systems	125
Figure IV-33: evolution of ferrite content in cementitious C systems	125
Figure IV-34: SEM-BSE microstructure of B-S8 paste hydrated for 1 day.....	126
Figure IV-35: SEM-BSE microstructure of B-S8 paste hydrated for 7 days	126
Figure IV-36: evolution of DH of cement from XRD in systems with Cement A	128
Figure IV-37: evolution of DH of cement from SEM-IA in systems with Cement A.....	128
Figure IV-38: evolution of DH of cement from XRD in systems with Cement B	128
Figure IV-39: evolution of DH of cement from SEM-IA in systems with Cement B.....	128
Figure IV-40: evolution of DH of cement from XRD in systems with Cement C	128
Figure IV-41: evolution of DH of cement from SEM-IA in systems with Cement C.....	128
Figure IV-42: variation of portlandite with time [77,140-144].....	130
Figure IV-43: CH average content from XRD and TGA normalised by cement weight versus time for system A	131
Figure IV-44: CH average content from XRD and TGA normalised by cement weight versus time for system B.....	131
Figure IV-45: CH average content from XRD and TGA normalised by cement weight versus time for system C.....	131
Figure IV-46: scheme to summarise how to assess phases from the oxides of slag	132
Figure IV-47: SEM-BSE picture of Cement C-Slag 8 hydrated for 90 days.....	132
Figure IV-48: SEM-BSE microstructure of B pastes hydrated for 7 days.....	134
Figure IV-49: SEM-BSE microstructure of B-S1 pastes hydrated for 7 days.....	134
Figure IV-50: SEM-BSE microstructure of B pastes hydrated for 90 days.....	134
Figure IV-51: SEM-BSE microstructure of B-S1 pastes hydrated for 90 days	134
Figure IV-52: SEM-BSE microstructure of B pastes hydrated for 2 years	134
Figure IV-53: SEM-BSE microstructure of B-S1 pastes hydrated for 2 years.....	134
Figure IV-54: example of regions of inner and outer C-S-H in Cement C 28 days paste	135
Figure IV-55: Al/Ca ratio plotted against Si/Ca atom ratio for individual X-ray microanalyses of Cement A hydrated for 28 days.....	136
Figure IV-56: S/Ca ratio plotted against Al/Ca atom ratio for individual X-ray microanalyses of Cement A hydrated for 28 days.....	136
Figure IV-57: mean of Ca/(Si+Al) atomic ratio in inner and outer C-S-H of different cementitious pastes hydrated for 28 days.....	137
Figure IV-58: mean of Al/Ca atomic ratio in inner and outer C-S-H of different cementitious pastes hydrated for 28 days.....	138
Figure IV-59: mean of S/Ca atomic ratio in inner and outer C-S-H of different cementitious pastes hydrated for 28 days.....	139
Figure IV-60: Ca/(Si+Al) atomic ratios in C-S-H for systems A	142
Figure IV-61: Ca/(Si+Al) atomic ratios in C-S-H for systems B	142
Figure IV-62: Ca/(Si+Al) atomic ratios in C-S-H for systems C	142
Figure IV-63: Al/Ca atomic ratios in C-S-H for systems A	143
Figure IV-64: Al/Ca atomic ratios in C-S-H and for systems B.....	143
Figure IV-65: Al/Ca atomic ratios in C-S-H for systems C	143
Figure IV-66: X-ray microanalyses of A-S1 pastes hydrated for 90 days, Mg/Ca atomic ratio versus Al/Ca atomic ratio	146
Figure IV-67: SEM-BSE picture of Cement B-Slag 8 paste hydrated for 1 year to illustrate the presence of AFm phases	148

Figure IV-68: XRD patterns angular window 8-12.5° that allows the AFm phases to be identified ..	148
Figure V-1: XRD patterns of Cement B hydrated for 90 days and Cement B-Slag 8 hydrated for 90 days after selective dissolution.....	159
Figure V-2: SEM-BSE image of Cement B-Slag 8 hydrated for 90 days after selective dissolution ..	159
Figure V-3: degree of reaction of slag from selective dissolution after corrections suggested in [169]	161
Figure V-4: DSC curves of anhydrous powders	163
Figure V-5: DSC curves of Cement A blended with Slag 8 at different ages.....	164
Figure V-6: DSC curves of hydrated OPC [178].....	164
Figure V-7: method for background removal algorithm on DSC curve of	165
Figure V-8: background removal algorithm on all DSC curves of Cement A-Slag 8 hydrated from 3 to 90 days	166
Figure V-9: degree of reaction of Slag 8 from DSC in Cement A-Slag 8 blended pastes	166
Figure V-10: DTA curve of C ₂ S [177].....	167
Figure V-11: DSC curve of Anhydrous Cement A and corresponding background removal algorithm which isolate the contribution of belite	168
Figure V-12: background removal algorithm for Cement A, Slag 8 and Cement A-Slag 8.....	169
Figure V-13: conventional BSE-image analysis illustrated on example of Cement A-Slag 1 paste hydrated for 28 days.....	171
Figure V-14: BSE-image analysis combined with elemental illustrated on example of Cement A-Slag 8 paste hydrated for 90 days	173
Figure V-15: degree of reaction of slag from SEM-IA-mapping in systems A.....	175
Figure V-16: degree of reaction of slag from SEM-IA-mapping in systems B.....	175
Figure V-17: degree of reaction of slag from SEM-IA-mapping in systems C.....	175
Figure V-18: degree of reaction of Slag 1 from SEM-IA-mapping in blended pastes	176
Figure V-19: degree of reaction of Slag 8 from SEM-IA-mapping in blended pastes	176
Figure V-20: degree of reaction of Slag 8 from selective dissolution and SEM-IA-mapping	177
Figure V-21: degree of reaction of Slag 8 from SEM-IA-mapping, DSC and selective dissolution....	177
Figure V-22: cumulative heat liberation of cements at 27 and 60°C [133].....	178
Figure V-23: normalised cumulative heat curves for systems A	180
Figure V-24: normalised cumulative heat curves for systems B	180
Figure V-25: normalised cumulative heat curves for systems C	180
Figure V-26: illustration to isolate the contribution of slag from cumulative heat curves of blended and quartz pastes	182
Figure V-27: cumulative heat per g of anhydrous and resulting difference curves which isolate the slag contribution.....	182
Figure V-28: calorimetry curves calibrated with SEM-IA-mapping in systems A	185
Figure V-29: calorimetry curves calibrated with SEM-IA-mapping in systems B	185
Figure V-30: calorimetry curves calibrated with SEM-IA-mapping in systems C	185
Figure V-31: evolution of chemical shrinkage for systems A.....	187
Figure V-32: evolution of chemical shrinkage for systems B.....	187
Figure V-33: evolution of chemical shrinkage for systems C.....	187
Figure V-34: chemical shrinkage calibrated SEM-IA-mapping for systems A.....	188
Figure V-35: chemical shrinkage calibrated SEM-IA-mapping for systems B.....	188
Figure V-36: chemical shrinkage calibrated SEM-IA-mapping for systems C.....	188
Figure V-37: calorimetry versus chemical shrinkage results for systems A.....	189
Figure V-38: calorimetry versus chemical shrinkage results for systems B.....	189

Figure V-39: calorimetry versus chemical shrinkage results for systems C.....	189
Figure V-40: comparison of degree of reaction of Slag 1 from ^{29}Si NMR and SEM-IA	192
Figure V-41: comparison of degree of reaction of Slag 8 from ^{29}Si NMR and SEM-IA	192
Figure V-42: reactivity indices M1 and M5 versus degree of reaction of slag.....	193
Figure VI-1: compressive strength evolution for air-entrained concrete [184].....	196
Figure VI-2: evolution of compressive strengths of all mortars with Cement A.....	199
Figure VI-3: evolution of compressive strengths of all mortars with Cement B.....	199
Figure VI-4: evolution of compressive strengths of all mortars with Cement C.....	199
Figure VI-5: evolution of compressive strengths of pure mortars	201
Figure VI-6: evolution of compressive strengths of mortars blended with Slag 1	201
Figure VI-7: evolution of compressive strengths of mortars blended with Slag 8	201
Figure VI-8: evolution of compressive strengths of selected mortars with Cement A.....	203
Figure VI-9: evolution of compressive strengths of selected mortars with Cement B.....	203
Figure VI-10: evolution of compressive strengths of selected mortars with Cement C	203
Figure VI-11: degree of hydration of cement from SEM-IA and XRD-Rietveld for 3 mortars containing 100% cement.....	205
Figure VI-12: degree of hydration of cement from SEM-IA and XRD-Rietveld for 3 mortars containing 60% cement-40% Slag 1.....	205
Figure VI-13: degree of hydration of cement from SEM-IA and XRD-Rietveld for 3 mortars containing 60% cement-40% Slag 8.....	205
Figure VI-14: difference of compressive strength versus degree of hydration of slag from SEM-IA- mapping for 6 blended mortars.....	206
Figure VI-15: compressive strength versus overall degree of reaction in blended systems	207
Figure VI-16: evolution of calculated total porosity and corresponding relation with compressive strength for systems A.....	210
Figure VI-17: evolution of calculated total porosity and corresponding relation with compressive strength for systems B.....	210
Figure VI-18: evolution of calculated total porosity and corresponding relation with compressive strength for systems C.....	210
Figure VII-1: heat curves of both slags activated by NaOH solution.....	216
Figure VII-2: cumulative heat curves for fly ash and silica fume blended pastes compared to the reference paste	217

GLOSSARY-NOTATION

A simplified notation is used when describing cement compounds, the cement shorthand notation:

C = CaO	F = Fe ₂ O ₃	N = Na ₂ O
S = SiO ₂	\$ = SO ₃	K = K ₂ O
H = H ₂ O	<u>C</u> = CO ₃	
A = Al ₂ O ₃	M = MgO	

This leads to the following abbreviations for anhydrous and hydrates phases:

C ₃ S	3CaO. SiO ₂	Tricalcium silicate
C ₂ S	2CaO. SiO ₂	Dicalcium silicate
C ₄ AF	4CaO. Al ₂ O ₃ . Fe ₂ O ₃	Ferrite
C ₃ A	3CaO. Al ₂ O ₃	Tricalcium aluminate
C\$H ₂	CaSO ₄ . 2 H ₂ O	Gypsum
<u>CC</u>	CaCO ₃	Calcium carbonate
CH	Ca(OH) ₂	Calcium hydroxide
C-S-H	CaO. SiO ₂ . H ₂ O	Calcium silicate hydrate
C-A-S-H	CaO. Al ₂ O ₃ . SiO ₂ . H ₂ O	Calcium silicate aluminate hydrate
AFt	3C ₃ A. 3C\$.H ₃₂	Ettringite
phase	3CaO. Al ₂ O ₃ . 3CaSO ₄ . 32H ₂ O	
	3C ₃ A. C\$.H ₁₂	Tricalcium monosulfo aluminate
	3CaO. Al ₂ O ₃ . CaSO ₄ . 12H ₂ O	
AFm	3CaO. Al ₂ O ₃ . 0.5Ca(OH) ₂ . 0.5 CaCO ₃ . 11.5H ₂ O	Calcium hemicarboaluminate
phases	3C ₃ A. <u>C</u> . H ₁₁	Calcium monocarboaluminate
	3CaO. Al ₂ O ₃ . CaCO ₃ . 11H ₂ O	

The following abbreviations are also used:

BSE	BackScattered Electron
DTA	Differential Thermal Analysis
DSC	Differential Scanning Calorimetry
EDS or EDX	Energy Dispersive X-Ray Spectroscopy
NMR	Nuclear Magnetic Resonance
OPC	Ordinary Portland Cement
PSD	Particle Size Distribution
SEM-IA	Scanning Electron Microscopy–Image Analysis
TGA	Thermogravimetric Analysis
w/c	Water to Cement ratio
wt%	Weight percent
XRD	X-Ray Diffraction
XRF	X-Ray Fluorescence

CHAPTER I: INTRODUCTION

I.1. BACKGROUND

Cementitious materials have been used since pre-Roman times and are now by far the most widely used construction material in the world.

The need to limit the environmental impact of cementitious materials and disposal of by-products leads to the increasing use of supplementary cementitious materials, such as slag, fly ash, silica fume, pozzolan either pre-blended with ground clinker or added during the fabrication of concrete. The use of these secondary raw materials in the cement industry increases fuel efficiency, reduces the production and capital costs and allows the utilisation of waste products.

The chemical composition of slag is fairly close to that of Portland cement. For a given source of slag, the chemical composition remains relatively constant, especially compared to fly ash (silica fume is also very constant in composition, for pozzolan it depends on sources). Figure I-1 shows the relative compositions of cementitious materials of different SCMs. Besides, it has advantages like low heat of hydration, high sulfate resistant and chloride ingress, higher ultimate strength, etc. These properties are especially beneficial towards certain applications such as hydroelectric dams, large bridges, power stations, metro systems, motorways, and harbours [1].

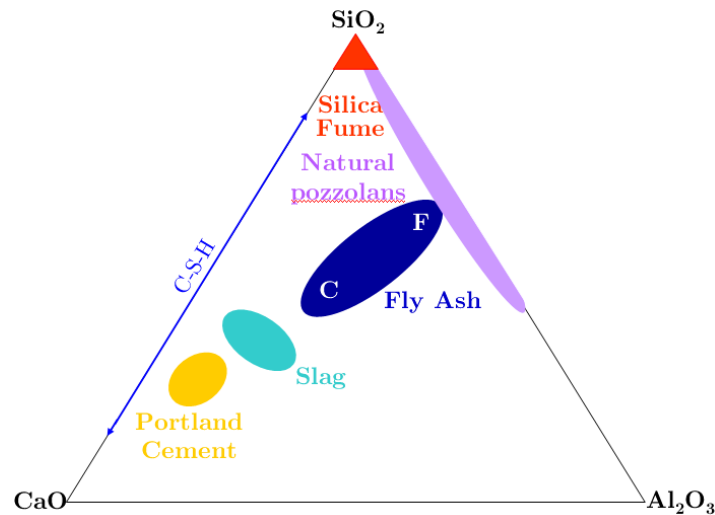


Figure I-1: ternary diagram of $\text{CaO}-\text{Al}_2\text{O}_3-\text{SiO}_2$ representing the composition of cementitious materials

I.2. OBJECTIVES AND RESEARCH SCOPE

It is well known that these SCMs generally react at relatively slower rates than cement clinker and this limits the levels of substitution, due to the need for sufficient properties at early ages.

To optimise the use of slag, the relations between the properties of the cement constituents and their performance in paste have to be better understood. For this reason, an accurate method is needed to determine the actual rate of reaction of the different components in blended systems.

The objective of the project was to develop a methodology to study the reactions of clinker and slag separately in blended cements. The presence of different phases requires the use of complementary techniques. X-ray diffraction allows investigation of the crystallized phases. However, in blended cement systems the amorphous structure of slag limits the application of this technique and requires other complementary methods like electron microscopy and thermal analysis. Reaction in cement blends can be also followed by isothermal calorimetry and chemical shrinkage.

I.3. CHOICE OF MATERIALS

A selection of raw materials was received, to begin with: 12 cements and 9 slags.

The cements were classified according different parameters influencing reactivity: C_3S , C_3A , alkali contents and granulometry, in order to distinguish similar cements and slags.

To avoid duplication of similar materials, the following materials were considered in our investigation (Table I-1):

Materials	Characteristics
Cement A	CEM I 52.5 White cement high C_3S , low C_3A , low alkali contents
Cement B	CEM I 32.5 R low C_3S , medium C_3A , high alkali contents
Cement C	CEM I high C_3S , medium C_3A , high alkali contents
Cement D	CEM I 52,5 N high C_3S , low C_3A , high alkali contents
Slag 1	high amorphous content typical used composition
Slag 8	high amorphous content a part of crystalline phase high alumina content

Table I-1: main characteristics of selected materials

The cements chosen included those with both low and high alkali contents. It is known that alkalis are the major factor in affecting the reactivity of SCMs: therefore, the methodology should work with both low and high alkali contents.

All cements in this selection contain little or no calcite.

I.4. OUTLINE OF THE THESIS

The thesis is composed of seven chapters and the appendices. The following paragraph gives a short outline of each chapter as part of the overall content.

The characterisation of anhydrous cementitious materials is described in Chapter II.

Chapter III presents the results of the investigations and improvements of methods to study hydrated cementitious materials

Chapters IV and V deal with the reactivity of slags in blended pastes, Chapter IV describes how the slag affects the reaction of cement, whereas Chapter V focuses on different methods investigated to measure the degree of reaction of slags in blended pastes.

Chapter VI presents an overview of the mechanical properties linked with microstructural development of blended mortars.

Chapter VII summarises the conclusions of the present work, discusses some points and outlines areas for further work.

CHAPTER II: QUANTITATIVE ANALYSIS OF ANHYDROUS CEMENTITIOUS MATERIALS

This chapter describes the strategy and the various techniques used to characterize the anhydrous materials.

II.1. QUANTITATIVE ANALYSIS ON ANHYDROUS CEMENTS

II.1.1. STATE OF THE ART

Cement and ground clinker are widely studied using X-ray fluorescence as an analytical tool for qualitative and quantitative oxide analysis. To estimate the potential phase composition from these oxides the Bogue calculation is the most widely applied method [2,3]. However, it is well recognised that estimated amounts of individual phases derived by the Bogue calculation show major deviations from the true values due mainly to variations in stoichiometry. Sorentino *et al.* [4] reported that even small errors in oxides analysis may lead to large errors in the estimation of phase contents.

Other physical methods such as optical microscopy, scanning electron microscopy (SEM) and X-ray diffraction have been shown to be effective to determine the phase composition of clinkers, other methods, such as infra-red spectroscopy, give an indication of the phases present but are less suitable for quantification [5].

By using point counting [6-11] or line counting methods [12], it is possible to obtain a quantitative phase composition of clinkers for alite and belite by optical microscopy.

The quantification of aluminate and ferrite interstitial phases by this method is often quite difficult because of their very small crystal size within the microstructure [5].

Some differentiation between the orthorhombic aluminate phases and ferrite can be possible if the ferrite phase is also orthorhombic with a typical dendritic or prismatic configuration [8].

As noted by Aldridge [7], optical microscopy gives accurate results for the quantitative determination of phases in clinkers, only with an experienced operator and adequate sampling. In addition, optical point counting is not sensitive to differences in chemical composition or different crystal modifications. As an alternative to point counting, image analysis (IA) of backscattered electron (BSE) images is widely used to increase the spatial resolution and the statistics [13].

The use of quantitative XRD to study the chemistry of cement is not new and has been widely reported, different approaches have been taken:

- comparison of measured intensities with precalculated diffractometric constants of pure clinker minerals using one reflection [14] or more [15] for each phase;
- matching the observed and computed patterns. For example, Gutteridge [16] collected data for a sample and pure phases and he matched the profiles, observed and calculated intensities integrated over selected ranges of angles;
- and more recently, combining the quantitative X-ray diffraction with the Rietveld method. Previous studies [17-19] showed that the XRD-Rietveld is a reliable analysis method to quantify cementitious phase amounts in multiple phase mixtures. This direct measurement uses the full profile fitting procedure that allows to overcome the problem of peak overlap.

Gutteridge [16] used X-ray intensity data collected from a set of some thirty synthesised cement minerals (primary standards) partially incorporate the effect of substitution and solid solution which occurs in the four principal cement phases of a Portland cement.

Rietveld phase analysis consists of appropriate refinement strategies using a well defined control file of the anhydrous cement. Over several years, this kind of essential control files have been established through extensive calibration with model mixtures of synthetic phases and with materials for which the actual composition is known by other independent methods [8,9,20].

Several advances in research reported in the literature [17-19] have used the Rietveld method and have shown that it is well adapted to quantify the phase composition of anhydrous cements. A recent Round Robin study [21] proved both the repeatability and reproducibility of the Rietveld method.

One of the main objectives of our study is to determine the composition of different cements by XRD-Rietveld incorporating the latest progress in the knowledge of the cementitious crystal structures and identify the limitation of this quantification.

To validate the quantitative analysis of anhydrous cements from XRD-Rietveld, the results were compared to those from ^{29}Si Nuclear Magnetic Resonance (NMR) made by Søren Poulsen at the University of Aarhus, in parallel to this project [22].

^{29}Si NMR represents an alternative tool for quantitative studies of the silicate phases. As it depends on local structural order it can detect equally amorphous and crystalline phases. However, due to the low natural abundance of ^{29}Si (4.7%) and its potentially long relaxation times, this method requires significantly longer instrument times as compared to XRD-Rietveld. As explained in [23], ^{29}Si NMR spectra of anhydrous Portland cements reflect the molar ratio of alite and belite [24,25]. This ratio came from deconvolution of the overlapping resonances from alite and belite and can provide a valuable estimate of the quantities of alite and belite when combined with the bulk SiO_2 content from an elemental analysis. Using this approach, quantities of alite and belite have been determined by ^{29}Si NMR for different cements and compared with our XRD results.

The basis for quantitative characterisation of clinker phases using NMR technique is more detailed in [23].

II.1.2. X-RAY DIFFRACTION ANALYSIS

II.1.2.a. Sample preparation for XRD

X-ray diffraction (XRD) data were collected using a PANalytical X'Pert Pro MPD diffractometer in a θ - θ configuration employing $\text{CuK}\alpha$ radiation ($\lambda=1.54 \text{ \AA}$) with a fixed divergence slit size 0.5° and a rotating sample stage. The samples were scanned between 7° and 70° with an X'Celerator detector.

A step size of 0.017° acquired for 40 s at a scan speed of $0.05^\circ.\text{s}^{-1}$, leading to a total scan time of 20 minutes.

The ground powders were manually frontloaded into a standard circular standard sample holder (diameter 3.5 cm) by lightly pressing with a frosted glass side to minimize preferred orientation. Backloading using a press was also used to check the effect of sample preparation.

II.1.2.b. Principle of the Rietveld analysis

The principle of Rietveld analysis [26] is to iteratively compare the experimental pattern with a pattern simulated of a mixture of known phases based on multiple parameters such as the presumed amounts, crystal parameters, and equipment parameters. All these parameters may be adjusted between iterations to minimise the difference between experimental and simulated patterns by least squares fitting.

Our approach is divided in two parts: first the crystal phases were identified, completely characterised and finally quantified. The strategy of XRD-Rietveld refinement started with approximate structures of cement phases and was optimised during the study to properly correspond to the phases in our cementitious systems. So in the following parts, the structures of cement phases are identified and the parameters of the refinement are detailed for each cement.

II.1.2.c. Identification of structures of phases in the anhydrous samples

The phase identification process was carried out in two steps: first search step, then match step consisting a confrontation of probable data with that is the possible chemical composition.

As shown in Table II-1, all the cementitious phases were initially identified using the X'Pert High Score Plus program from PANalytical with reference structures from the Inorganic Crystal Structure Database (ICSD).

Anhydrous phases	Formula	Crystal system	In materials	ICSD codes	Reference	
Cements and clinkers	Alite	Monoclinic/M ₃	A, B, C, D	-	Nishi <i>et al.</i> , 1985 [27]	
		Monoclinic/M ₁	L, C	94742	de La Torre <i>et al.</i> , 2002 [28]	
	Belite	Monoclinic/β	A, B, C, D, L	79550	Tsurumi <i>et al.</i> , 1994 [30]	
		Orthorhombic/α' _H	B	81097	Mumme <i>et al.</i> , 1995 [31]	
	Tricalcium aluminate	Ca ₃ Al ₂ O ₆	Cubic	A, B, C, D, L	1841	Mondal <i>et al.</i> , 1975 [32]
	Ferrite	Ca ₂ AlFeO ₅	Orthorhombic	B, C, D, L	9197	Nishi <i>et al.</i> , 1975 [33]
	Lime	CaO	Cubic	A, B, C, D	75785	Colville <i>et al.</i> , 1971 [34]
	Portlandite	Ca(OH) ₂	Rhombohedral	A, B, C, D	15471	Huang <i>et al.</i> , 1994 [35]
	Periclase	MgO	Cubic	A, B, C, D	104844	Petch, 1961 [36]
	Calcite	CaCO ₃	Rhombohedral	A, B, C, D	79674	Taylor, 1984 [37]
	Gypsum	CaSO ₄ · 2H ₂ O	Monoclinic	B, C, D	2059	Wartchow, 1989 [38]
	Hemihydrate	CaSO ₄ · 0.5H ₂ O	Monoclinic	A, B, C, D	73263	Cole <i>et al.</i> , 1974 [39]
	Anhydrite	CaSO ₄	Orthorhombic	A, B, C, D	40043	Abriel <i>et al.</i> , 1993 [40]
	Arcanite	K ₂ SO ₄	Orthorhombic	A, B, C, D	2827	Hawthorne <i>et al.</i> , 1975 [41]
					McGinnety, 1972 [42]	

Table II-1: structures of phases in the anhydrous samples

Choice of alite polymorph

For alite, the monoclinic M_3 structure from Nishi *et al.* [27] was initially used for the four main cements because the peaks corresponded quite well to our XRD patterns.

In the case of alite, the structure of the different C_3S polymorphs is complicated by the disorderly orientation of silicate ions. In order to correctly choose the alite polymorph, a detailed analysis of XRD patterns was made on windows from 31.5 to 33.5° and from 51 to 53°, as proposed in previous studies [29,43].

Using the approach discussed above, alite polymorphs were identified for our cements (see Figure II-1) and also confirmed by ^{29}Si NMR investigations [44]:

- the M_3 polymorph was observed in Cements A, B, D, so the recent structure from De La Torre *et al.* [28] was used for these three cements;
- the M_1 polymorph was identified in Clinker L and the corresponding structure from De Noirfontaine *et al.* [29] was used;
- a mixture of both polymorphs was found in Cement C. However, even if both polymorphs are present, it was found better [45] to use only one model for the refinement.

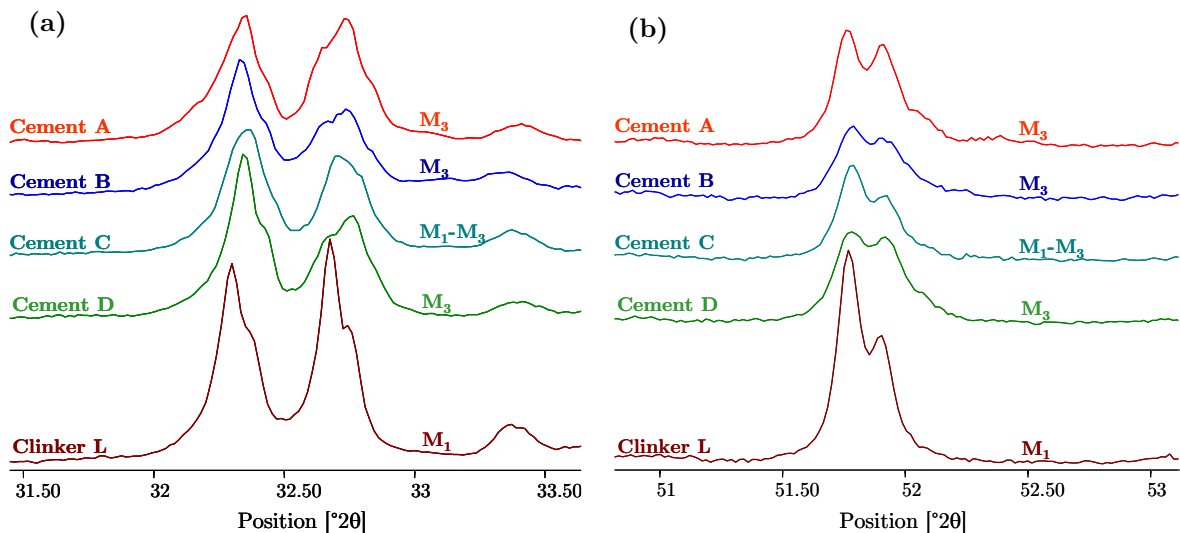


Figure II-1: XRD patterns with two angular windows (a) 31.5-33.5°, (b) 51-53° that allow the M_3 alite polymorph (Cements A, B and D), M_3+M_1 (Cement C) and M_1 (Clinker L) to be identified

Maki *et al.* [46] suggested that the polymorph of alite depends primarily on the amount of MgO in clinker. As shown in Figure II-2, an increase in MgO content induces changes in the alite polymorph from M_1 to M_3 through the mix of M_1 and M_3 . The presence of SO_3 in clinker favors the formation of M_1 polymorph.

Figure II-2 supports the occurrence of M_1 in the Clinker L according to the contents of MgO and SO_3 .

Assuming that the content of MgO in clinker is equivalent to that of the cements and estimating the SO_3 content of the clinker from the alkalis, the clinkers corresponding to Cements A, B, C and D are also represented in Figure II-2. Except for Clinker A, which is a particular case because it is a white clinker, Clinkers B and D correspond to the M_3 polymorphs and the Clinker C agrees the mix of M_1 and M_3 polymorphs.

These results support the conclusions of Maki *et al.* [46].

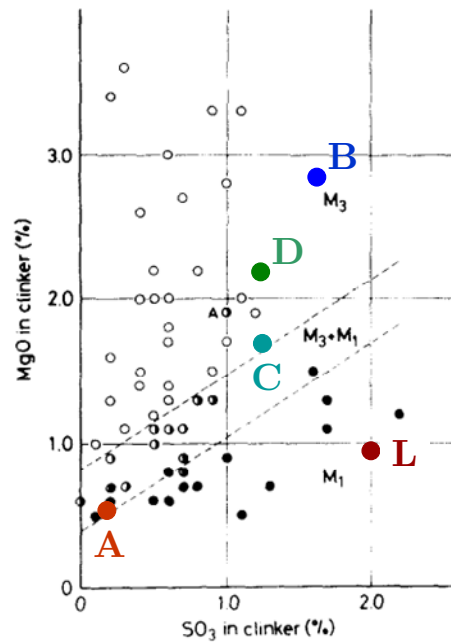


Figure II-2: dependence of the polymorphic modification of alite in clinkers on the MgO and SO_3 contents of the clinkers [46]

Other reference structures

The monoclinic structure of belite from Tsurumi *et al.* [30] is appropriate for the four cements and also for Clinker L. For Cement B, the α'_H form is identified using the approach reported by Mumme *et al.* [31].

For tricalcium aluminate phases, the cubic form from Mondal *et al.* [32] is found in all cements and clinker. However, the orthorhombic structure from Nishi *et al.* [33] is also present in Cements B, C and D.

The ferrite phase present in all compounds (except in Cement A which is a white cement) is identified using the structure described by Colville *et al.* [34].

For the minor phases, the reference structures are similar for all cements and Clinker L.

II.1.2.d. Quantification of XRD patterns by Rietveld refinement

Main parameters of Rietveld refinement

The following equations detail the parameters used in the Rietveld refinement.

The main following equation describes the calculated intensity at the i^{th} step in the data summing over the p phases in the mixture and where K corresponds to plane indices (hkl) [47].

The parameters, which were specifically considered in this work, are discussed in the following section.

$$y_{ci} = \sum_p \left[S_p \sum_K P_K L_K |F_K|^2 \Phi(\Delta\vartheta_{iK}) P_K \right] + y_{cbi} \quad \text{Equation 1}$$

$$F_K = \sum_j N_j f_j \exp^{[2i\pi(hx_j + ky_j + lz_j)]} \exp^{(-B_j)} \quad \text{Equation 2}$$

Structure factor-knowledge of the crystal structures of all phases:

$$\Phi(\Delta\vartheta_{iK}) = (1 - \eta) G(\Delta_{iK}, H_K) + \eta L(\Delta_{iK}, H_K) \quad \text{Equation 3}$$

Profile function to simulate the peak shape:

$$H_K^2 = U \tan^2 \vartheta_K + V \tan \vartheta_K + W \quad \text{Equation 4}$$

$$P_K = (R^2 \cos^2 \alpha_K + R^{-1} \sin^2 \alpha_K)^{-3/2} \quad \text{Equation 5}$$

Preferred orientation:

Where:

y_{ci} : calculated intensity at the i^{th} step in the data;

y_{cbi} : calculated intensity at the i^{th} step of the background;

S_p : scale factor proportional to the number of unit cells contributing to the scattering divided by the unit cell volume;

p_K : multiplicity factor;

L_K : Lorentz and polarisation factors;

F_K : structure factor;

x_j, y_j, z_j : coordinates of the j^{th} atom in the unit cell;

N_j : fractional occupancy for the j^{th} atomic site;

f_j : atomic X-ray scattering factor;

B_j : temperature factor;

Φ : profile function;

η : pseudo-Voigt mixing parameter;

H_K : Full Width at Half Maximum (FWHM);

U, V, W : refinable parameters;

P_K : preferred orientation function;

R : March coefficient (index of the extent of preferred orientation equal to unity for an ideal random powder sample);

α_K : angle between the preferred orientation direction and the normal to crystallites.

The background of anhydrous materials was refined by a fifth-order polynomial function (called Chebyshev polynomial function).

Structure factor F_K

To build the structure factor F_K , a knowledge of the crystal structures of all phases is required. Thus, the lattice parameters which define the unit cell of each structure are refined (see Table II-2), the scattering and occupancy factors can vary in this work but atomic coordinates (x_j, y_j, z_j) and the isotropic thermal displacement parameter B_j were kept constant.

Except for Cement A (which did not contain this phase), to take into account the solid solution of the ferrite phase, the fractional occupancy N_j of Al and Fe in octahedral and tetrahedral positions was refined. As described by Neubauer *et al.* [48]. The (020) reflection at 12.1° depends strongly on the distribution of Al and Fe in contrast to the main reflection (141) at 33.7° . The refinement of the occupancy factor enables better simulation of the (020) [45].

In other phases, the occupancy factor was not refined because their atoms do not have a large scattering factor, contrast is small and there is no clear description of the crystallographic sites where substitution occurs.

Profile function ϕ

To simulate the profile function of the phases the pseudo-Voigt function was used with a simple linear combination of Lorentzian L and Gaussian G functions. Then, as shown in the Equation 3, the variation of the full width at half maximum of the Gaussian and Lorentzian components were both modelled with the function described by Caglioti *et al.* [49].

Most of the time, the refinement of the W parameter was sufficient to simulate the peak shape precisely enough. In practice, the simultaneous refinement of U, V and W at the same time only introduces an error in the quantification of the corresponding phase by ± 0.5 wt%. So the U, V and η parameters are kept constant: $U=V=0$ and $\eta=0.6$, which corresponds to a value recommended by Roode-Gutzmer *et al.* [18], in the case of Bragg-Brentano X-ray diffraction patterns, in step scan mode and using CuK_α radiation.

Preferred orientation P_K

When the powder is compacted in the sample holder, some crystallographic planes become preferentially orientated parallel to the sample surface due to crystal morphology. This phenomenon modifies the intensities of the diffracted lines which can be quite different to a random distribution. This effect can be partially counteracted by the use of a PO correction.

For alite, the preferred orientation is often seen for the (60-6) plane at 32.25° . Without preferred orientation, this height of this peak is roughly the same as the height of the two close doublets at $32.51\text{-}32.66^\circ$ and $34.36\text{-}34.41^\circ$.

In the case of anhydrous cements, the preferred orientation may appear in alite, gypsum, anhydrite, hemihydrate and calcite which can be corrected in accordance to the March model, which Dollase [50] reported using a single pole-density profile with a relatively simple functional form.

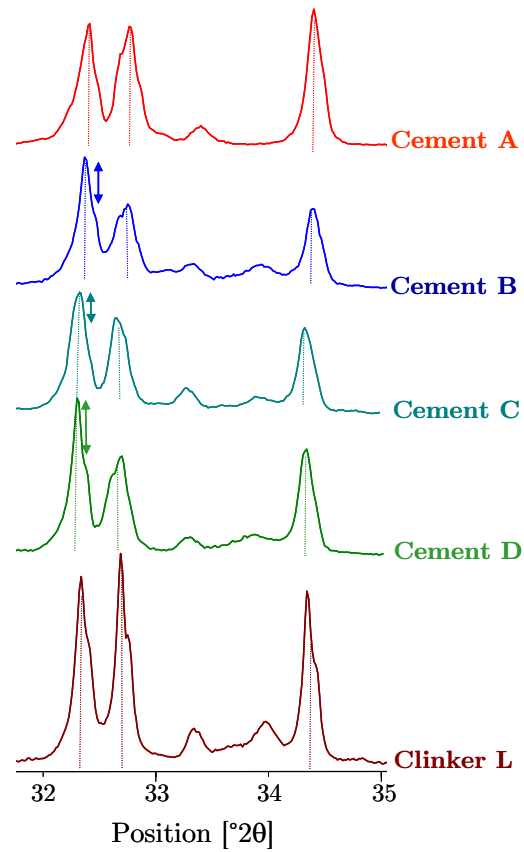


**Figure II-3: identification of preferred orientation
of alite for the 4 cements and Clinker L**

In the XRD patterns shown in Figure II-3, some preferred orientation is identified for alite in the case of Cement B, C and D.

As reported in previous studies [45], the preferred orientation can be reduced by a vertical loading of the cementitious powder. In our case, the vertical loading did not reveal significant difference on preferred orientation compared to the front loading pressed with a frosted glass.

Summary of our main refined parameters

Taking into account all the parameters previously described, each anhydrous cementitious material has its own control file with specific conditions for Rietveld analysis. The main parameters are summarised in the following table (Table II-2).

	Phases	In materials	Scale factor	Preferred orientation	Unit cells				Caglioti parameters		
					a	b	c	β	U	V	W
Cements and clinkers	Alite (M_3)	A, B, C, D	x	x	x	x	x	x	-	-	x
	Alite (M_1)	L, C	x	x	x	x	x	x	-	-	x
	Belite (β)	A, B, C, D, L	x	x	x	x	x	x	-	-	-
	Belite (α'_H)	B	x	-	x	x	x	x	-	-	-
	Aluminate (cubic)	A, B, C, D, L	x	-	x	x	x	-	-	-	-
	Aluminate (Orthorhombic)	B, C, D	x	-	x	x	x	-	-	-	-
	Ferrite	B, C, D, L	x	-	x	x	x	-	-	-	-
	Lime	A, B, C, D	x	-	x	x	x	-	-	-	-
	Portlandite	A, B, C, D	x	-	x	x	x	-	-	-	-
	Periclase	A, B, C, D	x	-	x	x	x	-	-	-	-
	Calcite	A, B, C, D	x	-	x	x	x	-	-	-	-
	Gypsum	B, C, D	x	x	x	x	x	x	-	-	x
	Hemihydrate	A, B, C, D	x	x	x	x	x	x	-	-	-
	Anhydrite	A, B, C, D	x	-	x	x	x	x	-	-	x
	Arcanite	B, C, D	x	-	x	x	x	x	-	-	-

Table II-2: refined parameters as a function of phases taken into account

II.1.2.e. Reproducibility of the Rietveld refinement

The use of hydraulic press with a defined pressure leads to generation of XRD data independent of the operator and a high reproducibility.

Therefore, it was made for the 4 main cements to establish the variation between pellet and powder samples (see details in Tables II-3 to II-6 which summarised the main fits of the XRD patterns obtained from the start to the end of our Rietveld refinement approach.).

In order to validate our XRD-Rietveld quantifications, the four main anhydrous cements samples were sent to Chancey (University of Texas at Austin) without any indications about the Rietveld refinement results previously found. He used a different Rietveld software: TOPAS (against X-Pert High Score Plus for us) and some NIST control files to refine the XRD patterns.

Taking into account the error for each phase, the contents of different phases found by The University of Texas are very close to ours and clearly validate our Rietveld refinement method.

Weight fractions of Anhydrous Cement A						
Phases	Formula	Fit on powder	Fit on pellet	Fit done by	Fit done using	Difference
		sample using M_3 -Nishi	sample using M_3 -Nishi	University of Texas	M_3 -De La Torre	
Alite	C_3S (M_3)	68.1	66.1	67.1	69.3	3.2
Belite	β - C_2S	23.6	23.6	23.0	23.8	0.8
	α' - C_2S	-	-	-	0.0	0.0
Ferrite	C_4AF	0.0	0.0	0.5	0.0	0.5
	cubic C_3A	2.9	3.0	3.0	3.7	0.9
Aluminate	orthorhombic C_3A	0.7	0.6	0.0	0.0	0.7
	Total C_3A	3.5	3.5	3.0	3.7	0.8
Lime	C	0.8	0.8	0.1	0.0	0.8
Periclase	M	0.0	0.4	0.6	0.0	0.6
Gypsum	$CaSO_4 \cdot 2H_2O$	0.0	0.0	0.1	0.0	0.1
Hemihydrate	$CaSO_4 \cdot 0.5H_2O$	0.5	1.0	1.7	1.0	1.1
Anhydrite	$CaSO_4$	2.9	2.9	2.5	2.2	0.8
Calcium sulfate		3.5	3.9	4.2	3.2	1.1
Arcanite	K_2SO_4	0.0	0.0	0.5	0.0	0.5
Portlandite	CH	0.5	0.4	0.3	0.0	0.5
Calcite	$CaCO_3$	0.0	1.1	0.8	0.0	1.1
Total		100.0	100.0	100.0	100.0	0.0
C_3S/C_2S ratio		2.9	2.8	2.9	2.9	0.1

Table II-3: different XRD-Rietveld refinements for Anhydrous Cement A

Weight fractions of Anhydrous Cement B						
Phases	Formula	Fit on powder	Fit on pellet	Fit done by	Fit done using	Difference
		sample using M_3 Nishi	sample using M_3 Nishi	University of Texas	M_3 -De La Torre and Belite α'_H	
Alite	$C_3S (M_3)$	51.3	51.5	51.7	49.3	2.4
Belite	β - C_2S	20.7	21.5	22.8	18.4	-
	α'_H - C_2S	-	-	-	5.8	-
	Total C_2S	20.7	21.5	22.8	24.2	3.4
Ferrite	C_4AF	10.2	9.9	9.2	10.0	0.9
	cubic C_3A	3.6	3.4	3.5	4.0	0.6
Aluminate	orthorhombic C_3A	2.6	3.3	3.7	1.7	2.1
	Total C_3A	6.3	6.7	7.2	5.7	2.7
Lime	C	1.6	1.5	-	1.4	0.2
Periclase	M	1.9	1.8	2.2	1.9	0.4
Gypsum	$CaSO_4 \cdot 2H_2O$	0.5	0.0	0.0	0.0	0.5
Hemihydrate	$CaSO_4 \cdot 0.5H_2O$	1.9	1.9	3.8	3.0	1.9
Anhydrite	$CaSO_4$	3.4	2.1	1.7	1.3	2.1
Calcium sulfate		5.8	4.0	5.4	4.3	1.8
Arcanite	K_2SO_4	0.0	0.0	1.4	2.1	2.1
Portlandite	CH	0.8	1.1	0.0	1.1	1.1
Calcite	$CaCO_3$	1.5	2.0	0.0	0.0	2.0
Total		100.0	100.0	100.0	100.0	0.0
C_3S/C_2S ratio		2.5	2.4	2.3	2.7	0.4

Table II-4: different XRD-Rietveld refinements for Anhydrous Cement B

Weight fractions of Anhydrous Cement C						
Phases	Formula	Fit on powder	Fit on pellet	Fit done by	Fit done using	Difference
		sample using M_3 Nishi	sample using M_3 Nishi	University of Texas	M_3 -De La Torre	
Alite	$C_3S (M_1-M_3)$	62.6	62.0	63.5	61.8	1.6
Belite	β - C_2S	17.6	19.1	17.6	17.4	1.7
	α'_H - C_2S	-	-	-	0.0	0.0
Ferrite	C_4AF	7.5	6.7	5.8	9.1	3.3
	cubic C_3A	4.5	3.8	5.0	5.6	1.8
Aluminate	orthorhombic C_3A	1.7	2.1	0.7	1.5	1.4
	Total C_3A	6.1	5.9	5.6	7.0	1.4
Lime	C	0.0	0.0	-	0.0	0.0
Periclase	M	0.7	0.7	0.8	0.0	0.8
Gypsum	$CaSO_4 \cdot 2H_2O$	0.6	0.9	0.0	0.0	0.9
Hemihydrate	$CaSO_4 \cdot 0.5H_2O$	1.7	1.5	2.6	1.6	1.1
Anhydrite	$CaSO_4$	2.0	2.1	2.4	1.6	0.8
Calcium sulfate		4.4	4.5	5.0	3.2	1.8
Arcanite	K_2SO_4	0.0	0.0	1.8	1.4	1.8
Portlandite	CH	0.6	0.6	0.0	0.0	0.6
Calcite	$CaCO_3$	0.5	0.5	0.0	0.0	0.5
Total		100.0	100.0	100.0	100.0	0.0
C_3S/C_2S ratio		3.6	3.2	3.6	3.6	0.4

Table II-5: different XRD-Rietveld refinements for Anhydrous Cement C

Phases	Formula	Weight fractions of Anhydrous Cement D				Difference
		Fit on powder	Fit on pellet	Fit done by	Fit done using	
		sample using M_3	sample using M_3	University of	M_3 -De La Torre	
		Nishi	Nishi	Texas		
Alite	C_3S (M_3)	68.2	66.9	66.5	65.6	2.6
Belite	β - C_2S	13.5	14.7	16.0	15.1	2.5
	α' - C_2S	-	-	-	0.0	0.0
Ferrite	C_4AF	8.8	9.8	10.2	10.8	2.1
	cubic C_3A	3.6	3.7	2.7	3.5	1.0
Aluminate	orthorhombic C_3A	0.0	0.0	0.0	0.0	0.0
	Total C_3A	3.6	3.7	2.7	3.5	1.0
Lime	C	0.8	0.0	-	0.0	0.8
Periclase	M	0.6	0.8	0.9	0.0	0.9
Gypsum	$CaSO_4 \cdot 2H_2O$	2.0	2.3	1.6	2.1	0.7
Hemihydrate	$CaSO_4 \cdot 0.5H_2O$	0.6	0.0	0.8	1.1	1.1
Anhydrite	$CaSO_4$	1.1	1.2	0.5	1.1	0.8
Calcium sulfate		3.7	3.5	2.9	4.2	1.3
Arcanite	K_2SO_4	0.0	0.0	1.0	0.7	1.0
Portlandite	CH	0.0	0.0	0.0	0.0	0.0
Calcite	$CaCO_3$	0.8	0.6	0.0	0.0	0.8
Total		100.0	100.0	100.0	100.0	0.0
C_3S/C_2S ratio		5.1	4.5	4.2	4.3	0.9

Table II-6: different XRD-Rietveld refinements for Anhydrous Cement D

Despite the large number of parameters to refine, the Rietveld method shows an improvement in both within and between laboratory repeatability and reproducibility as seen in the last round robin study [51]. Table II-7 below summarises the final results and the corresponding standard deviation obtained from 10 XRD-Rietveld refinements for the 4 anhydrous cements and the Clinker L.

The XRD patterns of anhydrous cements and clinker are given in Appendix 1.

Phases	Formula	Anhydrous Cement A		Anhydrous Cement B		Anhydrous Cement C		Anhydrous Cement D		Anhydrous Clinker L	
		Average (wt%)	SD (wt%)	Average (wt%)	SD (wt%)	Average (wt%)	SD (wt%)	Average (wt%)	SD (wt%)	Average (wt%)	SD (wt%)
Alite	C ₃ S (M ₃)	68.0	0.8	49.1	0.6	64.5	1.5	67.1	0.8	-	-
	C ₃ S (M ₁)	-	-	-	-	-	-	-	-	66.4	0.5
Belite	β-C ₂ S	25.3	0.8	19.4	0.7	16.2	0.7	13.8	0.6	14.2	0.3
	α' _H -C ₂ S	0.0	0.0	6.2	0.2	0.0	0.0	0.0	0.0	-	-
	Total C ₂ S	25.3	0.8	25.5	0.8	16.2	0.7	13.8	0.6	14.2	0.3
Ferrite	C ₄ AF	0.0	0.0	10.7	0.3	8.7	0.2	10.5	0.1	14.2	0.3
Aluminate	cubic C ₃ A	3.6	0.1	4.2	0.1	5.6	0.2	3.6	0.1	5.2	0.1
	orthorhombic C ₃ A	0.0	0.0	1.6	0.1	1.1	0.2	0.0	0.0	0.0	0.0
	Total C ₃ A	3.6	0.1	5.8	0.1	6.7	0.2	3.6	0.1	5.2	0.1
Lime	C	0.0	0.0	1.6	0.2	0.0	0.0	0.0	0.0	-	-
Periclase	M	0.0	0.0	2.2	0.2	0.0	0.0	0.0	0.0	-	-
Gypsum	CaSO ₄ -2H ₂ O	0.0	0.0	0.0	0.0	0.0	0.0	2.2	0.2	-	-
Hemihydrate	CaSO ₄ -0.5H ₂ O	0.7	0.1	2.5	0.5	1.1	0.4	0.6	0.3	-	-
Anhydrite	CaSO ₄	2.4	0.3	0.9	0.3	1.5	0.3	1.2	0.1	-	-
Calcium sulfate		3.1	0.3	3.4	0.7	2.6	0.6	4.0	0.4	-	-
Arcanite	K ₂ SO ₄	0.0	0.0	1.6	0.2	1.3	0.2	1.0	0.2	-	-
Portlandite	CH	0.0	0.0	0.0	0.0	0.0	0.0	0.0	0.0	-	-
Calcite	CaCO ₃	0.0	0.0	0.0	0.0	0.0	0.0	0.0	0.0	-	-
Total		100.0	-	100.0	-	100.0	-	100.0	-	100.0	-

Table II-7: phases composition from XRD-Rietveld for the 4 anhydrous cements and the Clinker L

II.1.3. SEM-POINT COUNTING

It was decided to carry out point counting by SEM to have an independent method of measurement of alite and belite contents.

II.1.3.a. Preparation of samples for SEM examination

Because the principle of SEM-Point counting is to precisely identify and count the grains of alite and belite, one of the challenges of the sample preparation is to obtain very well defined and correct phase boundaries. When the cement powder is fine, this is more difficult to obtain. A series of polishing tests were made on the finer Cement A to obtain correct phase boundaries.

Initially, the anhydrous cements for SEM examination were pressed in compact pellets and impregnated under vacuum in epoxy resin, carefully polished with decreasing grades of diamond powders down to 0.25 μm and covered by a 20 nm carbon coating to create a conducting layer which does not interfere with X-ray microanalysis. The polished sections of each specimen were studied in backscattered electron (BSE) mode using FEI quanta 200 SEM at an accelerating voltage of 15 kV in order to maximize contrast from compositional differences and minimization that resulting from topography [5]. The volume of cement phase analyzed in each individual spot measurement is in the order of 1 μm^3 .

As shown in Figure II-5, when Cement A is impregnated with epoxy resin, the differences between the hard cement grains and the soft resin created some edge effects which induced some intensive charging on the edges of the grains and generated some artifacts in the conventional image analysis treatment.

To reduce these edge effects, a new method of specimen preparation was established with Condé, from the Laboratory of Mechanical Metallurgy at EPFL. As shown in Figure II-4, this method was an infiltration of metal under pressure and consisted of:

- The anhydrous cement was pressed in a pellet and introduced in an alumina crucible with NaCl salt on the back (to protect and maintain the cement pellet at a good position).

- A metal alloy was placed with the top of NaCl salt. The chosen alloy Al-5,7Ni was selected in order to have a very different back-scattered coefficient from the cementitious components to be able to do better contrast for image analysis treatment.

- The crucible was then put for two hours and a half in the furnace under vacuum. The temperature is increased to 710°C to melt metal;

- A pressure of 80 bars was introduced inside the system to force the liquid metal to penetrate the cement pellet;

- After infiltration, the crucible is lowered and cooled against a cooled copper plate, inducing directional solidification;

- After the sample cooled down, it was cut and polished.

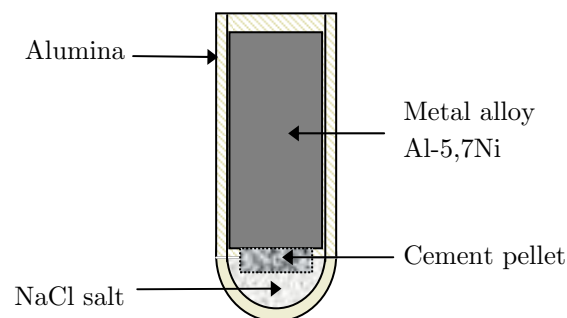


Figure II-4: infiltration of metal under pressure

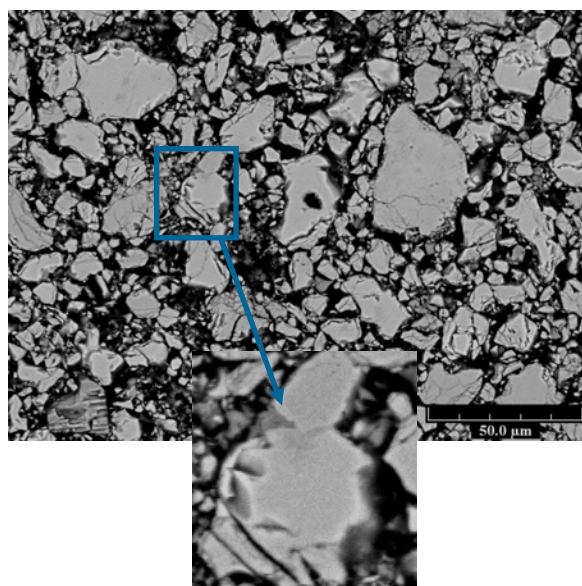


Figure II-5: SEM-BSE picture of Cement A impregnated in epoxy resin with lots of grain fracturing, edge poorly defined and accumulation of charges

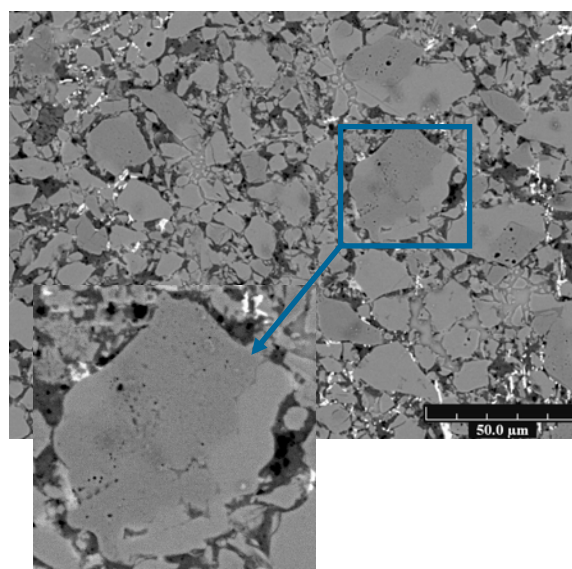


Figure II-6: SEM-BSE picture of Cement A impregnated in metal alloy which reduces the border effects and does not allow accumulation of charges

This impregnation in metal alloy was optimised for Cement A. However, it should be noted that the edge effects are also prominent in other resin impregnated cements. Figure II-6 clearly shows that the surface aspect is improved which reduces the artifacts due to border identification in image analysis and gives better distinction between alite and belite.

Metallic impregnations, thin sections and gold coating on polished sections were investigated but did not significantly improve the charges effects on the edges of the grains.

Finally, except for Cement A, the three other cement specimens were investigated on conventional resin impregnated polished sections.

II.1.3.b. Microstructure of anhydrous cements

Cement A (White cement) has a particular microstructure mainly composed of alite and belite (see Figure II-7). For Cement B, alite, belite, ferrite and aluminates are well defined with a very coarse interstitial part between aluminates and ferrite (see Figure II-8). It could be noted that this separation between aluminates and ferrite is also present in Cement C and D (see Figures II-9 and II-10).

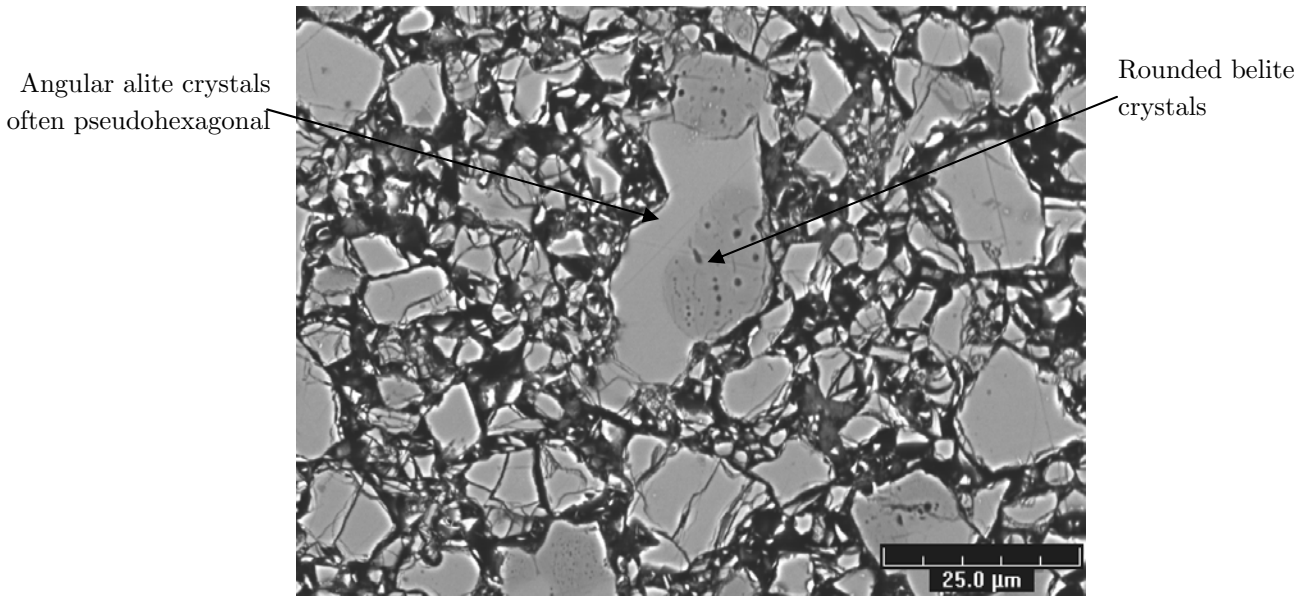


Figure II-7: representative SEM-BSE image of anhydrous Cement A (White cement)

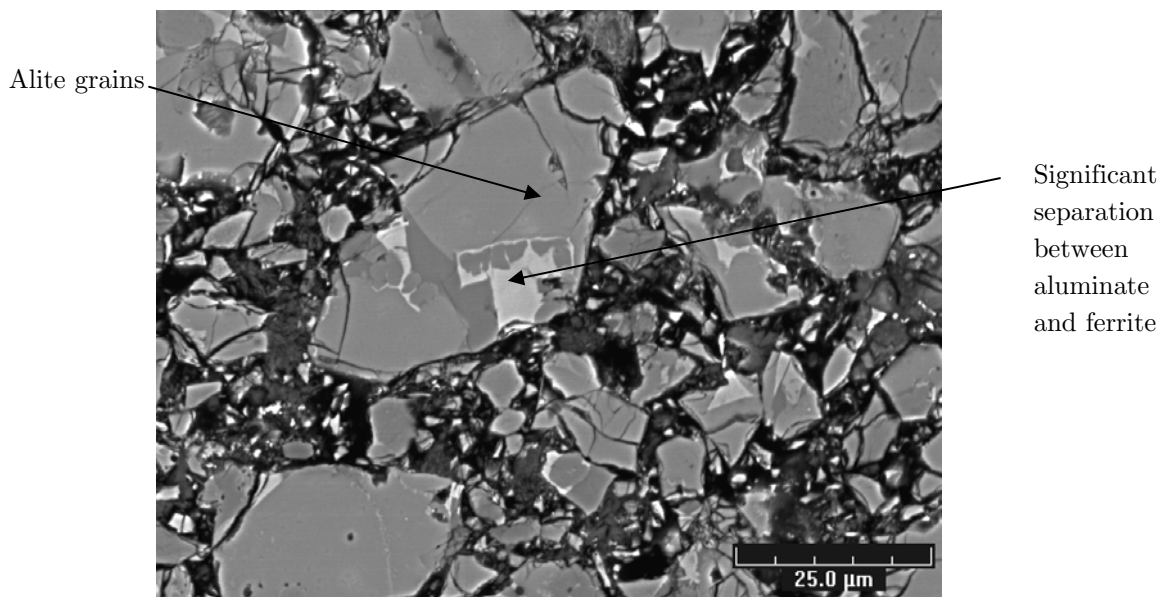


Figure II-8: representative SEM-BSE image of anhydrous Cement B

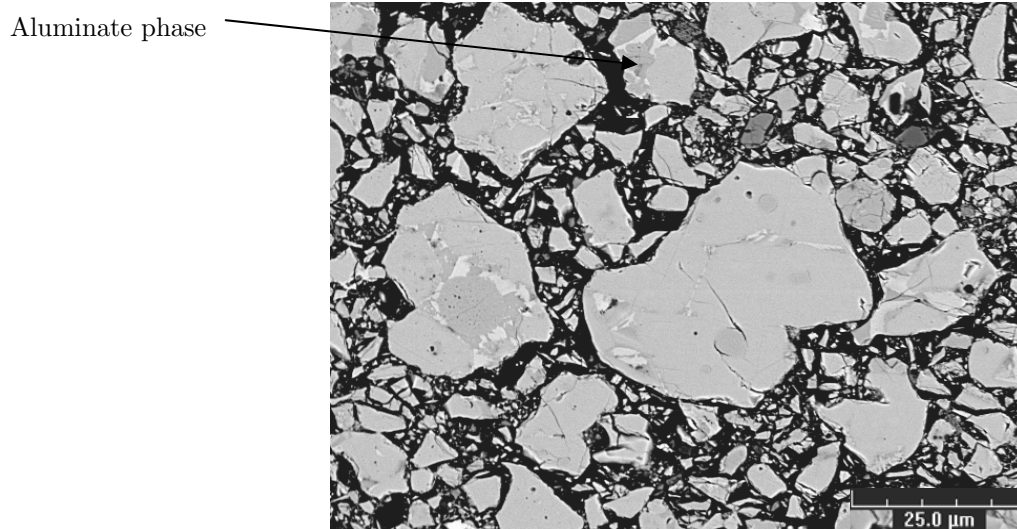


Figure II-9: representative SEM-BSE image of anhydrous Cement C

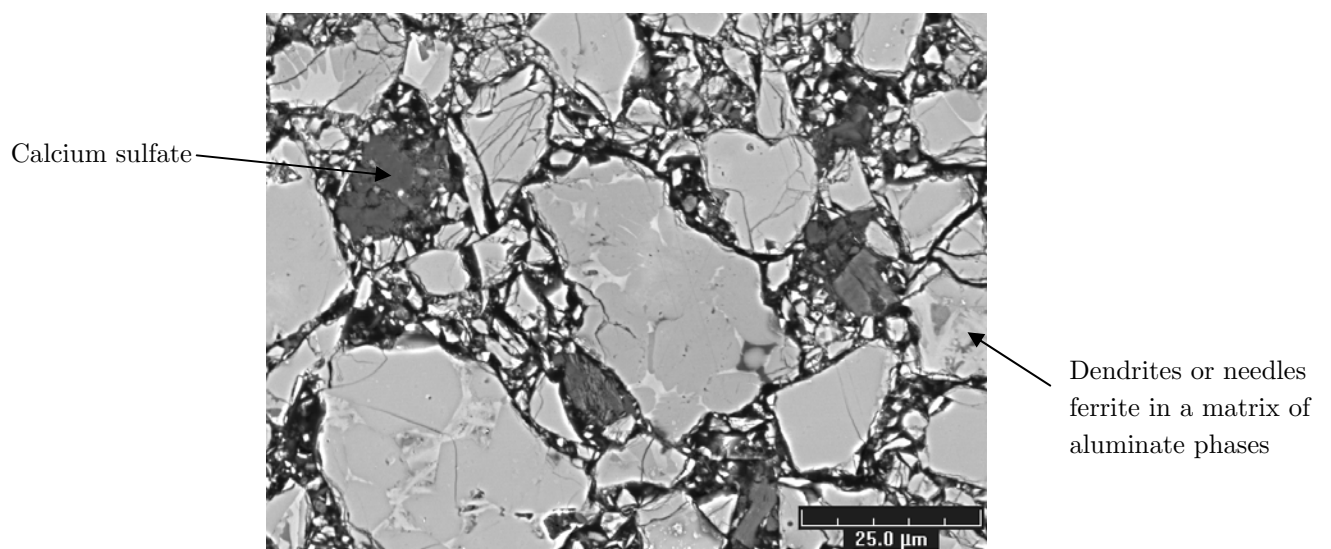


Figure II-10: representative SEM-BSE image of anhydrous Cement D

II.1.3.c. SEM-Point counting method

The first preliminary study on point counting analysed 108 points/SEM-BSE picture and each point was assigned to a particular phase manually, but the number of points was too low to generate realistic results. So then an automatic method was tried to increase the accuracy of the point counting method. For this, a more representative sample and more precise image analysis treatment was used (as it was suggested in [12]), which, in our case, consisted of:

- taking 100 SEM-BSE pictures (0.37 $\mu\text{m}/\text{pixel}$) on Cement B and C, and 400 SEM-BSE pictures (0.185 $\mu\text{m}/\text{pixel}$) on Cement A and D depending on the grain size;
- applying detail image processing to remove noise and imaging artifacts;
- placing a superimposed grid of 7 000 random points/image;
- attributing each point to the corresponding phase with an automatic identification algorithm based on grey level.

The statistical approach by point counting was found to be better than an area counting in order to better identify phases without border effects.

Each point was attributed to the corresponding phase by the following automatic treatment: For each proposed point, there were 7 possibilities: resin, alite, belite, aluminate, ferrite, gypsum or border between alite and belite. The treatment only counted points when they were in alite or belite phase, in other cases, they were excluded.

To reduce the problem of border effect, an edge filter type Roberts was used to well define the edges of the grains. This morphological filter is based applying a horizontal and vertical filter in sequence. Both filters are applied to the image and summed to form the final result (see method in Figure II-11).

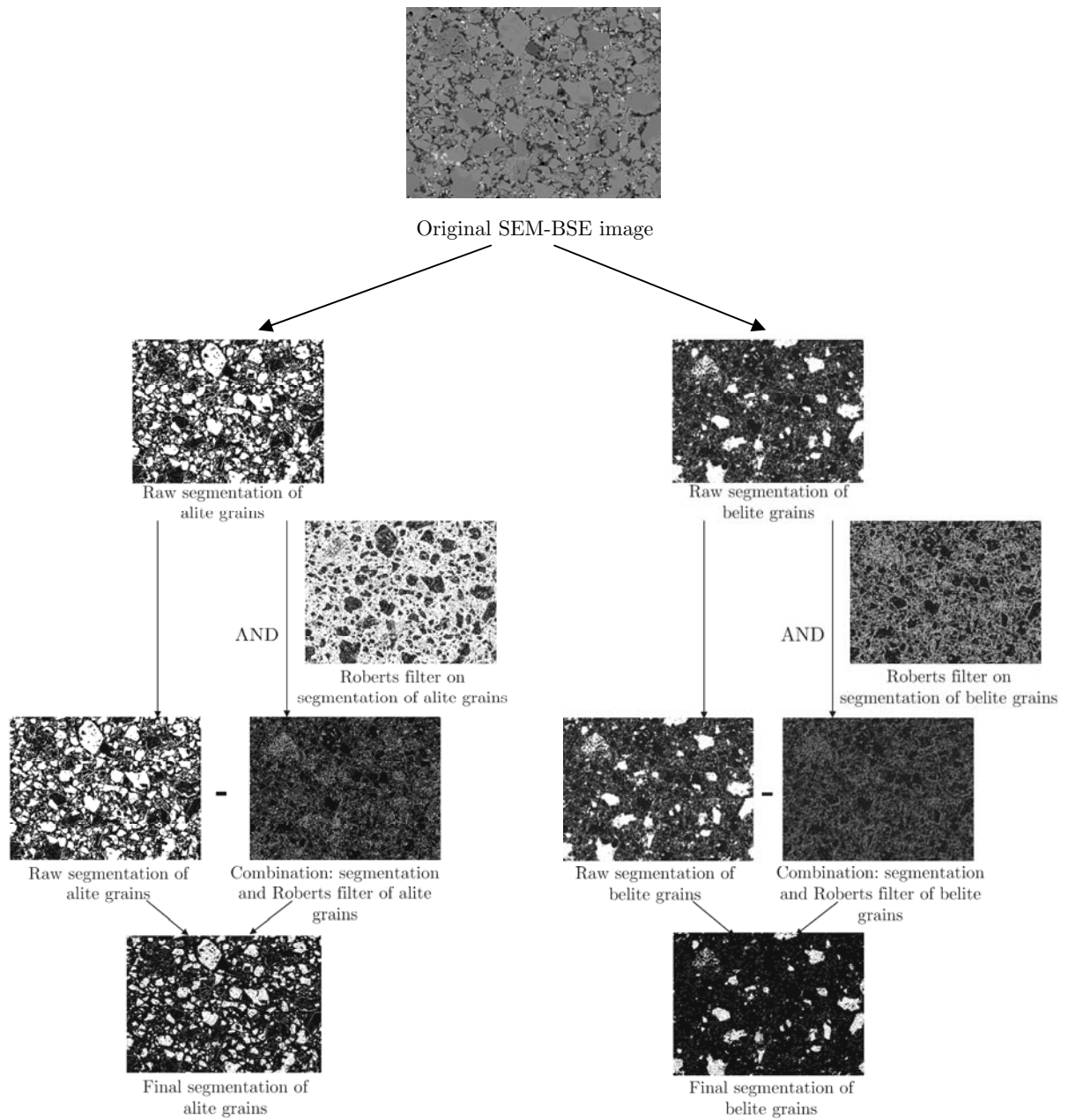


Figure II-11: method of segmentation from the original SEM-BSE image to the final segmented images of alite and belite grains

II.1.3.d. Results of SEM-Point counting

The area fraction is directly equivalent to the volume fraction as proved mathematically [52] irrespective of the shape of the phases provided only that the sample is statistically isotropic. So the area fraction of alite to belite is a direct estimate of the alite to belite volume ratio. This can be corrected to weight fraction. The Rietveld results can be converted to volume fraction VF or to weight fraction W to acquire the weight ratio (see equations below).

$$VF_{\alpha} = \frac{S_{\alpha} V_{\alpha}^2}{\sum_p S_p V_p^2} \quad \text{and} \quad W_{\alpha} = \frac{S_{\alpha} \rho_{\alpha} V_{\alpha}^2}{\sum_p S_p \rho_p V_p^2} \quad \text{Equations 6 and 7}$$

Where:

S: surface of phase;

ρ : density;

V: unit cell volume.

The values of densities came from the calculation of the unit cell which was provided by the ICSD file and the stoichiometric formula (Table II-1). It could also be determined by actual formula which took into account the minor elements from energy dispersive X-ray spectroscopy results (EDS results are detailed in Table II-10).

As shown in Table II-8, both methods to determine densities slightly differed. However, the difference in densities was low on alite and belite (less than 0.02) and this difference introduced a small error in the calculation of weight fraction content.

		Density (g/cm ³)		
		Alite	Belite	
			β	α'_H
Cement A	Stoichiometric formula (using cell parameters from XRD)	3.16	3.30	-
	Actual formula (with minor elements from EDS)	3.15	3.29	-
	Difference	0.01	0.01	-
Cement B	Stoichiometric formula (using cell parameters from XRD)	3.17	3.31	3.27
	Actual formula (with minor elements from EDS)	3.15	3.32	3.28
	Difference	0.02	0.01	0.01
Cement C	Stoichiometric formula (using cell parameters from XRD)	3.16	3.30	-
	Actual formula (with minor elements from EDS)	3.17	3.32	-
	Difference	0.01	0.02	-
Cement D	Stoichiometric formula (using cell parameters from XRD)	3.17	3.30	-
	Actual formula (with minor elements from EDS)	3.16	3.29	-
	Difference	0.01	0.01	-

Table II-8: density values from stoichiometric and actual formulas

Figure II-12 shows the weight and volume ratios deduced by XRD-Rietveld refinement and SEM-Point counting. The error bars for XRD-Rietveld correspond to the error corresponding to the reproducibility measurements.

In SEM-Point counting method, the border effect was taken into account using a morphological filter. To evaluate the errors induced by its restriction on borders of cement grains, the strength of the edge filter was changed. The alite to belite ratios were measured for 2 extremes values.

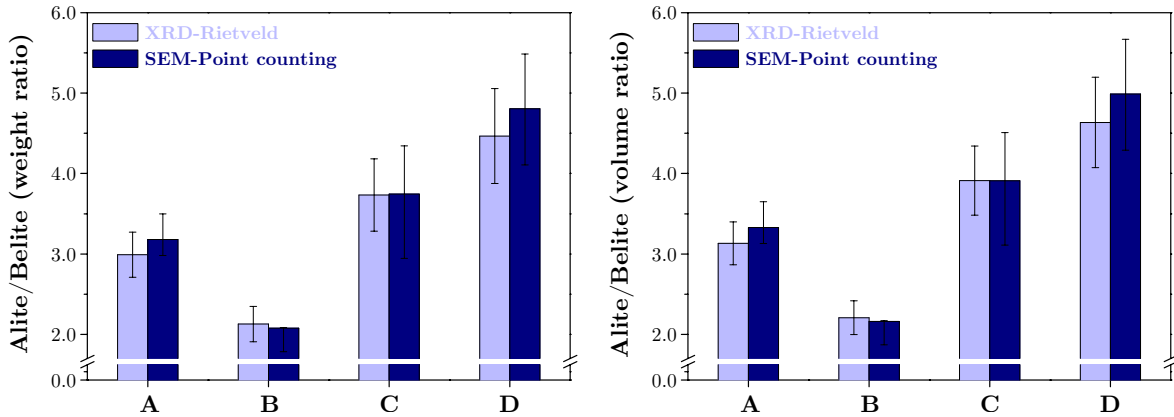


Figure II-12: comparison of the results achieved by XRD-Rietveld and SEM-Point counting for the 4 main cements in weight and volume ratios

A very good agreement was observed between XRD-Rietveld and SEM-Point counting data that supports the validity of our XRD-Rietveld refinement data.

II.1.4. COMPARISON OF XRD, NMR AND SEM

Figure II-13 presents the alite to belite weight ratios from XRD-Rietveld refinement, ^{29}Si NMR and SEM-Point counting.

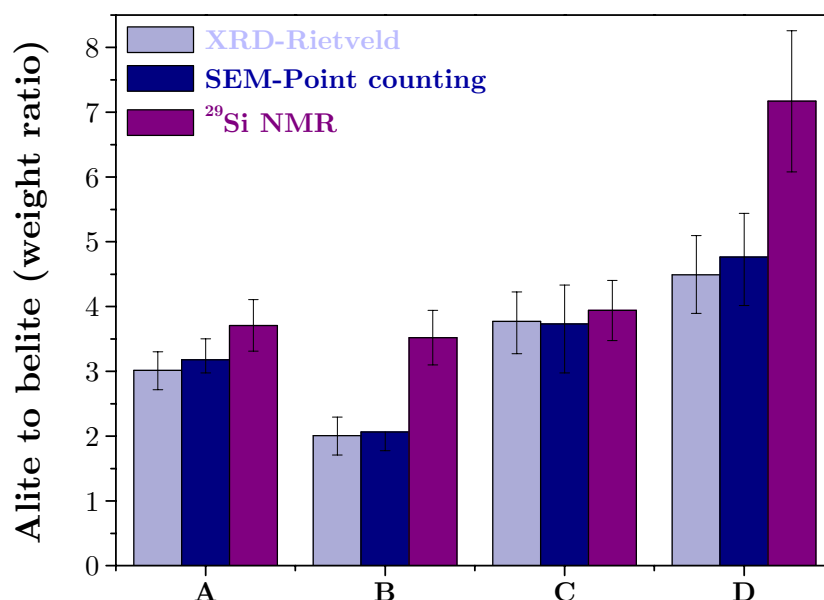


Figure II-13: comparison of the results achieved by XRD-Rietveld, SEM-Point counting and ^{29}Si NMR for the 4 main cements

For the four anhydrous cements, a very good agreement was found between SEM-Point counting and XRD-Rietveld data. However, comparisons of both techniques with ^{29}Si NMR exhibited an important difference for Cement B and D.

It is noted that the ^{29}Si NMR method underestimates the belite content and overestimates the alite content as compared to the XRD-Rietveld analysis. As explained in [23], the systematic variations in alite and belite content may reflect the difference in nature of the ^{29}Si NMR and XRD experiments, which primarily depend on the local and long-range order in the materials, respectively. In addition, the content of amorphous phase in anhydrous cement could modify the alite to belite ratio. It is still controversial [53].

II.1.5. ACCURACY OF X-RAY FLUORESCENCE

X-ray fluorescence (XRF) measurements were carried out by an external company (APC Solutions SA, CH-1021 Denges) using a Bruker AXS S4 Explorer spectrophotometer operating at a power of 1 kW and equipped with a Rh X-ray source.

Crystal used were OVO55FC for Na, F, Cl with 0.46° divergence collimator, PET for Al, Si, P et Mn with 0,23° divergence collimator and LiF220, with 0,23° divergence collimator for all other elements.

The chemical composition of the four cements and Clinker L determined by XRF is given in Table II-9.

Oxides	Cement A	Cement B	Cement C	Cement D	Clinker L	SD
SiO ₂	24.68	20.51	21.01	21.03	19.72	0.40
Al ₂ O ₃	2.11	5.10	4.63	5.01	5.44	0.20
Fe ₂ O ₃	0.43	3.33	2.60	2.54	3.85	0.10
CaO	68.67	61.29	64.18	63.45	66.11	0.40
MgO	0.58	2.82	1.82	2.05	0.92	0.10
SO ₃	1.82	2.78	2.78	3.01	2.07	0.10
K ₂ O	0.06	1.40	0.94	1.02	0.53	0.04
Na ₂ O	0.17	0.24	0.20	0.26	0.38	0.03
MnO	0.01	0.05	0.03	0.04	0.04	0.01
TiO ₂	0.05	0.19	0.14	0.16	0.19	0.01
P ₂ O ₅	0.45	0.37	0.40	0.08	0.39	0.01
LOI	0.97	1.94	1.26	1.34	0.33	0.10
Cl	-	-	-	-	< 0.01	-
Na ₂ Oeq	0.22	1.16	0.81	0.93	0.73	0.06
CO ₂	1.30	0.80	1.40	0.50	-	0.20
Total	100	100	100	100	100	-

Table II-9: oxides composition of the 4 cements from XRF analysis and CO₂ content from TGA analysis

In this table, the standard deviations (SD) are reported for XRF analysis. These errors are typical of those amongst laboratories for chemical analysis of cement [54]. Analyses of our samples were also made in two different laboratories and provided us with results within these error bars. As an example, for Cement B, these two laboratories assigned for CaO respectively an oxide amount of 61.29; 61.68 wt% and 20.51; 20.13 wt% for SiO₂. If the other oxides amounts are kept equal for the set of data regardless of the phase compositions, the amount of alite increases by 5 wt% and the amount of belite is reduced by 5 wt% when these values are used in the Bogue calculation. The variation in alite/belite ratio is 0.8 which illustrates the extreme sensitivity to the input values.

II.1.6. COMPOSITION OF THE CEMENT PHASES FROM EDS

The real compositions of each anhydrous cement phase (alite, belite, aluminate and ferrite) were measured by energy dispersive X-ray spectroscopy using the Princeton Gamma-Tech (PGT) energy dispersive X-ray analyser (see Table II-10).

For each anhydrous cement phase, a series of points from EDS analyses were made to identify the different phases (see previous Figures II-7 to II-10). In Cement A, four main phases were identified: alite, belite, aluminate and calcium sulfate. In the other cements, ferrite phase is present in addition to these phases.

The atomic proportions of K, Na, Ca, Mg, Fe, Al, Si and S were measured by EDS. The corresponding chemical compositions of cement are given in Table II-10 by atomic ratio composition of the main anhydrous phases to provide input data for the modified Bogue calculation. These values are very close to the average phase composition proposed by Taylor ((T¹: table p 10 of [55], T²: formulas p 7-26 of [55]).

The chemical composition can also be expressed in terms of the parent structural formula units: for alite Ca₃SiO₅ normalizing the atomic composition to 5 oxygen atoms, for belite to 4 oxygen atoms (although it is possible that vacancies occur in the oxygen sites for belite), for aluminate to 6 atoms and for ferrite to 5 atoms (Table II-11).

As reported by Taylor [5], the significant substitutions in alite are of Na⁺, K⁺, Mg²⁺ and Fe³⁺ for Ca²⁺ and of Al³⁺, (less significant: P⁵⁺, S⁶⁺) for Si⁴⁺.

These substitutions are taken into account according to Taylor [55] and the equivalent atomic ratios for the four clinker phases are presented as following:

in alite:



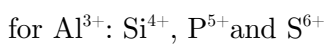
in belite:



in aluminate:



in ferrite:



Alite	Ca	Na	K	Mg	Fe	Si	Al	S	O	Ca _{eq}	Si _{eq}	Ca _{eq} /Si _{eq}	N'
Cement A	31.5	0.06	0.00	0.47	0.17	10.0	0.7	0.01	57.0	32.2	10.7	3.000	53
Cement B	30.9	0.08	0.00	1.03	0.35	10.0	0.8	0.01	56.8	32.4	10.8	2.999	87
Cement C	32.6	0.03	0.03	0.56	0.51	10.6	0.7	0.01	55.0	33.7	11.2	3.001	75
Cement D	31.0	0.07	0.00	0.91	0.37	9.70	1.1	0.01	56.9	32.3	10.8	3.000	82
T ¹	32.3	0.11	<0.11	0.67	0.22	10.7	0.4	<0.11	55.6	33.3	11.2	2.971	-
T ²	32.7	-	-	0.33	0.11	10.8	0.6	-	55.6	33.1	11.3	2.922	-

Belite	Ca	Na	K	Mg	Fe	Si	Al	S	O	Ca _{eq}	Si _{eq}	Ca _{eq} /Si _{eq}	N'
Cement A	27.8	0.07	0.00	0.13	0.14	12.7	1.2	0.04	57.9	28.0	13.8	2.029	88
Cement B	27.5	0.12	0.03	0.30	0.39	12.6	0.9	0.03	58.1	27.9	13.5	2.067	78
Cement C	28.8	0.07	0.23	0.06	0.45	13.2	0.8	0.12	56.3	29.1	14.0	2.079	74
Cement D	27.7	0.06	0.00	0.31	0.34	12.5	1.1	0.09	57.9	28.0	13.6	2.059	70
T ¹	28.0	0.14	0.43	0.29	0.29	13.0	1.0	0.14	56.7	28.9	14.0	2.064	-
T ²	28.1	0.14	0.29	0.29	0.29	12.9	0.9	0.14	57.0	28.8	13.8	2.087	-

Aluminate	Ca	Na	K	Mg	Fe	Si	Al	S	O	Ca _{eq}	Al _{eq}	Ca _{eq} /Al _{eq}	N'
Cement A	25.7	0.77	0.00	0.27	0.37	2.6	14.8	-	55.4	26.8	17.8	1.502	54
Cement B	25.8	0.47	0.07	0.54	1.33	1.9	14.7	-	55.2	26.9	17.9	1.501	39
Cement C	27.0	0.40	0.15	0.38	3.16	1.6	13.9	-	53.4	27.9	18.6	1.498	26
Cement D	24.0	0.30	0.03	2.59	2.75	2.3	12.9	-	55.2	26.9	17.9	1.502	47
T ¹ cubic	24.9	0.82	0.37	0.82	1.55	1.6	15.2	-	54.8	26.9	18.3	1.473	-
T ² cubic	25.3	0.55	0.27	0.73	2.01	1.6	14.6	-	54.9	26.8	18.3	1.464	-
T ¹ ortho.	24.1	0.45	2.09	0.73	2.09	1.8	14.3	-	54.5	27.3	18.2	1.502	-
T ² ortho	25.2	2.63	-	-	1.35	1.1	15.6	-	54.1	27.8	18.0	1.541	-

Ferrite	Ca	Na	K	Mg	Fe	Si	Al	S	O	Ca _{eq}	(Al+Fe) _{eq}	Ca _{eq} / (Al+Fe) _{eq}	N'
Cement B	22.3	0.01	0.02	1.64	8.05	1.6	11.1	-	55.4	22.3	22.3	0.999	50
Cement C	23.8	0.00	0.00	1.34	10.98	1.2	10.3	-	52.3	23.8	23.9	0.998	32
Cement D	22.2	0.02	0.00	2.14	6.71	2.3	11.0	-	55.5	22.2	22.2	0.999	46
T ¹	22.2	0.11	0.11	1.90	6.94	1.6	11.2	-	56.0	22.4	21.6	1.037	-
T ²	22.3	-	-	2.23	6.70	1.7	11.2	-	55.9	22.3	21.8	1.023	-

Table II-10: atomic ratio composition of the main anhydrous phases in cements A-D by EDS analyses (N' is the number of analyses) and average compositions given by Taylor in [55] (T¹: table p 10, T²: formulas p 7-26)

Cement A	K	Na	Ca	Mg	Fe	Al	Si	S	O	Number of points
Alite	0	<1	292(3)	4(1)	2(1)	7(3)	95(3)	<1	500	53
Ca _{2.92} Mg _{0.04} Al _{0.07} Fe _{0.02} Si _{0.95} O ₅	298			102						
Belite	0	<1	199(3)	<1	<1	8(3)	92(3)	<1	400	88
Ca _{1.99} Al _{0.08} Fe _{0.01} Si _{0.92} O ₄	199			100						
Aluminate	0	8(4)	280(10)	3(2)	4(1)	165(18)	30(12)	<1	600	54
Ca _{2.80} Mg _{0.03} Na _{0.08} Al _{1.65} Fe _{0.04} Si _{0.30} O ₆	291			199						
Ferrite	Crystal size not sufficient for analysis									-
Cement B	K	Na	Ca	Mg	Fe	Al	Si	S	O	Number of points
Alite	<1	<1	284(5)	8(2)	4(2)	9(5)	93(4)	<1	500	87
Ca _{2.84} Mg _{0.08} Al _{0.09} Fe _{0.04} Si _{0.93} O ₅	296			102						
Belite	<1	<1	198(3)	2(1)	3(1)	7(3)	92(3)	<1	400	78
Ca _{1.98} Mg _{0.02} Al _{0.07} Fe _{0.03} Si _{0.92} O ₄	200			102						
Aluminate	<1	5(2)	273(5)	5(1)	15(3)	168(10)	22(8)	0	600	39
Ca _{2.73} Mg _{0.05} Na _{0.05} Al _{1.68} Fe _{0.15} Si _{0.22} O ₆	283			205						
Ferrite	<1	<1	194(5)	15(3)	76(13)	100(15)	14(5)	<1	500	50
Ca _{1.94} Mg _{0.15} Al _{1.00} Fe _{0.76} Si _{0.14} O ₅	194			205						
Cement C	K	Na	Ca	Mg	Fe	Al	Si	S	O	Number of points
Alite	<1	<1	293(4)	5(1)	4(2)	6(2)	93(2)	<1	500	75
Ca _{2.93} Mg _{0.05} Al _{0.06} Fe _{0.04} Si _{0.93} O ₅	302			99						
Belite	2(2)	<1	200(5)	<1	3(2)	5(3)	91(4)	<1	400	74
Ca _{2.00} Al _{0.05} Fe _{0.03} Si _{0.91} O ₄	202			99						
Aluminate	1(3)	5(2)	277(9)	11(12)	14(4)	162(9)	22(4)	<1	600	114
Ca _{2.77} Mg _{0.01} Na _{0.05} Al _{1.62} Fe _{0.14} Si _{0.22} O ₆	294			198						
Ferrite	<1	<1	206(3)	18(3)	57(5)	104(8)	17(6)	<1	500	116
Ca _{2.06} Mg _{0.18} Al _{1.04} Fe _{0.57} Si _{0.17} O ₅	206			196						
Cement D	K	Na	Ca	Mg	Fe	Al	Si	S	O	Number of points
Alite	0	<1	289(3)	8(2)	3(1)	9(2)	93(2)	<1	500	82
Ca _{2.89} Mg _{0.08} Al _{0.09} Fe _{0.03} Si _{0.93} O ₅	300			102						
Belite	<1	<1	198(2)	2(1)	2(1)	8(2)	91(3)	<1	400	70
Ca _{1.98} Mg _{0.02} Al _{0.08} Fe _{0.02} Si _{0.91} O ₄	200			101						
Aluminate	<1	3(2)	268(15)	23(22)	19(5)	148(19)	28(11)	0	600	94
Ca _{2.68} Mg _{0.23} Na _{0.03} Al _{1.48} Fe _{0.19} Si _{0.28} O ₆	294			195						
Ferrite	<1	<1	209(5)	19(5)	46(6)	109(11)	20(9)	<1	500	146
Ca _{2.09} Mg _{0.19} Al _{1.09} Fe _{0.46} Si _{0.20} O ₅	209			194						
Clinker L	K	Na	Ca	Mg	Fe	Al	Si	S	O	Number of points
Alite	<1	<1	305(2)	3(1)	3(1)	8(1)	88(2)	<1	500	124
Ca _{3.05} Mg _{0.03} Al _{0.08} Fe _{0.03} Si _{0.88} O ₅	311			96						
Belite	<1	<1	205(3)	<1	3(1)	8(1)	81(3)	5(3)	400	44
Ca _{2.05} Al _{0.08} Fe _{0.03} Si _{0.81} O ₄	205			97						
Aluminate	<1	1(1)	300(6)	5(2)	17(5)	150(13)	21(9)	1(1)	600	141
Ca _{3.00} Mg _{0.05} Na _{0.01} Al _{1.50} Fe _{0.17} Si _{0.21} O ₆	306			188						
Ferrite	<1	<1	211(4)	13(3)	76(8)	93(7)	11(4)	1(1)	500	108
Ca _{2.11} Mg _{0.13} Al _{0.93} Fe _{0.76} Si _{0.11} O ₅	194			205						

Table II-11: atomic ratios for phases in Cement A to D and Clinker L calculated from EDS

Some wavelength-dispersive spectrometry (WDS) measurements were made by an external laboratory in order to compare it with the EDS data. From a statistical standpoint, the data was not exhaustive to use as a relevant data-set.

II.1.7. REVERSE BOGUE CALCULATION

In the reverse Bogue calculation, the elemental oxide compositions are calculated from phase content deduced by Rietveld analysis. The phase composition and the standard deviation from EDS measurements are used in the elemental composition calculation and the respective error bars. If phase compositions are not available, extreme values for substitution in phases can be used to establish the error bars. This, however, leads to large errors: for example ± 2 wt% for CaO is calculated as opposed to ± 0.9 wt% if EDS data are used. In such an event, the comparison does not serve with relevance to detect problem in the Rietveld quantification.

The data from XRD-Rietveld with EDS were used to calculate the overall chemical composition-termed reverse Bogue and the results were compared with XRF data.

Reverse Bogue calculation was be used to check if any major error occurs.

The results show (Figure II-14) there is a very good agreement between calculated oxide compositions from Rietveld analysis, reverse Bogue and XRF. The small differences for the Al_2O_3 and Fe_2O_3 content in Cement B may be due to higher uncertainties in the Rietveld quantification as a two forms of belite are used to describe the pattern.

For Cement C and D the SiO_2 and Al_2O_3 contents disagreed. However, a slight variation on the input data can lead to other trends.

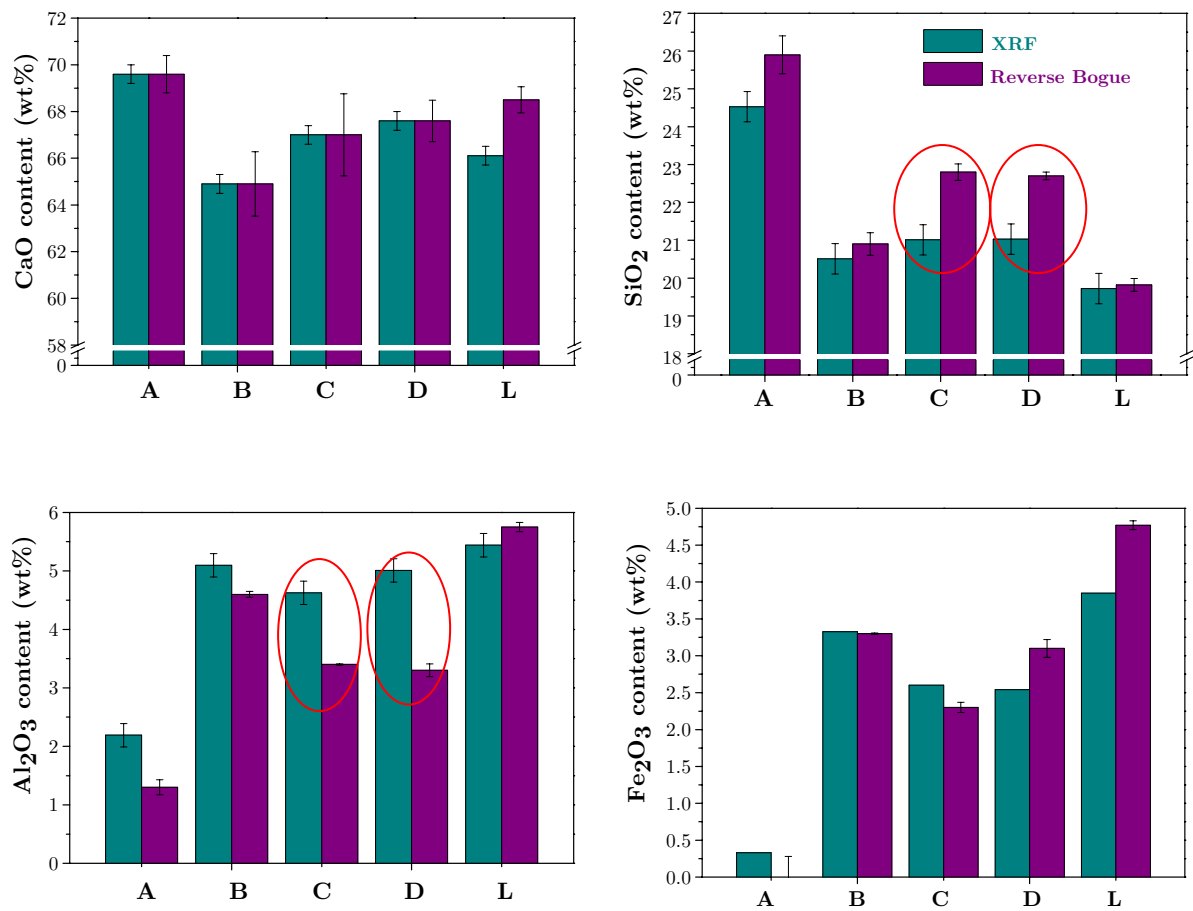


Figure II-14: anhydrous phases contents for 4 cements achieved by reverse Bogue calculation and XRF elemental composition

II.1.8. STANDARD BOGUE CALCULATION PROCEDURE

Using XRF and TGA results, the standard Bogue calculation [2] uses the following procedure without taking into account the minor compounds (see details in Appendix 3):

- Assumptions of compositions of the four major phases are C_3S , C_2S , C_3A and C_4AF .
- Assumption that all the Fe_2O_3 occurs as C_4AF .
- Assumption that the remaining Al_2O_3 occurs as C_3A .
- Deduction from the CaO content the amounts attributable to C_4AF , C_3A and free lime, and solve two simultaneous equations to obtain the contents of C_3S and C_2S .

II.1.9. MODIFIED BOGUE CALCULATION PROCEDURE

The procedure for the modified Bogue calculation [3] takes into account the real composition of each phase (not only the main elements but also minor ions because phases are solid solutions) and also estimates the contents of alkali and sulfate components.

The modified Bogue calculation is corrected for free lime because in our case there is no limestone added to the cement, calcite (from the XRD-Rietveld refinement) could be also included in the free lime correction.

II.1.10. COMPARISON OF XRD, NMR, BOGUE AND MODIFIED BOGUE

In the following part (see Figures II-15 and II-16), XRD-Rietveld results are compared to results from ^{29}Si NMR, Bogue and modified Bogue calculations (1: using the composition proposed by Taylor [5] and 2: using the composition deduced by EDS referred to Table II-11).

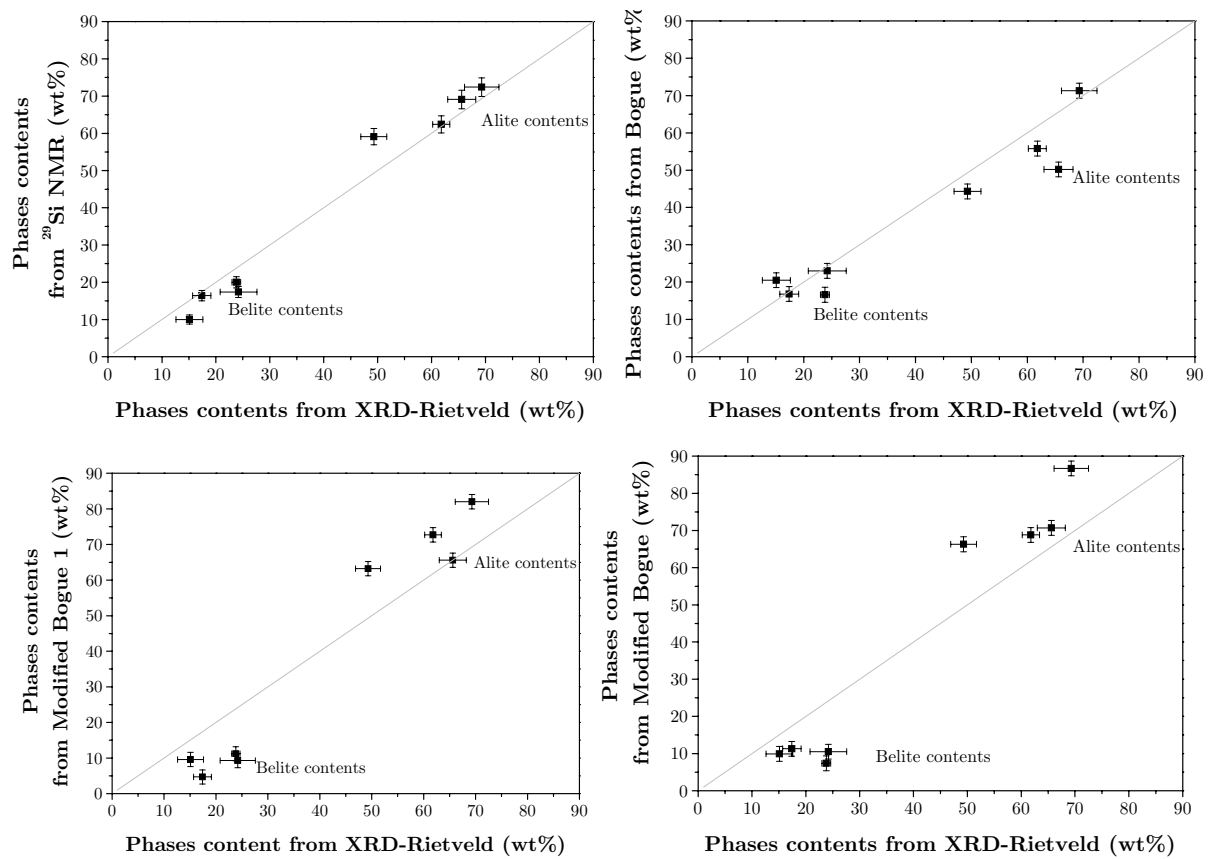


Figure II-15: phases contents from ^{29}Si NMR analysis, Bogue and modified Bogue calculations versus XRD-Rietveld results

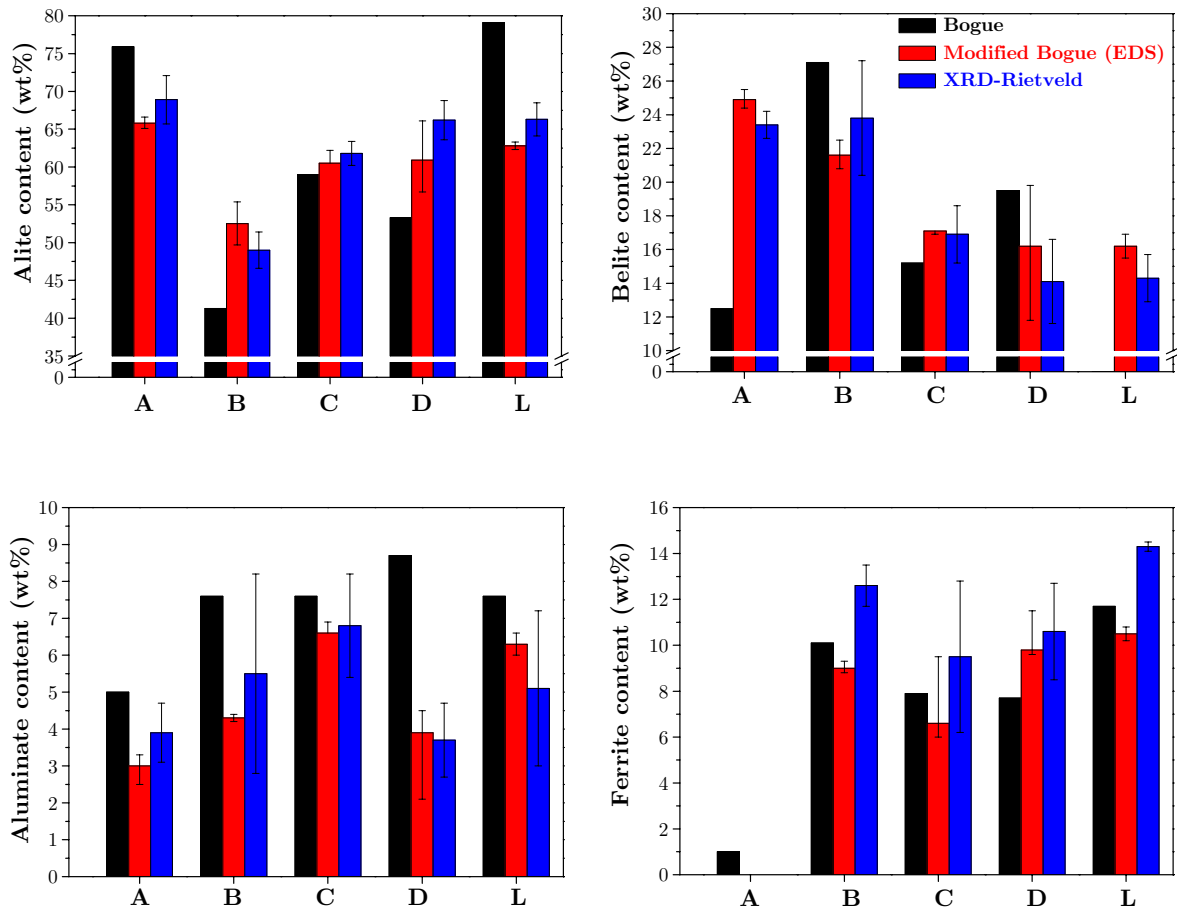


Figure II-16: comparison of the results achieved by Bogue, modified Bogue calculations and XRD-Rietveld quantification

Bogue calculation [2] is the most widely used method of estimating the potential phase composition of cement from the oxide analysis. However, this calculation gives inaccurate results because the phases do not have the compositions that stoichiometric compositions assumed.

In addition, even a small error in XRF data induces a large deviation on Bogue calculations which renders the Bogue approach mathematically imprecise.

As the modified Bogue calculation requires a matrix inversion, the error bars cannot be easily deduced from XRF and EDS errors. The error bars on modified Bogue calculation presented in Figure II-16 are calculated by modifying the phase composition with respect to the stoichiometry using the standard deviation of EDS measurements and do not take into account the error in XRF data.

A significant dispersion of the values obtained from the different methods is observed. However, we know the modified Bogue calculation is rather unstable with respect to small changes in values. In addition, for Cement A, the alumina ratio ($AR=Al_2O_3/Fe_2O_3$) is equal to 6.4 but as the modified Bogue calculation is meant for ratios from 1,5 to 3, this value is well outside the range recommended by Taylor [5].

However, small errors in XRF analysis result into significant errors by the calculation (± 5 wt% for C_3S and C_2S). Although, we cannot expect a good agreement between the modified Bogue calculation and Rietveld analysis due to large error.

II.2. CHARACTERISTICS OF ANHYDROUS SLAGS

In the framework of this work, two ferrous blast furnace slags called Slag 1 and Slag 8 are studied, as blast furnace slags are the most common used in cementitious applications. So in the following part, only the blast furnace slags will be discussed.

Blast furnace slag is a by-product from the production of iron. BFS is formed from the combination of limestone fluxes, coke ash and residues from the reduction of iron ore and is mainly composed of SiO_2 - CaO - Al_2O_3 - MgO .

The molten slag is quenched from $\sim 1440^\circ\text{C}$ to $< 100^\circ\text{C}$ using either air or water. If cooled rapidly enough, it forms a glassy material having latent hydraulic properties: ground blast furnace slag (GBFS). When ground, a sharp-pointed, irregular shaped and granulated material is obtained: ground granulated blast furnace slag (GGBFS). The finished product is ground to the same fineness as cement. The final product contains an amount of glassy phase, which depends on the rate of cooling (review from [56,57]).

Quenched slag, mainly consisting of glass, can be distinguished from slow-cooled slag, which consists of crystalline phases. The quickly cooled granulated slag has characteristically high latent hydraulic properties [58].

When ground to a powder of the same approximate fineness as OPC (about 3000-6000 cm^2/gr Blaine), the final product is called ground granulated blast furnace slag (GGBFS or simply slag) and is used as an addition to current cement and concrete [59].

GBFS has successfully been used with Portland cement to produce blends that are of high quality, more economical and more environmentally friendly [60]. In addition, the use of slag-blended cements can improve the performance of concrete, in terms of physical properties and durability.

The use of GBFS in cementitious systems is directly linked to its physico-chemical properties.

II.2.1. MINERALOGY

Slags used in blended cements have less than 15% of crystalline phases. These crystalline species can be represented in a ternary diagram as shown in Figure II-17 [58,59,61].

The crystalline fraction is usually melilite which is a solid solution of gehlenite (C_2AS) and akermanite (C_2MS_2); but depending on the origin and composition of the slag, some traces of pseudo-wollastonite (SC), rankinite (C_3S_2), merwinite (C_3MS_2), monticellite (CMS) and oldhamite ($((C,M,F)S)$) can also be found.

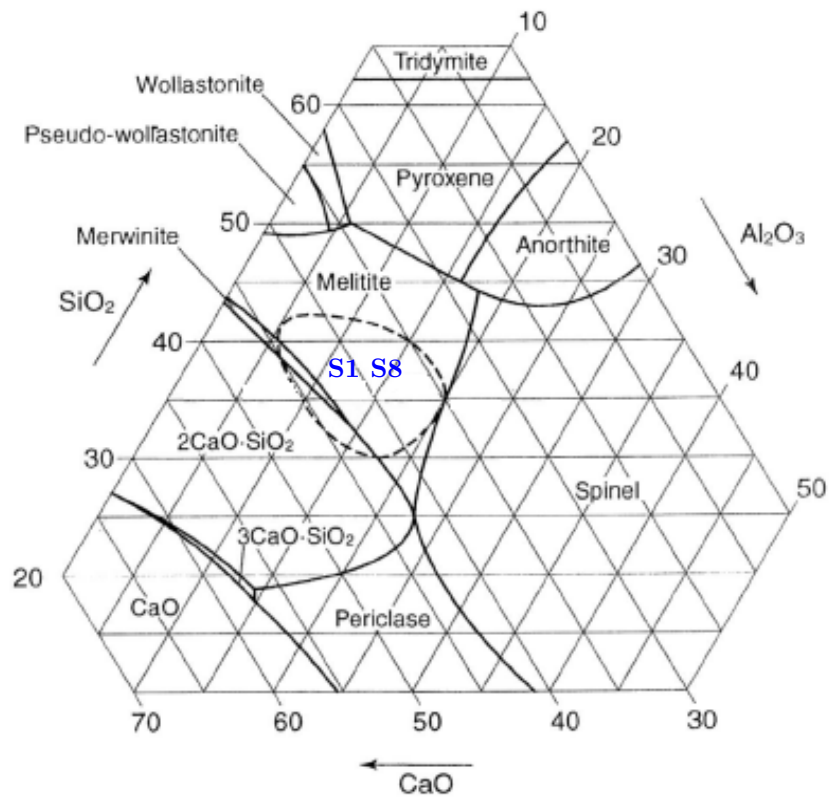


Figure II-17: ternary diagram of $CaO-Al_2O_3-SiO_2$ with 10 wt% MgO representing the main field of chemical compositions of blast furnace slags [62]

The following table (Table II-12) summarises the crystalline constituents of blastfurnace slag.

Mineral name	Mineralogical formula			Simplified formula	
Silicates	<i>Melilite</i>	Gehlenite	2 CaO Al ₂ O ₃ SiO ₂	C ₂ AS	
		Akermanite	2 CaO MgO 2 SiO ₂	C ₂ MS ₂	
	<i>Merwinite</i> *		3 CaO MgO 2 SiO ₂	C ₃ MS ₂	
	<i>Diopside and other pyroxenes</i> **		CaO MgO 2 SiO ₂	CMS	
	<i>Dicalcium Silicate</i> *	α Bredigite			
		β Larnite	2 CaO	SiO ₂	C ₂ S
		γ			
	<i>Rankinite</i>		3 CaO 2 SiO ₂	C ₃ S ₂	
	<i>Wollastonite</i>		CaO SiO ₂	CS	
	<i>Pseudo-Wollastonite</i>		CaO SiO ₂	CS	
	<i>Monticellite</i> *		CaO MgO SiO ₂	CMS	
	<i>Forsterite</i>		2 MgO SiO ₂	M ₂ S	
	<i>Enstatite</i> **		MgO SiO ₂	MS	
	<i>Anorthite</i> **		CaO Al ₂ O ₃ 2 SiO ₂	CAS ₂	
<i>Leucite</i>	(K ₂ O, Na ₂ O)	Al ₂ O ₃ 4 SiO ₂	(K,N)AS ₄		
<i>Augite</i>	Complex silicates of Ca, Mg, Fe, Ti, Al				
Oxides	<i>Spinel</i>		MgO Al ₂ O ₃	MA	
			FeO Fe ₂ O ₃		
	<i>Perovskite</i>		CaO TiO ₂		
Sulfurs	<i>Oldhamite</i>	(Ca, Mg, Fe) S		(C,M,F)S	
Others	Carbonaceous, sulphurous, nitrogenous compounds, alkali thiosulphates, etc.				

* only in basic slags, ** only in acidic slags

Table II-12: mineral compositions of crystallised blastfurnace slags [61]

II.2.2. STRUCTURE OF THE SLAG

The hydraulic properties of GBFS are determined by its chemical composition, and by its vitreous state. Slags used for blending with cement have a glassy content between 90 and 100% [58].

Uchikawa *et al.* [59] showed that the variations in reactivity are mainly linked to the chemical composition, the initiation temperature of cooling, and the cooling method. They also found that the chemical composition of slags with high amorphous content is microscopically homogeneous whereas slags rich in crystalline phases have a heterogeneous chemical composition. In addition, in the case that crystalline phases are present, this phase tends to have less Al₂O₃ and a higher MgO than the glass.

Several reviews propose [59,63,64] that the structure of the glassy phase is a supercooled liquid silicate. The silicate glass content is approximated by considering the vitreous silica in which some Si-O-Si bonds are broken and neutralised by metal cations called structure modifiers. Silica tetrahedra are isolated or polymerised with bridging oxygen atoms (see Figure II-18).

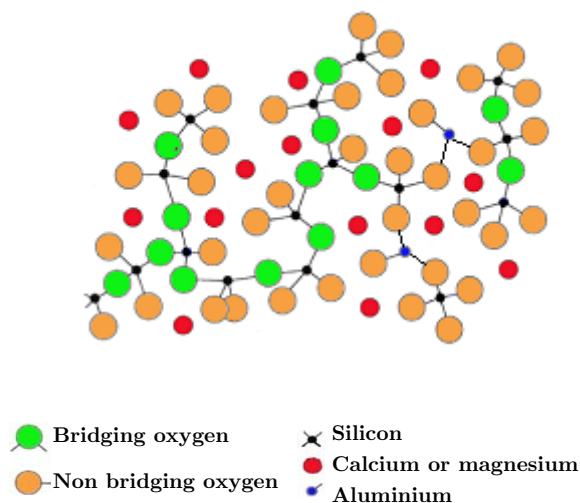


Figure II-18: schematic structure of a glassy slag [64]

The idea of reactivity indices stems from the role of the different oxides in forming a glass structure and expresses the fact that hydraulic activity is broadly favoured by more basic composition [56].

SiO₂ is basically the glass forming oxide with four covalent bonds in an ideal network. But slag consists of four-coordinated network formers, such as SiO₄⁴⁻, AlO₄⁵⁻ and six coordinated network modifiers, such as Ca²⁺, Al³⁺, Mg²⁺, Na⁺, K⁺ [59]. These modifiers ions, particularly Ca²⁺ and Mg²⁺ are expected to disrupt the network structure. According to several studies [61,65,66], it was found that CaO and MgO contents of slag used in blend mortar have a positive effect on strength, whereas SiO₂ has a negative influence. However, the effect of Al₂O₃ is complex and controversial.

It could be noted that if there is evidence of individual contribution of oxides on strength development, there is no direct relationship with strength when these oxides are combined with slags of different compositions. For this reason, the different moduli do not always agree linearly with the order of reactivity of slags.

The comparison of all these ratios with the strength results clearly invalidated the possibility to estimate the reactivity of slag in blended systems, given that the initial oxides composition was the only known parameter.

II.2.3. CHEMICAL COMPOSITION OF SLAG

The composition of slag varies depending on the raw materials. However, in general, slag is high in calcium oxide (30-40%) with significant amounts of silica (28-38%) and alumina (8-24%). In addition, slag contains small amounts of magnesium oxide (1-18%) and sulfides (1-2,5%), such as calcium sulfide (CaS), manganese sulfide (MnS) and iron sulfide (1-3% FeS).

The chemical composition of slag was carried out by XRF analysis (see Table II-13). The standard deviations correspond to 10 repeatability tests on our powders.

Oxides content	Slag 1		Slag 8	
	Concentration (%)	SD (%)	Concentration (%)	SD (%)
SiO ₂	36.61	0.04	34.60	0.04
Al ₂ O ₃	12.21	0.02	19.98	0.03
Fe ₂ O ₃	0.85	0.00	0.47	0.00
CaO	41.59	0.02	32.48	0.02
MgO	7.18	0.02	9.17	0.02
SO ₃	0.63	0.00	1.99	0.01
K ₂ O	0.28	0.00	0.78	0.00
Na ₂ O	0.18	0.01	0.16	0.01
MnO	0.14	0.00	0.06	0.00
TiO ₂	0.35	0.00	0.67	0.00
P ₂ O ₅	0.01	0.00	0.01	0.00
LOI	-0.03	-	-0.37	-
Na ₂ O _{eq}	0.36	-	0.67	-
Total	100.00	-	100.00	-

Table II-13: oxides composition of two slags from XRF analysis

To initially estimate the reactivity of slag, empirical formulas linked to the chemical composition can be used. The different moduli are listed in Table II-14.

The chemical composition of slag can be used as an apriori estimator of the reactivity. According to Smolczyk [61], the Al_2O_3 , CaO and MgO contents have a positive effect on strength, whereas SiO_2 has a negative influence.

Formula of moduli	Slag 1	Slag 8	Comments
$M_1 = \frac{CaO}{SiO_2}$	1.18	0.97	M_1 is the basicity index. When it increases, the solubility and thus the reactivity of slag increases [67]. Slag 1 has a higher M_1 ratio which corresponds to higher solubility and reactivity.
$M_2 = \frac{CaO + MgO}{SiO_2}$	1.37	1.23	Deriving from the basicity index, two moduli are defined to judge the melting conditions of the slag [61]: M_2 and M_3 ratio.
$M_3 = \frac{CaO + MgO}{SiO_2 + Al_2O_3}$	1.02	0.77	The European Standard EN 197-1 recommends $M_2 \geq 1$ which is in favour of Slag 1.
$M_4 = \frac{Al_2O_3}{SiO_2}$	0.34	0.59	The M_4 ratio is defined to evaluate slags for cement application. When the range is $0,55 \leq M_4 \leq 0,53$, it is an indication of good performance in blended cements.
$M_5 = \frac{CaO + MgO + Al_2O_3}{SiO_2}$	1.71	1.82	The two following hydraulic moduli can be defined: the M_5 and M_6 ratios. Depending on this value, the quality is evaluated [68]: <ul style="list-style-type: none"> ▪ $1.5 < M_5$ means that the slag has poor hydraulic properties; ▪ $1.5 \leq M_5 \leq 1.9$ means that the slag has good hydraulic properties which is the case of Slag 1 and Slag 8; ▪ $M_5 > 1.9$ means that the quality of the slag is very good.
$M_6 = \frac{CaO \times Al_2O_3}{(SiO_2 + Al_2O_3)^2}$	0.22	0.23	Dron [69] defined an index of reactivity: M_6 and he found that the slag with a suitable quality should have this ratio is equal or higher than 0.18. So Slag 1 and Slag 8 have a good quality.

Table II-14: main characteristic moduli of slag [61,67-69]

All the moduli are convenient tools to rapidly estimate the quality of slag. Nevertheless, some studies [65,70] reported that in practice, the modulus ratios do not always correlate with strength, particularly at early ages.

II.2.4. IDENTIFICATION OF STRUCTURES OF PHASES IN THE ANHYDROUS SLAGS

All the crystalline phases of slags were identified using the X'Pert High Score Plus program from PANalytical with reference structures from the Inorganic Crystal Structure Database (ICSD).

	Phases	Formula	Crystal system	Materials	ICSD codes	Reference
Slags	Melilite	$\text{Ca}_2(\text{Mg}_{0.5}\text{Al}_{0.5})(\text{Si}_{1.5}\text{Al}_{0.5}\text{O}_7)$	Tetragonal	S8	67689	Swainson <i>et al.</i> , 1992 [71]

Table II-15: structures of phases in the anhydrous slag samples

The slag samples were prepared in the same way as anhydrous cement phases.

The SEM-BSE examinations of Slags 1 and 8 reveal a homogeneous composition for the amorphous part (see Figures II-19 and II-20). However, small amounts of crystalline phases were observed as dendrites inclusions in the case of Slag 8 (see Table II-15 and Figure II-21).

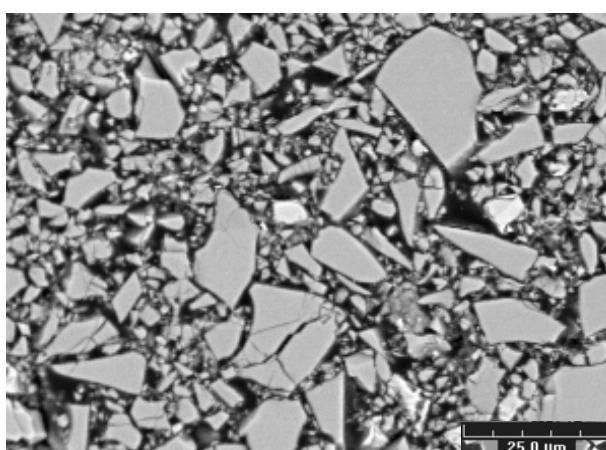


Figure II-19: SEM-BSE image of anhydrous Slag 1

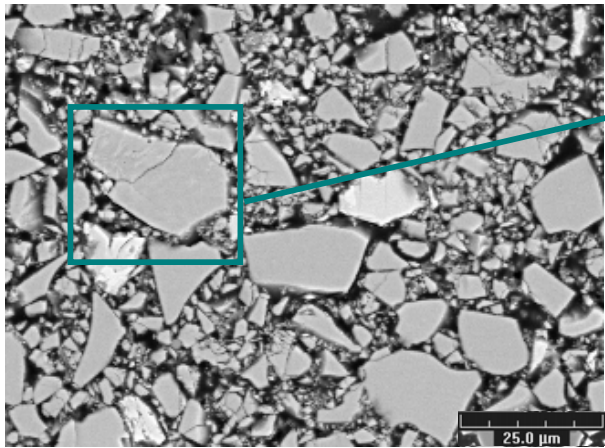


Figure II-20: SEM-BSE image of anhydrous Slag 8 with crystalline phase

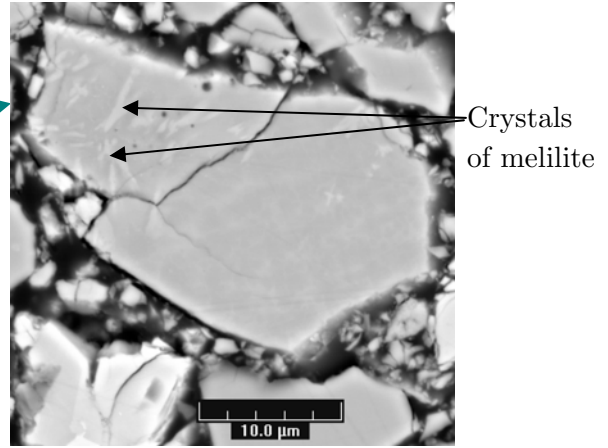


Figure II-21: SEM-BSE image of crystals of melilite in Slag 8

From EDS (Table II-16) and XRD analyses, the crystalline phase in Slag 8 was identified as melilite. As previously explained [72], it typically occurs as elongated, more or less as dendritic inclusions in the glass resulting from solid solutions from gehlenite (C_2AS_2) to akermanite (C_2MS_2).

Both slags had a homogeneous composition even the Slag 8. It was previously reported that in slags of high glass content, the composition is uniform but can be lower in Al_2O_3 near to melilite crystals [73].

	Si/Ca		(Si+Al)/Ca		Ca/(Si+Al)		Al/Ca		S/Ca	
	Average	SD	Average	SD	Average	SD	Average	SD	Average	SD
Slag 1	0.76	0.04	1.07	0.04	0.94	0.04	0.31	0.01	0.030	0.004
Slag 8	0.94	0.06	1.56	0.08	0.64	0.04	0.62	0.04	0.037	0.008

Table II-16: EDS of anhydrous slags

II.2.5. MEASUREMENT OF THE GLASS CONTENT

Due to the lack of structural order, the glass content is difficult to quantify. Nevertheless, several methods have been studied to quantify the glass content. The most useful method appears to be XRD, but DTA or DSC which depend on recrystallisation of slag have also been used.

Thermal analyses

The oldest method used to determine the glass content is thermal analysis: differential thermal analysis (DTA) is the most employed [67,74-78]. Differential scanning calorimetry (DSC) [79] is also used as an alternate method using the same principal as thermal analysis.

As shown in Figure II-22, the first reversible exothermic peak in the temperature range 700-800°C corresponds to the glass-transition temperature T_g (pseudo second order phase transition in which the coefficient of thermal expansion changes sharply). This transition temperature mainly depends on thermal history (cooling rate) and structure [80].

The two exothermic peaks with well-defined maxima in the range 925-1040°C are attributed to the devitrification process. Using XRD, these peaks were respectively assigned to merwinite (metastable phase) and melilite with minor components (such as larnite) [75,79].

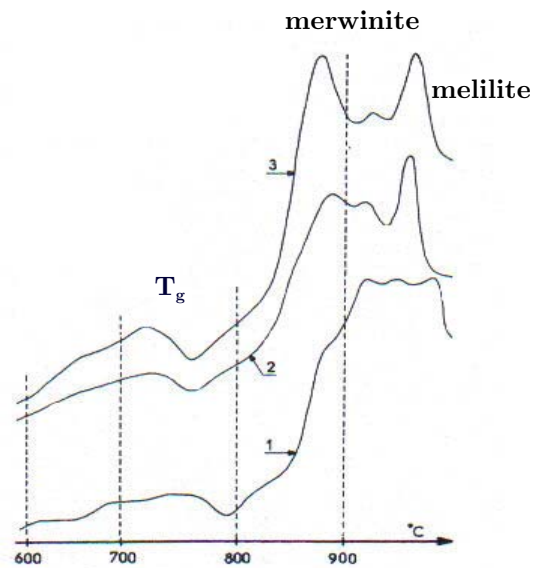


Figure II-22: DTA curves of three different anhydrous slags with recrystallisation peaks at high temperature [75]

As shown in Figure II-23, the two endothermic events at about 1280-1315°C, involve the melting of some crystal phases.

This method will be more detailed in Chapter V.

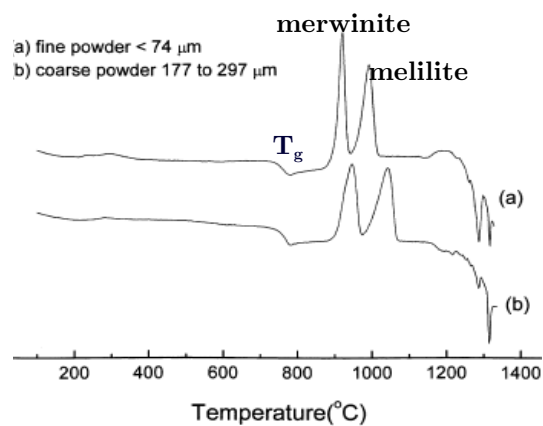


Figure II-23: DSC curves of a powdered anhydrous glass samples [79]

Quantification of amorphous content by XRD-Rietveld analysis

Several XRD experiments were made to assess slag glass content. First, two studies [81,82] used a quantitative X-ray diffraction method to compute the mass percentages of crystals (α -quartz, mullite, magnetite and hematite) and deduce the glass content by difference. No details however, are given concerning the error in these measurements.

Recent XRD measurements combined with Rietveld refinement [83,84] have also allowed the amorphous content of slags to be quantified. As the amount of crystalline standard is known by internal or external standard method, the true crystalline and amorphous contents can be calculated.

To calculate the amorphous content, there are two kinds of standard methods: the internal and the external standard methods.

- In the internal standard method, by using a defined quantity of crystalline standard material mixed with the sample, it is possible to determine the ratio of crystalline material in the sample to the crystalline standard and thus calculate the content of amorphous material in the sample [85].

- In the external standard method [86], to avoid complications that might be caused by grinding the sample and mixing it with an internal standard (homogenization for example) diffraction data may be measured separately for the sample and the standard under the same conditions [84].

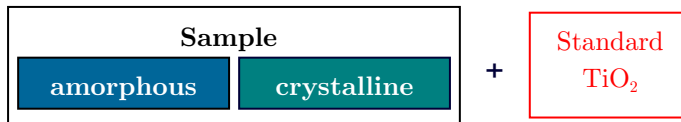
In the case of our study, the external standard method was used to calculate the amount of amorphous content in the blended anhydrous samples and a known amount of rutile (TiO_2) was chosen.

In this method, diffraction data are measured separately for the sample and the standard under the same conditions. The validity of this method has been already reported on cement-slag model mixtures [84].

The crystalline part of sample to standard ratio is determined by Rietveld quantification. The values obtained are divided by the ratio of the measured to true amount of standard.

The difference between the total of the corrected phase quantities and 100 wt% gives the amount of amorphous phases. This approach is summarised in the following Figure II-24.

1. **Sample preparation:** adding of a defined amount of crystalline standard



2. **Rietveld quantification:** determination of the ratio crystalline part of the sample to standard



3. **Recalculation:** determination of the amorphous part of the sample



Figure II-24: schematic calculation of the amorphous content using an external standard

The validity of this method was tested on Cement D with slag model mixtures and according to Le Saoût [84], down to 10 wt%, the correlation of the actual weight and analyzed weight of the slag content by both internal and external standard methods is very good, as shown in Figure II-25.

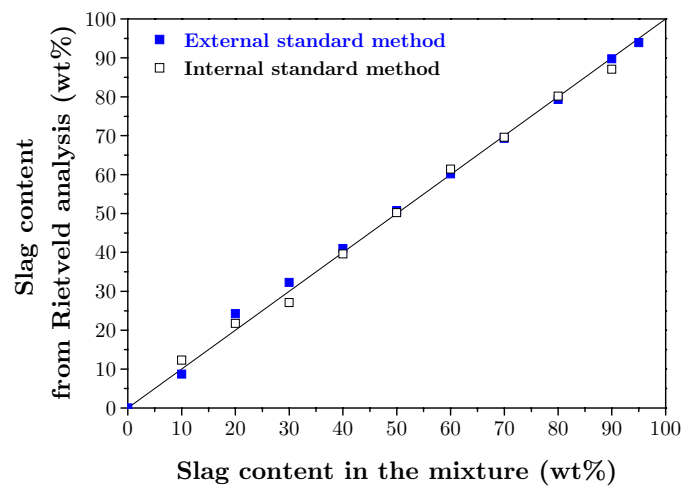


Figure II-25: comparison between the actual weight and Rietveld analyzed amount of slag in cement–slag model mixtures [84]

Using the external standard method, the amorphous content was determined in pure anhydrous slags (see results in Table II-17) and in blended anhydrous powders (see Table II-18).

Phases	Formula	Anhydrous Slag 1		Anhydrous Slag 8	
		Average	SD	Average	SD
Quartz	SiO ₂	0.5	0.1	0.0	0.0
Melilite	Ca ₂ (Mg _{0.5} Al _{0.5})(Si _{1.5} Al _{0.5} O ₇)	0.0	0.0	5.8	0.5
Amorphous		99.5	1.0	94.2	1.0
Total		100.0	-	100.0	-

Table II-17: phases composition from XRD-Rietveld for the 2 anhydrous slags

Phases	Formula	Anhydrous A-S1		Anhydrous B-S1		Anhydrous C-S1		Anhydrous A-S8		Anhydrous B-S8		Anhydrous C-S8	
		Average	SD	Average	SD	Average	SD	Average	SD	Average	SD	Average	SD
		Alite	C ₃ S (M ₃)	43.0	0.1	29.7	1.1	36.4	1.3	41.7	0.3	37.7	6.3
Belite	β-C ₂ S	15.4	0.3	9.5	0.1	11.0	0.5	10.6	0.2	9.3	0.7	8.0	0.5
	α' _H -C ₂ S	0.0	0.0	3.1	0.1	0.0	0.0	0.0	0.0	2.1	1.2	0.0	0.0
	Total C ₂ S	15.4	0.3	12.7	0.4	11.0	0.5	10.6	0.2	11.4	1.1	8.0	0.5
Ferrite	C ₄ AF	0.0	0.0	6.7	0.2	4.6	0.7	0.0	0.0	4.9	2.8	3.6	0.2
	cubic C ₃ A	2.2	0.0	2.4	0.2	3.3	0.2	1.6	0.1	2.1	0.1	3.0	0.1
Aluminate	orthorhombic C ₃ A	0.0	0.0	0.8	0.2	0.7	0.0	0.0	0.0	0.3	0.3	0.2	0.3
	Total C ₃ A	2.2	0.0	3.3	0.0	4.0	0.2	1.6	0.1	2.4	0.3	3.3	0.3
Lime	C	0.0	0.0	0.0	0.0	0.0	0.0	0.0	0.0	0.0	0.0	0.0	0.0
Periclase	M	0.0	0.0	1.4	0.0	0.4	0.4	0.0	0.0	0.7	0.4	0.0	0.0
Gypsum	CaSO ₄ -2H ₂ O	0.0	0.0	0.0	0.0	0.0	0.0	0.0	0.0	0.0	0.0	0.0	0.0
Hemihydrate	CaSO ₄ -0.5H ₂ O	0.9	0.1	0.9	0.0	0.9	0.1	0.0	0.0	0.9	0.5	0.8	0.2
Anhydrite	CaSO ₄	1.6	0.1	0.5	0.5	0.8	0.1	0.4	0.3	1.2	0.6	0.0	0.0
Calcium sulfate		2.5	0.2	1.4	0.5	1.7	0.0	0.4	0.3	2.1	0.3	0.8	0.2
Arcanite	K ₂ SO ₄	0.0	0.0	1.6	0.0	1.5	0.2	0.0	0.0	0.5	0.5	0.2	0.3
Portlandite	CH	0.0	0.0	0.0	0.0	0.0	0.0	0.0	0.0	0.0	0.0	0.0	0.0
Calcite	CaCO ₃	0.0	0.0	0.8	0.0	0.0	0.0	0.0	0.0	0.0	0.0	0.0	0.0
Quartz	SiO ₂	0.0	0.0	0.6	0.6	0.3	0.3	0.0	0.0	0.0	0.0	0.0	0.0
Melilite	Ca ₂ (Mg _{0.5} Al _{0.5})(Si _{1.5} Al _{0.5} O ₇)	-	-	-	-	-	-	1.6	0.3	1.7	0.4	2.7	0.2
Amorphous		36.9	0.7	42.0	2.5	40.2	2.5	44.0	0.4	38.7	2.2	41.9	1.3
Total		100.0		100.0		100.0		100.0		100.0		100.0	

Table II-18: phases composition from XRD-Rietveld for the 8 anhydrous slag-cements mixes

II.3. CONCLUSIONS AND DISCUSSION ON ANHYDROUS CEMENTITIOUS MATERIALS

Cements

Considering the results obtained using various techniques, the results indicate that cementitious phases can be satisfactorily quantified by XRD-Rietveld refinement if an adequate experimental procedure and a correct approach of Rietveld refinement are applied. However, even with the assumption that the best available procedures are used, the accuracy in the end is not better than the errors reported in for each phase in Table II-7.

The alite to belite ratio can be determined by SEM-Point counting measurements and the results agree the one from XRD-Rietveld. The disagreement with ^{29}Si NMR could not be well explained. It may be related to the presence of some amorphous material on the surface of the alite grains.

The repeatability of the ^{29}Si NMR analyses is good. However, when compared with XRD-Rietveld refinements, the ^{29}Si NMR results seem to provide systematically lower belite content (more details are given in [23]). The work also addressed the Bogue calculation of the clinker minerals and showed that small errors in the oxide composition results in variation in C_3S and C_2S content at about 3 to 5%. The XRD-Rietveld results cannot be reproduced by the Bogue calculation, however, the modified Bogue calculation correlates in terms of repeatability and reproducibility.

As with reverse Bogue calculation, good agreement was found between SEM-Point counting and XRD-Rietveld data this suggests that the errors lies with the ^{29}Si NMR method and the corresponding limitations.

The results do indeed differ, probably often markedly, from the true phase compositions, notably in underestimating alite and overestimating belite, and it is unlikely that equilibrium is maintained during cooling, but the direct source of error is that the compositions of the clinker phases differ considerably from those of the pure compounds.

Slags

The composition of amorphous phase is an indicator of disorder of glass structure. It is generally closely related to the overall chemistry. Thus moduli from the bulk chemistry are often used. However, they can be modified by the crystalline phases.

Considering the Gibbs free energy [87], the amorphous phase is much more reactive than the crystalline phase. However, small percentages of crystalline phases may change the composition of the glass phase and make it more reactive [72]. The particle surface defects and relaxation of glasses are also important parameters in determining the reactivity of the slag.

The reactivity of slag in cement has been reported to depend on a variety of factors, including activators used, slag content, temperature, time, slag characteristics such as vitreous fraction, chemical composition and fineness.

According to Hinrichs *et al.* [77], the slag dosage in the range of 25-70% by mass of cement replacement did not have a significant effect. In another study, Escalante *et al.* [88] reported that reactivity decreased above 30-50% replacement. Battagin *et al.* [89] claimed that the blend with the lowest slag replacement had the lowest slag reactivity.

Since researchers have obviously obtained contradictory results, this is good motivation to investigate more work on the reactivity on slag in composite cements.

CHAPTER III: INVESTIGATION AND IMPROVEMENTS OF METHODS TO STUDY HYDRATED CEMENTITIOUS MATERIALS

In concrete and mortar, the study of the hydration process of Portland cement is complicated by the presence of the aggregates, so many methods have been investigated on cement pastes in order to define different characteristics such as: measurement of the chemically water bound using loss on ignition [90,91] or quasi-elastic neutron scattering [92], the quantification of phases by XRD [8,16,93], the characterisation of the microstructure from scanning electron microscopy combined with image analysis (SEM-IA) [93,94] and the kinetics of reaction using calorimetry.

This chapter describes the use of a combination of independent techniques to study the hydration of blended cements with slags. Quantitative X-ray diffraction with Rietveld analysis was the main techniques used to investigate the content of crystalline phases and deduce the degree of reaction of cement. Thermogravimetric analysis (TGA) was employed to quantify the content of calcium hydroxide.

Scanning electron microscopy of polished surfaces combined with image analysis was used as a complementary technique to assess the degree of reaction of cement.

Because they have the advantage of following continuously the hydration of cement, isothermal calorimetry and chemical shrinkage were used in parallel. Isothermal calorimetry measures the kinetics of reaction over the time due to the exothermic nature of hydration while chemical shrinkage follows the shrinkage due to hydration.

This chapter gives the conditions in which the different techniques were used, established the limits of utilisation as a function of the materials studied and compares the results between techniques where possible.

III.1. EXPERIMENTAL CONDITIONS

III.1.1. MIX DESIGN

Different blended systems corresponding to the reference systems were made. The water to binder volume ratio of blended pastes was kept constant and equal to the water to cement volume ratio of the unblended systems.

Table III-1 summarises the main materials used and their characteristics in pastes. The density of each raw powder was determined using helium pycnometer.

Materials	Substitution ratio of cement-SCM in paste	Density of the raw powder (g/cm ³)	Water/Binder (volume ratio)	Water/Cement (volume ratio)	Water/Binder (weight ratio)	Water/Cement (weight ratio)
Cement A	100%-0%	3.14	1.27	0.13	0.40	0.40
Cement B	100%-0%	3.18	1.27	0.13	0.40	0.40
Cement C	100%-0%	3.18	1.27	0.13	0.40	0.40
Cement D	100%-0%	3.18	1.27	0.13	0.40	0.40
Slag 1	-	2.93	-	-	-	-
Slag 8	-	2.91	-	-	-	-
Quartz	-	2.71	-	-	-	-
Cement A-Slag 1	60%-40%	3.04	1.27	0.23	0.41	0.69
Cement B-Slag 1	60%-40%	3.06	1.27	0.23	0.42	0.69
Cement C-Slag 1	60%-40%	3.06	1.27	0.23	0.42	0.69
Cement A-Slag 8	60%-40%	3.02	1.27	0.23	0.42	0.69
Cement B-Slag 8	60%-40%	3.03	1.27	0.23	0.42	0.70
Cement C-Slag 8	60%-40%	3.03	1.27	0.23	0.42	0.70
Cement A-Quartz	60%-40%	2.97	1.27	0.24	0.42	0.71
Cement B-Quartz	60%-40%	2.99	1.27	0.24	0.43	0.71
Cement C-Quartz	60%-40%	2.99	1.27	0.24	0.42	0.71

Table III-1: main systems and their characteristics in pastes

III.1.2. SAMPLE PREPARATION

III.1.2.a. Mix procedure for cementitious pastes

The mixes were made at ambient temperature (20°C) in a 25 mL polyethylene box large enough to place the paddle of the vertical mixer IKA LABORTECHNIK RW20.n.

For each mix, the cement and the corresponding SCMs were weighed out and the resulting powder was premixed in a TURBULA shaker-mixer before the addition of water to ensure a good homogenisation of the mixture. The mixing container undergoes a three-dimensional movement that exposes the product to always changing, rhythmically pulsing motion. Good homogenization required a minimum of 5 hours mixing after checking of the powder dispersion under SEM.

To keep the water to binder volume ratio constant at 1.27, the corresponding the water to binder weight ratio is given in Table III-1.

Water was added to the premixed powder and the resulting paste was mixed with a paddle at a rotation speed of 500 rpm during 3 minutes, then the mixing was stopped during 2 minutes and finally mixed again at 2000 rpm for 2 minutes.

III.1.2.b. Stopping hydration by freeze drying for early age samples

For early age specimens whose hydration was stopped at 12 hours, paste was cast in small cylinders (15 mm in diameter and 30 mm in length).

Especially with these relatively young pastes, the problem often arises of removing excess water after the specified time of curing to stop the hydration reactions. So the hydration of 12 hours samples was stopped using the freeze drying technique.

This process removes the free water by sublimation (transformation from a solid directly into a gas).

Practically, the specimens were carefully sealed into a plastic container, plunged into a Dewar filled with a cold mixture of solid CO₂ and ethanol at -80°C. The samples were left long enough (3-4 hours) in the Dewar in order to freeze completely the water. Finally the specimens were placed in a TELSTAR Cryodos Freeze-dryer to quickly remove the frozen water.

Except for ettringite, freeze drying has been shown to be effective with regard to microstructure preservation [95-97].

III.1.2.c. Solvent replacement for other samples

For later ages, specimens whose hydration was stopped at 1 day or after, the paste was cast in cylinders (30 mm in diameter and 50 mm in length). After 24 hours, the cylinders were demoulded, covered with tap water and kept saturated. The first layer (1 mm thick) of the paste cylinders exposed to water was systematically discarded in order to remove the possible leaching of Ca^{2+} induced by the curing.

At the appropriate ages, two slices about 4 mm thick were sawn from the cylinder. These slices were immediately placed in the diffractometer for XRD analysis, then dried by solvent exchange using immersion in isopropanol for 7 days. The water in the sample is exchanged with isopropyl alcohol, which does not react with cement.

The specimen should preferably be thin to allow for rapid exchange. Furthermore, the hydration should have passed the acceleration period, corresponding to maturity at 1 day.

After 7 days, the samples were put in a desiccator over silica gel and under pumping to evaporate the alcohol. Then the samples were placed again in the diffractometer for XRD analysis. Part of the slice was reserved for TGA, the rest of the slice was impregnated with epoxy resin, polished down to 0.25 μm and carbon coated for SEM examination.

The solvent exchange is considered to be gentle to the cement paste microstructure, minimizing the collapse of the C-S-H structure [98].

After stopping hydration, all the specimens were stored in a nitrogen purged chamber to protect them against possible carbonation and further hydration due to humidity.

III.2. QUANTITATIVE ANALYSIS BY XRD-RIETVELD

III.2.1. XRD EXPERIMENTAL CONDITIONS

The data of hydrated slice samples were collecting under the same conditions as for the anhydrous ones (see II.1.2.a).

For each specimen hydrated for 12 hours, after the freeze-drying procedure, the material was ground and the resulting powder was analysed by XRD.

For other ages (more than 1 day), two slices were analysed by XRD in a standard circular sample before stopping hydration with isopropanol (diameter 3.5 mm).

The XRD experiments were duplicated, hence each point represents an average of two experiments.

III.2.2. SCOPE OF REFINEMENT FOR HYDRATED PASTES

III.2.2.a. Identification of structures of hydrated phases

As for the anhydrous phases, all Rietveld refinements were made using the X'Pert High Score Plus program from PANalytical with the following structures taken from the Inorganic Crystal Structure Database (ICSD) for hydrated paste (see Table III-2).

	Hydrated phases	Formula	Crystal system	ICSD codes	Reference
	Portlandite	CH	Hexagonal P	15471	Petch, 1961 [36]
	Ettringite	C ₃ A(C\$) ₃ H ₃₂	Hexagonal P	16045	Moore <i>et al.</i> , 1970 [99] Getz-Neunhoeffer <i>et al.</i> , 2006 [100]
Hydrates from cement	Calcium monocarboaluminate	C ₄ AĈH ₁₁	Triclinic P	59327	Francois <i>et al.</i> , 1998 [101]
	Calcium monosulfoaluminate	C ₄ A\$H ₁₂	Hexagonal	100138	Allmann, 1977 [102]
	Calcium hemicarboaluminate	C ₄ AĈ _{0.5} H _{11.5}	Rhombohedral	041-0221 (PDF Number)	Pöllmann <i>et al.</i> , 1989 [103] Fisher <i>et al.</i> , 1982 [104]
	Calcium Silicate Hydrates	C-S-H Ca _{1.5} SiO _{3.5} xH ₂ O	Unknown	033-0306 (PDF number)	Mohan <i>et al.</i> , 1980 [105]
Hydrates from slag	Hydrotalcite	Mg ₆ Al ₂ (CO ₃)(OH) ₁₆ , 4H ₂ O	Hexagonal	81963	Bellotto <i>et al.</i> , 1996 [106]

Table III-2: structures of phases in the hydrated samples

Some of the hydration products are amorphous to X-rays and so do not produce sharp diffraction peaks.

As in the previous chapter, the Rietveld refinement is carried out for each different cementitious system. For instance, the incorporation of improved existing structure models such as the recent ettringite structure [107] have been tested and included in the control file. For slag blended systems, the hydrotalcite like phase could be identified: it is not exactly natural hydrotalcite which the formula is $Mg_6Al_2(OH)_{16}CO_3 \cdot 4H_2O$ but it is more like quintinite, with the formula $Mg_4Al_2(OH)_{12}CO_3 \cdot 4H_2O$ (it was validated by EDX analyses). However, the peaks do not get affected (quintinite is isostructural with hydrotalcite) and it could be noted that there is no pattern for quintinite.

III.2.2.b. Ferrite phase

In hydrated cement, the occupancy parameter values were taken to be the same as those of the corresponding anhydrous cement and were not refined. As shown in Figure III-1, the XRD-Rietveld quantification of ferrite phase was greatly improved in hydrated samples using this strategy.

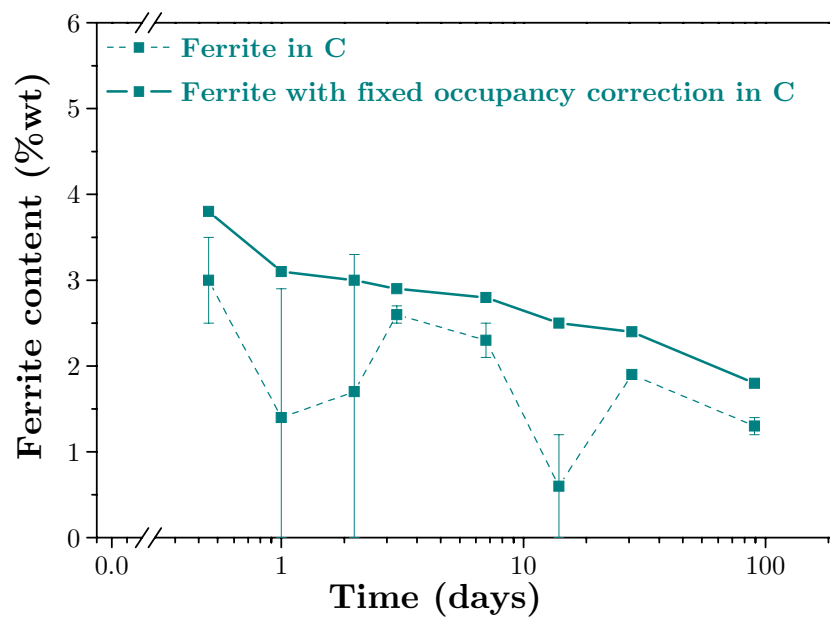


Figure III-1: influence of refinement of ferrite occupancy in Cement C

III.2.2.c. Calcite phase

As shown in Figure III-2, at 29.40° , there is an overlap between a peak of calcite and one of the poorly crystalline C-S-H phase.

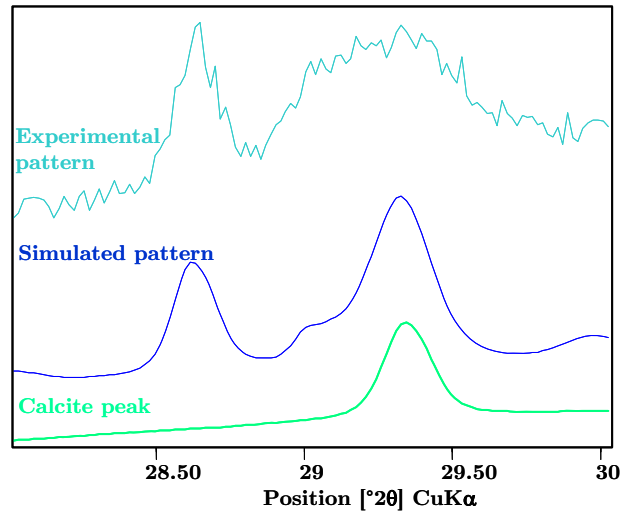


Figure III-2: part of XRD pattern of Cement C hydrated for 14 days

If calcite phase is refined at every age, its contribution is overestimated due to the presence of C-S-H. For example, for Cement C hydrated for 14 days, the calcite content would be estimated at 5 wt% whereas it was 0.4 wt% for 1 day.

The initial calcite content was low for all the anhydrous cements used (see Table II-7) and there is no strategy to differentiate calcite and C-S-H contributions. So for all cementitious mixes hydrated more than for 14 days, it was decided to not include anymore the phase of calcite in the Rietveld refinement, because of the predominance of C-S-H.

III.2.2.d. C-S-H and background contribution

For all the hydrated mixtures, the polynomial function did not describe well the amorphous hump so a background correction using the Sonneveld algorithm [108] was applied before the refinement. For long ages of hydration even, this correction did not fit the background well enough, in this case a manual correction was done to precisely achieve simulation of the C-S-H contribution.

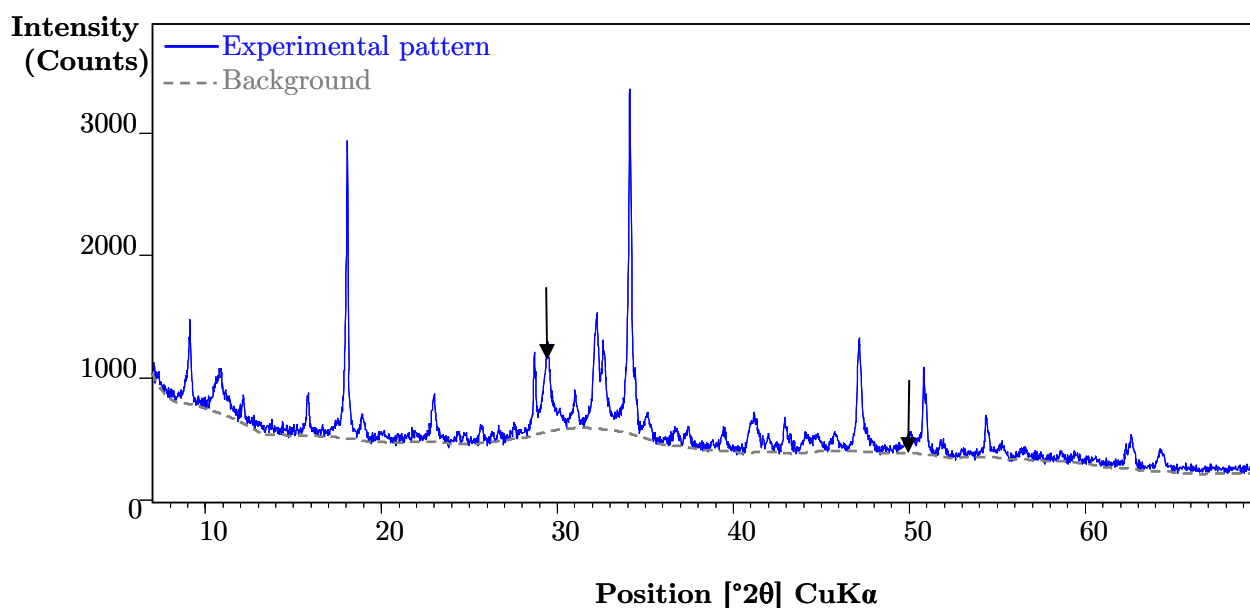


Figure III-3: XRD pattern of Cement B hydrated for 28 days

An example of XRD pattern of Cement B hydrated for 28 days is presented in Figure III-3. The presence of unfitted large peaks at about 29 and 50° (2θ CuK α) corresponds to the ill crystallized phase C-S-H. However, due to the lack of structural data, the C-S-H pattern cannot be included in the control file nor refined.

In order to refine the C-S-H contribution, a manual fit of the background is made and leads to a better simulated pattern as shown in the following figures.

The difference between manual or automatic background increased with the hydration time (see Figures III-4 and III-5).

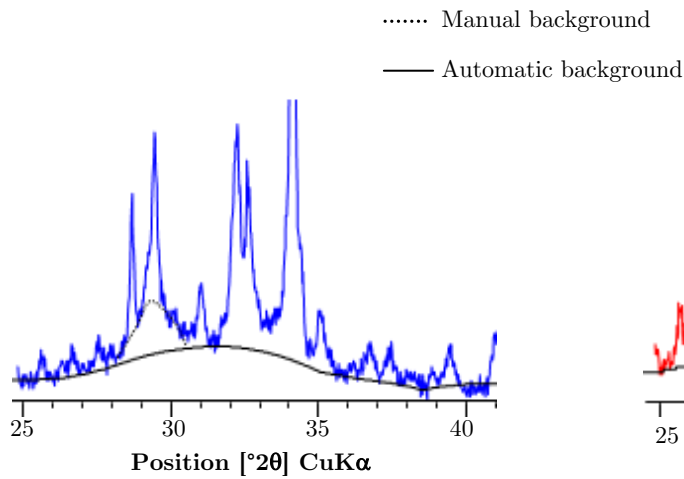


Figure III-4: XRD patterns of Cement B hydrated for 28 days with and without manual fit of background

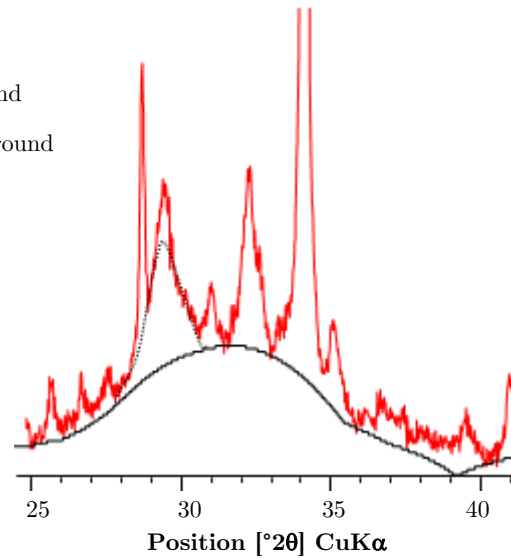


Figure III-5: XRD patterns of Cement B hydrated for 2 years with and without manual fit of background

The content of C-S-H corresponds to the amorphous content (detailed below) in the case of pure hydrated pastes.

At early ages, the difference between 2 backgrounds was not significant. However, for 2 years hydrated cements, the content of C-S-H could change 10% as a function of the choice of the background.

III.2.2.e. AFm phases

As previously noticed by comparing XRD and ^{27}Al NMR experiments some AFm phases [109,110] have low crystallinity and variations in composition that lead to changes in position and intensity of reflections in the XRD patterns.

The quantification of AFm phases by Rietveld analysis is therefore not reliable. Furthermore, the calcium hemicarboaluminate when present cannot be refined due to the lack of structural data. For this reason, ^{27}Al NMR was also used to investigate the AFt and AFm phases [111].

As shown in Figure III-6, three kinds of AFm phases could be identified by XRD analyses:

- around 9.75° : peak of calcium monosulfoaluminate;
- around 10.75° : peak of calcium hemicarboaluminate;
- around 11.5° : peak of calcium monocarboaluminate.

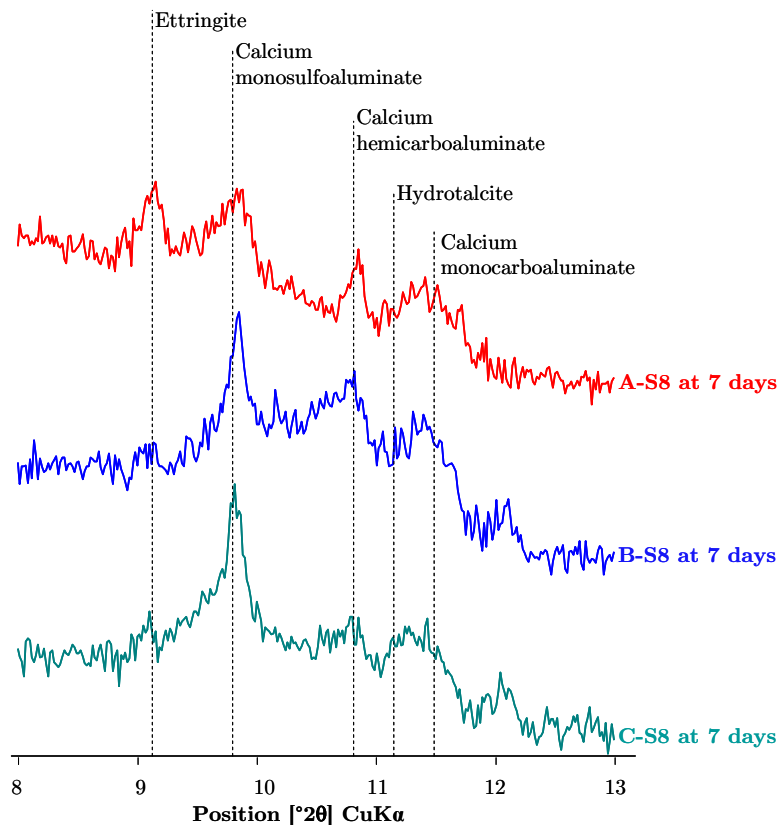


Figure III-6: XRD pattern of Cement B-Slag 1 paste hydrated for 28 days

Taking into account all the parameters for each hydrated phase and the one already defined for anhydrous phase, a control file was defined for each cementitious system.

III.2.2.f. Degree of hydration of cement

To calculate the degree of hydration of cement from XRD, the content of amorphous part is necessary. The Rietveld analysis gives the sum of the mass of phases present normalized to 100%. The result of Rietveld analysis gives the weight fraction of the anhydrous phase in the cement paste $mf_{anh}(t)$. The degree of hydration of cement is then defined as:

$$DH_{XRD}^{Cement}(t) = \frac{W_{anhydrous}(t=0) - W_{anhydrous}(t)}{W_{anhydrous}(t=0)} = 1 - \frac{W_{anhydrous}(t)}{W_{anhydrous}(t=0)} = 1 - Wf_{anhydrous}(t) \quad \text{Equation 8}$$

Where:

$W_{anhydrous}(t=0)$: initial anhydrous weight of cement;

$W_{anhydrous}(t)$: anhydrous weight of cement at time t ;

$Wf_{anhydrous}(t)$: weight fraction of cement at time t .

III.2.3. KNOWN PROBLEMS-IMPROVEMENTS

III.2.3.a. Preferred orientation

Preferred orientation corrections for sulfate phases, portlandite and ettringite were made in accordance to the March model after Dollase [50]. In order to stabilize the refinement, the shifts of these parameters, except scale factor, were damped taking care that no bounds were reached when the refinement is finished.

III.2.3.b. Reference sample as an indicator of the stability of the diffractometer

An analysis of the standard was made before and after each series of acquisitions not only to calculate the amorphous content but also to examine any possible instability of the diffractometer with time. An example of problems with the XRD generator is given in Figure III-7.

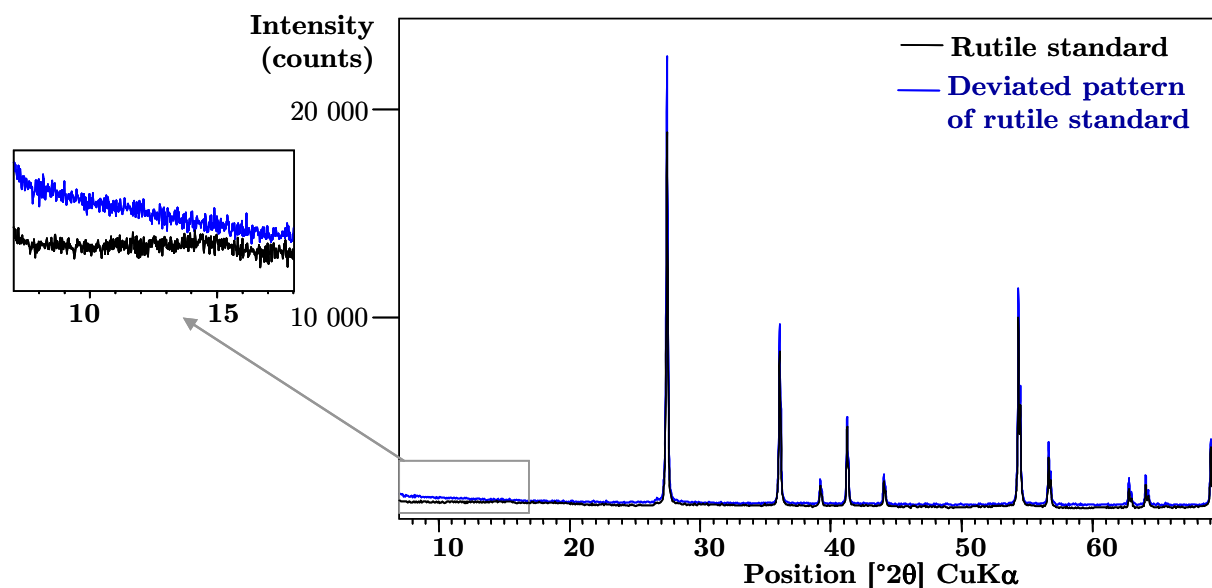


Figure III-7: XRD patterns of rutile standard with and without deviation

As shown in Figure III-8, for alite and amorphous contents, a difference in experimental acquisition conditions between the standard and the sample can lead to an important error in the quantification of the amorphous content and consequently of the other phases.

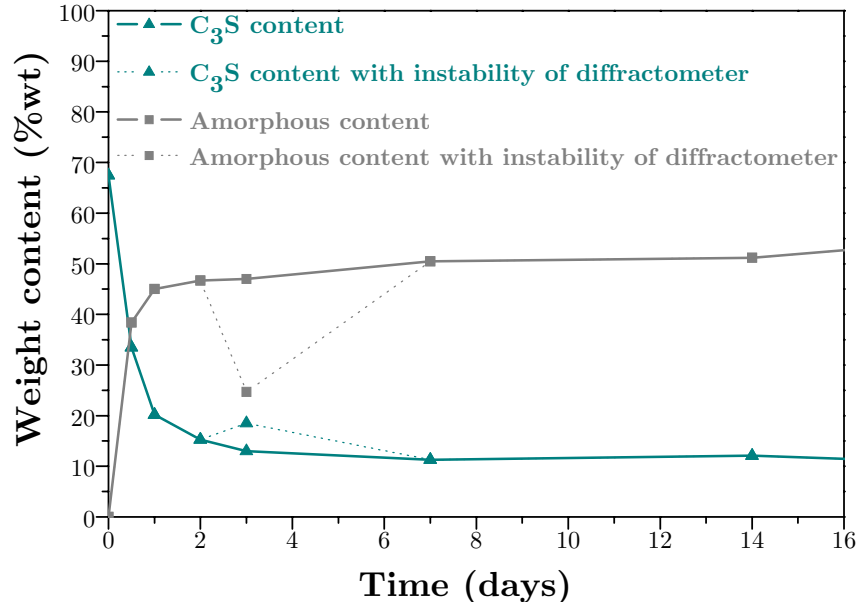


Figure III-8: evolution of amorphous and C₃S contents of Cement D with or without an instability of the diffractometer

III.2.3.c. Influence of isopropanol

For all experiments, X-ray diffraction patterns were recorded before and after stopping hydration. The results retained correspond to the refinement just after cutting the slices to avoid the possible evolution of phases after one week in isopropanol.

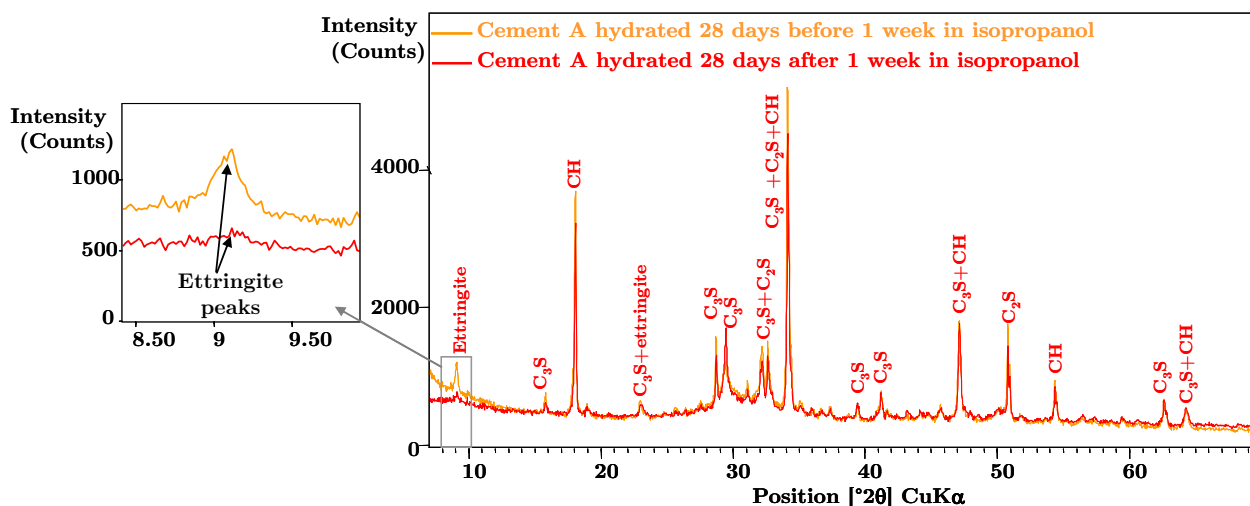


Figure III-9: XRD patterns of Cement A with influence of isopropanol

In Figure III-9, the effect of stopping hydration is shown on the same slice before and after one week in isopropanol.

As observed previously [84], it is clear that ettringite is damaged by storage in isopropanol. The corresponding quantification decreased from 8 to 5 wt% which induced also small changes in the quantification on the other phases due to the 100% normalisation of Rietveld refinement and confirmed current protocol to measure immediately after cutting.

III.2.3.d. Dilution effect

The output from the Rietveld quantification includes all crystalline and amorphous phases, hydrates and anhydrous, except water and gives the sum of the phases present normalise to 100 wt%. But this system cannot be considered closed, because in the case of hydrated paste, the total absolute mass will change with time due to the external mass (water) which enters the solid phases during hydration.

XRD measurements were made on surface of the slices which are quickly dried under nitrogen before acquisition. The X ray penetration depth can be considered around 10 µm in the case of cement and in the investigated volume, there is no or little amount of free water. Therefore, the water combined by hydration is calculated from the Rietveld output and this calculated water is added to the phases quantified by Rietveld, resulting in a closed system (see Figure III-10).

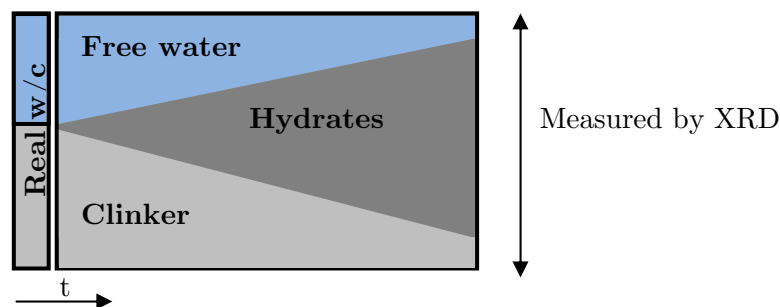


Figure III-10: schematic description of a closed system based on calculations

The formula to calculate the phase content taking into account the dilution effect is:

$$\%Phase_{\text{with correction of dilution}}(t) = \frac{100 \times \%Phase \text{ from Rietveld } (t)}{100 - LOI} \quad \text{Equation 9}$$

Where:

LOI: Loss On Ignition, weight loss from TGA measurement on anhydrous systems.

As shown in Figures III-11 and III-12, the contents of raw crystalline phases will be decreased by the correction of the dilution effect. This correction is important at early ages.

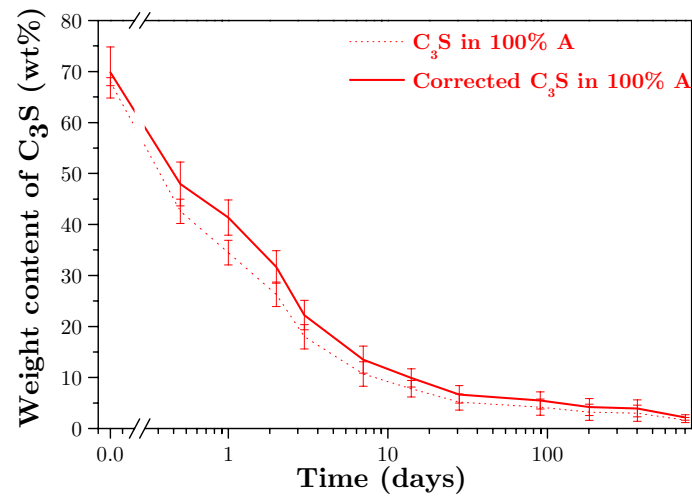


Figure III-11: evolution of C₃S corrected or not by dilution effect in the 4 cements mixes

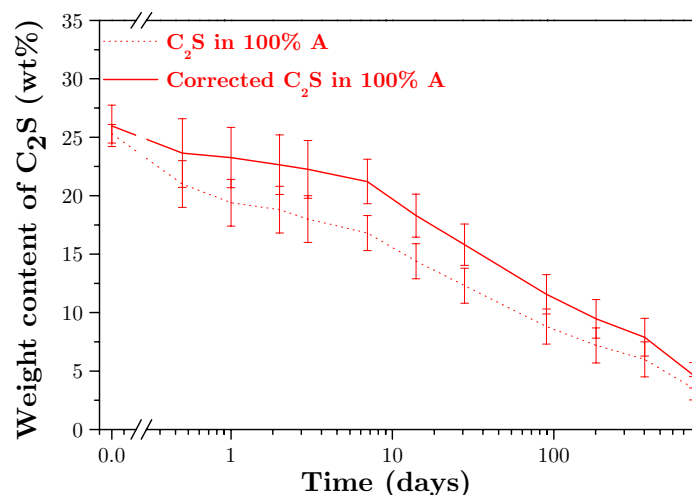


Figure III-12: evolution of C₂S corrected or not by dilution effect in the 4 cements mixes

III.2.4. REPRODUCIBILITY, REPEATABILITY AND ACCURACY

III.2.4.a. Reproducibility from the influence of the mixing

In order to test the reproducibility, a new series of samples of Cement D were acquired at 1, 2, 3, 7, 14 and 28 days. The XRD patterns provided comparable results to the duplicates from the first mixes (so 3 points are on Figure III-13 for each age).

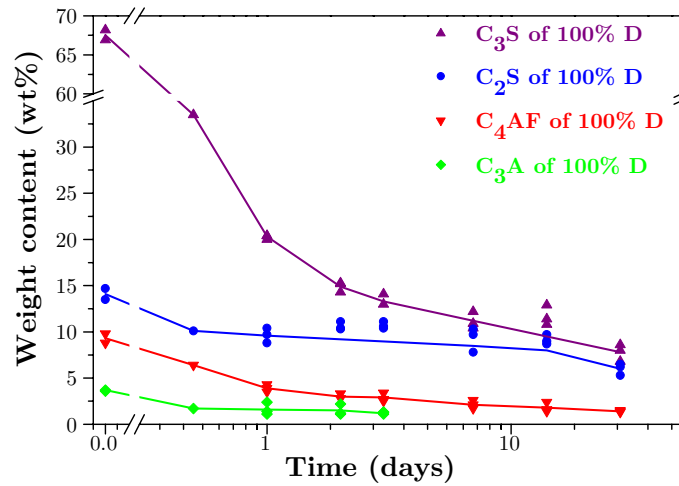


Figure III-13: evolution of contents of clinker phases in Cement D

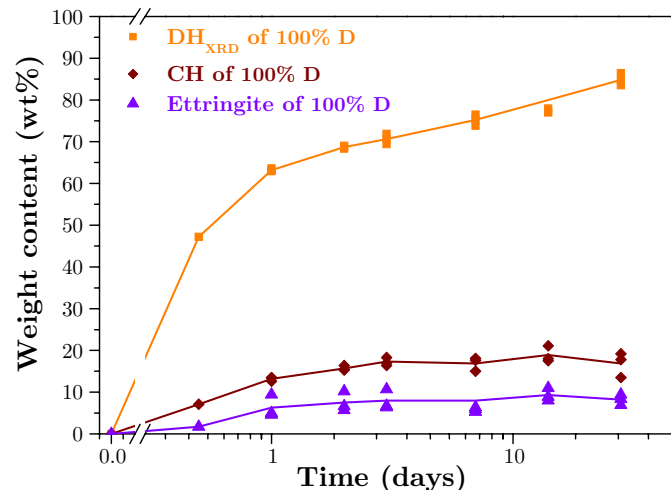


Figure III-14: evolution of portlandite, ettringite and degree of hydration of Cement D

As shown in Figures III-13 and III-14, the refined contents of phases and the degree of reaction of cement obtained from different mixes are quite close from both mixes. Indeed, between two mixes, there is less than 1 wt% of error on the different contents of each phase.

III.2.4.b. Repeatability from the influence of the Rietveld refinement

As for the refinement of anhydrous materials, the quantifications were made several times as a function of parameters previously defined.

In order to precisely establish the error bars on the final results, we considered the maximum difference between the refinements made on each phase. The results are acceptable and the corresponding errors are represented in the graphs.

III.2.4.c. Reproducibility compared to results from ^{29}Si NMR

Some comparisons were done for Cement A and C between ^{29}Si NMR from another study [22] and our XRD results. As shown in Figures III-15 and III-16, it was found that the results for Alite in Cement A agreed well.

For belite in both cements, the ^{29}Si NMR underestimate the results compare to XRD but the ranges are similar and at the moment ^{29}Si NMR did not provide any error bars.

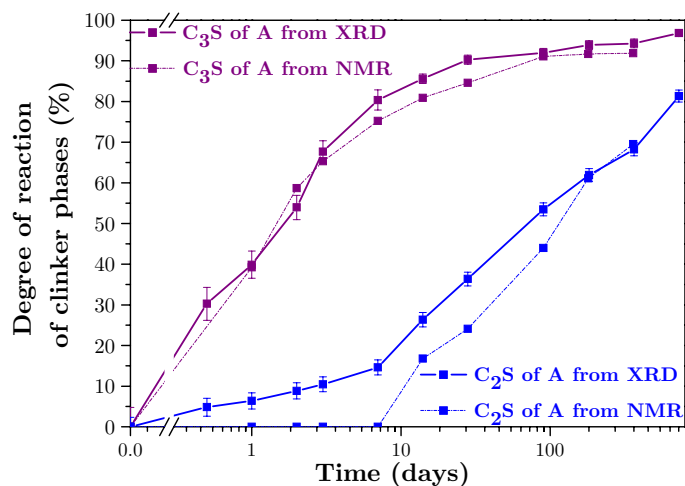


Figure III-15: degree of reaction of alite and belite from XRD-Rietveld and ^{29}Si NMR for Cement A

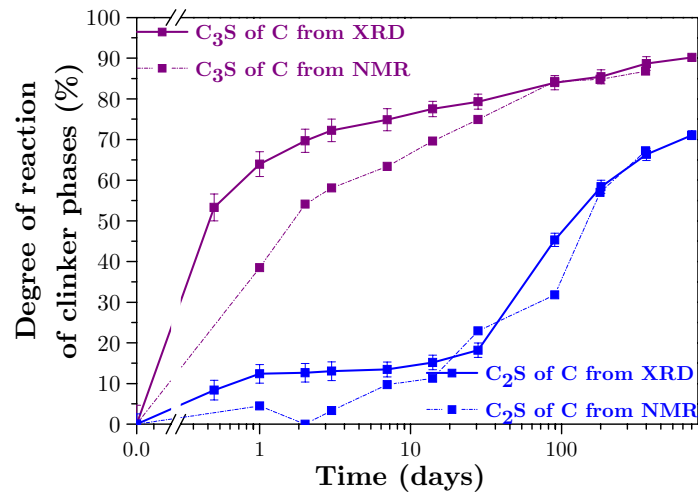


Figure III-16: degree of reaction of alite and belite from XRD-Rietveld and ^{29}Si NMR for Cement C

III.3. THERMAL ANALYSIS

III.3.1. TGA EXPERIMENTAL CONDITIONS

Thermogravimetry analyses were carried out in a dry nitrogen atmosphere with a Mettler Toledo TGA/SDTA851e. The dry pastes were crushed to powders, put in 40 mL crucibles and an alumina lid was placed over each crucible to prevent carbonation and/or other kind of contamination.

The samples were heated from 30 to 950°C at a constant rate of 10°C/min under a nitrogen flow rate of 30 ml/min.

III.3.2. PRINCIPLE

Thermogravimetric analysis depends on measuring the dynamic weight loss from a sample as it is heated at a controlled rate. The corresponding derivative thermogravimetric (DTG) curve is often calculated to better identify the changes.

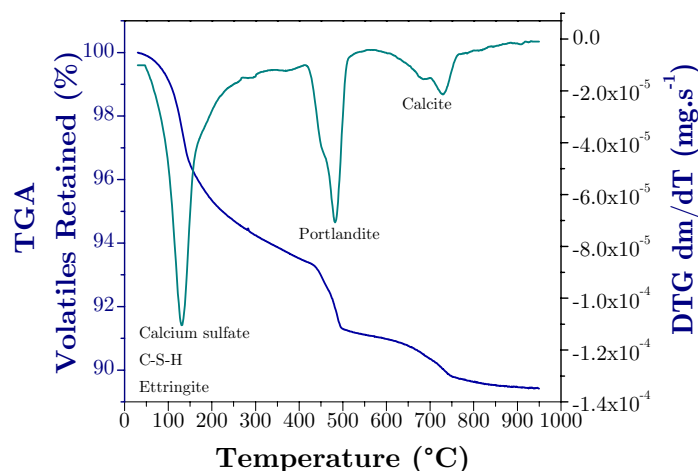


Figure III-17: TGA and DTG curves for Cement B hydrated for 12 hours

Figure III-17 shows an example of TGA and DTG curves of a cement paste.

- From 25 to 415°C: part of the bound water in C-S-H escapes and there is also the decomposition of calcium sulfate components around 180-300°C.
- From the thermogravimetric (TG) curve, a weight loss due to dehydration of calcium hydroxide occurs in the region of 420 and 550°C and the chemical reaction is:



The weight loss corresponding to one mole of water originates from the dehydroxylation of one mole of calcium hydroxide.

- If there is evidence of carbonation, which occurs in the temperature range 600-780°C, then the amount detected on the TG output must be accounted for.

Carbonation equation from calcite or even vaterite (normally this reaction should not occur in nitrogen atmosphere during TG measurements):



Decarbonation equation:



A correction to the portlandite content can be made by quantify the amount of carbonated CH which can be detected in the decarbonation process between 600 and 900°C. However, it is an assumption because C-S-H may also carbonate directly. Thus, to take into account the total portlandite content, the following equation was used [112]:

$$CH_{\text{tot}} = \Delta CH \times M_{\text{Ca(OH)}_2} / M_{\text{H}_2\text{O}} + \Delta C\hat{C} \times M_{\text{Ca(OH)}_2} / M_{\text{CO}_2} \quad \text{Equation 13}$$

Where:

ΔCH : weight loss due to the dehydration of calcium hydroxide;

$\Delta C\hat{C}$: weight loss due to decarbonation of calcite;

$M_{\text{Ca(OH)}_2}$: molar weight of portlandite (74 g.mol⁻¹);

$M_{\text{H}_2\text{O}}$: molar weight of water (18 g.mol⁻¹);

M_{CO_2} : molar weight of carbon dioxide (44 g.mol⁻¹).

However, it must be noted that the second term of the equation relating to carbonation is only used if a weight loss due to carbonation is seen on the TG curve.

III.3.3. DATA TREATMENT

Two kinds of determination of portlandite and calcite contents were investigated:

- the tangent method;
- the derivative method.

Tangent method

At 425-550°C, there is a change in TGA slope which is due primarily to decomposition of portlandite. Even if the loss of bound water from the decomposition of the C-S-H mainly occurs from 180 to 300°C [5], some water loss from the C-S-H also occur in this temperature range and beyond.

So the tangent method takes into account the C-S-H contribution.

The amount of portlandite and calcite were calculated using the “tangent method” as illustrated in Figure III-18.

The onset and final temperature for the weight loss of water from CH was marked on the plotted TG curve (blue). Tangent lines were drawn from each point along the TG curve (blue lines). A line was then drawn between the onset point and the final temperature point along the slope of the TG curve.

The mid-point was found and a vertical line (blue arrow) between the two blue tangent lines was then drawn which passes through the mid-point.

The length of the vertical line is related to the percentage weight loss on the plot (the Y axis) and corresponded to the weight loss of water from CH.

The same procedure was used in the temperature range 600-780°C on the TG curve for calcite determination (red part in Figure III-18).

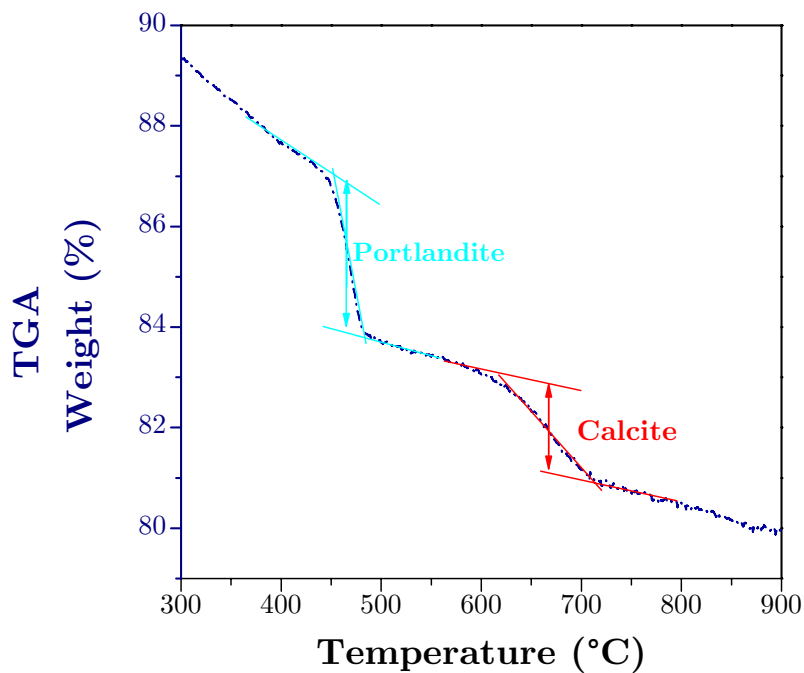


Figure III-18: determination of portlandite and calcite contents by tangent method

III.3.3.b. Derivative method

An alternative method is to calculate the amount of portlandite and calcite using the first derivative curve.

The DTG curve better marks all different processes than TGA because it have marked inflexion points, plateaus, features that are not clear in the TGA curves.

The principle of this method consists to trace the derivative curve, find the beginning and the end of the derivative peak and measure the weight loss corresponding (see Figure III-19).

It is very simple to derivate the curve and calculate the integration of the peak to find the weight lost.

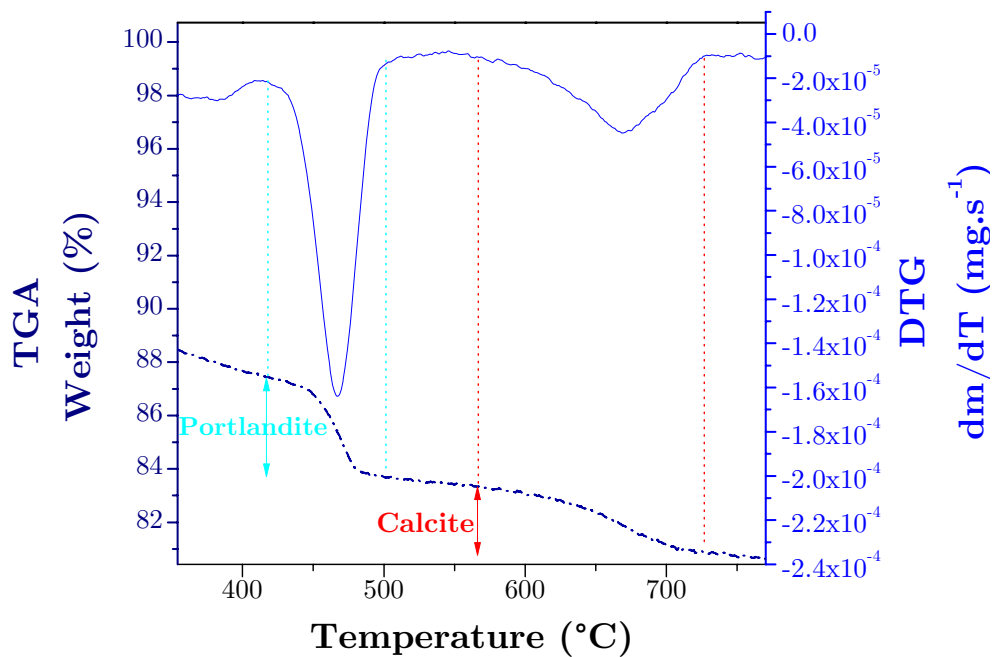


Figure III-19: determination of portlandite and calcite contents by derivative method

Comparison between tangent and derivative methods

As shown in Figure III-20, the results from tangent and derivative methods deviated more than 2%. The results from tangent method appeared to be pretty reproducible because the method is easy to apply. However, with the derivative method, it is so easy to define the start and end points. In addition, the tangent method is more realistic because some C-S-H contribution can be taken into account whereas the derivative method does not provide the background modification induced by C-S-H in the same temperature range.

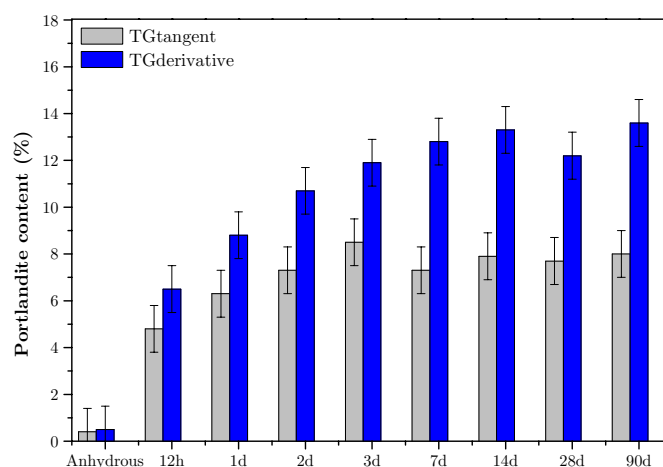


Figure III-20: results of TGA measurements for Cement A-Slag 8

III.3.4. SAMPLING EFFECT

Because the quantity used for TGA analysis was very small (between 20 and 40 mg) when the experiment was redone, if the result was reproducible it was assumed to be representative of the whole specimen that it was extracted from.

So the sampling effect is investigated by considering two kinds of samples at 28 days:

- one from the border of the slice;
- the second from the centre.

As shown in the following table (Table III-3), the results between the two samples were not significantly different. This indicates that effects of leaching are negligible. Nevertheless, samples were always taken from the centre of the slice.

		Center	Border
Portlandite content	Tangent method	7.7	7.6
	Derivative method	12.2	11.8
Calcite content	Tangent method	1.0	0.8
	Derivative method	4.4	4.4

Table III-3: results of sampling effect from Cement B-Slag 8 pastes hydrated for 28 days

About the storage, the samples are kept under nitrogen atmosphere so they should be protected against carbonation; however, calcite was always present on TGA curves even if the content in the initial cement was low (it could be introduced with mixing water).

The samples can stay several hours exposed to air waiting for their turn in the device to be analysed. To study if this was the reason for the unexpected content of calcite, the place of specimen in the analysis sequence was also tested. A specimen was analysed at the beginning of a series of samples and a similar specimen was analysed at the end of this series. There was no significantly difference.

When no lid was used, the shape of the DTG curve was modified by an apparent weight gain as shown in Figure III-21, just after the dehydration weight loss of portlandite and may be due to an instrument drift. This was resolved by recalibration of the equipment. Other cares were done using a bigger sample and systematically placing a lid over the sample.

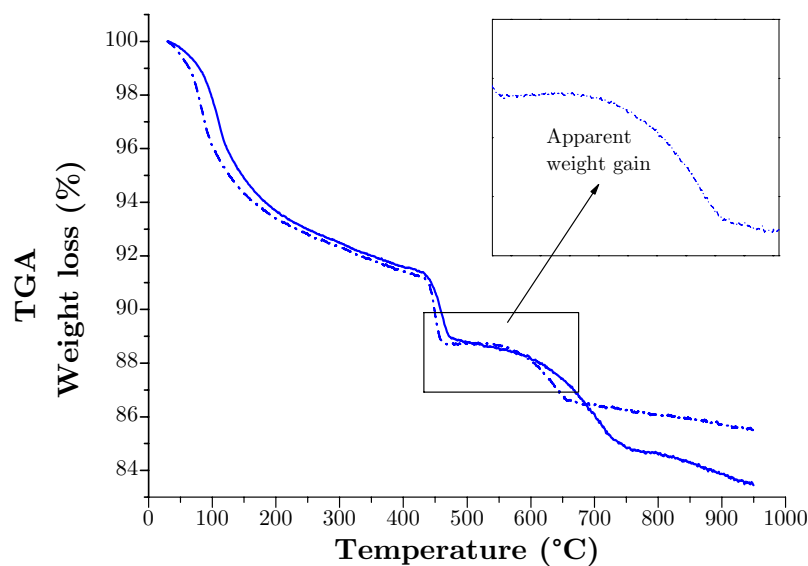


Figure III-21: TG curves with an apparent weight gain in case of problem of calibration or contamination

III.3.5. REPEATABILITY AND REPRODUCIBILITY

A series of 8 different samples from the same specimen (Cement A hydrated for 2 days) were acquired by TGA. As shown in Figure III-22, the results were repeatable with a very low standard deviation value of 0.47%.

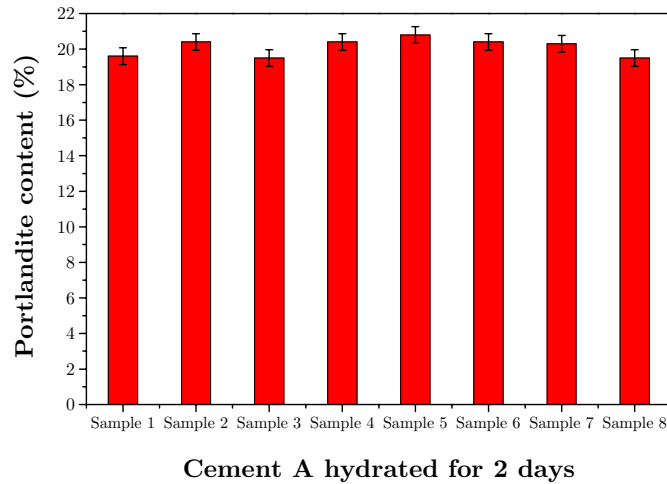


Figure III-22: repeatability tests of Portlandite content from TGA measurements of Cement A hydrated for 2 days

Some samples from B-S8 batch were sent to EMPA for independent checking. Taking into account the errors, the values of portlandite were close except at 3 days. However, as shown in Figure III-23, the experimental conditions could vary for one lab to another one, particularly concerning the storage of samples (we kept under N₂ atmosphere).

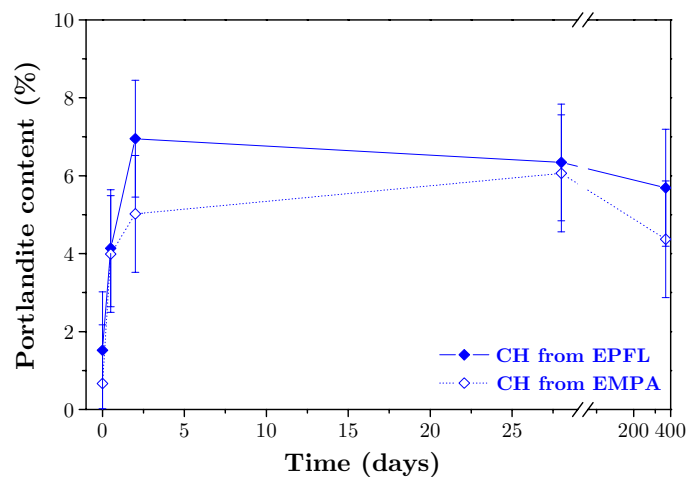


Figure III-23: Portlandite content in B-S8 pastes determined by TGA measurement in two different laboratories

III.4. SCANNING ELECTRON MICROSCOPY

III.4.1. PRINCIPLE

Scanning electron microscopy is one of the most useful technique to investigate the microstructure of materials and has been extensively used to study both quantitatively and qualitatively the microstructural evolution of cementitious materials during their hydration [94,95,113-117]. The technique has many advantages, polished sections can be observed with minimal disturbance of the microstructure.

The SEM samples were prepared as already described in Chapter II.

III.4.2. IMAGE ANALYSIS

Backscattered electrons imaging is used to detect the contrast between areas with different chemical compositions. These can be observed especially when the average atomic number of the various regions is different. The heavier the sample atoms are, the more electrons are backscattered, and the brighter the image will be. The yield, energy spectrum and depth of escape of backscattered electrons are directly related to the average atomic number of the considered phase or material, and/or its internal microporosity. This leads to a specific contrast which allows phase discrimination on the basis of their brightness on the screen. In the case of cementitious materials, depending on the acceleration voltage, the depth of interaction volume from which BSE are detected is about 0.05-0.2 μm across.

Quantitative analysis by imaging is based on the principles of stereology which deals with the interpretation of three-dimensional structures by means of their two-dimensional sections. One of the oldest proofs in stereology shows that the volume percentage in 3D is equal to the area percentage in a 2D surface.

The image analysis was carried out from the procedure developed in our lab by Gallucci, based on the grey level histogram which is the frequency plot of its grey levels.

For a SEM-BSE image of a polished paste, porosity appears black, unhydrated grains bright, portlandite light grey and C-S-H darker grey. A typical example of SEM-BSE image for

hydrated paste and its corresponding grey level histogram is presented in Figures III-24 and III-25. A recent work detailed what causes differences of C-S-H gel grey levels in backscattered electron images [118].

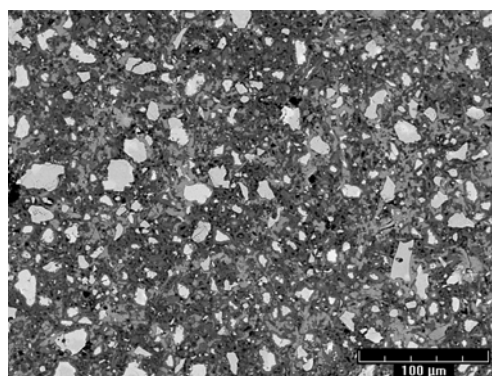


Figure III-24: SEM-BSE picture of Cement A hydrated for 3 days

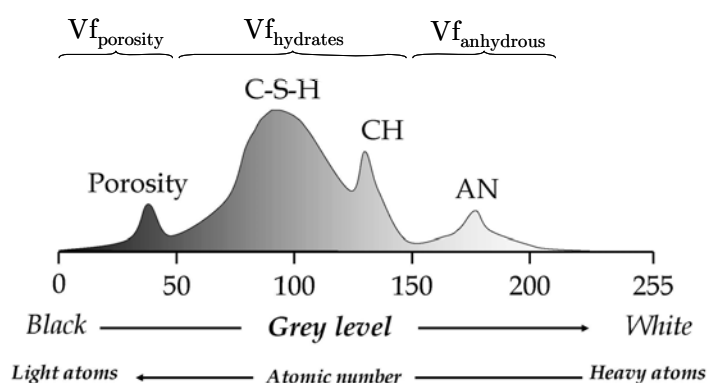


Figure III-25: corresponding grey level histogram

For the SEM-IA, from 70 to 100 images for cementitious pastes (and 100 images for mortars) were acquired at a nominal magnification of $\times 800$ (pixel size = $0.375 \mu\text{m}$). As further work [116], the anhydrous material was segmented by setting a threshold at the minimum grey level between the peaks corresponding to anhydrous and hydrated phases.

To reduce the noise produced by imperfections in the image, some image processing such as filtering (median), hole filling, etc. is applied. Once the phases are isolated, a quantitative and qualitative analysis of the microstructure can be made. So the contrast between the anhydrous grains and their surroundings is sufficient to allow quantification of their total area and size distribution by image analysis, thus measuring directly the degree of hydration of cement.

The challenge in this approach was to correctly discriminate anhydrous grains from Portland cement, hydrated products, porosity and to measure their area fractions.

III.4.3. DEFINITION OF DEGREE OF HYDRATION OF CEMENT BY SEM-IA

The volume ratio between the anhydrous phase and the total volume of the cement paste including porosity can be easily deduced from the SEM-IA results.

At time $t=0$, the volume fraction of the anhydrous phase is:

$$Vf_{\text{anhydrous}}(t=0) = \frac{V_{\text{anhydrous}}(t=0)}{V_{\text{anhydrous}}(t=0) + V_{\text{water}}(t=0)} \quad \text{Equation 14}$$

Where:

$V_{\text{anhydrous}}(t=0)$: initial volume of cement;

$V_{\text{waters}}(t=0)$: initial volume of water.

Then we considered that the total volume of the cement paste (including porosity) is constant with time. Any error induced by this hypothesis is small compared to other sources of errors.

The degree of hydration of cement is then defined as:

$$DH_{\text{SEM}}^{\text{Cement}}(t) = \frac{Vf_{\text{anhydrous}}(t=0) - Vf_{\text{anhydrous}}(t)}{Vf_{\text{anhydrous}}(t=0)} \quad \text{Equation 15}$$

Where:

$Vf_{\text{anhydrous}}(t=0)$: initial volume fraction of cement;

$Vf_{\text{anhydrous}}(t)$: volume fraction of cement at time t .

III.4.4. REPEATABILITY AND REPRODUCIBILITY

100 SEM-BSE pictures were recorded for 3 sets: two different batches of pictures from same mix of Cement A and the third batch of pictures from a different mix (see Figure III-26).

The standard errors induced by acquisition showed that both the dispersion from an image to another one inside the same set of pictures and the deviation between two different sets of pictures are not significantly different and reveals a very low error (0.1%).

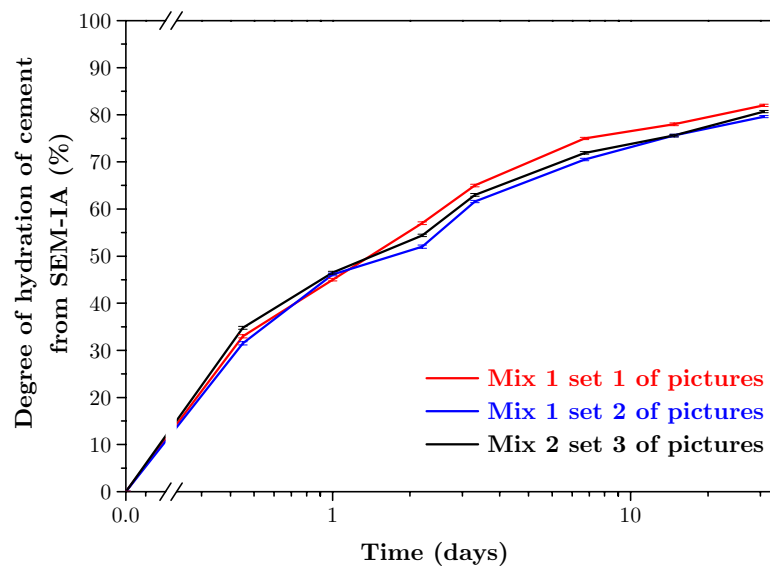


Figure III-26: different degrees of hydration of cement from SEM-IA as a function of different mixes

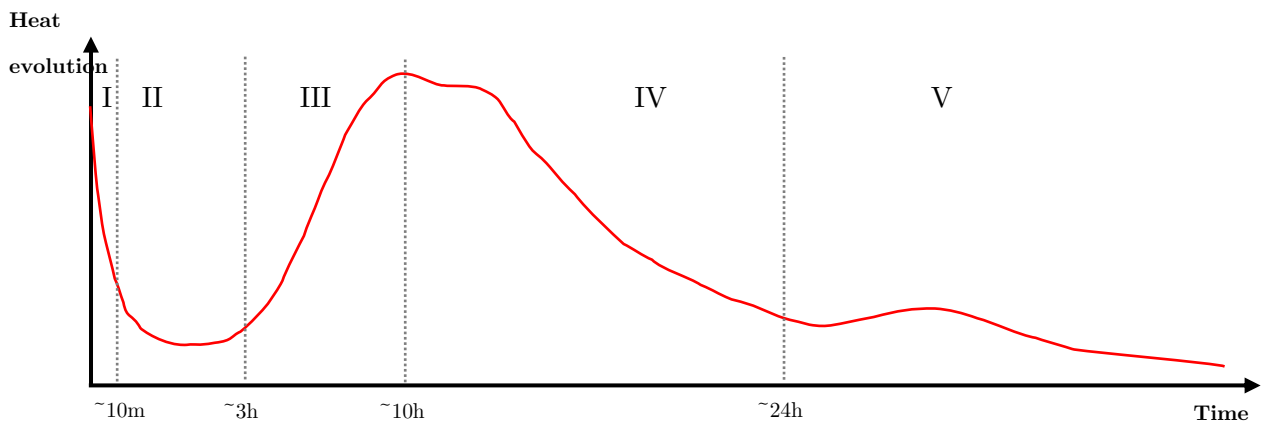
III.5. ISOTHERMAL CALORIMETRY

III.5.1. PRINCIPLE

Calorimetry is one of the techniques used to follow the hydration process. As the reaction is most of the time highly exothermic, it is possible to study its kinetics.

The advantage of this technique is that the hydration process can be followed continuously at realistic water/cement ratios in situ without the need for drying and aims at giving an indication of the overall rate of reaction while following the overall rate of heat evolution.

The typical rate of heat evolution for a hydrating cement shows several periods as shown in Figure III-27.



- I. Initial dissolution: early reaction of cement.
- II. Induction: steady and slow reaction. The degree of hydration changes little.
- III. Acceleration period: rapid precipitation of C-S-H and CH.
- IV. Deceleration period.
- V. Slow reaction period: in IV and V periods, the reaction happens mainly by diffusion through hydrate layer.

Figure III-27: rate of heat evolution during the hydration of cement

The disadvantage is that only the overall heat evolution can be measured which is the sum of the heat evolved by all the reactions occurring at any particular time. Indeed, if exothermic and endothermic reactions take place simultaneously the rate of heat output could be negligible even when the rate of reaction is high. Therefore, calorimetry can only be used as a global measure of the degree of hydration.

III.5.2. PROCEDURE

Cementitious pastes were examined at 20°C using an isothermal calorimeter TAM Air from Thermometric Sweden.

It consists of 8 parallel twin type measurement channels maintained at a constant temperature: one from the sample, the other for the reference vessel.

The reference vessel is used to reduce the signal to noise ratio and to correct measurement and temperature artefacts. 20ml glass ampoules are used for both the sample and the reference container. Heat is conducted from the sample to the reference sample (water with same thermal mass) so hydration is effectively isothermal. The small temperature difference between the hydrating cement and the reference is proportional to the rate of heat evolution of the cement; this is measured by a thermocouple.

Each channel is independent from the other channels and was calibrated before any experiments were made.

The thermal inertia is expressed by the time constant of a calorimeter which depends on two parameters: the sample heat capacity and the heat transfer properties of the calorimeter. The measured time constant has been used to correct the output signal (Tian correction) for the thermal inertia of the calorimeter especially at very early ages as shown below:

$$P(t) = \varepsilon \left(U + \tau \frac{dU}{dt} \right) \quad \text{Equation 16}$$

Where:

$P(t)$: the thermal power produced in the sample (Watts);

U : the voltage output of the heat flow sensors (Volts);

ε : the calibration factor (W/V);

τ : the time constant of the calorimeter (s) which has been calculated to be 4 minutes.

III.5.3. OPTIMISATION OF EXPERIMENTAL CONDITIONS

Work made in our laboratory for the Nanocem Calorimetry Workshop Internal Project [119] show some differences on heat evolution of pastes as a function of reference sample and also as a function of quantity introduced in the glass ampoule.

Previous results were made with a glass ampoule completely filled up with cementitious pastes (around 40 g) and without reference sample (empty cell).

The specific heat has to be well balanced which is particularly important at later ages. So these studies use a reference with the same specific heat as the cement paste. We choose to work with a deionized water reference ampoule and using the following law of mixture equation, we calculated the corresponding specific heat for a paste [120]:

$$C_p^{paste} = x^{water} C_p^{water} + x^{cement} C_p^{cement} \quad \text{Equation 17}$$

Where:

x^{water} : mass fraction of water in paste;

x^{cement} : mass fraction of cement in paste;

C_p^{water} : specific heat of water;

C_p^{cement} : specific heat of water.

Considering, the water-cement ratio of 0.4, $C_p^{water}=4.18$ J/(g.K) [121] and $C_p^{cement} = 0.75$ J/(g.K) (based on the measured values for tricalcium silicate and dicalcium silicate [122]) we found a specific heat of cement paste of 1.75 J/(g.K).

Figure III-28 shows the difference between the heat evolution of cementitious pastes with or without new experimental conditions.

The experimental modifications lead to slight differences on the heat evolution of cementitious pastes. There are some changes in intensity but the relative shapes of peak are similar.

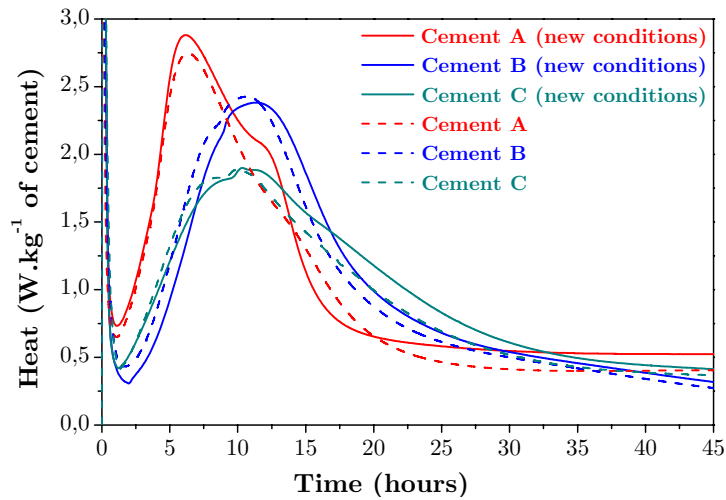


Figure III-28: heat flow of 3 cements with different experimental conditions

So to improve the detection with the calorimeter sensors, the quantity of paste was reduced to 15 g and to balance the specific heats, a 6,3 g glass ampoule of water was used as a reference.

A special care was also taken concerning the quantity of paste used in the mixer. In the following Figure III-29, 3 different quantities of paste were mixed and generated similar global reaction, but with some shifts. We chose to work with 160 g of paste to provide all the specimens for complementary analyses (XRD, SEM, TGA, chemical shrinkage).

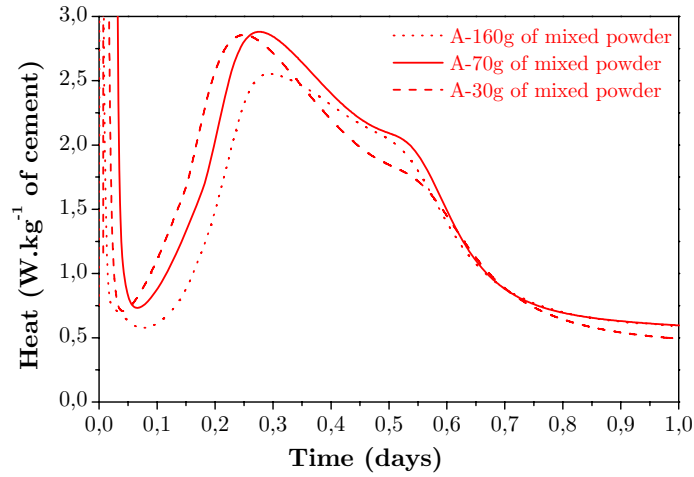


Figure III-29: heat release for 3 pastes mixed with 3 different quantities

III.6. CHEMICAL SHRINKAGE

III.6.1. PRINCIPLE

The mechanism of chemical shrinkage is a rapid and convenient method for monitoring hydration rates. This method is based on the fact that the volume occupied by the hydration products is lower than that of the reactants. This is due to the fact that “water” has a lower specific volume when bound to a solid than when free in a liquid as reflected in the following equation:

$$V_{\text{cement}}(t = 0) + V_{\text{water}}(t = 0) > V_{\text{hydrates}}(t) \quad \text{Equation 18}$$

Where:

$V_{\text{cement}}(t=0)$: initial volume of cement;

$V_{\text{waters}}(t=0)$: initial volume of water;

$V_{\text{hydrates}}(t)$: volume of hydrates at time t .

The method chosen here is dilatometry based on the protocol developed by Geiker [123] and optimised in our laboratory by Costoya [124] (see Figures III-30 and III-31).

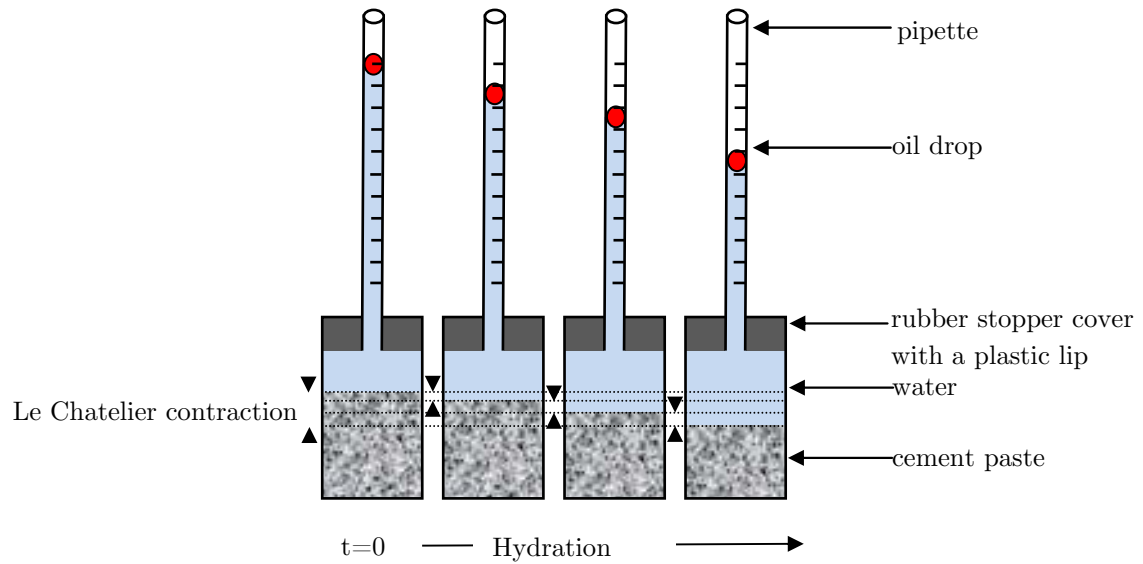


Figure III-30: schematic description of chemical shrinkage



Figure III-31: picture of the mounting of chemical shrinkage

III.6.2. EXPERIMENTAL CONDITIONS

The chemical shrinkage setup was designed at the Laboratory of Construction Materials and it consists of a flask that contains the paste, on top of which a pipette is connected. As it was previously found that the cylindrical flasks were found to work the best (compared to erlenmeyer flask) [124] and were used for the remainder of the experiments. Cylinders used for the experimentation had 2 cm height by 1 cm of diameter. The thickness of paste introduced was kept constant in all measurements and equal to 1 cm (5 g of paste). The paste was tapped in order avoid the presence of entrapped bubbles. Water was added immediately to the top of the paste, taking special care to minimize mixing risking the dilution of the paste.

Water is filled on top of the cement paste until it fills also the pipette. The system is sealed at the interface between the pipette and the flask with rubber lids and on top of the pipette with a coloured oil drop. This coloured oil drops are also used as tracers in the image analysis of the pictures of the capillary taken with the webcam. The flasks are maintained in a thermostatic bath at 20°C to avoid effects of heat release on volumetric changes of the paste.

As the hydration proceeds and the paste shrinks, the level of water in the pipette decreases. This level is monitored using a webcam connected to a computer that allows automated acquisition every 5 minutes. To extract the level of water in the pipette, the pictures were numerically processed with a control file of various pictures developed by Bishnoi at the LMC.

Each curve presented is the average of a minimum of 3, but mostly 6, replicas of a cement paste system.

III.7. COMPARISON OF ALL TECHNIQUES

III.7.1. COMPARISON OF DEGREE OF HYDRATION OF CEMENT BY XRD AND SEM

The definition of degree of hydration of cement can be different according to the technique used but the degree of reaction of cement from XRD-Rietveld and SEM-IA are similar.

The results for the two techniques are compared in Figure III-32. The tendency of SEM-IA to overestimate the degree of reaction of cement compare to XRD-Rietveld, could be linked to a certain error on $V(t=0)$ which could introduce systematic error coming from the experimental mix design.

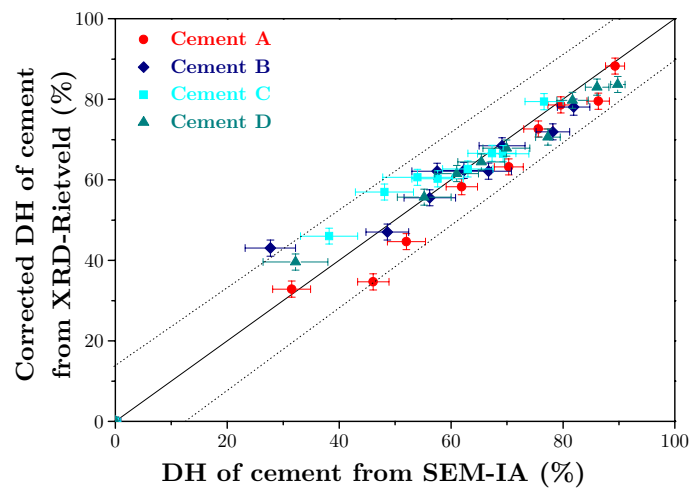


Figure III-32: degree of hydration of cement with dilution effect from XRD-Rietveld versus that from SEM-IA for 4 cements pastes

At 1 day, the degree of hydration of cement measured by XRD-Rietveld is significantly higher than that by SEM-IA, for 4 cements.

Normally, the errors induced by SEM-IA at early ages could be explained by the assumption that small anhydrous grains (inferior to 0.5 μm) are often not detected by SEM-IA. Omission of these small grains will lead to overestimation of the degree of reaction of cement. But here, it is the opposite case so XRD seems to overestimate the degree of hydration of cement.

Globally, there is a reasonable agreement between two techniques (see Figures III-33 to III-35).

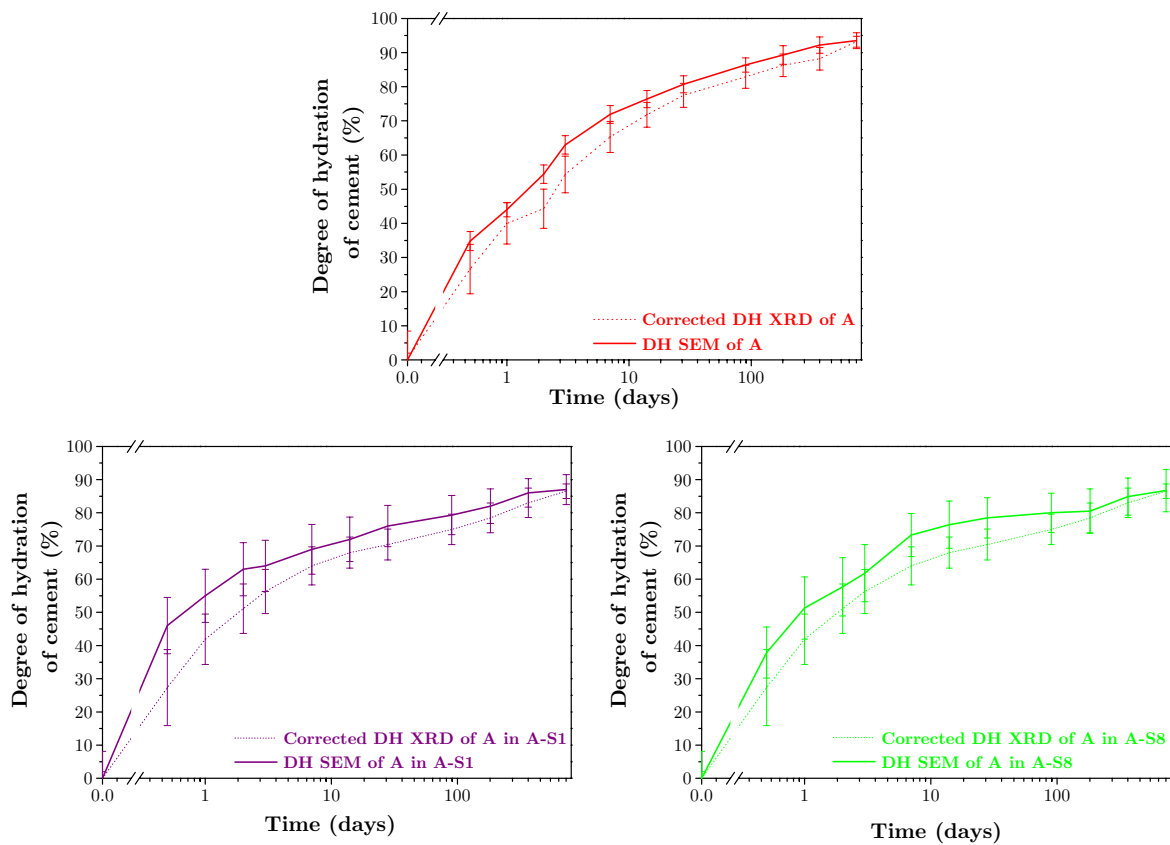


Figure III-33: degree of hydration of Cement A with dilution effect from XRD versus that from SEM-IA for all A systems

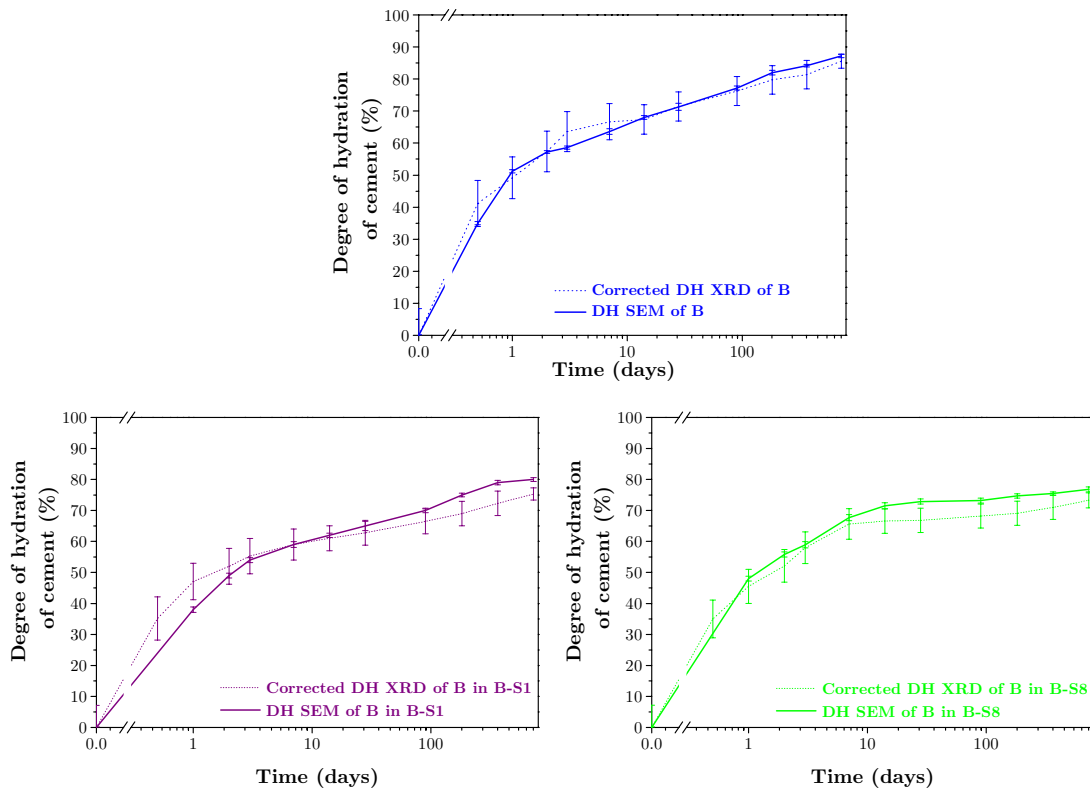


Figure III-34: degree of hydration of Cement B with dilution effect from XRD versus that from SEM-IA for all B systems

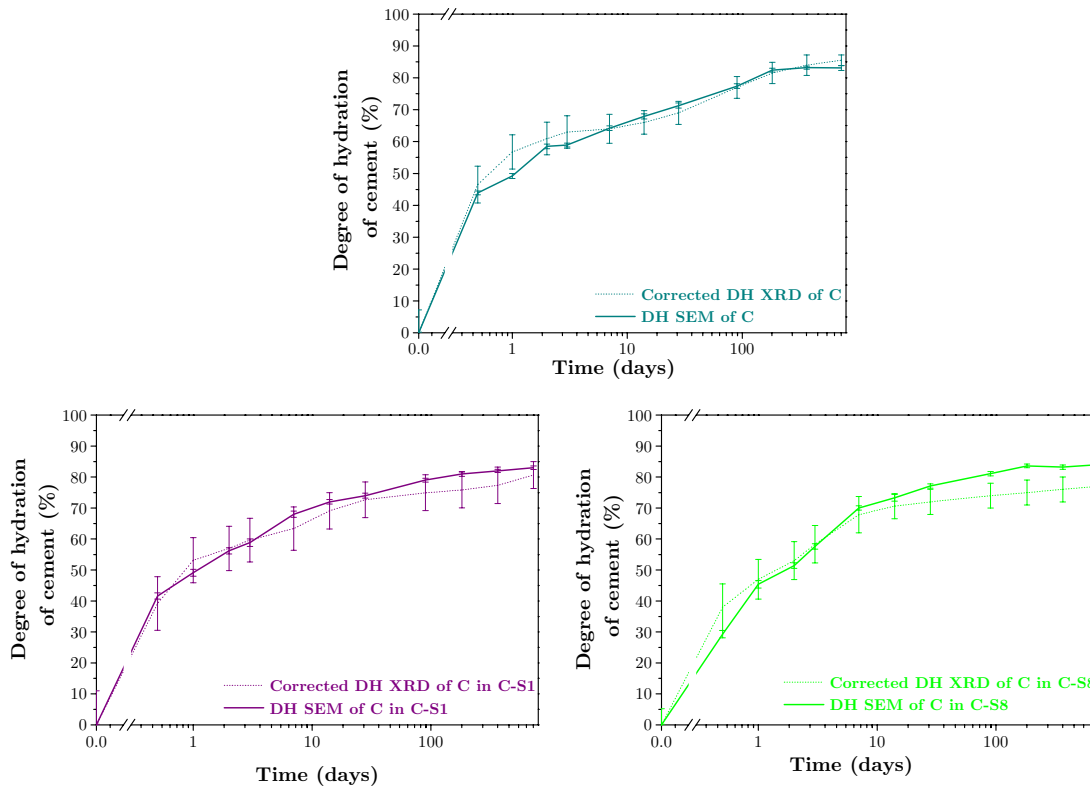


Figure III-35: degree of hydration of Cement C with dilution effect from XRD versus that from SEM-IA for all C systems

III.7.2. DEGREE OF HYDRATION OF CEMENT DEFINED BY CALORIMETRY

For Portland cement pastes, the following definition of degree of hydration of cement can be deduced by calorimetric experiments:

$$DH_{\text{Calorimetry}}^{\text{Cement}} = \frac{\text{Cumulative heat of hydration}}{Q_{\text{pot}}} \quad \text{Equation 19}$$

with Q_{pot} the potential heat of hydration liberated if all phases have reacted as it was suggested by Taylor [5] using least squares regression analysis:

$$Q_{\text{pot}} = q_1 C_3\text{Swt}\% + q_2 C_2\text{Swt}\% + q_3 C_3\text{Awt}\% + q_4 C_4\text{AFwt}\% \quad \text{Equation 20}$$

Where:

q_1 : enthalpy of hydration of the pure alite;

q_2 : enthalpy of hydration of the pure belite;

q_3 : enthalpy of hydration of the pure aluminat;

q_4 : enthalpy of hydration of the pure ferrite;

$C_3\text{Swt}\%$: weight percentage of C_3S deduced by Rietveld analysis;

$C_2\text{Swt}\%$: weight percentage of C_2S deduced by Rietveld analysis;

$C_3\text{Awt}\%$: weight percentage of C_3A deduced by Rietveld analysis;

$C_4\text{AFwt}\%$: weight percentage of C_4AF deduced by Rietveld analysis.

The values for the enthalpy of reaction are given in literature [5] [125] and [126] as following:

	Reaction	Equations	Enthalpy (kJ/mol)
Exothermic reactions	Dissolution of C ₃ S	$C_3S + (3-x+y)H \rightarrow C_x-S-H_y + (3-x)CH$	-118
	Dissolution of C ₂ S	$C_2S + (2-x+y)H \rightarrow C_x-S-H_y + (2-x)CH$	-45
		$C_3A + CH + 12H \rightarrow C_4AH_{13}$	-314
		$C_3A + 6H \rightarrow C_3AH_6$	-245
	Dissolution of C ₃ A	$2C_3A + C_6A_3H_{32} + 4H \rightarrow 3C_4A_3H_{12} (AFm)$	-238
		$C_3A + 3C_2H_2 + 26H \rightarrow C_6A_3H_{32} (AFt)$	-452
		$C_3A + 3C_2H_2 + 10H \rightarrow C_4A_3H_{12}$	-309
	Dissolution of C ₄ AF	$C_4AF (+ CH + H) \rightarrow C_3(A,F)H_6$	-203
		$C_4AF + 3 C_2H_2 + 30H \rightarrow C_6A_3H_{32} + CH + FH_3$	-352
	Endothermic reactions	Precipitation of C-S-H	$C_3S + (3-x+y)H \rightarrow C_x-S-H_y + (3-x)CH$
		$C_2S + (2-x+y)H \rightarrow C_x-S-H_y + (2-x)CH$	
Precipitation of Portlandite		$C_3S + (3-x+y)H \rightarrow C_x-S-H_y + (3-x)CH$	20
		$C_2S + (2-x+y)H \rightarrow C_x-S-H_y + (2-x)CH$	

Table III-4: enthalpy values for main reactions in cement

Taylor [5] noted that in principle, it should be possible to calculate the heat of hydration from the quantitative phase compositions of the unreacted mix and of the paste using standard enthalpies of formation. However, the reaction speed and the enthalpy are very different as a function of the reactions taken into account, particularly for aluminate phase. So it is not actually possible to dissociate the contribution of each reaction with good accuracy and to quantify them.

At this time, the degree of hydration of cement from isothermal calorimetry cannot be compared with the one from XRD-Rietveld and SEM-IA, so it is not used in this project.

III.8. CONCLUSIONS AND DISCUSSIONS ON HYDRATED CEMENTITIOUS MATERIALS

For XRD, a control file was made for each different system with all the crystalline phase previously identified and the incorporation of improved existing structure models was used (like the recent ettringite structure [107]).

The amorphous content was calculated using the external standard method.

To simulate the actual system, the raw Rietveld output were corrected by dilution effect the reproducibility of the quantification was checked.

The amount of phases deduced from Rietveld analysis shows good general agreement with other results from TGA and SEM-IA techniques. It provides the clinker reactivity as a function of the different systems of our study, all the graphs on the evolution of clinker phases are given in the last part of this chapter and lead to the following conclusions:

- As it was previously found [5], gypsum and other calcium sulfate phases are usually no longer detectable after 1 day.

- The clinker phases were consumed at differing rates: alite and aluminate phases reacted quickly in the first 7 days of hydration compared to belite and ferrite phases. For all systems, if we compared cements in one hand and blended pastes on the other hand, we clearly see that the alite contents were significantly different before 7 days with respect of the order of initial contents. Indeed, the alite content in Cement A systems were always higher than respectively the one in Cement C and B systems. After 7 days of hydration, the rate of reaction of alite was not significantly different from one type of paste to another one. After 6 months of hydration, little alite is detectable.

- As expected, the belite phase reacted slowly compared to alite phase but there was a delay of the hydration of belite until around 14 days for all the systems. As for alite contents, until 6 months, the hydration of belite respected the initial order of the belite proportion: $A > B > C$. At this time, the determination of C_2S is less precise because the amorphous signal and C_2S peaks are in the same area in the XRD pattern.

- The Rietveld refinement software allows to refine C_3A even if the quantity is low. However, when C_3A content was lower than 1 wt%, it was not enough significant to be refined. Regarding the very fast C_3A hydration, the order of the initial contents was preserved ($C > B > A$) for all the systems from 12 hours to 14 days.

- Considering the ferrite phase, there was a fast hydration in the first 7 days with ferrite contents from B pastes always higher than in C pastes, with respect of their initial ferrite content. This is in agreement with previous work made by Taylor [5] which observed that the rate of reaction of the ferrite decreases with the Fe/Al ratio. After 7 days, there was no main difference for blended pastes whereas in the case of cements Cement B still had the higher ferrite content.

Figures III-36 to III-47 show the content of the clinker phases from XRD-Rietveld as a function of type of cementitious systems (pure or blended systems).

The XRD-Rietveld refinement reveals different points which could be more investigated:

- The incorporation of new structure models, for calcium hemicarboaluminate, in control file.

- Find a solution to differentiate the calcite contribution to the one of C-S-H.

Indeed, a comparison of the different amount of cement phases deduced by Rietveld analysis with the thermodynamic modeling predictions [127] could be helpful.

Furthermore, the experimental procedures were detailed for calorimetry and chemical shrinkage which will be some of the useful techniques used to isolate the contribution of slag (as described in Chapter V).

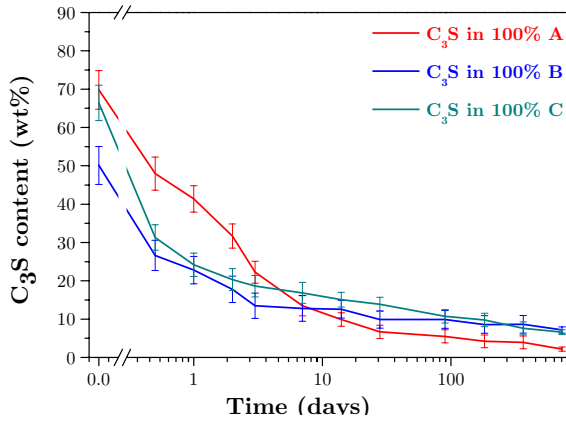


Figure III-36: evolution of C_3S in 4 cements

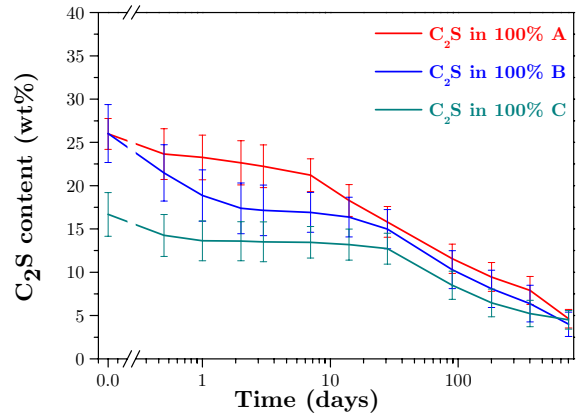


Figure III-37: evolution of C_2S in 4 cements

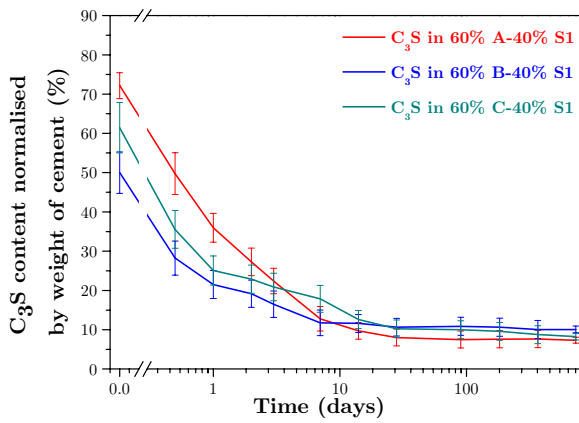


Figure III-38: evolution of C_3S in 3 cements blended with Slag 1

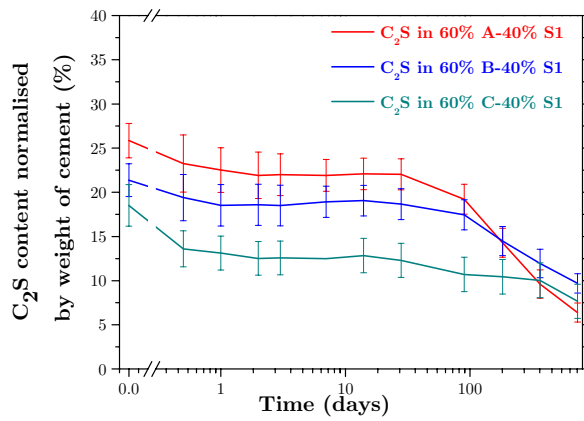


Figure III-39: evolution of C_2S in 3 cements blended with Slag 1

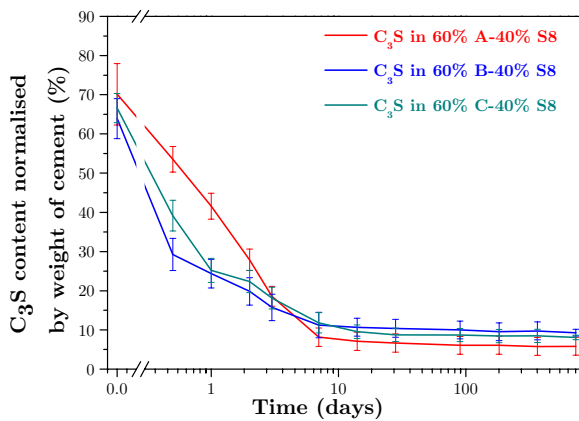


Figure III-40: evolution of C_3S in 3 cements blended with Slag 8

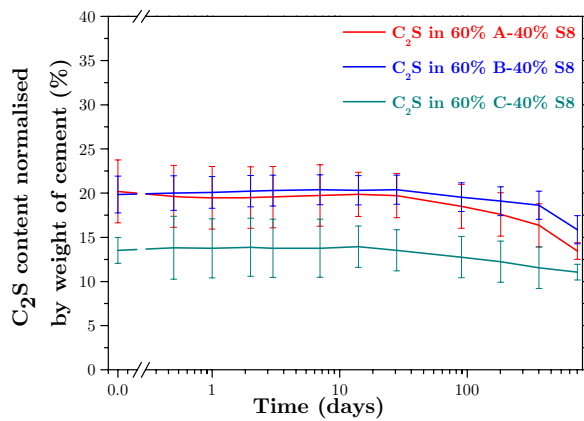


Figure III-41: evolution of C_2S in 3 cements blended with Slag 8

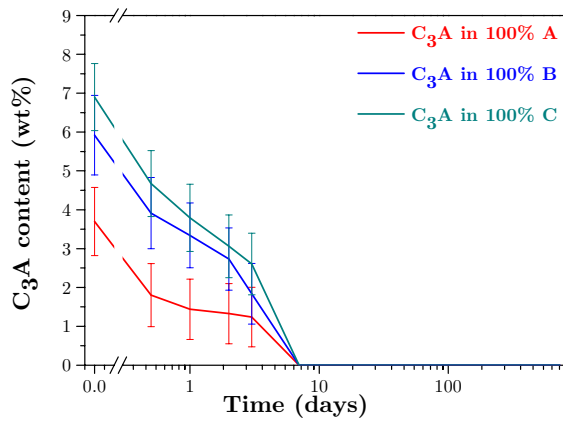


Figure III-42: evolution of C_3A in 4 cements

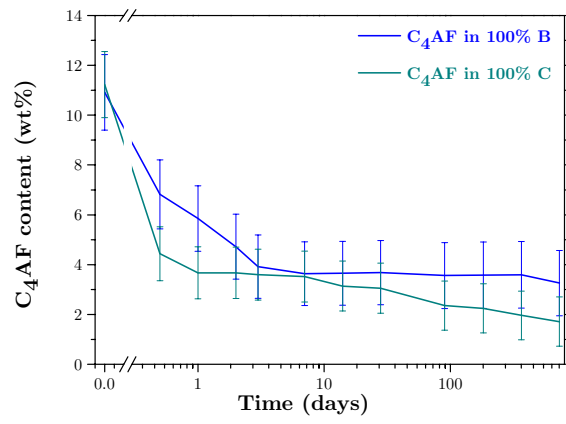


Figure III-43: evolution of C_4AF in 3 cements

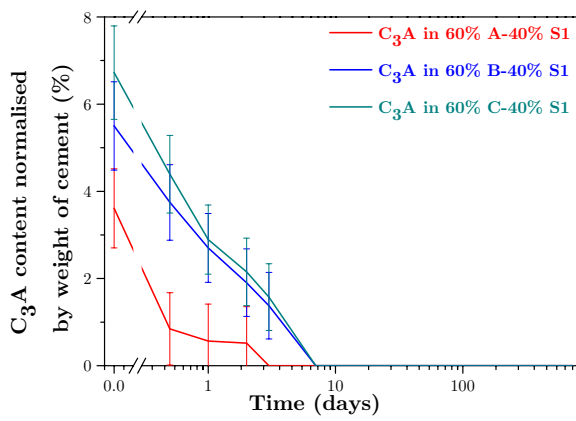


Figure III-44: evolution of C_3A in 3 cements blended with Slag 1

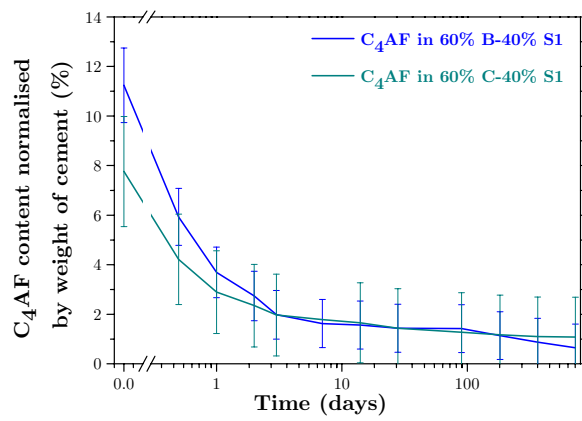


Figure III-45: evolution of C_4AF in 2 cements blended with Slag 1

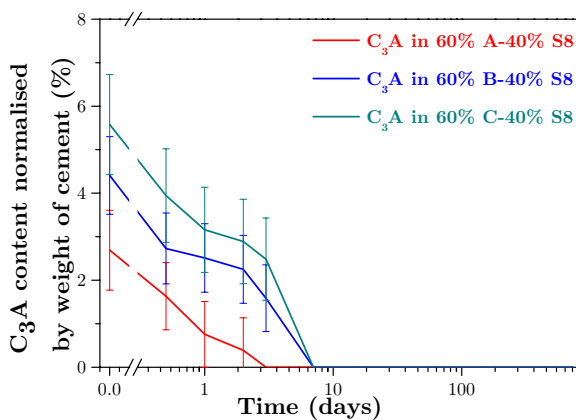


Figure III-46: evolution of C_3A in 3 cements blended with Slag 8

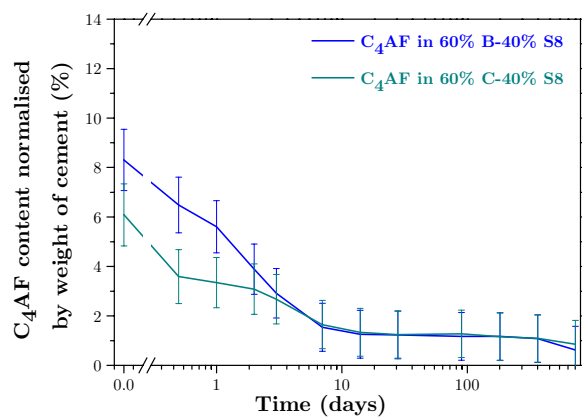


Figure III-47: evolution of C_4AF in 2 cements blended with Slag 8

CHAPTER IV: HOW THE SLAG AFFECTS THE REACTION OF CEMENT?

After studying the different techniques used to follow the hydration of cementitious materials in the previous chapter, this chapter presents the effect of slag on the reaction of cement with the following outline:

- First, the heat released from calorimetry curves gives a general idea of the overall pattern of reaction and particularly shows significant changes in the reaction of the aluminate phases from blended systems as compared to pure systems.
 - Effect of slag on silicate phases is presented.
 - The influence of slag on the aluminates phases is analysed in more detailed.
 - The effect of slag on the ferrite and belite phases, and on the overall degree of reaction of cement is presented.
- Finally, the impact of slag on the evolution of portlandite and C-S-H is highlighted.

IV.1. INFLUENCE OF SLAG ON HEAT RELEASED

The influence of slags on the hydration of blended pastes can be studied using isothermal calorimetry.

Partial replacement of cement with slag changes both the rate of heat evolution and the total amount of heat evolved.

In this section, the isothermal calorimetry has been used in order to assess the overall effect of adding slag in blended pastes, on the rate and total heat of hydration at 20°C.

Figures IV-2 to IV-4 illustrate the heat evolution of the cementitious pastes: pure cement pastes, reference pastes blended with quartz and also cementitious pastes of blends with the two slags. In order to isolate the slag contribution, with the consideration that it did not react so much at early ages, all the heat curves are normalised by the weight of cement.

The reactions associated with each part of the isothermal calorimetry curves are detailed below.

Calorimetry data clearly shows the different influence of slag addition on cement hydration, depending on the cements used in the blend.

It could be noted here that quartz inert filler was used with a similar particle size distribution compare to OPC and slags powders (see Figure IV-1).

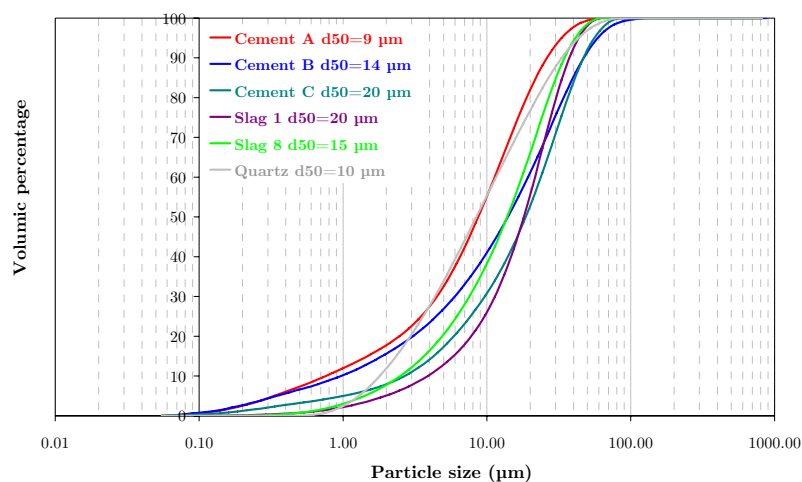


Figure IV-1: particle size distribution of cements, slags and quartz obtained with Malvern mastersizer laser granulometer

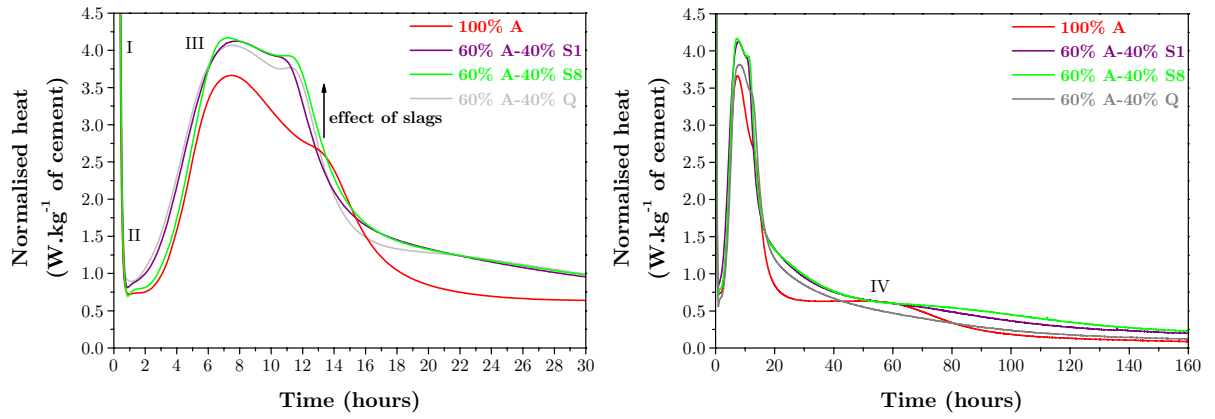


Figure IV-2: heat flow of cementitious A pastes

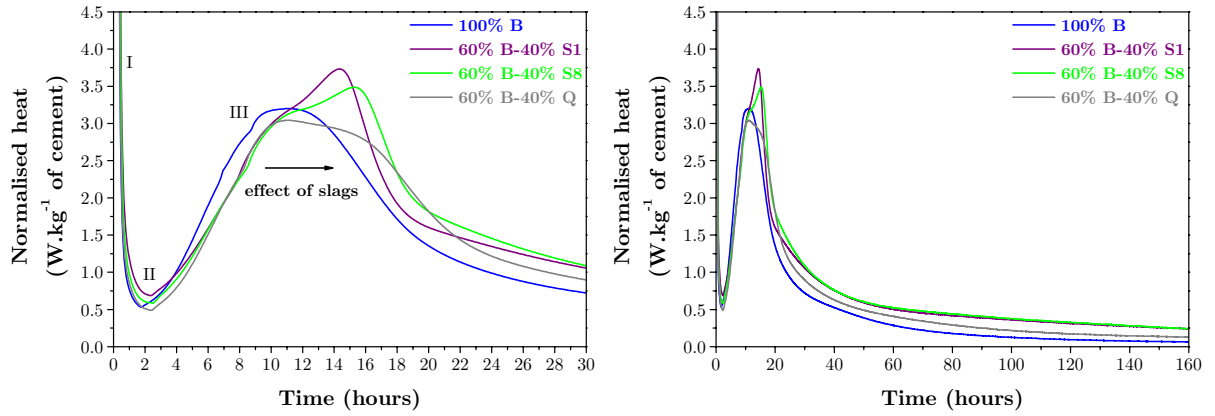


Figure IV-3: heat flow of cementitious B pastes

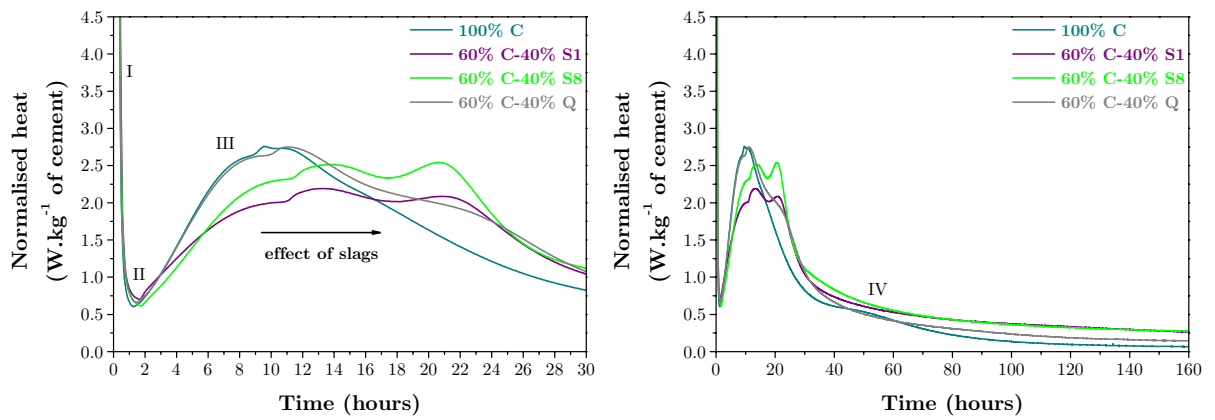


Figure IV-4: heat flow of cementitious C pastes

The peak I is associated with dissolution: heat of wetting of the cement, hydration of free lime, hydration of calcium sulfate hemihydrate and the formation of ettringite primarily from the aluminate phases.

After the initial peak, an induction period (II) occurs during which the heat output significantly decreases.

After this induction period, a sudden increase in the rate of heat output occurs resulting in peak III which is generally believed to be primarily the result of alite hydration and the production of calcium hydroxide and C-S-H gel. The setting of the paste occurs before the maximum of peak III.

In the case of blended pastes, there was generally a slight retardation of peak III. In addition, this peak III had a shoulder for systems A and B and it was even a double peak for systems C. This double peak was also found in previous studies [82,112,128-134] when slag was used as a substitution for cement.

The XRD-Rietveld refinement at 12 hours for pastes blended with Cement A and B and the refinement at 24 hours for pastes blended with Cement C reveal the presence of ettringite but not AFm. So the second peaks are probably due to the formation of ettringite, as suggested previously [131] and not due to AFm as has been also proposed [135].

In the case of pure systems with Cement A and C, the peak IV is thought to be the result of reaction of C_3A with AFt to AFm transformation as it was previously found [136,137].

IV.2. EFFECT OF SLAG ON SILICATE PHASES

The calorimetry curves indicate a slight acceleration and enhancement of the silicate reaction for the slags with Cement A, but a slight retardation and suppression with Cement B and C. However, the XRD results do not show any clear difference in the alite consumption when the errors of the technique are taken into account (see Figures IV-5 to IV-7).

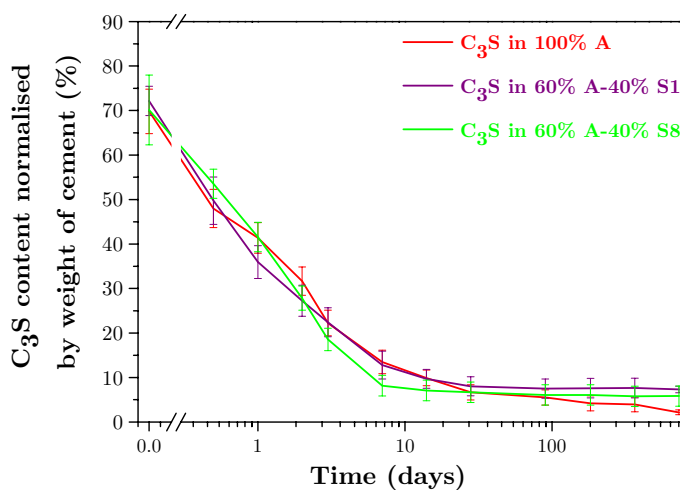


Figure IV-5: evolution of C_3S content in cementitious A systems

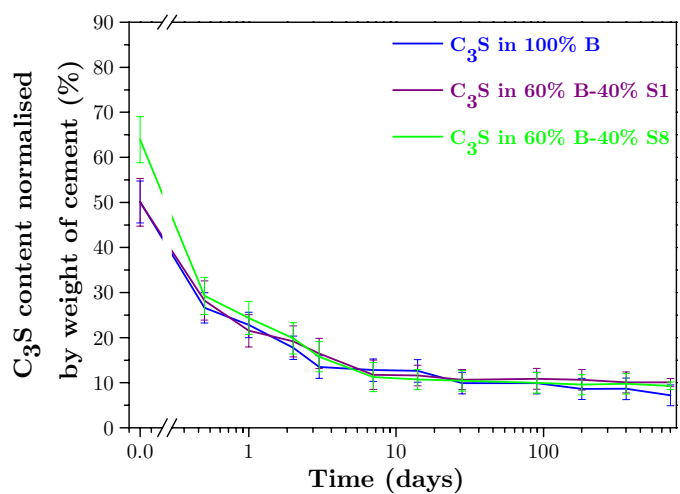


Figure IV-6: evolution of C_3S content in cementitious B systems

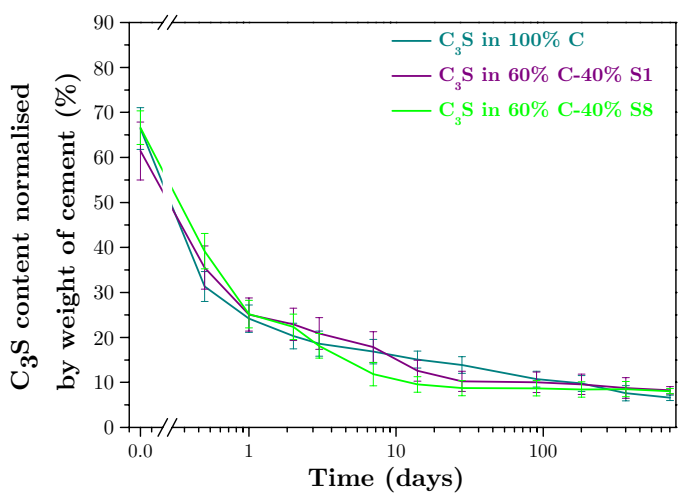


Figure IV-7: evolution of C_3S content in cementitious C systems

IV.3. CONTRIBUTION OF SLAG ON ALUMINATE PHASES

The calorimetry curves showed a strong effect of the slag, there was an impact of filler on aluminate hydration even with inert powders as shown in the following figure. So an impact of filler contribution of slag can be identified on aluminate hydration which justifies a further investigation on effect of slag on aluminate phases.

On the peak attributed to the reaction of the aluminate phases, it might be thought that the slag itself makes a contribution to this reaction. However, previous work in our group [138] has shown similar effects with additions of inert material (Figure IV-8).

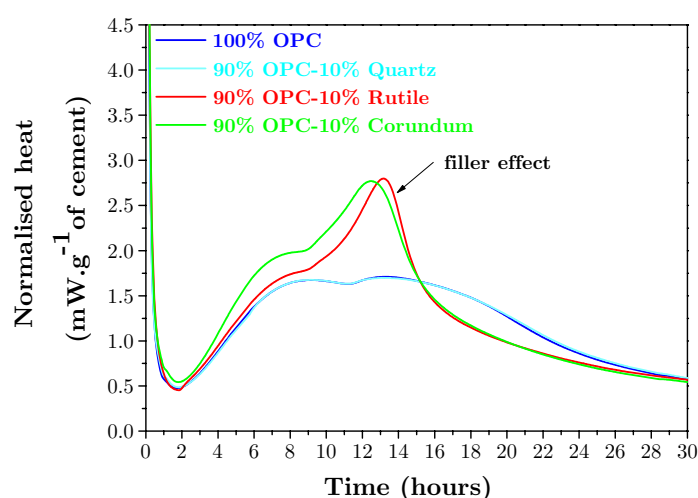


Figure IV-8: rate of heat release of pastes with cement blended with different kinds of filler [138]

IV.3.1. XRD DATA

In Cement A systems, reaction of C_3A phases was exhausted after one day of hydration both with and without slag (see Figures IV-9 to IV-11).

For all systems, slags did not have a strong influence on hydration of C_3A phases and taking into account the low content of C_3A and the corresponding error, it was difficult to highlight any relevant difference between blended paste and corresponding pure pastes.

We can note that the influence of slag on C_3A was not strong as in the case of Fernandez's thesis [139] where pozzolan was used but here the slag is coarser than the pozzolan used by Fernandez (d_{50} of S1=20 μm and d_{50} of S8=15 μm against d_{50} of pozzolan < 10 μm).

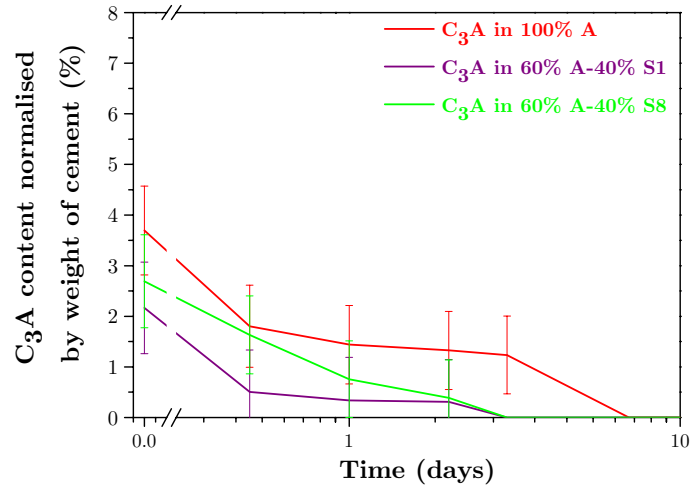


Figure IV-9: evolution of C₃A content in cementitious A systems

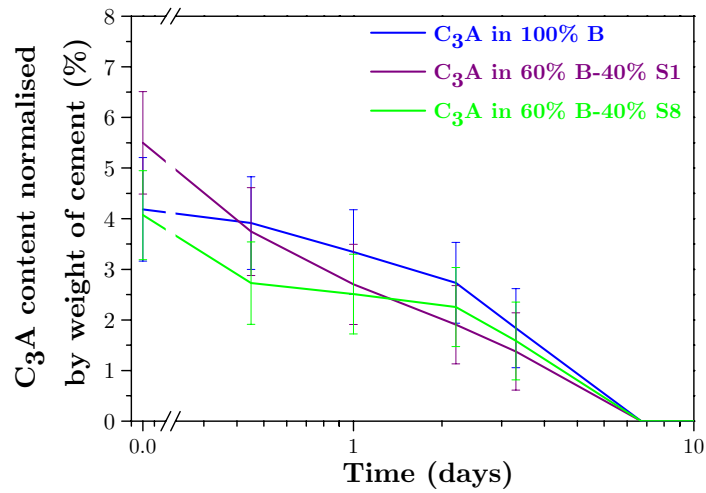


Figure IV-10: evolution of C₃A content in cementitious B systems

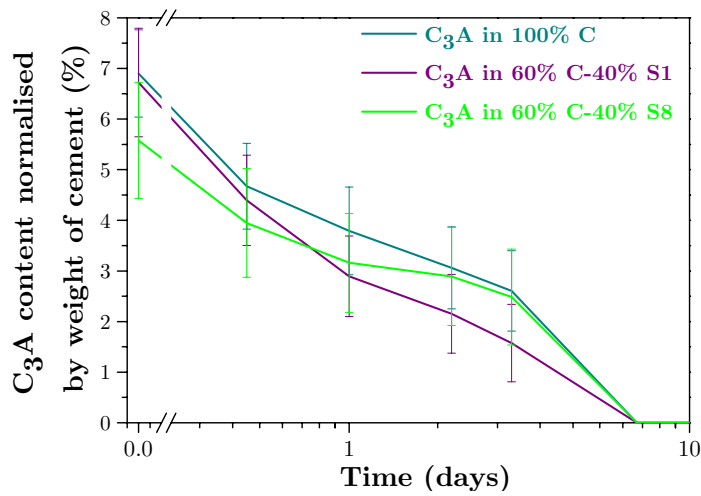


Figure IV-11: evolution of C₃A content in cementitious C systems

IV.3.2. EFFECT OF SLAG ON PEAKS III AND IV ASSOCIATED WITH ALUMINATES

It was clear that slag had a drastic effect on peaks III and IV associated with the aluminate reaction. Further investigations were made to determine if slag itself reacted.

The association of the peak III with aluminate reaction was previously highlighted by Richardson [131] using additional gypsum to show how its position varies.

In this study, progressive gypsum additions were used and a separation method was optimised to separate the contributions of silicate and aluminate in cement and blended systems.

In order to avoid possible ageing effect, all isothermal calorimetry curves for a given system were acquired at the same time.

IV.3.3. SEPARATION TREATMENT TO ISOLATE ALUMINATE REACTION

First for each given system, calorimetry measurements were made for 4 additions of gypsum as shown as example for B-S1 systems in Figure IV-12.

We should note than in this section, when there is percentage of gypsum it corresponds to additional gypsum.

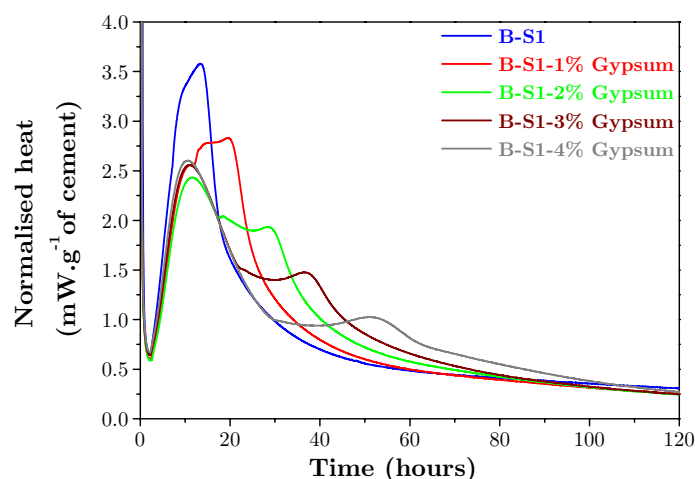


Figure IV-12: normalised heat evolution profiles for B-S1 blended pastes plus varying additional gypsum contents

From this series of curves a reference for the shape of the silicate peak could be extracted.

Then, as illustrated in Figure IV-13, a subtraction was made between the representative curve of contribution of silicate phases and the normalised heat curves with different gypsum contents. The resulting curves for B-S1 systems are given in Figure IV-14.

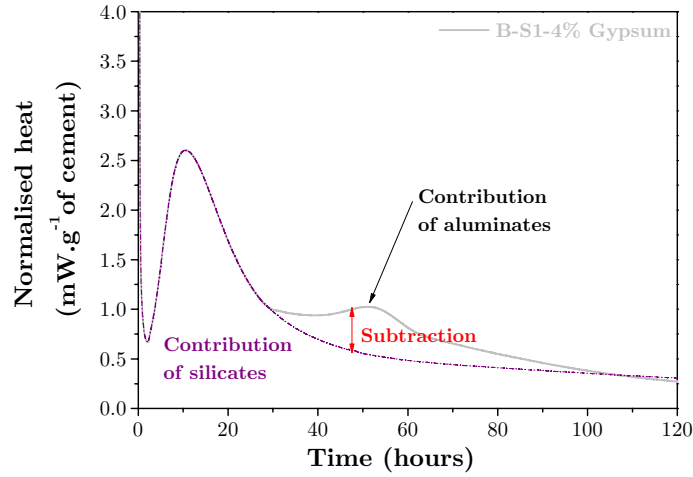


Figure IV-13: illustration of contribution of silicate and aluminate phases

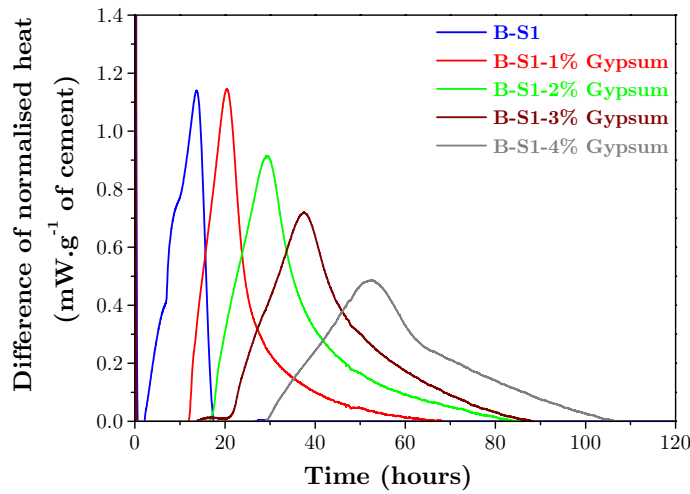


Figure IV-14: difference of normalised heat evolution for B-S1 blended pastes plus varying additional gypsum contents

In this case, the 0% additional gypsum system exhibits a significantly different behaviour than those systems with the higher contents of gypsum.

The next step of the separation treatment was to do an affine transformation, which consists of a linear transformation followed by a translation, with two main hypotheses:

1st hypothesis: The gypsum additions were supposed to affect only the kinetics which led to a delay of each peak to shift the reference position according to the following equation:

$$t'_i = \alpha(t_i - t_0) \quad \text{Equation 21}$$

Where:

t'_i : transformed time;

α : kinetics factor;

t_i : time for a given i point;

t_0 : delay.

The choice of the reference curve for the shift in time was done for a curve where the peaks were well defined. In the case of B-S1 the heat curve with 1% gypsum was used as the reference because the two peaks were well separated (see resulting curves in Figure IV-15).

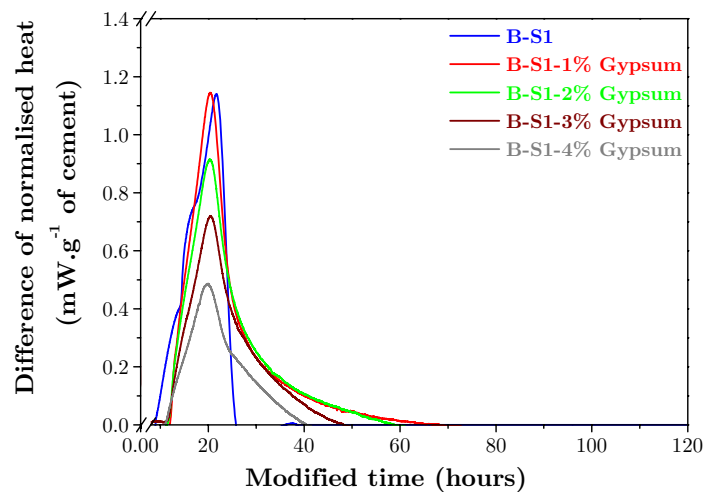


Figure IV-15: difference of normalised heat evolution rescaled on time for B-S1 blended pastes plus varying additional gypsum contents

2nd hypothesis: As the main point of interest was the amount of reaction represented by this peak, it was important to keep a constant area under the curve. The resulting heat transformed is given by the following equation:

$$Q'(t) = \frac{A_0}{A} Q(t) \quad \text{Equation 22}$$

Where:

$Q'(t)$: transformed heat at time t ;

$Q(t)$: heat at time t ;

A_0 : area of reference peak which formula is $A_0 = \frac{1}{2} \sum_0^i (Q_{i+1} + Q_i) (t_{i+1} - t_i)$;

A : area of transformed peak which formula is $A = \frac{\alpha}{2} \sum_0^i (Q_{i+1} + Q_i) (t_{i+1} - t_i)$.

In some cases the aluminate contribution clearly consisted of two peaks. When the first peaks were aligned the second peaks were misaligned. These second peaks were also very sensitive to the subtraction of the silicate contribution.

It is important to note that the heat signature of the affine transformation was kept constant and the resulting peaks can be thus compared (see Figure IV-16).

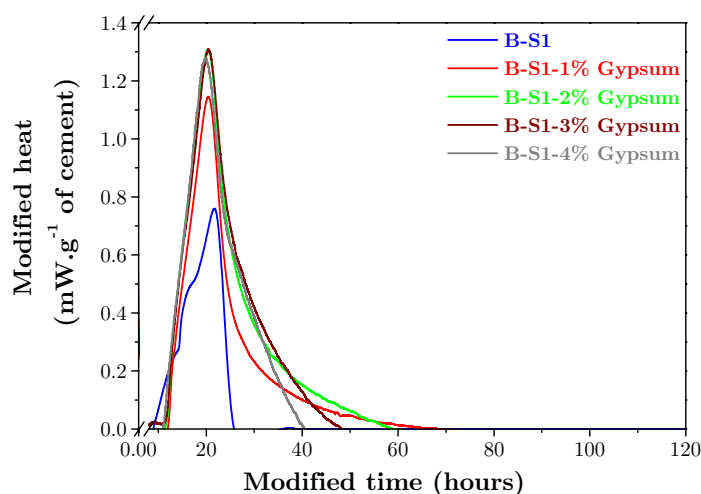


Figure IV-16: modified heat evolution rescaled on time for B-S1 blended pastes plus varying additional gypsum contents

It was observed that the impact of additional gypsum appeared to be very different on aluminate reaction in the systems containing Cement A compared to the ones with Cement B and C.

For Cement A (white cement), it was found that the addition of gypsum changed the shape of the curve not only concerning the contribution of aluminate phases but also regarding the contribution of silicate phases, as shown in Figures IV-17 to IV-19. Thus, it was not possible to apply the separation treatment for Cement A systems.

The initial and resulting curves for the systems B and C are shown in Figures IV-20 to IV-25.

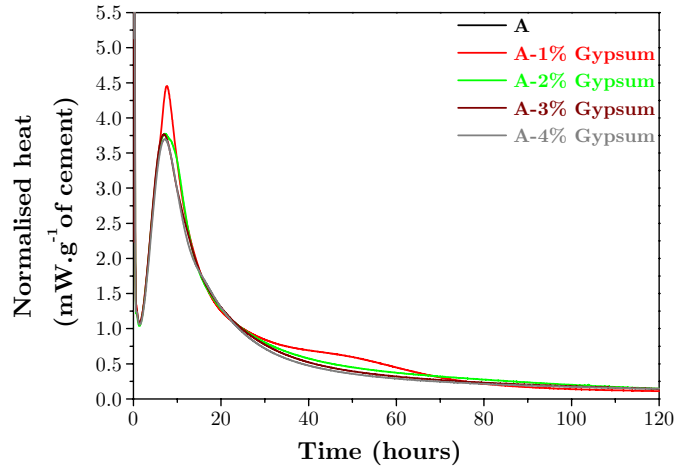


Figure IV-17: initial heat curves from A pastes plus varying additional gypsum contents

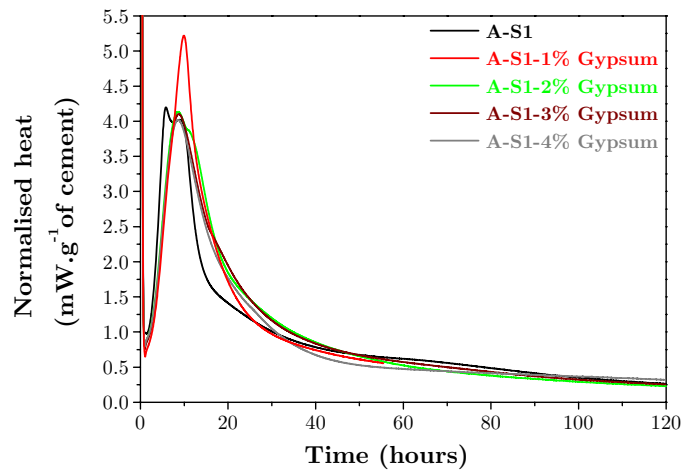


Figure IV-18: initial heat curves from A-S1 pastes plus varying additional gypsum contents

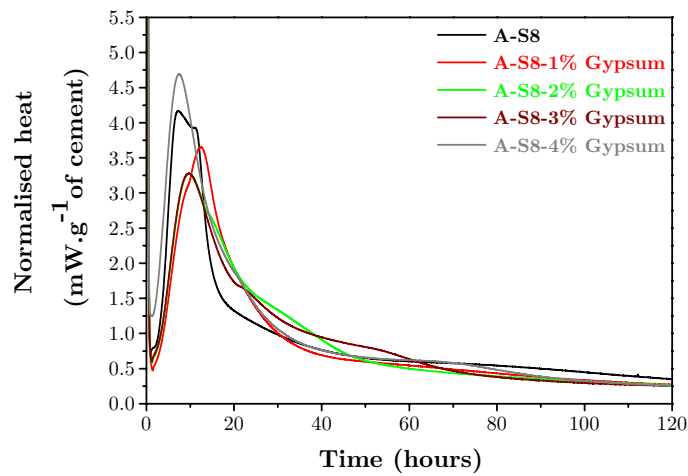


Figure IV-19: initial heat curves from A-S8 pastes plus varying additional gypsum contents

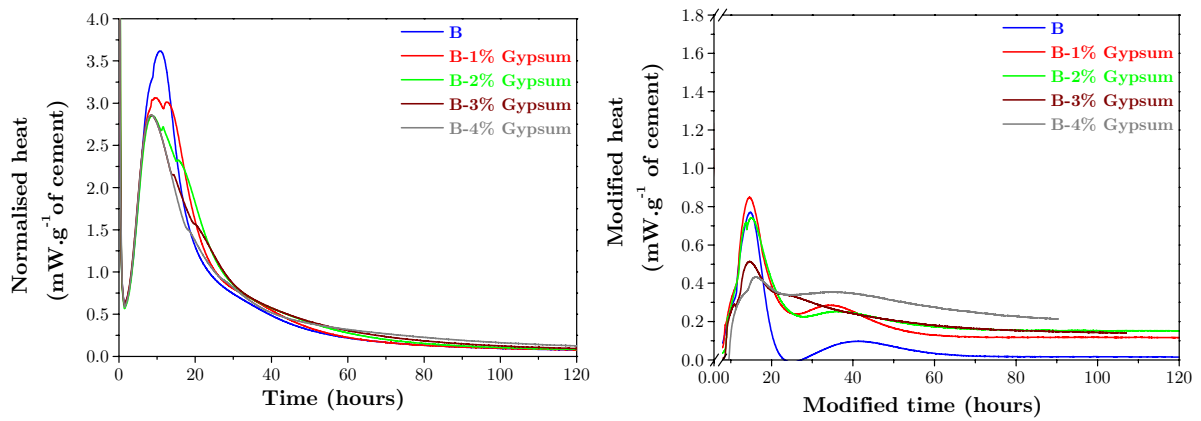


Figure IV-20: initial and modified heat curves from separation treatment of B pastes plus varying additional gypsum contents

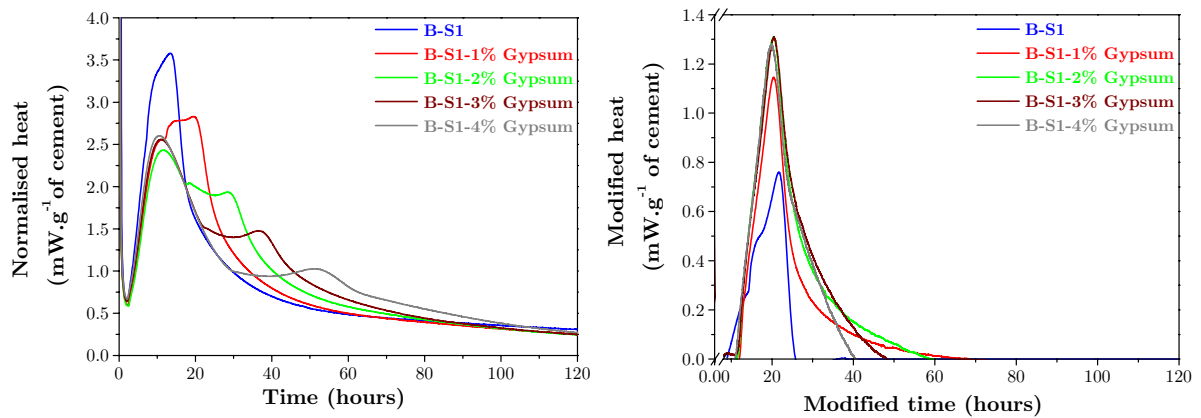


Figure IV-21: initial and modified heat curves from separation treatment of B-S1 pastes plus varying additional gypsum contents

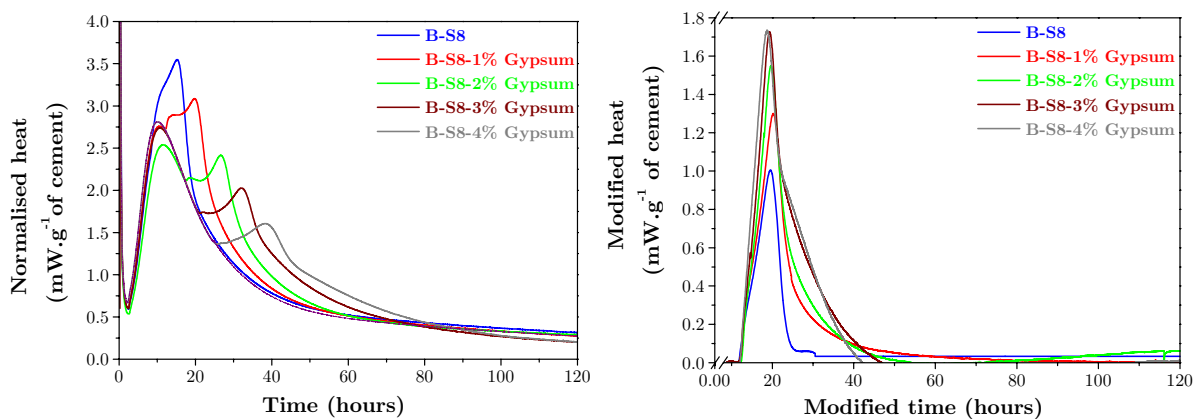


Figure IV-22: initial and modified heat curves from separation treatment of B-S8 pastes plus varying additional gypsum contents

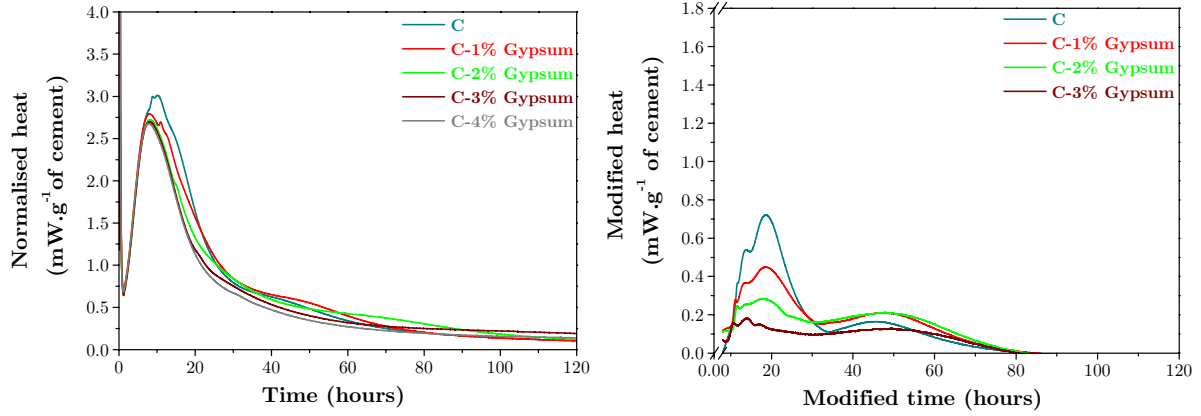


Figure IV-23: initial and modified heat curves from separation treatment of C pastes plus varying additional gypsum contents

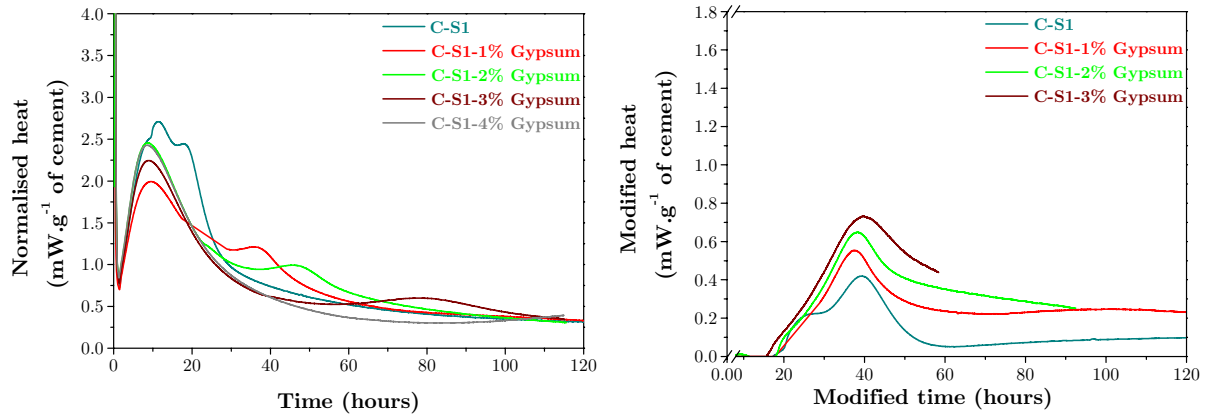


Figure IV-24: initial and modified heat curves from separation treatment of C-S1 pastes plus varying additional gypsum contents

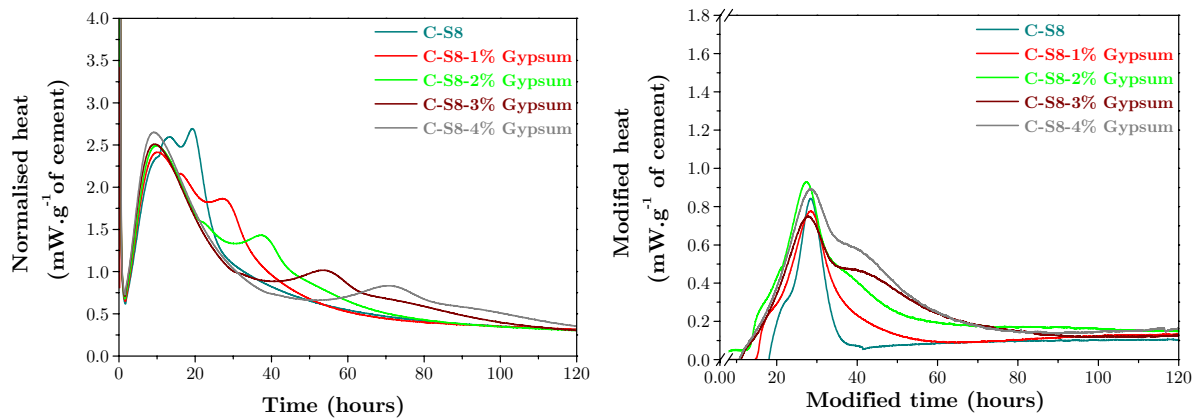


Figure IV-25: initial and modified heat curves from separation treatment of C-S8 pastes plus varying additional gypsum contents

IV.3.3.a. Quantification of first peak from separation

To quantify the reaction of aluminate in initial systems (without additional gypsum), the areas under the first aluminate peaks were calculated for all the systems (see Figures IV-26 and IV-27).

Assuming that all C_3A is dissolved and AFt is precipitated, we used the following relationship to evaluate the enthalpy of aluminate reaction:

$$\Delta H_{\text{reaction}} = \Delta H_{\text{dissolution of } C_3A} + \Delta H_{\text{formation of AFt}} = -160 - 320 = -480 \text{ kJ.mol}^{-1} \quad \text{Equation 23}$$

The area under the peak is then divided by this value and the corresponding results are given in Table IV-1.

	C_3A content from separation (mmol/g of cement)	% of reacted C_3A
B	3.3	77-85%
B-S1	3.8	65-74%
B-S8	3.9	86-94%
C	5.3	77-82%
C-S1	5.1	74-78%
C-S8	4.4	76-82%

Table IV-1: results from separation treatment for systems B and C without additional gypsum

Regarding the results and keeping in mind the possible error on the quantification of the area of the first peak, the range of resulting aluminate were not significantly different in blended paste compared to pure pastes. So there was no evidence of slag itself reacting and the effect of slag on aluminate phases can be only attributed to a filler effect.

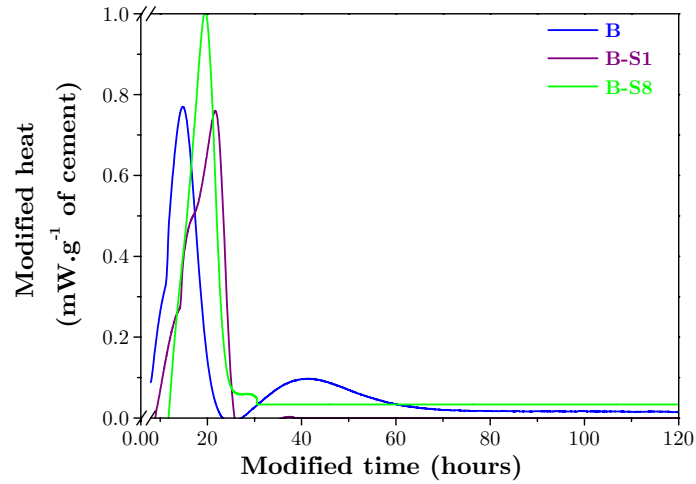


Figure IV-26: all resulting B curves from separation treatment

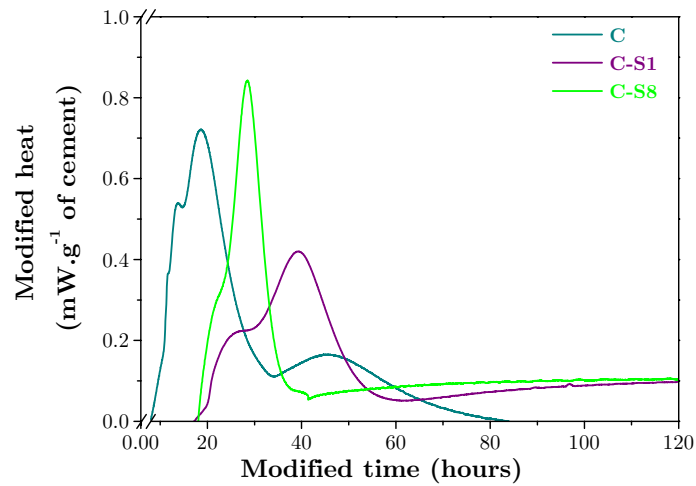


Figure IV-27: all resulting C curves from separation treatment

IV.3.3.b. Second peak from separation treatment

Particular care to the second peak should be taken because it could be very affected by the choice of the silicate contribution.

This second peak or shoulder from separation treatment could be identified as reaction of AFm phases.

The raw calorimetry curves of A and C pure system showed a peak (called IV) which was attributed to monosulfoaluminate reaction just around 60 hours of reaction. In this way, calcium hemicarboaluminate and monocarboaluminate could be some possible AFm phases corresponding to the second peak of aluminate. But there is no evidence of that and it could be some monosulfate. The corresponding XRD patterns did not show any peaks corresponding to AFm phases at early ages which indicate a very low content if they are present.

IV.4. INFLUENCE OF SLAG ON BELITE PHASE

The following figures (Figures IV-28 to IV-30) show the evolution of belite phase in the different reference and blended systems. At early age, for all systems there was just a little reaction of belite.

The substitution of cement by both slags seems to result in a delay in the hydration of belite in the first days, contrary to previous work [130], which claimed that slag accelerated the rate of hydration of belite. This was more marked influence on Cements A and B systems but also evident in the case of Cement C systems.

Comparing the effect of the two slags, in all systems, the belite of Slag 1 pastes always appeared to react faster than the one of Slag 8 pastes.

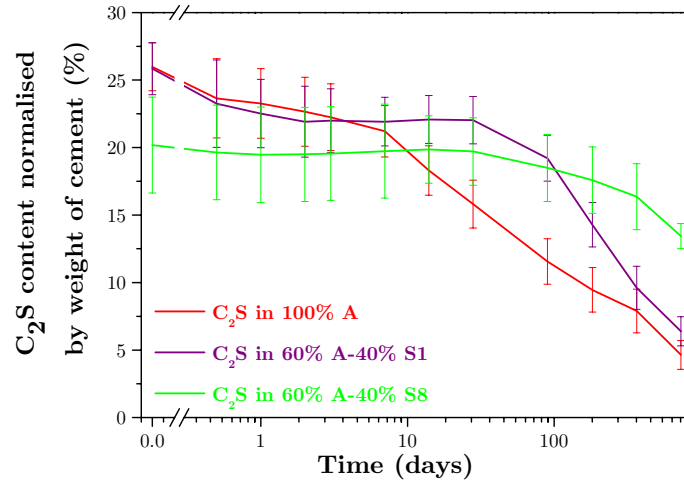


Figure IV-28: evolution of C₂S content in cementitious A systems

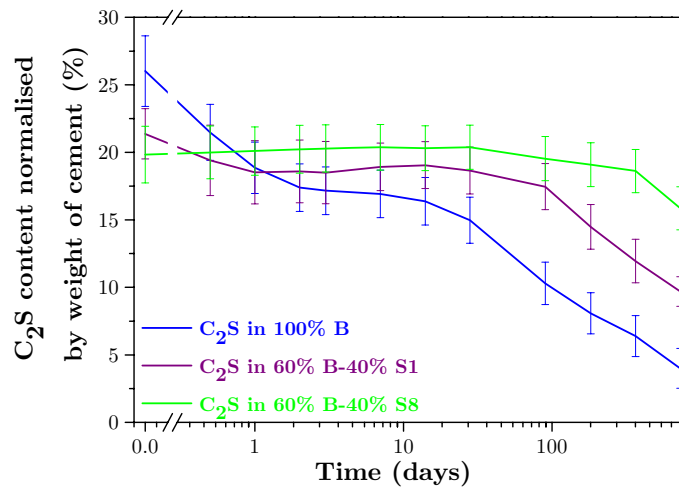


Figure IV-29: evolution of C₂S content in cementitious B systems

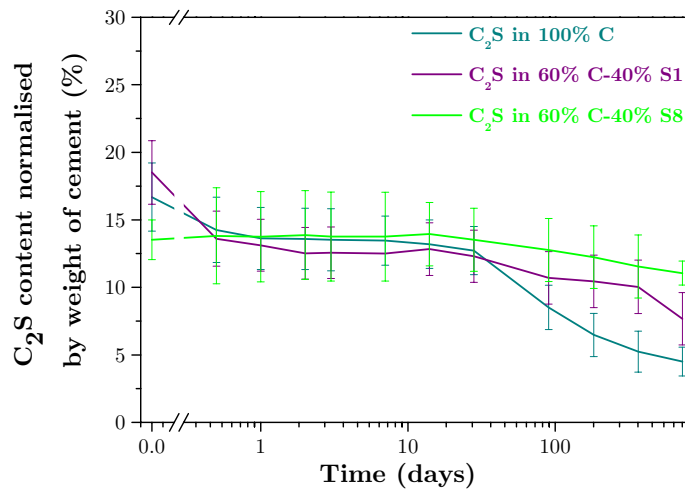


Figure IV-30: evolution of C₂S content in cementitious C systems

IV.5. INFLUENCE OF SLAG ON FERRITE PHASE

The trends of slag on ferrite phase are reproducible and similar for systems with Cement B and C (there was no ferrite in Cement A because it is a white cement).

The slags seem to favour the hydration of the ferrite phase as shown in Figures IV-32 and VI-33.

There was first a slight decrease of the ferrite phase in XRD pattern and this decrease was strongly accentuated between 12 hours and 3 days as shown in Figure IV-31.

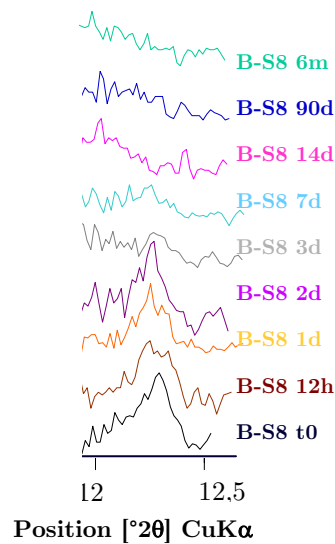


Figure IV-31: evolution of ferrite content in cementitious B-S8 systems

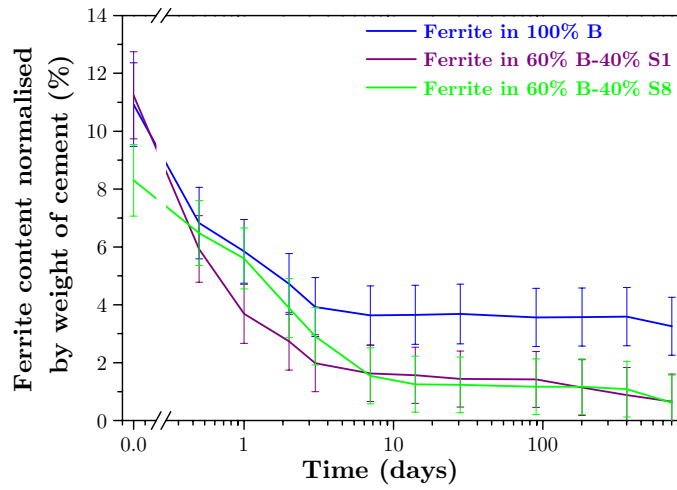


Figure IV-32: evolution of ferrite content in cementitious B systems

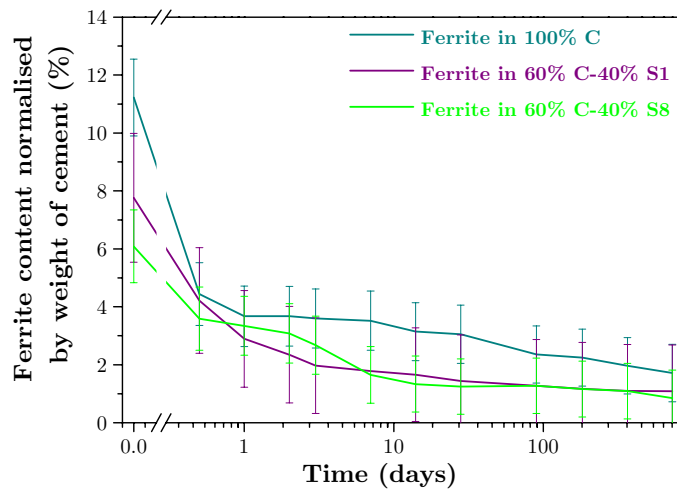


Figure IV-33: evolution of ferrite content in cementitious C systems

The significant reaction of ferrite phase shown by XRD patterns was also identified by SEM-SEM-BSE examination.

Figure IV-34 shows the microstructure of B-S8 paste hydrated for 1 day in which ferrite phase is significantly present whereas in B-S8 paste hydrated for 7 days, the ferrite phase is clearly consumed as shown in Figure IV-35.

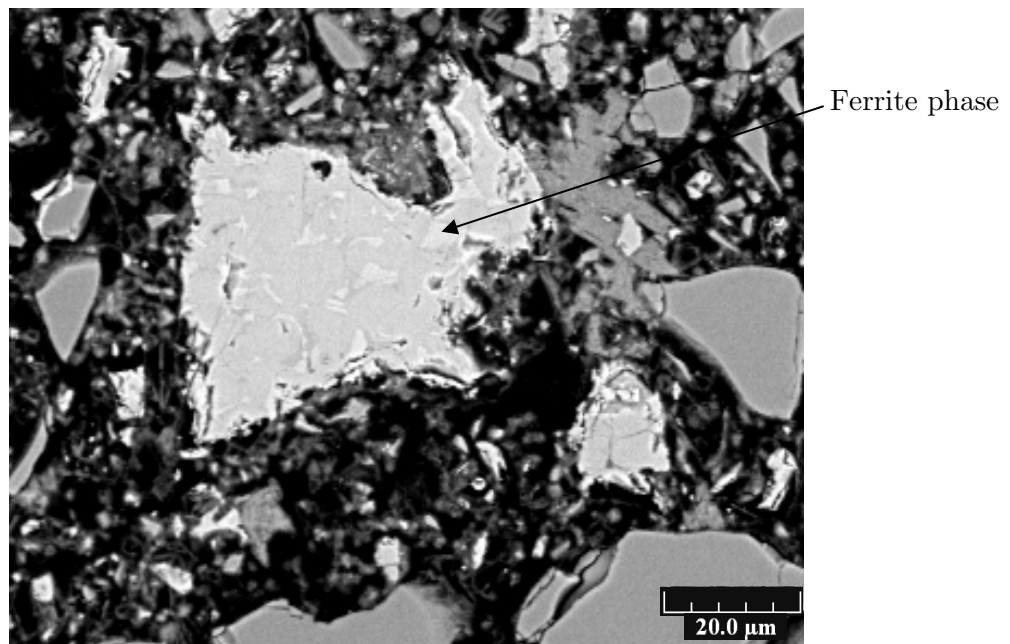


Figure IV-34: SEM-BSE microstructure of B-S8 paste hydrated for 1 day

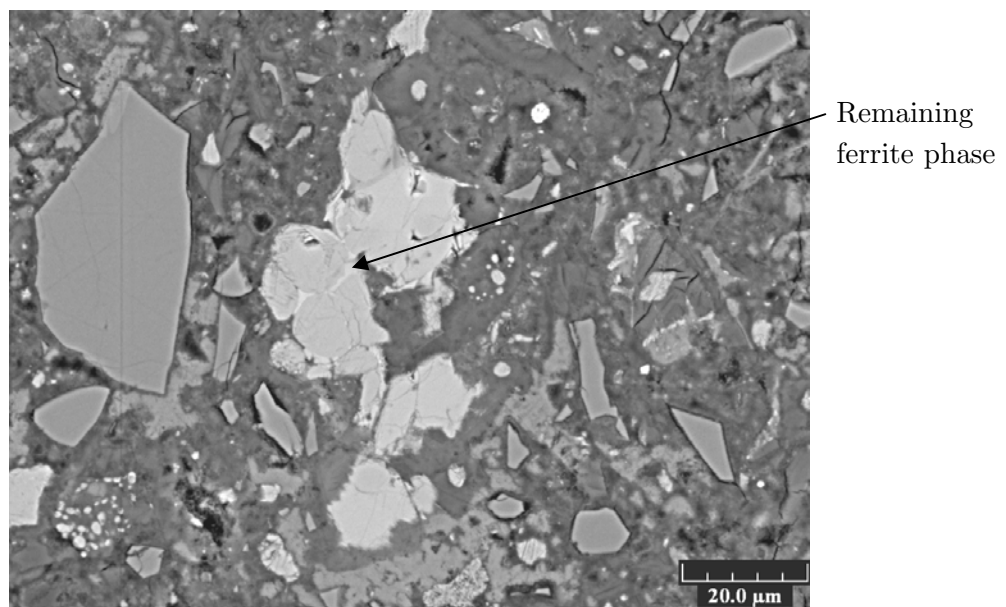


Figure IV-35: SEM-BSE microstructure of B-S8 paste hydrated for 7 days

IV.6. INFLUENCE OF SLAG ON THE DEGREE OF REACTION OF CEMENT

In this part, the degrees of reaction of cement were quantified by SEM-IA and XRD-Rietveld. As discussed in Chapter III, the corrected Rietveld analysis takes into account the dilution effect.

From XRD-Rietveld refinement and SEM-IA, the degree of reaction of cement did not seem to be strongly affected by the slag (see Figures IV-36 to IV-41). However, regarding the results at 2 years, the cements from pure pastes were always more hydrated than the one from blended pastes. In addition, the cements included in systems blends with Slag 8 seemed reacting slower than the ones in systems blends with Slag 1.

Because the evolution of alite did not reveal any significant difference between pure and blended pastes, the trends of degree of reaction of cement could be directly linked to the evolution of belite. Indeed, the reaction of belite was always faster in pure pastes than in blended pastes and the blended pastes with Slag 8 also appeared to react slower than the one with Slag 1.

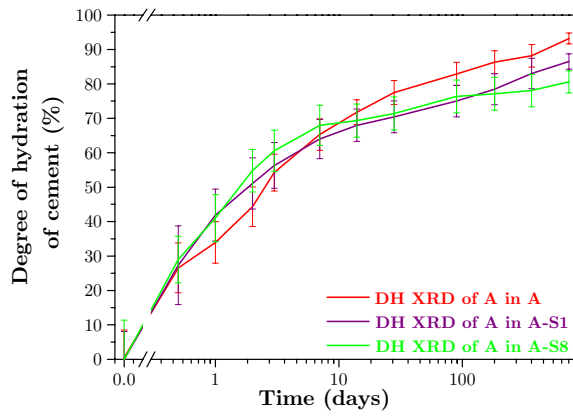


Figure IV-36: evolution of DH of cement from XRD in systems with Cement A

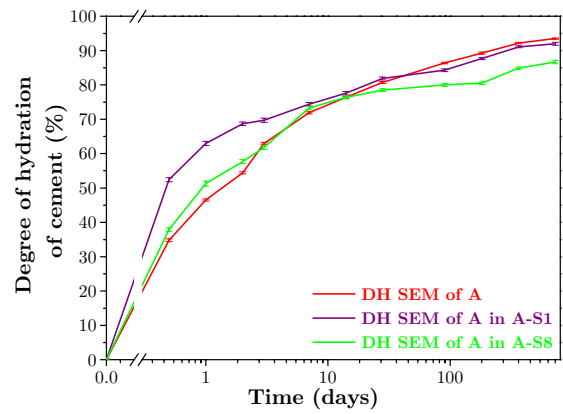


Figure IV-37: evolution of DH of cement from SEM-IA in systems with Cement A

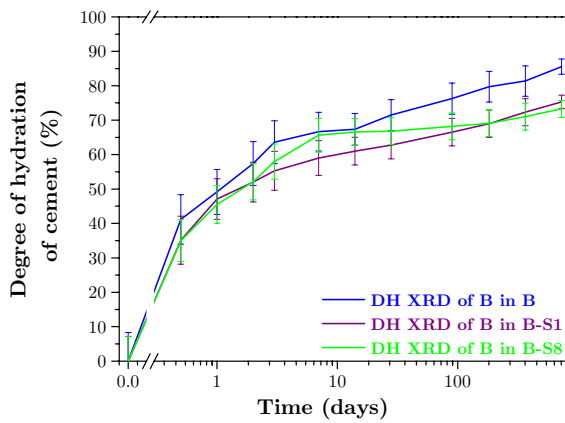


Figure IV-38: evolution of DH of cement from XRD in systems with Cement B

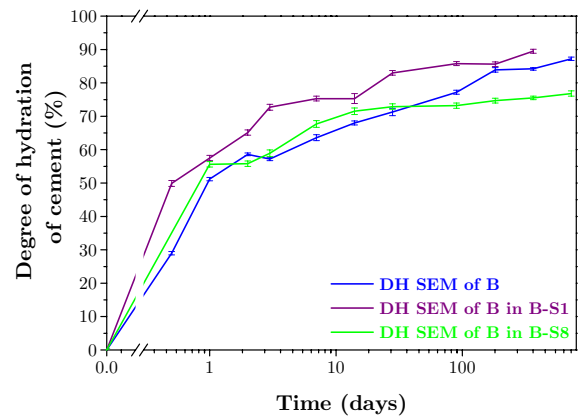


Figure IV-39: evolution of DH of cement from SEM-IA in systems with Cement B

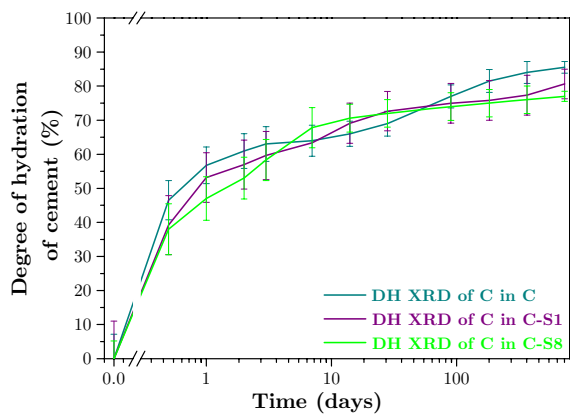


Figure IV-40: evolution of DH of cement from XRD in systems with Cement C

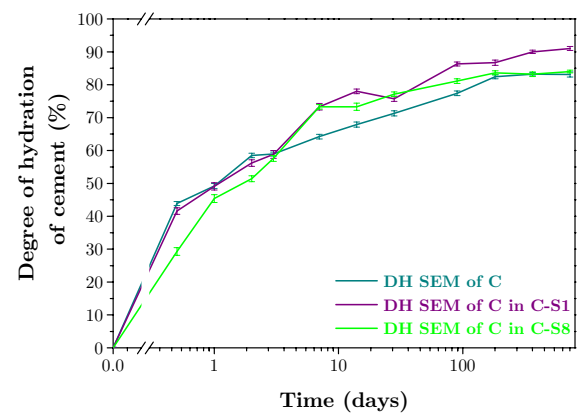


Figure IV-41: evolution of DH of cement from SEM-IA in systems with Cement C

IV.7. INFLUENCE OF SLAG ON PORTLANDITE

IV.7.1. STATE OF THE ART ON PORTLANDITE CONTENT IN SLAG SYSTEMS

Assuming that there is a pozzolanic reaction, the portlandite content in blended paste was often claimed to be an indicator of the reactivity of slag in blended pastes. However, even if the C/S ratio in slag is a bit different than that found in pure OPC paste, it is still in the range of C/S of C-S-H and slags are usually considered mainly latently hydraulic rather than pozzolanic.

An overview of the previous work reveals confused trends due to high errors (see Figure IV-42):

- In previous studies [77,140] a decline in portlandite evolution has been shown. However, taking into account the low value and the errors, this conclusion is questionable.
- In another study, Luke [141] showed the portlandite content passing through a maximum followed by a continuous decrease. As an explanation, their values must be normalised to cement content, otherwise they were too high to be relevant. Taylor [56] mentioned that this is observed when slag is used at 60% replacement levels. However, there was no information about the standard deviation on each value and the decline is insignificant.
- Finally, the portlandite content is stable or increases, several works [142-144] clearly saw that there was no obvious decrease of portlandite.

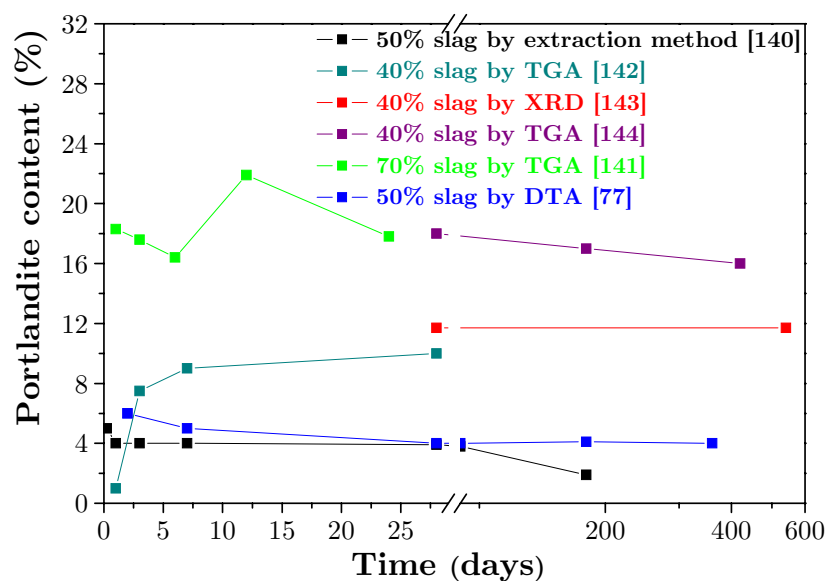


Figure IV-42: variation of portlandite with time [77,140-144]

Considering all these studies, none of the techniques have a precision of more than 2%, even XRD with Rietveld refinement shows significant error margins.

So the close examination of the experimental methods and accuracy of previous investigations provides little evidence of any significant decrease of calcium hydroxide content with hydration time. The decrease in portlandite content with time cannot be taken as an indicator of slag reactivity.

IV.7.2. PORTLANDITE CONTENT OF BLENDS FROM TGA AND XRD

Figures IV-43 to IV-45 illustrate the portlandite average content from XRD and TGA normalised by cement weight (in blended pastes there is only 60 wt% of cement).

It was evident from our data that the portlandite content of blended pastes decreased very slightly and between 7 and 90 days, it remained almost constant. It suggested that the portlandite demand of our hydrating slag pastes was quite modest.

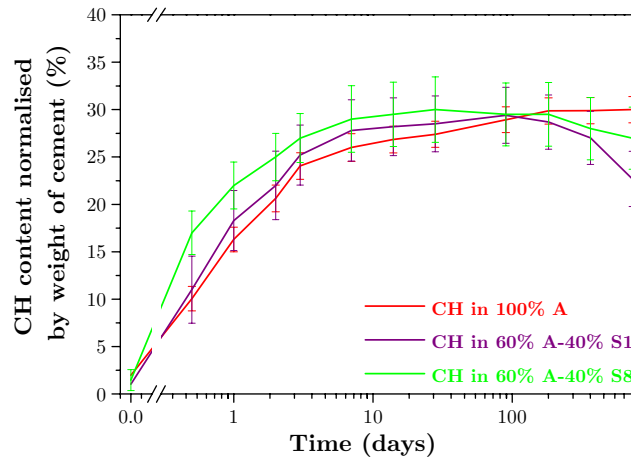


Figure IV-43: CH average content from XRD and TGA normalised by cement weight versus time for system A

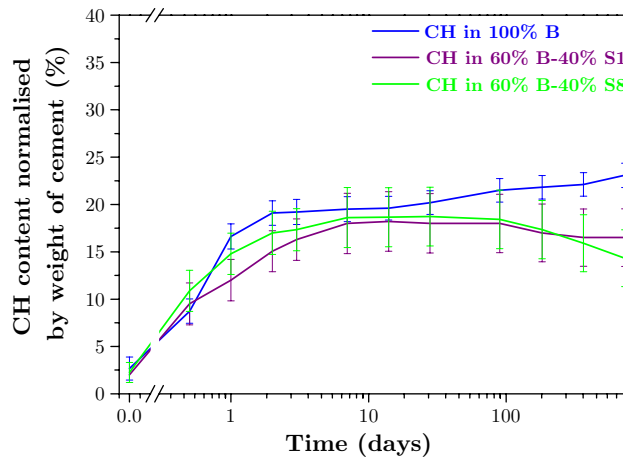


Figure IV-44: CH average content from XRD and TGA normalised by cement weight versus time for system B

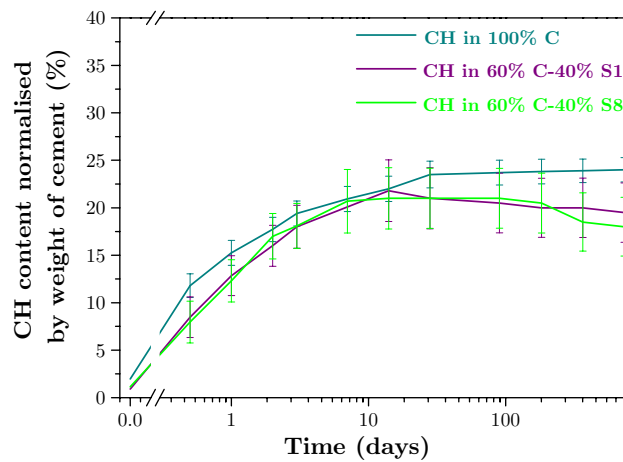


Figure IV-45: CH average content from XRD and TGA normalised by cement weight versus time for system C

IV.8. INFLUENCE OF SLAG ON THE COMPOSITION OF C-S-H AND OTHER HYDRATES

The main phases present in a slag hydrated blended paste have been reported as C-S-H, $\text{Ca}(\text{OH})_2$, sulfoaluminate phases AFt, AFm and hydrotalcite like phase. Considering the oxides present in slag, the following scheme (Figure IV-46) summarises the hydration products which can form.

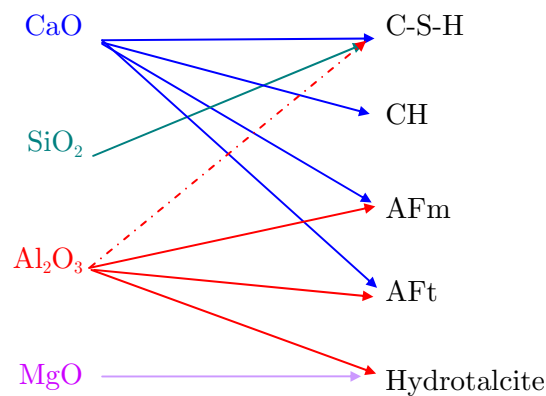


Figure IV-46: scheme to summarise how to assess phases from the oxides of slag

In the case of blended pastes with slag, there were typical hydrates rims generating around the slag grain as shown in Figure IV-47.

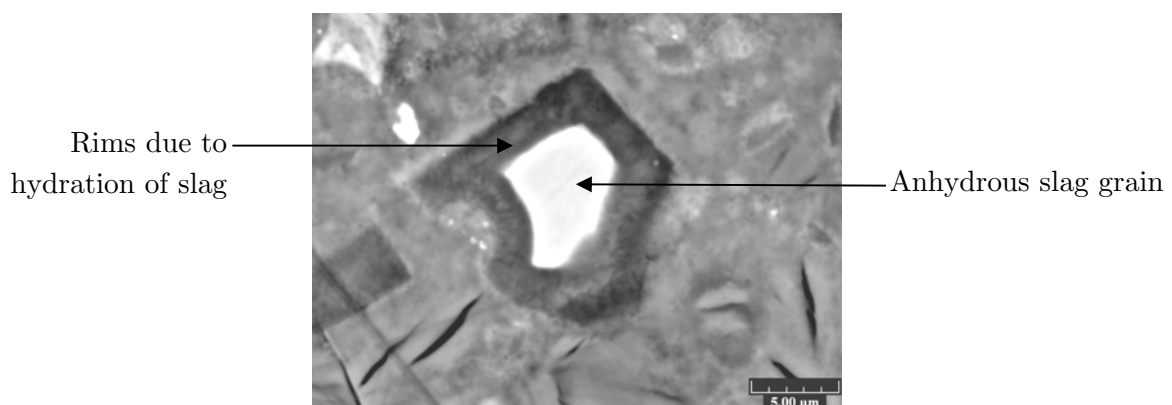


Figure IV-47: SEM-BSE picture of Cement C-Slag 8 hydrated for 90 days

With the addition of the slag, only minor differences in the microstructure between the three cement systems were evident at different ages. However, the comparison between the microstructure of blended pastes and the one of corresponding reference pastes clearly shown the contribution of slag in the evolution of hydration.

The following SEM-BSE pictures illustrate the differences of B pastes with B-S1 pastes for three given ages (it can be noted that the following comments on the microstructural development of blended pastes compare to pure pastes are also available for Cements A and C).

At 7 days, the inner C-S-H can be observed in around cement grains whereas nothing is relevant around the slag in blended samples (see Figures IV-48 and IV-49).

At 28 days, there was less anhydrous cement left and larger rims of slag in the blended sample as compared to the pure paste. For both samples, the microstructure is clearly densified by the hydration products (see Figures IV-50 and IV-51).

At 2 years, the reaction of slag is evident not only with large reacted rims around the slag grain but also with relicts of slag. In both cementitious pastes, in the cement grain, almost all the alite phases were reacted which generated a wide rim of inner C-S-H and mainly grains of belite were remaining (see Figures IV-52 and IV-53).

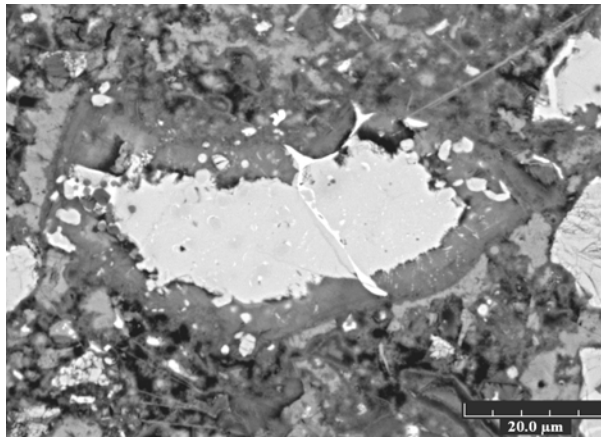


Figure IV-48: SEM-BSE microstructure of B pastes hydrated for 7 days

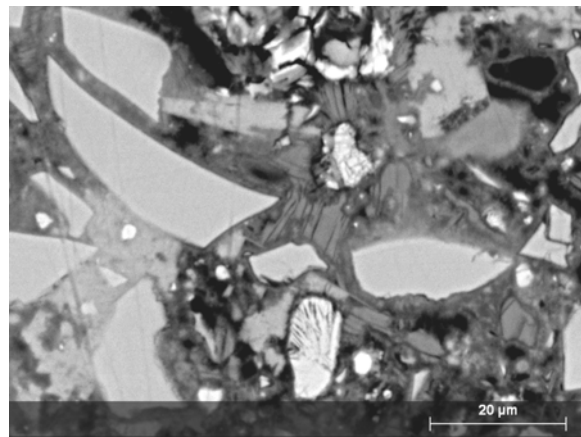


Figure IV-49: SEM-BSE microstructure of B-S1 pastes hydrated for 7 days

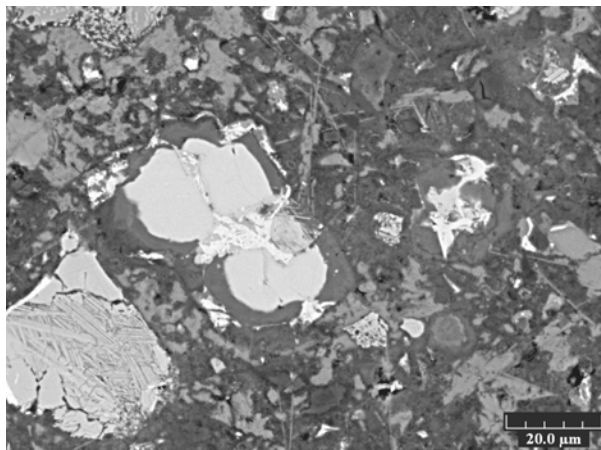


Figure IV-50: SEM-BSE microstructure of B pastes hydrated for 90 days

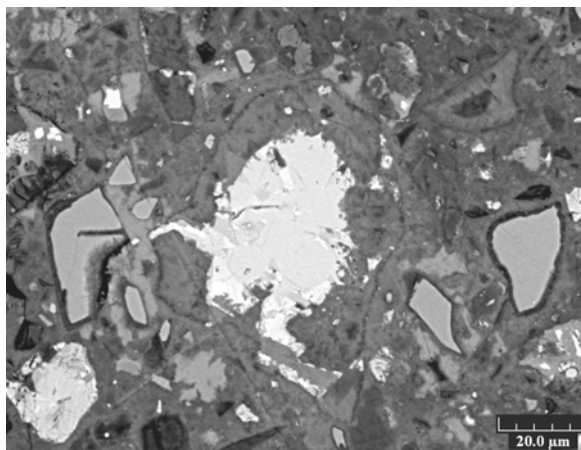


Figure IV-51: SEM-BSE microstructure of B-S1 pastes hydrated for 90 days

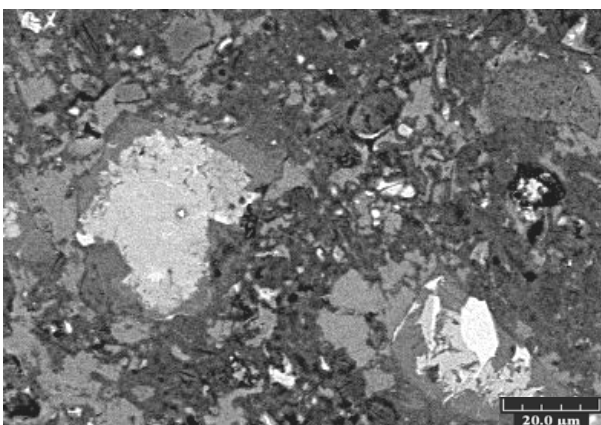


Figure IV-52: SEM-BSE microstructure of B pastes hydrated for 2 years

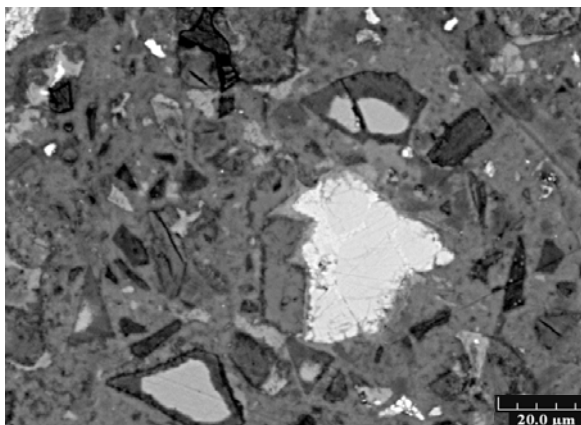


Figure IV-53: SEM-BSE microstructure of B-S1 pastes hydrated for 2 years

IV.8.1. C-S-H

The chemical composition of C-S-H in the various pastes hydrated for 28 days were established with EDS. For each type of C-S-H, 200 analyses were made (see an example Figure IV-54).

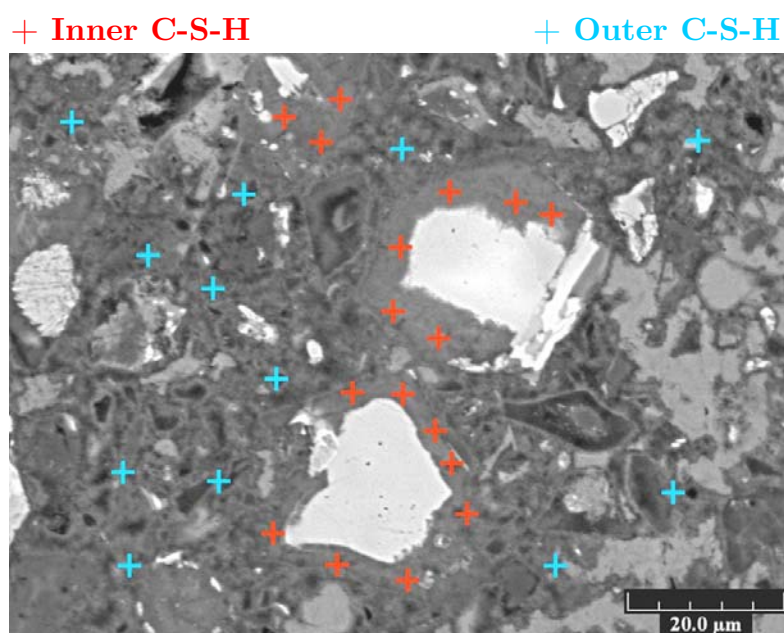


Figure IV-54: example of regions of inner and outer C-S-H in Cement C 28 days paste

The results from EDS measurements were examined in terms of element ratios because of the complexity of the spectra such as intermixing of the phases or inhomogeneties.

As shown in Figures IV-55 and IV-56, the EDS points not only include inner or outer C-S-H, but also some other phases which came from the excited volume in EDS analysis (about $1 \mu\text{m}^3$) or a mixing between C-S-H and some other phases like ettringite, AFm, portlandite, and phases high in magnesium in case of blended pastes.

Microanalyses were taken at locations where the inner C-S-H was thick enough to minimize the contribution of adjacent phases.

To select the C-S-H composition, different ratios were taken into account (Al/Ca versus Si/Ca and S/Ca versus Al/Ca) in order to remove the values which correspond to AFm, AFt, CH and the resulting mixture with C-S-H. Thus, the plots kept for inner C-S-H were the circles indicating the actual range and for the outer C-S-H, the values mixed with AFm and CH were removed.

So all major atomic ratios were considered in selecting the points most representative of C-S-H with minimal intermixing of secondary phases.

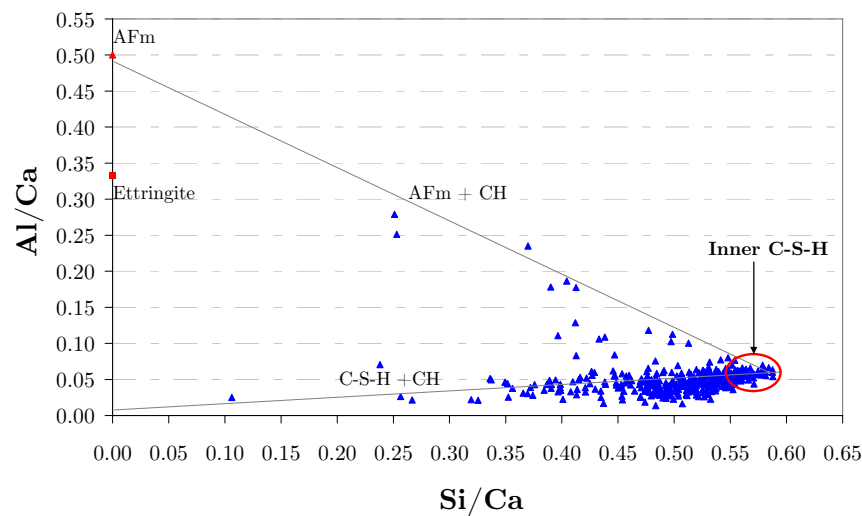


Figure IV-55: Al/Ca ratio plotted against Si/Ca atom ratio for individual X-ray microanalyses of Cement A hydrated for 28 days

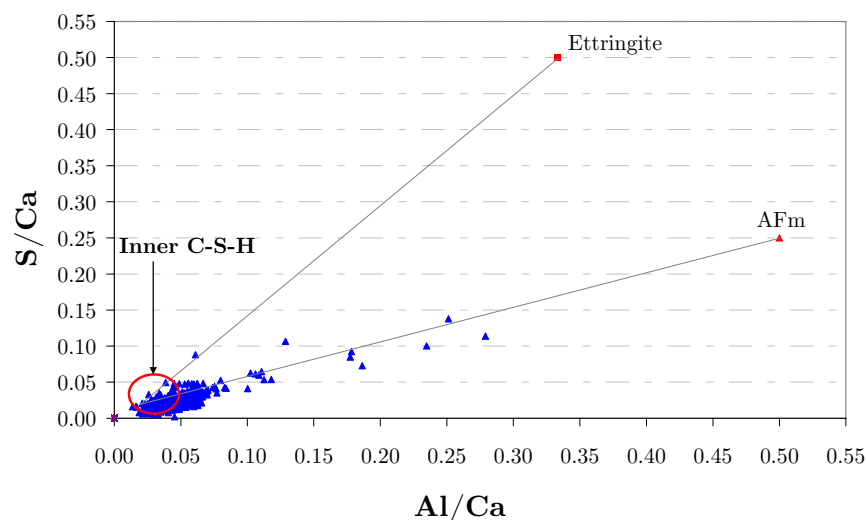


Figure IV-56: S/Ca ratio plotted against Al/Ca atom ratio for individual X-ray microanalyses of Cement A hydrated for 28 days

IV.8.1.a. Comparison for one given age-at 28 days

In the silicate chains of C-S-H, Aluminium can substitute for silicon [145]. So instead of the Ca/Si ratio, the Ca/(Si+Al) ratio is shown for the 9 cementitious pastes (see Figure IV-57).

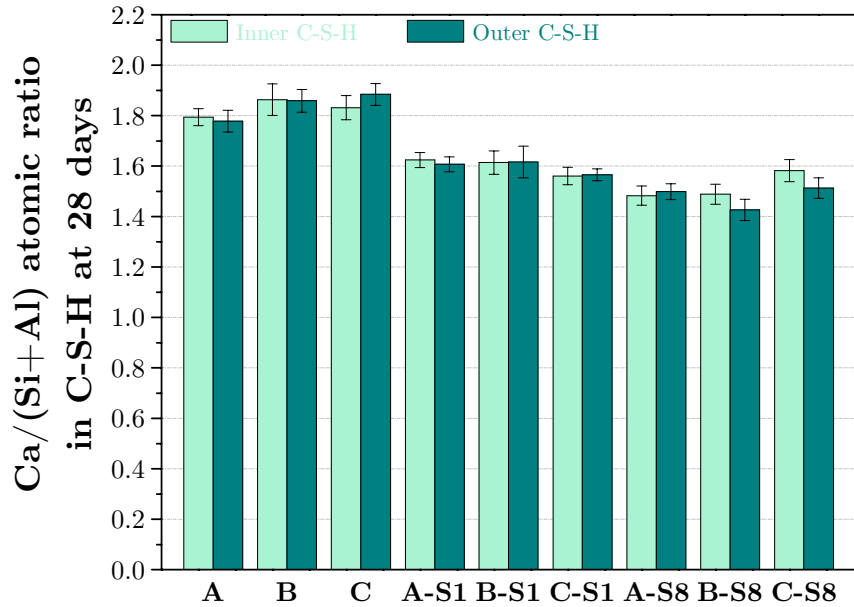


Figure IV-57: mean of Ca/(Si+Al) atomic ratio in inner and outer C-S-H of different cementitious pastes hydrated for 28 days

The mean Ca/(Si+Al) atomic ratio of the C-S-H in blended pastes is lower than that found in cement pastes as noted in previous studies [144,146]. For cement pastes, the Ca/(Si+Al) atomic ratios are very similar at a value around 1.9-2.0 in contrast to the lower ratios for blended pastes (around 1.55) due to the low Ca/(Si+Al) ratio of slag respectively 0.94 for Slag 1 and 0.97 for Slag 8.

Comparing the inner and outer C-S-H, there is no significant difference in Ca/(Si+Al) atomic ratio. This indicates homogenisation of C/S ratios throughout the C-S-H.

Figure IV-58 shows the average of Al/Ca ratio in inner and outer C-S-H for the 9 cementitious pastes.

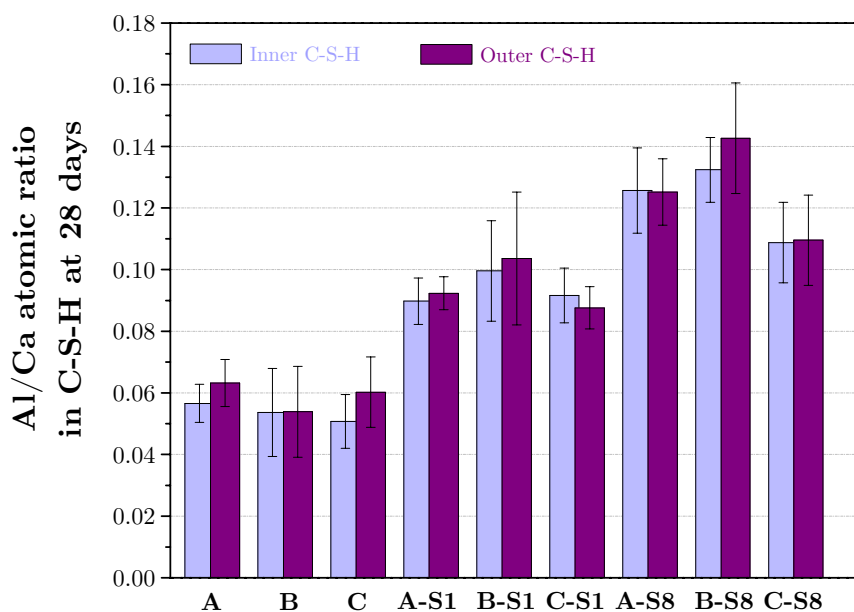


Figure IV-58: mean of Al/Ca atomic ratio in inner and outer C-S-H of different cementitious pastes hydrated for 28 days

With both slags a significant increase in the aluminium content of both inner and outer C-S-H is observed in blended pastes as compared to pure pastes with a high range in the outer C-S-H.

The fact that the Al/Ca atomic ratios are systematically higher in outer than in inner C-S-H can be explained by the presence of more intermixed phases in the outer products.

The higher Al/Ca ratios with Slag 8 is clearly linked to the high initial content of aluminium from this slag as compared to Slag 1.

The Al/Ca ratios do not seem to be significantly affected by the type of cement.

Some others minor elements were found in the C-S-H analyses such as potassium, iron, magnesium and sulphur, this last element is reported to be absorbed by C-S-H [147].

Figure IV-59 shows the average of S/Ca ratio in inner and outer C-S-H for the 9 cementitious pastes.

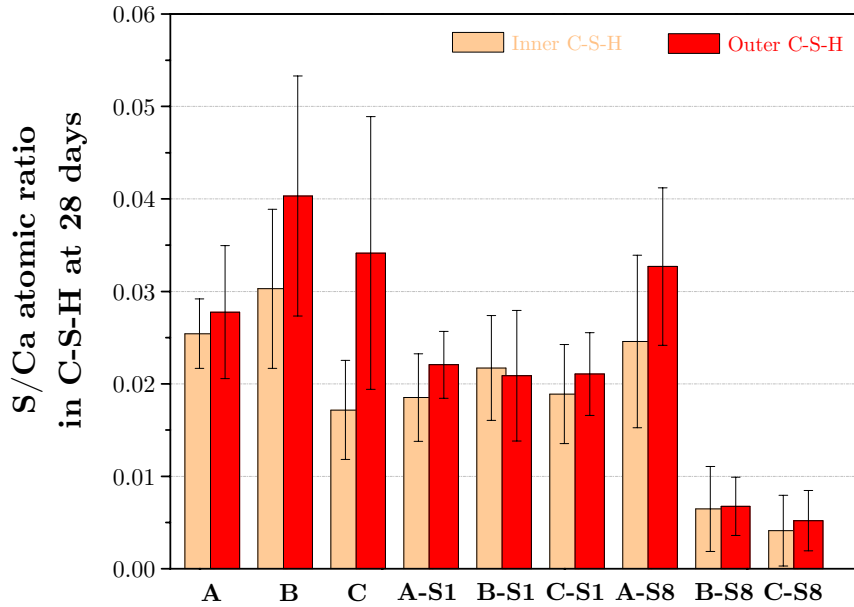


Figure IV-59: mean of S/Ca atomic ratio in inner and outer C-S-H of different cementitious pastes hydrated for 28 days

Due to the low content of sulphur, fairly large errors are observed. The errors correspond to a statistical dispersion which is not the accurate representation of error.

Even if the S/Ca ratio is very small compared to Ca/(Si+Al) ratio, sulphur absorption seems to change between the systems.

The blended pastes with Slag 8 had systematically lower S/Ca atomic ratio compared to the one with Slag 1. It could be explained by consumption of sulphur by other hydrates such as AFm phases in the case of pastes blended with Slag 8.

The quantity of sulphur in C-S-H from pastes composed of Cement B is higher than the other pure cementitious pastes. It should be noted that the alkali content of Cement B is the highest ($\text{Na}_2\text{O}_{\text{eq}}=1.14$) and in the presence of alkalis, the solubility of ettringite increases, which in turn increases amount of sulphur in solution and can be absorbed by C-S-H [148].

For systems A, the S/Ca ratios appear unaffected by the addition of slag.

For systems B and C, the S/Ca ratios were clearly decreased in C-S-H of blended pastes compared to pure pastes. It could be linked to the dilution of cement in blended pastes compared to the ones of pure pastes.

It is seen that the addition of slag can lower the amount of sulphur absorbed on the C-S-H this may be due to changes in alkali concentration or to the formation of more sulfoaluminate hydrates.

IV.8.1.b. Comparison of different systems as a function of time

The evolution of in the composition of the C-S-H with time is presented in the following section (see Figures IV-60 to IV-65 where Ip are inner products and Op outer products).

Ca/(Si+Al) atomic ratio

First, the substitution with slag induced a significant decrease of Ca/(Si+Al) atomic ratio in both inner and outer C-S-H compared to pure pastes.

In addition, the Ca/(Si+Al) atomic ratios in C-S-H of blended pastes clearly show a distinct decrease at early ages compared to Ca/(Si+Al) atomic ratios in C-S-H of pure pastes. This could be explained by a type of pozzolanic reaction not in the sense of portlandite consumption but in the way of consumption of ions coming from C-S-H.

In the case of both inner and outer C-S-H of systems blended with Slag 8, the Ca/(Si+Al) atomic ratios are always slightly lower than in the C-S-H from pastes blended with Slag 1.

This could be due to the higher reactivity of Slag 8 compared to Slag 1 or to the influence of other ions in the system.

Al/Ca atomic ratio

First, compared to pure pastes, the substitution with slag led to a significant increase of Aluminum in the composition of inner and outer C-S-H.

For the 3 different cementitious systems, C-S-H in the pastes blended with Slag 8 had always a higher Al/Ca ratio than the one in the pastes blended with Slag 1. This phenomenon can be explained by the initial Al/Ca ratio in slag which is much higher in Slag 8 than Slag 1 (0.31 in Slag 1 and 0.62 in Slag 8).

There is little evolution in composition after 28 days even when more slag is reacted.

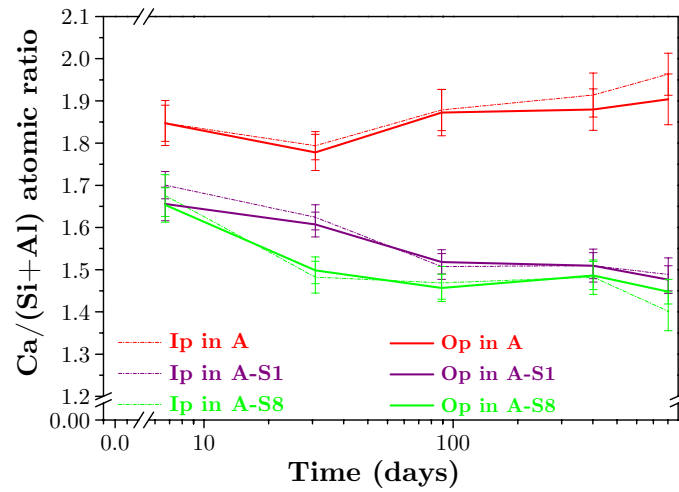


Figure IV-60: Ca/(Si+Al) atomic ratios in C-S-H for systems A

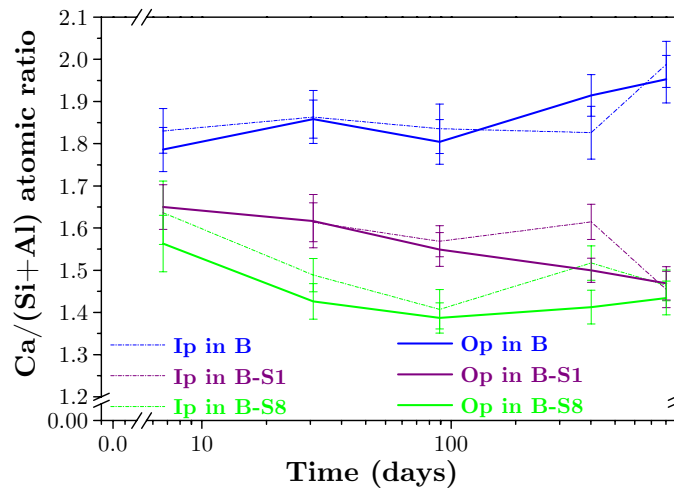


Figure IV-61: Ca/(Si+Al) atomic ratios in C-S-H for systems B

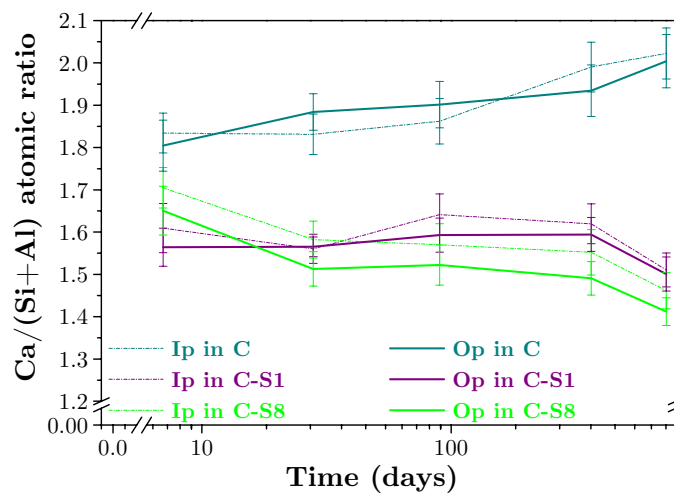


Figure IV-62: Ca/(Si+Al) atomic ratios in C-S-H for systems C

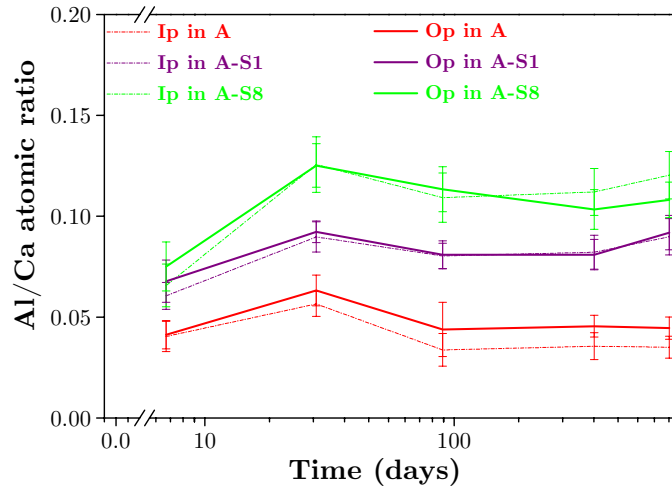


Figure IV-63: Al/Ca atomic ratios in C-S-H for systems A

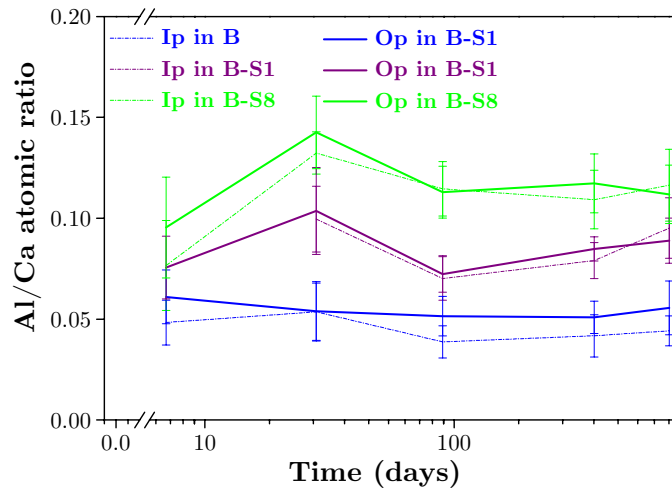


Figure IV-64: Al/Ca atomic ratios in C-S-H and for systems B

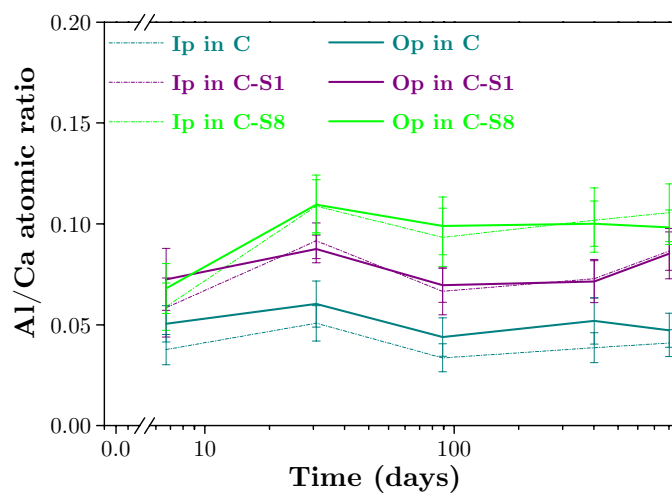


Figure IV-65: Al/Ca atomic ratios in C-S-H for systems C

IV.8.1.c. Comparison of SEM analyses with TEM analyses

Comparative EDS analyses were done on a selection of samples using TEM by Liu and Richardson from University of Leeds.

The TEM-EDS results always underestimated the ratio as compared to SEM-EDS results. The differences can be explained by the fact that the SEM-EDS analyses will be more likely to contain some contributions from other phases intermixed at the submicronic scale (for instance CH, AFt and AFm).

However, as shown in the following tables (Tables IV-2 and IV-3), considering the standard deviation, except in the case of A-S8 hydrated for 7 days, there is a good agreement between both techniques, as it was also previously found [112].

		TEM			Number of selected points	SEM			Difference between TEM and SEM
		Number of analyses	Ca/Si	SD		Number of total points	Ca/Si	SD	
A 7 d	Inner C-S-H	32	1.73	0.05	65	191	2.00	0.05	0.27
	Outer C-S-H	34	1.92	0.20	66	221	2.00	0.04	0.08
A-S1 7d	Inner C-S-H	15	1.70	0.13	52	248	1.90	0.03	0.20
	Outer C-S-H	9	1.86	0.21	41	268	1.86	0.03	0.00
A-S8 7 d	Inner C-S-H	14	1.48	0.09	75	194	1.88	0.04	0.40
	Outer C-S-H	27	1.52	0.14	75	212	1.89	0.04	0.37
B-S1 7d	Inner C-S-H	8	1.65	0.02	Inner C-S-H were not large enough				
	Outer C-S-H	23	1.73	0.09	53	231	1.88	0.04	0.15
A-S8 28d	Inner C-S-H	15	1.46	0.07	25	197	1.75	0.03	0.29
	Outer C-S-H	35	1.52	0.08	79	226	1.77	0.04	0.26

Table IV-2: comparative Ca/Si results from TEM and SEM EDS analyses

		TEM			Number of selected points	SEM			Difference between TEM and SEM
		Number of analyses	Al/Si	SD		Number of total points	Al/Si	SD	
A 7 d	Inner C-S-H	32	0.11	0.02	65	191	0.08	0.01	0.03
	Outer C-S-H	34	0.11	0.04	66	221	0.08	0.01	0.02
A-S1 7d	Inner C-S-H	15	0.08	0.02	52	248	0.11	0.01	0.03
	Outer C-S-H	9	0.12	0.03	41	268	0.13	0.02	0.00
A-S8 7 d	Inner C-S-H	14	0.14	0.03	75	194	0.12	0.02	0.01
	Outer C-S-H	27	0.14	0.02	75	212	0.14	0.02	0.00
B-S1 7d	Inner C-S-H	8	0.11	0.01	Inner C-S-H were not large enough				
	Outer C-S-H	23	0.12	0.02	53	231	0.14	0.03	0.02
A-S8 28d	Inner C-S-H	15	0.15	0.02	25	197	0.20	0.02	0.05
	Outer C-S-H	35	0.16	0.02	79	226	0.20	0.02	0.04

Table IV-3: comparative Al/Si results from TEM and SEM EDS analyses

IV.8.1.d. Comparison with literature results

X-ray microanalysis studies [58,77,149-154] have shown that the C-S-H in blended pastes had a Ca/Si ratio lower than that found in pure OPC paste (see Table IV-4).

It is consistent with our results which showed that the Ca/Si ratios of C-S-H in pure cement are around 2 against 1.8-1.7 in blended pastes.

References	Outer C-S-H			Mix composition	Remarks
	Si/Ca	Al/Ca	Mg/Ca		
Uchikawa, 1986 [59]	0.62	0.44	-	60%cement-40%slag	EMPA, 4 years, 20°C, W/C=0.4
	0.49	0.06	-	100%cement	EMPA, 4 years, 20°C, W/C=0.4
Harrison <i>et al.</i> , 1987 [144]	0.56	0.06	-	60%cement-40%slag	SEM-EDS, 28 days, 25°C
	0.50-0.53		-	100%cement	SEM-EDS, 28 days, 25°C
Barker, 1989 [155]	0.57 ± 0.07	0.06 ± 0.03	0.03 ± 0.02	50%cement-50%slag	EMPA, 90 days, 20°C, W/C=0.5
Richardson <i>et al.</i> , 2002 [156]	0.60 ± 0.06	0.08 ± 0.02	0.08 ± 0.04	70%cement-30%slag	EDS-SEM, 32 days, 35°C

Table IV-4: composition of C-S-H in blended cements [59,144,155,156]

IV.8.2. SLAG HYDRATION RIMS

Slag rims are characterized by a high Magnesium concentration, due to the low mobility of magnesium ions in the alkaline pore solution. MgO is incorporated in a hydrotalcite-like product [151] that exists as an intimate microscale mixture with C-S-H gel.

The composition of the hydrotalcite phase in the slag hydrates can be determined by plotting the Mg/Ca ratio against the Al/Ca ratio from EDS analyses [144], as shown in Figure IV-66.

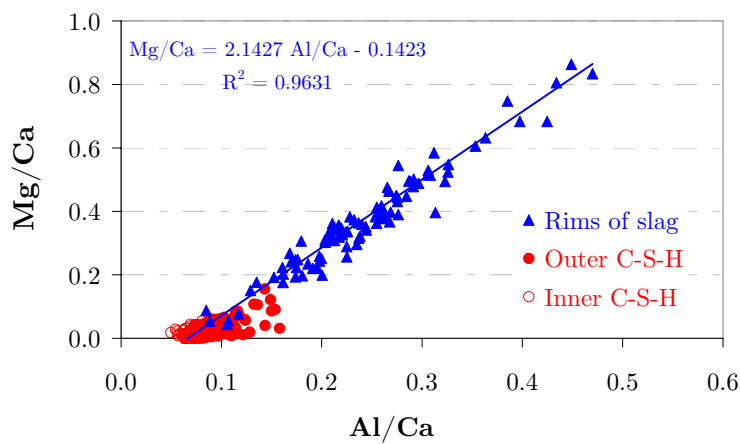


Figure IV-66: X-ray microanalyses of A-S1 pastes hydrated for 90 days, Mg/Ca atomic ratio versus Al/Ca atomic ratio

Table IV-5 summarises the Mg/Al atomic ratios found in blended pastes.

This ratio varied around 2 which corresponded to the Mg/Al ratio of hydrotalcite probably a bit mixed with C-S-H.

For Slag 1 the Mg/Al ratio seems to be around 2.1 whereas it is a bit lower in Slag 8 (around 1.8).

Mg/Al atomic ratio in rim and relicts of slag from SEM-EDX analysis				
	28 days	90 days	1 year	2 years
A-S1	2.0	2.1	1.9	1.8
B-S1	2.0	2.2	2.2	2.2
C-S1	2.0	1.8	2.2	2.0
A-S8	1.9 (1.86 from TEM)	1.7	1.9	1.7
B-S8	1.7	1.8	1.8	2.0
C-S8	1.7	1.7	1.8	1.8

Table IV-5: Mg/Al atomic ratio in rim and relicts of slag from SEM-EDS analyses

A number of previous investigations [56,58,63,129,157-159] observed hydrotalcite-like phase crystallites. Natural hydrotalcite has the formula $Mg_6Al_2(OH)_{16}CO_3 \cdot 4H_2O$ [144] with Mg/Al equal to 3 but other studies of slag blends also indicated that this ratio tends towards 2 (see Table IV-6), except from Barker studies [155] where Mg/Al probably corresponds to a mix of hydrotalcite and C-S-H.

Slag hydration products in the rims					
References	Si/Ca	Al/Ca	Mg/Al (hydrotalcite)	Mix composition	Remarks
Regourd, 1980 [157]	0.77-1.11	0.21-0.22	-	30%cement-70%slag	EMPA, 28 days, 20°C
Tanaka <i>et al.</i> , 1983 [160]	0.48-0.61	0.17-0.20	-	-	-
Harrison <i>et al.</i> , 1987 [144]	0.62	0.09	2.63	60%cement-40%slag	SEM-EDS
Barker, 1989 [155]	0.57 ± 0.07	0.06 ± 0.03	4.35	50%cement-50%slag	EMPA, 90 days, 20°C, W/C=0.5
Duchesne <i>et al.</i> , 1995 [153]	0.75	0.099	-	50%cement-50%slag	EMPA, 3 years, 38°C, W/B 0,5
Richardson <i>et al.</i> , 1992 [149]	-	-	2.40	-	EMPA, TEM
Richardson <i>et al.</i> , 1995 [154]	-	0.101	-	50%cement-50%slag	EMPA
Richardson <i>et al.</i> , 2002 [156]	0.65	0.28±0.18	-	70%cement-30%slag	EDS-SEM, 32 days, 35°C
Dyson, 2005 [112]	-	-	1.89	75%cement-25%slag	TEM, 1 day, W/C= 0.67

Table IV-6: composition of slag hydrates in blended cements from literature

[112,144,149,153-157,160]

IV.8.3. AFM PHASES

Some AFm phases were visible on SEM examination (Figure IV-67) and with XRD patterns not only monosulfoaluminate (Ms) and monocarboaluminate (Mc) but also some hemicarboaluminate was identified at low angles (Figure IV-68). However, it was not always possible to refine accurately these phases to due the low content.

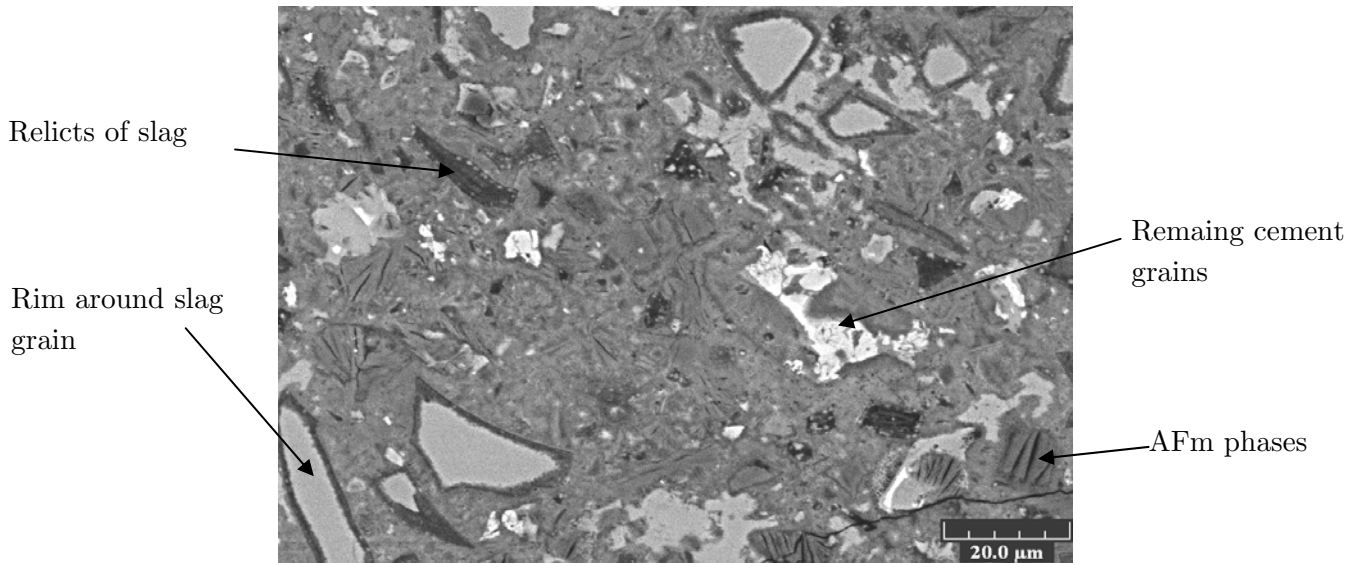


Figure IV-67: SEM-BSE picture of Cement B-Slag 8 paste hydrated for 1 year to illustrate the presence of AFm phases

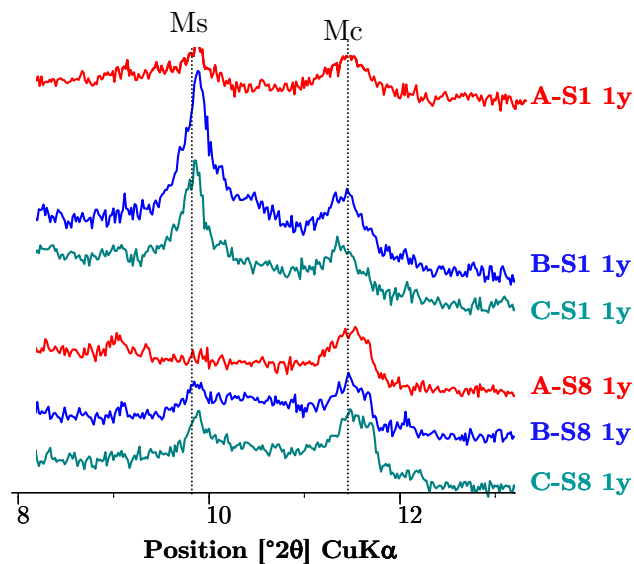


Figure IV-68: XRD patterns angular window 8-12.5° that allows the AFm phases to be identified

IV.9. CONCLUSIONS AND DISCUSSION ON THE EFFECT OF SLAG ON REACTION OF CEMENT

The presence of slag had a significant impact on the hydration of the belite phase and hence on the overall degree of hydration of the cement. Both of which were lower than in the unblended systems. On the other hand, the hydration of the ferrite phase was enhanced.

Calorimetry curves show a big impact of slag on the peaks attributed to the aluminate reactions. However, detailed analysis of these peaks did not provide any evidence that there was any reaction of the slag itself during these peaks

It appears rather than the C_3A reaction occurs over a shorter time period and so is more intense. Similar effects can be produced by inert fillers such as rutile.

The reaction of the slag, with a lower C/S ratio than the clinker led first to a decrease in the Ca/(Si+Al) ratio of the C-S-H and then at later ages to some decrease in CH. Furthermore Al/Ca increased.

CHAPTER V: MEASURING THE DEGREE OF REACTION OF SLAGS IN BLENDED PASTES

To optimise the use of slag, the relations between the properties of the cement constituents and their performance in paste have to be better understood. For this, an accurate method is needed to determine the actual rate of reaction of the different components in blends.

This chapter evaluates five methods to measure the degree of reaction of slag in blended pastes:

- Selective dissolution;
- Recrystallisation of slag from differential scanning calorimetry;
- Image analysis and mapping treatment procedures from SEM;
- Cumulative heat evolution curves from isothermal calorimetry;
- Chemical shrinkage curves.

V.1. STATE OF THE ART

V.1.1. MEASUREMENT OF BOUND WATER

The classic method for measurement of degree of reaction is extrapolation of overall degree of reaction from the bound water content [91,161,162]. However, this depends on an assumption of the quantity of water bound by the hydrate phases (see the following equations system where the initial water molecules are in blue).

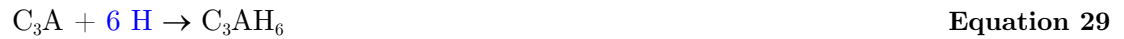
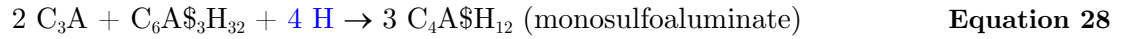
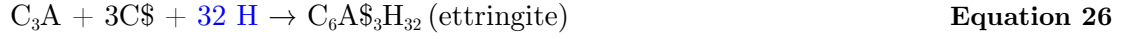
Hydration of tricalcium silicate:



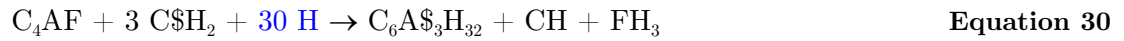
Hydration of dicalcium silicate:



Hydration of tricalcium aluminate with calcium sulfate:



Hydration of tetracalcium aluminoferrite:



Even for typical Portland cements, the stoichiometry of the hydration reaction is not precisely known. In particular it has been shown that the amount of water bound in the C-S-H varies with temperature and the overall water combined by aluminates changes over time due to sulfate and carbonate contents, to a certain degree as a result of ferrite reactions all of which remains unclear [148].

When slag is present, the use of bound water as a measure to the overall degree of hydration becomes completely unusable due to the unknown stoichiometries (for reaction of silicon, aluminium, calcium and magnesium) and the nature of reactions of slag with various clinker phases. Up to pH 10, the hydrolysis of the slag network is accomplished and leads to the dissolution of glass. However, even if slag has hydraulic properties, the rate of the reaction with water is slow. The reaction can be activated by several methods (in blended cements, slags are chemically activated by calcium hydroxide and by gypsum) but the end product is always C-S-H rich in alumina and magnesium.

V.1.2. METHODS TO MEASURE REACTION IN BLENDED CEMENTS

As discussed in Chapter III, the use of image analysis [94] and quantitative X-ray diffraction [19,53,93,163], particularly coupled by Rietveld analysis, have proven to be effective for the measurement of degree of reaction of clinker in cement pastes. There is good agreement between these techniques [83,93]. These techniques can also be used to compute the degree of reaction of the clinker components even in blended materials.

However, the degree of reaction of the SCM itself poses new challenges. The reactive part of most of these materials is amorphous, so cannot be measured directly by X-ray diffraction but the homogeneous regions of slag can be detected and quantified by image analysis [164,165].

Several authors [88,89,166-170] have used a selective dissolution method based on preferential chemical dissolution of the reaction products and unhydrated cement can be implemented to study the effect of slag separately from cement.

It has also been suggested [75,161] that differential thermal analysis (DTA) can be used to recrystallise slag at high temperatures (between 800 and 1100°C). By quantifying the corresponding peak, this method has proven to be promising to determine the degree of reaction of slag.

Some studies [133,171] have reported the use of the cumulative heat evolution obtained from isothermal calorimetry. The advantage of this methodology is that the plot is continuous. The problem, however, is to convert the heat evolution to a degree of slag reaction. In the same way, chemical shrinkage experiments allow to obtain an overall reaction but need more investigations to calculate the degree of reaction of slag.

More details of previous research related to each of five methods are presented at the beginning of the following sections. The experimental details of these approaches are also detailed. It is important to note that consideration of measurement errors is vital in terms of interpretation of the results.

V.2. SELECTIVE DISSOLUTION

V.2.1. STATE OF THE ART

One of the main and oldest methods for the estimation of the degree of reaction of the slag is based on a preferential chemical dissolution of the reaction products and unhydrated cement [88,89,166-170] leaving the unreacted slag.

In recent studies [88,112,170] a modified method is presented which we implemented in this work.

The principle of this method is based on the assumption that clinker phases and their hydrates, and the hydrates formed from the slag are mostly dissolved leaving the unhydrated slag as a residue. Ethylenediaminetetraacetic acid (EDTA), triethanolamine and sodium hydroxide solution are claimed to dissolve the clinker minerals and calcium sulfate, at pH 11.5, without a notable dissolution of the slag. Precipitation of silica and hydroxides is avoided by the addition of sodium hydroxide [166].

By means of a comparative study, Luke and Glasser [169] concluded that this EDTA based modified method of Demoulian [166] was the most suitable.

V.2.2. PROTOCOL OF THE DISSOLUTION TECHNIQUE

Selective dissolution was used according to the protocol given by Luke and Glasser [169] and recently used by Dyson [112]. The following solutions were used:

- 0.05 M ethylenediaminetetraacetic acid (EDTA);
- 0.1 M Na₂CO₃ solution;
- a 1:1 solution (by volume) of triethanolamine:water mixture;
- 1.0 M NaOH.

The different steps are the following:

- 125 ml of EDTA and 125 ml of Na₂CO₃ were mixed together in a one litre conical flask.
- 12.5 ml of the triethanolamine/water mixture were then added and the pH was checked to be 11.6 ± 0.1 . If necessary, the pH was adjusted by addition of small quantities of 1.0 M NaOH.
- A 0.25 g sample was then weighed out accurately and slowly added to the mixture in the conical flask while agitating the flask at intervals to avoid agglomeration.
- Then the mixture was shaken, by means of a mechanical shaker, for 30 minutes.
- The mixture was filtered through a proprietary vacuum filter assembly using GF/C filter paper supported on a glass frit.
- Care was taken to wash all residual material from the conical flask and also the walls of the funnel on to the filter. Prior to incorporation in the funnel assembly, the GF/C filter paper was dried in an oven at 105°C and weighed.
- The residue on the filter paper was washed with de-ionized water seven times and three times with methanol.
- The filter paper was carefully removed and dried in an oven at 105°C until a constant weight was achieved.

This method was followed for cement, and cement plus slag hydrated samples. In order to study the reliability of the selective dissolution, the residues were analysed by XRD and examined by SEM.

V.2.3. MATERIALS INVESTIGATED

The three main anhydrous cements (A, B and C), the anhydrous Slag 8 and the three following anhydrous cement-slag mixes (60 wt%-40 wt%) were analysed:

- Cement A-Slag 8;
- Cement B-Slag 8;
- Cement C-Slag 8.

The following hydrated blended mixes were ground and dissolved:

3 cement-slag mixes (60 wt%-40 wt%) hydrated for 1 day:

- Cement A-Slag 8 hydrated for 1 day;
- Cement B-Slag 8 hydrated for 1 day;
- Cement C-Slag 8 hydrated for 1 day.

3 cement-slag mixes (60 wt%-40 wt%) hydrated for 90 days:

- Cement A-Slag 8 hydrated for 90 days;
- Cement B-Slag 8 hydrated for 90 days;
- Cement C-Slag 8 hydrated for 90 days.

V.2.4. RESULTS FROM SELECTIVE DISSOLUTION

Under these controlled conditions, the solution should dissolve the unhydrated cement grains and their hydration products, leaving only the unreacted slag grains as undissolved residue.

The degree of hydration of slag grains in pastes was calculated from the following equation:

$$DH_{\text{Selective dissolution}}^{\text{Slag}} = \frac{R_{\text{cement}} - R_{\text{paste}}}{R_{\text{cement}}} \quad \text{Equation 33}$$

Where:

R_{cement} : undissolved residue from the blended anhydrous cement;

R_{paste} : undissolved residue from the cement paste.

Table V-1 contains the percentage of non-dissolved materials and the corresponding degree of reaction of slag for the hydrated mixes. From the data shown in Table V-1, it was evident that the undissolved materials (expressed as a percentage of the total amount), did not correspond to the pure undissolved slag because the percentage was much higher than the initial content of the slag (40 wt%). This difference in fraction led to computation of negative degree of reaction of slag which is an impossibility.

Label of samples	Undissolved materials (%)		Degree of reaction of slag (%)	
	Average	Standard deviation	Average	Standard deviation
Anhydrous S8	60.1	6.0	-	-
Anhydrous A-S8	67.5	5.7	-	-
Anhydrous B-S8	63.8	5.0	-	-
Anhydrous C-S8	61.9	5.9	-	-
A-S8 hydrated for 1 day	71.6	1.8	-79.0	4.4
B-S8 hydrated for 1 day	66.5	1.8	-66.3	4.6
C-S8 hydrated for 1 day	65.2	5.8	-63.1	14.6
A-S8 hydrated for 90 days	72.8	4.2	-82.0	10.5
B-S8 hydrated for 90 days	77.4	3.5	-93.5	8.8
C-S8 hydrated for 90 days	70.1	4.0	-75.1	9.9

Table V-1: undissolved materials and corresponding degree of reaction of slag after selective dissolution

Figure V-1 compares XRD patterns of Cement B-Slag 8 hydrated for 90 days after selective dissolution and the one of Cement B hydrated for 90 days (to indicate the peaks of the phases which are supposed to be dissolved). It is clear that belite, hydrated, portlandite and C-S-H were remains in the selective dissolution residue.

In addition, the Cement B-Slag 8 hydrated for 90 days after selective dissolution was studied with SEM. As shown in Figure V-2, this clearly shows the presence of undissolved cement grains, hydrated phases and agglomerates.

The XRD patterns and SEM examinations of all anhydrous materials clearly showed that selective dissolution did not completely dissolve the anhydrous phases for Cements B and C (see summary in Table V-2). Dissolution was enhanced for Cement A probably due to its high fineness as compared to Cements B and C.

For the hydrated mixes, only ettringite and ferrite were 100% dissolved, the other anhydrous and hydrated phases were not completely dissolved and hydrotalcite was also observed in the residue by XRD, as shown in the example of Cement B-Slag 8 hydrated for 90 days (Figure V-1).

The characterisation of the different phases in the selective dissolution residues by XRD analysis and SEM are summarised in Table V-2. It was established than the residues contained undissolved phases in both, anhydrous cements and hydrated samples.

	100% dissolved phases	Partly dissolved phases	Non dissolved phases
Anhydrous A-S8	C ₃ S, C ₂ S, C ₃ A, anhydrite	-	Slag 8
Anhydrous B-S8	C ₂ S, C ₃ A, C ₄ AF, anhydrite	C ₃ S	Slag 8
Anhydrous C-S8	C ₂ S, C ₃ A, anhydrite	C ₃ S	C ₄ AF, Slag 8
Hydrated A-S8	Ettringite	C ₃ S, C ₂ S, C-S-H, CH	Hydrotalcite, Slag 8
Hydrated B-S8	C ₄ AF, ettringite	C ₃ S, C ₂ S, C-S-H, CH	Hydrotalcite, Slag 8
Hydrated C-S8	C ₄ AF, ettringite	C ₃ S, C ₂ S, C-S-H, CH	Hydrotalcite, Slag 8

Table V-2: results of analysis of residues after selective dissolution

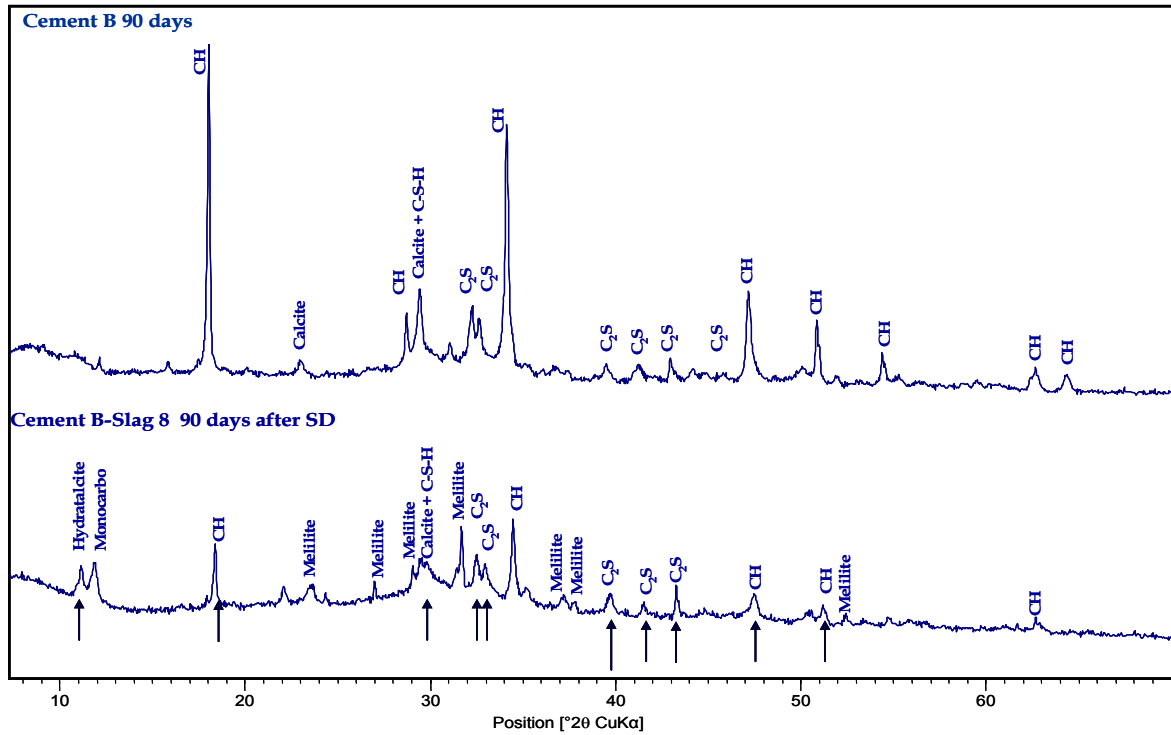


Figure V-1: XRD patterns of Cement B hydrated for 90 days and Cement B-Slag 8 hydrated for 90 days after selective dissolution

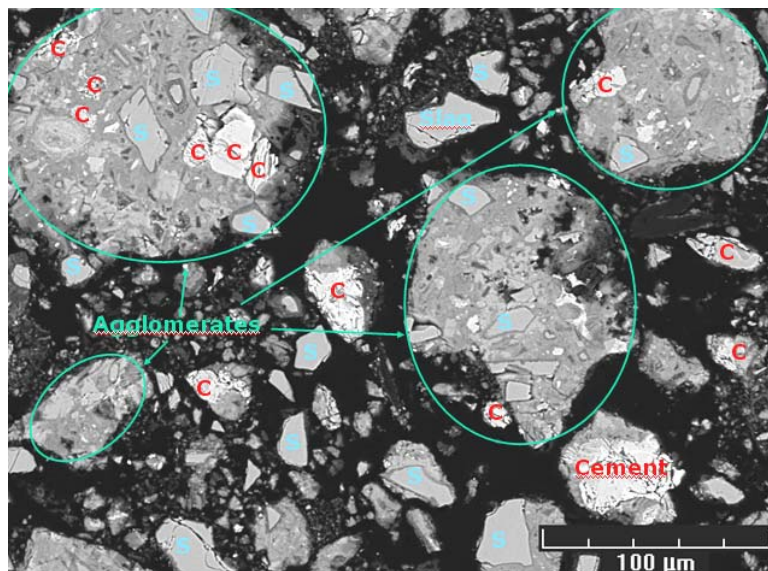


Figure V-2: SEM-BSE image of Cement B-Slag 8 hydrated for 90 days after selective dissolution

Since the sample mass of 0.25 g appeared very small, measurements were repeated adapting the procedure with higher masses (0,5 g, 1,0 g and 1,5 g....) and some tests with smaller filtration system were also conducted.

Even after these modifications in the procedure, some cement phases still remain undissolved.

The same phenomenon was previously reported in the literature. Taylor and Mohan [172] noted that large corrections must be made for incomplete dissolution of others phases, and the results are probably reliable within an error margin of $\pm 10\%$. In the studies of Luke and Glasser [141,173], the authors mentioned that even if slag was undissolved, some cementitious phases (such as periclase, aluminate) and hydrated phases from slag (hydrotalcite) are not dissolved by selective dissolution. In addition, Goguel [174] identified the high percentages of undissolved products: 2 to 5% of the hydrated cement undissolved.

Some authors [169] have proposed a minor/major modification to recalculate the degree of reaction of slag with the following formula:

$$DH_{\text{Selective dissolution}}^{\text{Slag}}(t) = 100 - \left(\frac{W_R(t)}{W_S(t) \%_{\text{SLAG}}(t=0)} - \frac{\%_{\text{CR}}(t) \%_{\text{CEMENT}}(t=0)}{W_S(t) \%_{\text{SLAG}}(t=0)} \right) \quad \text{Equation 34}$$

Where:

$W_R(t)$: weight of undissolved residue of the blended sample at every age directly obtained from the weight of residue after the selective dissolution;

$W_S(t)$: weight of blended sample before selective dissolution at every given age of hydration;

$\%_{\text{CR}}(t)$: percentage of undissolved cement residue obtained from the selective dissolution on pure cement (around 1-5%);

$\%_{\text{SLAG}}(t=0)$: percentage of initial slag in the blended cement (equal to 40%);

$\%_{\text{CEMENT}}(t=0)$: percentage of initial cement in the blended cement (equal to 60%).

Following the modified approach, we obtained the results given in Figure V-3 which led to reasonable range of overall degree of reaction (not anymore negative) but the degrees of reaction of slag at 1 day were unreasonably high and for B-S8 and C-S8 lower values were obtained at 90 days than the one at 1 day.

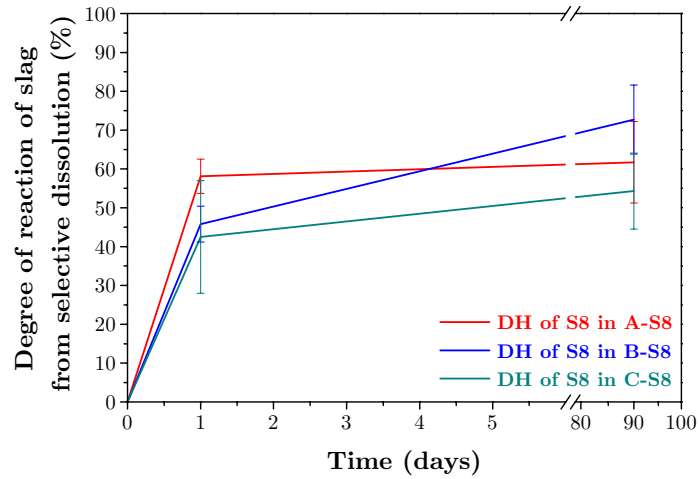


Figure V-3: degree of reaction of slag from selective dissolution after corrections suggested in [169]

While such methods could be suitable to enrich materials with respect to certain phases for other characterisation methods such as ^{29}Si NMR [173,175], they cannot be considered as reliable for the quantitative determination of the degree of reaction of slag. Therefore, it was decided that this method was not suitable for the quantification of the amount of slag.

V.3. DIFFERENTIAL SCANNING CALORIMETRY

V.3.1. STATE OF THE ART

In previous studies [75,161,176,177], it has been suggested that differential scanning calorimetry can be used to recrystallise slag at high temperatures (from 800 to 1100°C). By quantifying the corresponding peak, this method could be used to determine the degree of reaction of slag.

For both techniques, the contribution of anhydrous slag is not always easy to deconvolute mainly because of the background contribution. Past attempts to assign peaks in slag DTA curves to particular reactions have failed because of this complexity [74].

V.3.2. PROTOCOL FOR DSC MEASUREMENT

Differential scanning calorimetry measurements were made with a Netzsch DSC/DTA Model 404 C Pegasus, using a 10°C/min heating rate.

The hydrated samples were ground, weighed (20 ± 4 mg) and placed in an alumina crucible pan, an empty alumina crucible being used as a reference. A nitrogen flux was maintained in the heating chamber to avoid carbonation of the samples during the experiment. Heat flow data were recorded using a computer-based data acquisition system.

V.3.3. RESULTS FROM DSC

Figure V-4 shows the DSC curves of three anhydrous powders: pure Cement A, pure Slag 8 and the A-S8 blended powder.

For raw slag and even blended powder, the recrystallisation peaks were identified between 850 and 1050°C whereas nothing seemed to happen in this area for the pure cement (but there is in fact a small contribution from belite which is discussed later).

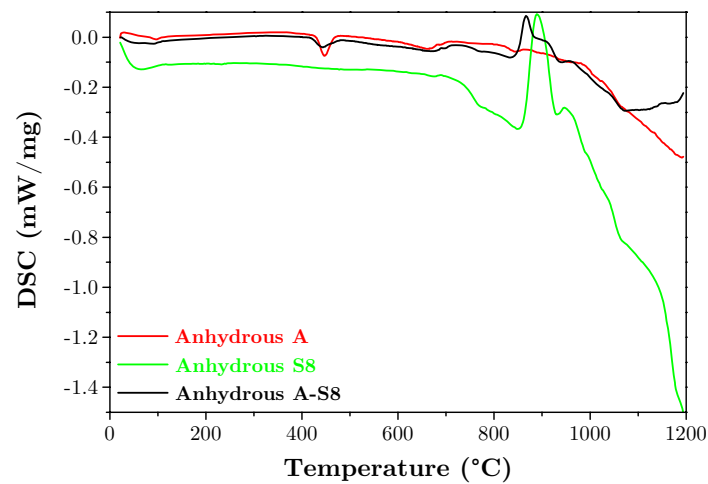


Figure V-4: DSC curves of anhydrous powders

The objective was to develop a method to study only the recrystallisation peak in order to optimise a separation method so as to quantify the degree of reaction of slag. Therefore, the experiments were conducted on one type of blended pastes (Cement A-Slag 8).

Figure V-5 shows that, as expected, the recrystallisation peak almost disappeared with time however, it was clearly affected by the background.

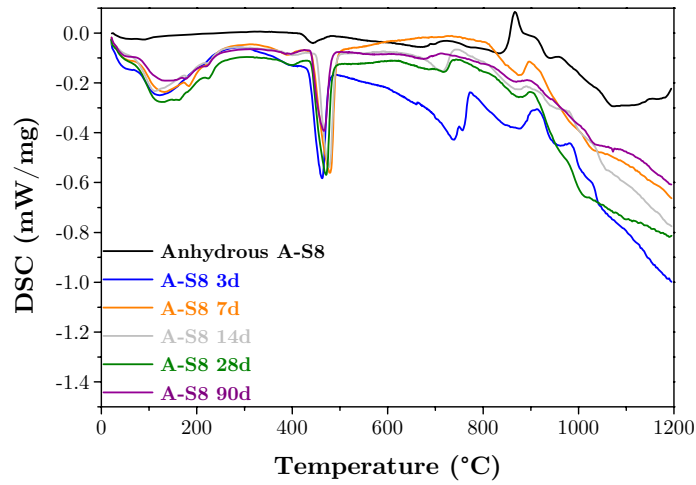


Figure V-5: DSC curves of Cement A blended with Slag 8 at different ages

The huge contribution of the background was an effect already obtained in previous DSC analyses of plain OPC as shown in the following example from literature [178] (Figure V-6).

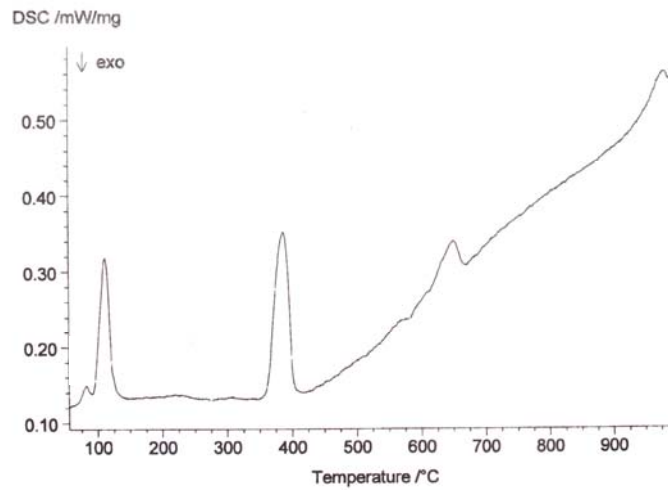


Figure V-6: DSC curves of hydrated OPC [178]

To remove the contribution of the background, a manual method with the DSC software appeared to be too subjective. So a background removal algorithm (see details in Appendix 2) was applied with two different choices of reasonable backgrounds which led to two different fits and two different degree of reaction of slag for each analysed sample. An example of the method is shown in Figure V-7 and all the results are shown in Figure V-8.

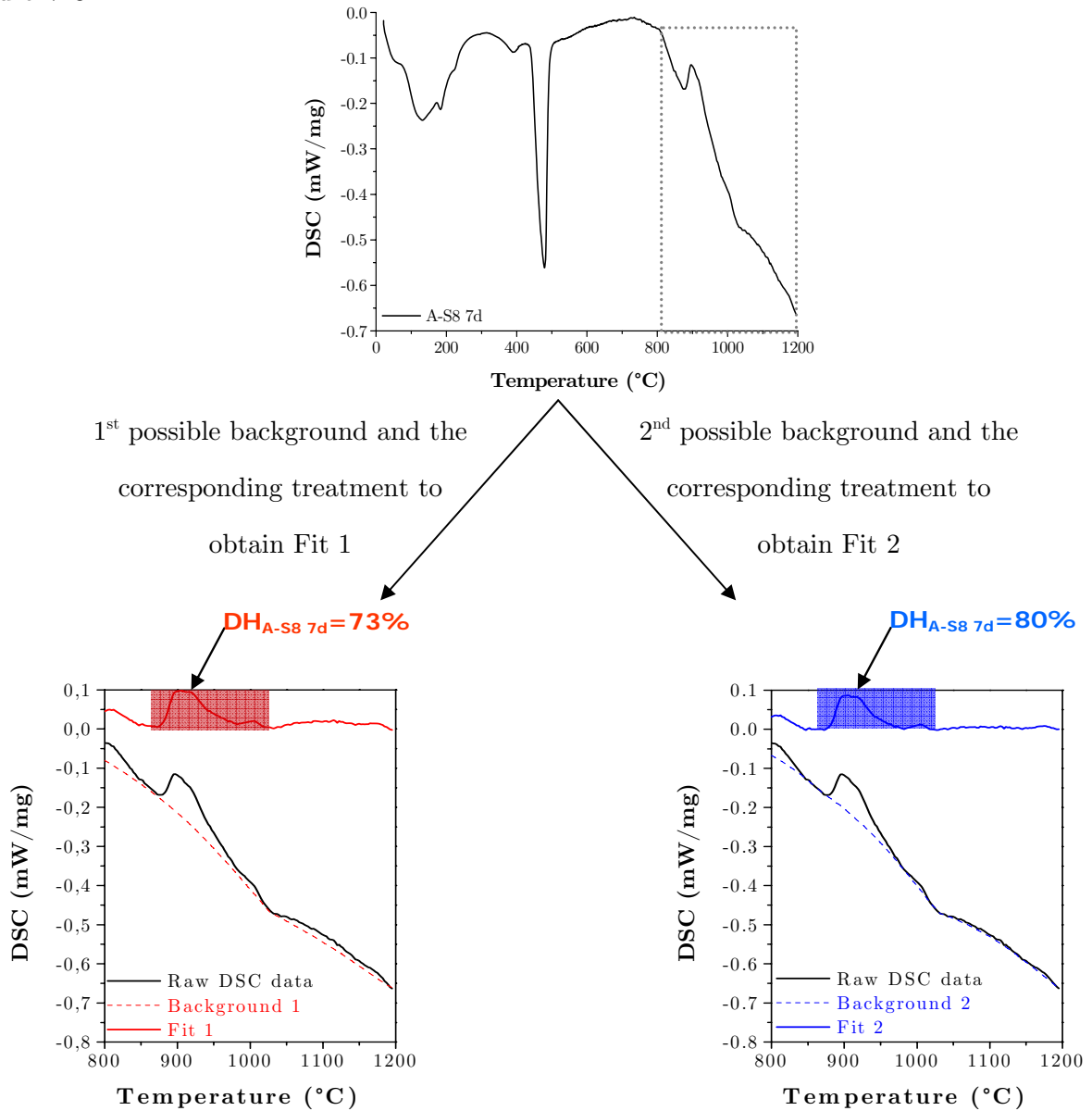


Figure V-7: method for background removal algorithm on DSC curve of Cement A-Slag 8 hydrated for 7 days

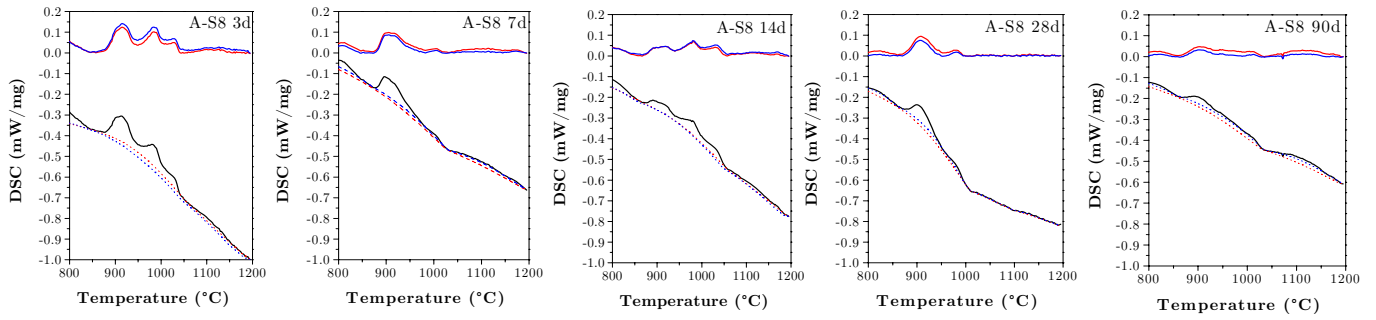


Figure V-8: background removal algorithm on all DSC curves of Cement A-Slag 8 hydrated from 3 to 90 days

The background removal algorithm led to 2 values of degree of reaction of slag per sample (see Figure V-8). The average value is represented at each time and gives the following curve. From 7 to 90 days, there was no significant change of DH of slag. However, as for results from selective dissolution, an unreasonably high degree of hydration of slag at 7 days and little evolution in time thereafter is observed in Figure V-9.

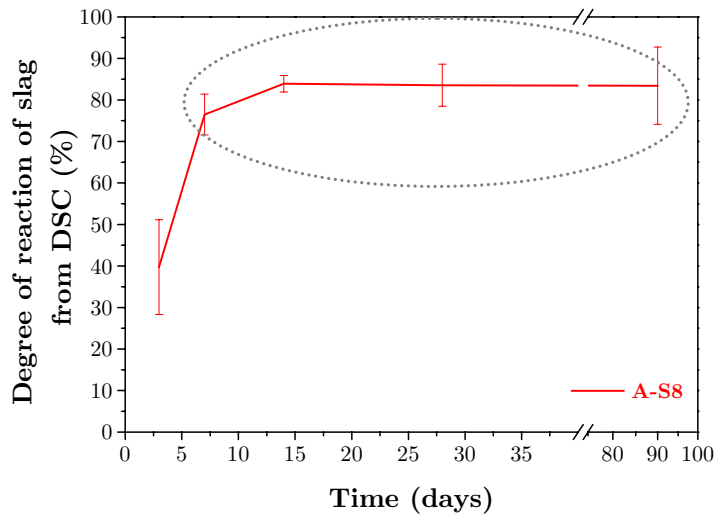


Figure V-9: degree of reaction of Slag 8 from DSC in Cement A-Slag 8 blended pastes

To understand the reason behind the complexity of isolating and quantify the slags by DSC, we consulted the literature on DSC analysis.

According to [177], at temperatures above 900°C, there are exothermic peaks from crystallisation of belite and aluminoferrite phases (see Table V-3 and Figure V-10).

DTA peak	Reaction	Temperature
Endothermic	Nucleation of C_3A	650-770°C
Exothermic	Crystallisation of C_3A	700-890°C
Endothermic	Nucleation of aluminoferrite	950°C
Exothermic	Crystallisation of aluminoferrite	980-1000°C
Exothermic	Crystallisation of C_2S	1130°C

Table V-3: DTA data of devitrification of glass of clinker [177]

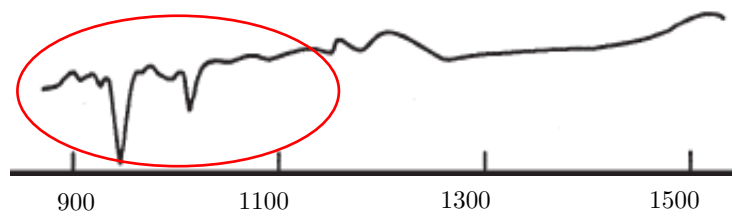


Figure V-10: DTA curve of C_2S [177]

As shown in Figure V-11, when a sample of Cement A without additional phases or blends was run and treated with the background removal algorithm that we described previously, the contribution of belite was established and quantified at 35 J/g. There was no contribution of ferrite because in this case we worked with the white cement (Cement A), which contains no ferrite.

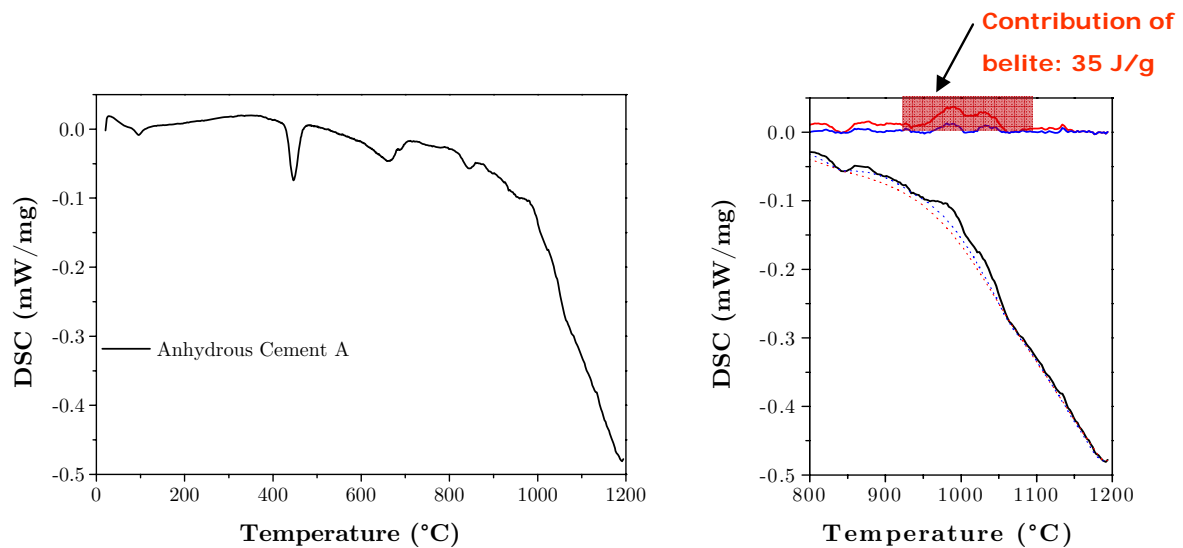


Figure V-11: DSC curve of Anhydrous Cement A and corresponding background removal algorithm which isolate the contribution of belite

Figure V-12 illustrates the background removal algorithm for three anhydrous samples: Slag 8, Cement A and Cement A-Slag 8. It isolates the contribution of belite from Cement A between 950 and 1050°C.

The recrystallisation peak of pure Slag 8 was identified between 850 and 1100°C.

The curve of anhydrous A-S8 clearly shows that there are both contributions of belite and slag between 950 and 1100°C. It appeared too complicated to try to correct the contribution of belite using a systematic method.

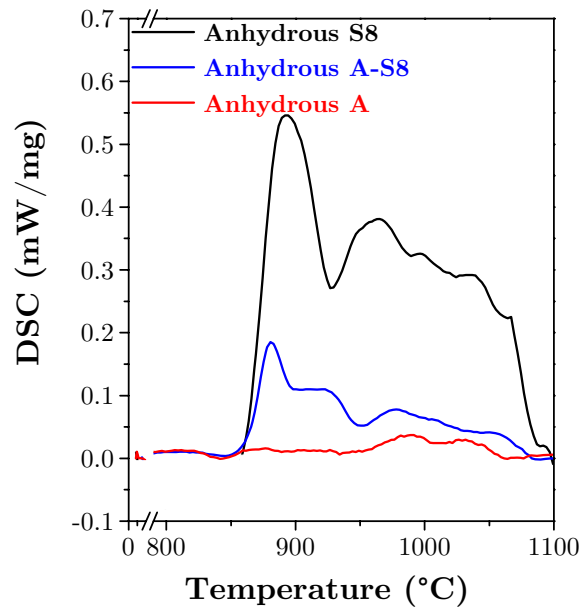


Figure V-12: background removal algorithm for Cement A, Slag 8 and Cement A-Slag 8

With inferences from the literature and the results on anhydrous Cement A, we concluded that in the case of blended paste, the signal due to the crystallisation of belite was being superposed due to the contribution of the slag.

One reason for the inability to well separate the contribution from the slag recrystallisation is the presence of signal from the belite in the same range. However, there seem to be other unknown influences on the background and the general shape of the peaks is too imprecise for any separation technique to make sense.

So this technique is not effective for quantification of degree of reaction of slag.

V.4. SEM WITH BSE-IMAGE ANALYSIS AND ELEMENTAL MAPPING

In previous work [165,179] BSE-image analysis has been shown to be used to quantify by compositional contrast the slag content in hydrated cementitious samples.

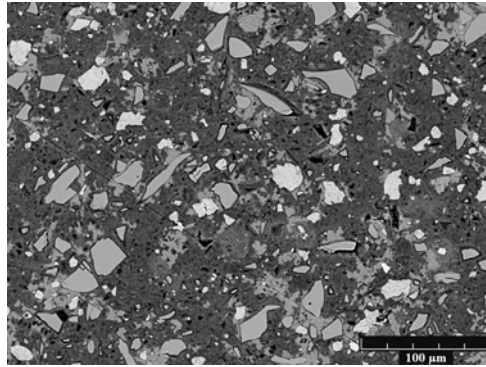
Polished sections of hydrated samples were prepared as described in Chapter II.

V.4.1. METHOD

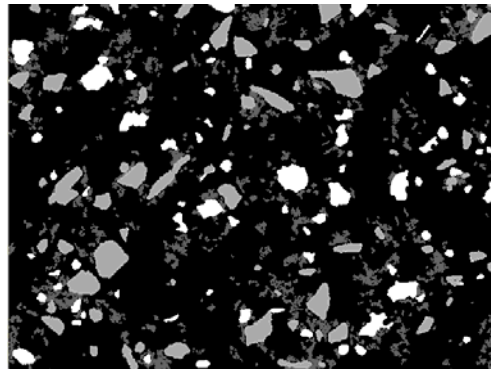
For blended pastes with Slag 1, a conventional grey level segmentation was initially used to quantify the content of slag. It basically consists of subsequent segmentation and interpretation of the corresponding histogram as illustrated in Figure V-13.

However, for the cement-Slag 8 systems, this image analysis treatment proved to be inaccurate. Due to an overlap between portlandite and slag grey levels. In order to isolate slag and portlandite, which had similar backscattered coefficients, chemical maps of Magnesium were acquired because it is only present in slag and not in portlandite.

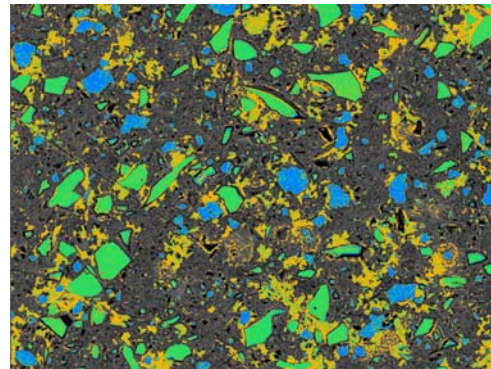
The relevance of energy dispersive X-ray (EDX) dot maps, acquired concurrently with the SEM-BSE was previously demonstrated in the case of alkali-activated cement mortars with silica sand [165].



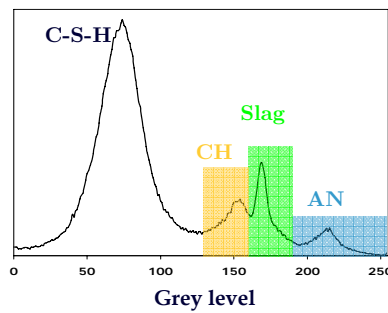
Original SEM-BSE picture



Segmented SEM-BSE picture



Coloured SEM-BSE picture



Corresponding grey scale histogram showing the different components

Figure V-13: conventional BSE-image analysis illustrated on example of Cement A-Slag
1 paste hydrated for 28 days

The challenge of this approach using Mg map is the time taken to get Mg maps with conventional EDS detectors. To improve this, an EDS detector for high resolution X-ray spectroscopy was obtained. It was a silicon drift detector (SDD), type XFlash 4030 Detector from Bruker AXS Microanalysis which can accept a maximum input count rate of 1 000 000 cps. It also had a large active detecting area of 30 mm² (against 10 mm² for the previous EDS detector) and at the same time achieved very good energy resolution of 133 eV (Mn K α) at 100 000 counts per second (cps).

In order to have consistent methodology for quantification of degree of reaction of slag, this approach using the SEM-BSE image combined with Mg map was chosen for both slag systems.

For all blended systems, as illustrated in Figure V-14, the image analysis was combined with mapping and consisted of:

- Acquisition of 150-200 SEM-BSE images combined (recorded in 30 sec) with Mg maps (recorded in 1 min 30 sec), at a nominal magnification of $\times 1000$ (corresponding to 254x190 μm), with an accelerating voltage of 15 kV and a number of counts between 80 000 and 100 000 cps (the spot size was adapted as a function of these counts).

- Combination of each set of one SEM-BSE image and one image of Mg distribution. Mg is present in both the raw slag and in its reaction products, but the grains of unreacted slag were identified when the grey level of the pixel corresponded to the slag (from the SEM-BSE image) and contained Mg (from the EDS mapping image) using in-house codes developed by Gallucci.

- The grains of slag were isolated as a function of its chemical composition and the degree of reaction of slag was calculated according to Equation 35.

Despite the fast EDS detector, this method is time consuming: an average of 10 hours of acquisition was necessary.

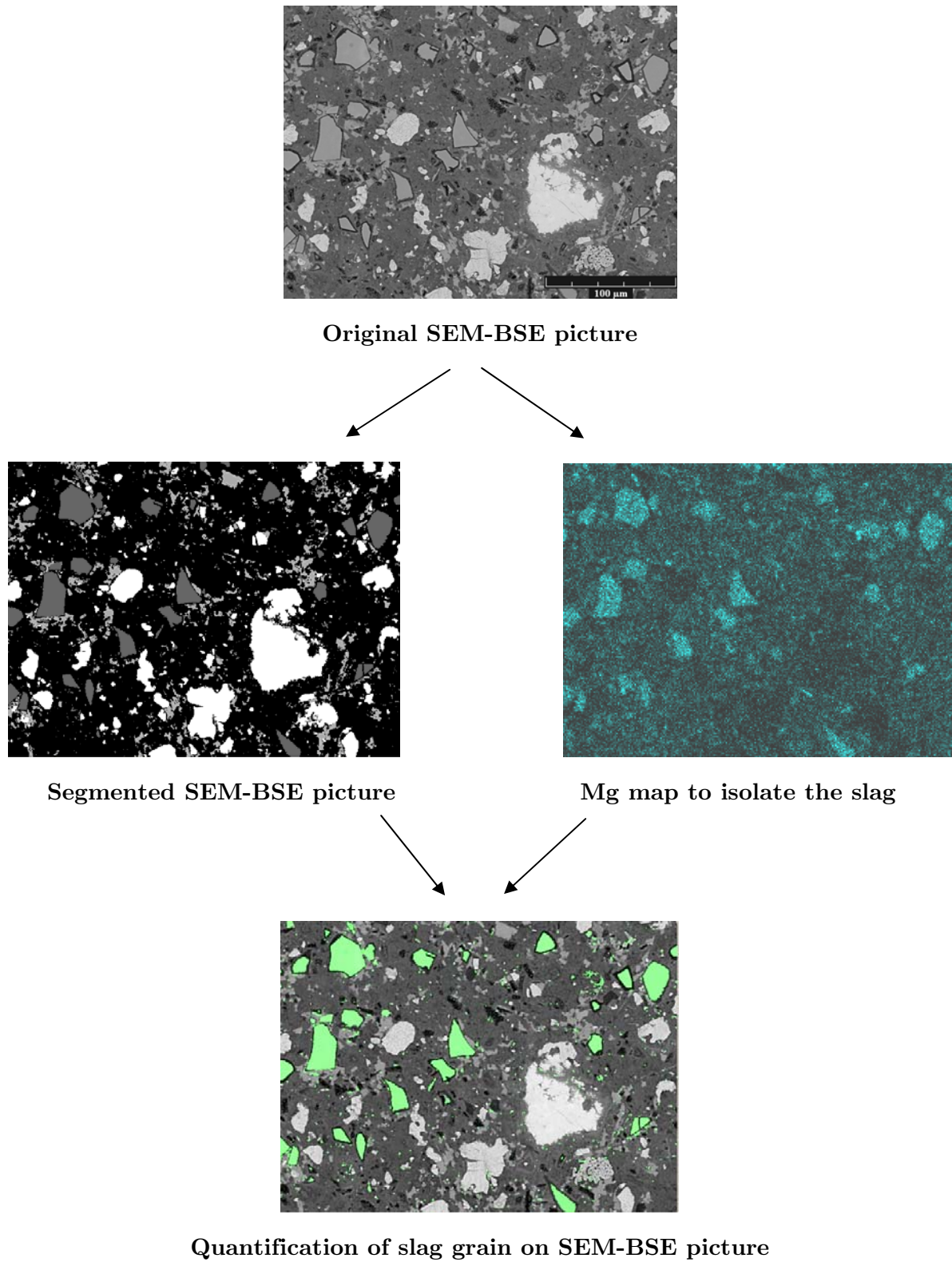


Figure V-14: BSE-image analysis combined with elemental illustrated on example of Cement A-Slag 8 paste hydrated for 90 days

V.4.2. RESULTS FROM IMAGE ANALYSIS-MAPPING

Assuming the original volume of the slag in the paste, the degree of reaction of slag is then defined as:

$$DH_{SEM}^{Slag}(t) = \frac{Vf_{\text{anhydrous slag}}(t=0) - Vf_{\text{anhydrous slag}}(t)}{Vf_{\text{anhydrous slag}}(t=0)} \quad \text{Equation 35}$$

Where:

$Vf_{\text{anhydrous slag}}(0)$: remaining volume fraction of initial anhydrous slag;

$Vf_{\text{anhydrous slag}}(t)$: remaining volume fraction of unreacted slag after time t .

Despite being a time consuming method, the determination of the degree of reaction of slag using SEM with image analysis and elemental mapping treatment proved as the most efficient method.

In addition, with the new powerful EDS detector, we obtained fairly precise results. The errors on the curves take into account the deviation between different sets of images from the same sample and also the deviation induced by different kinds of morphological corrections on the segmented images. It could be noted that the errors are higher at early ages.

Figures V-15 to V-17 present the degree of reaction of slag for all the systems as a function of type of cement and show that for all cementitious systems, even after taking into account the errors, Slag 8 is more reactive than Slag 1. It was, however, observed that despite higher reactivity of Slag 8, its reactivity reduced the same level as Slag 1 at 730 days.

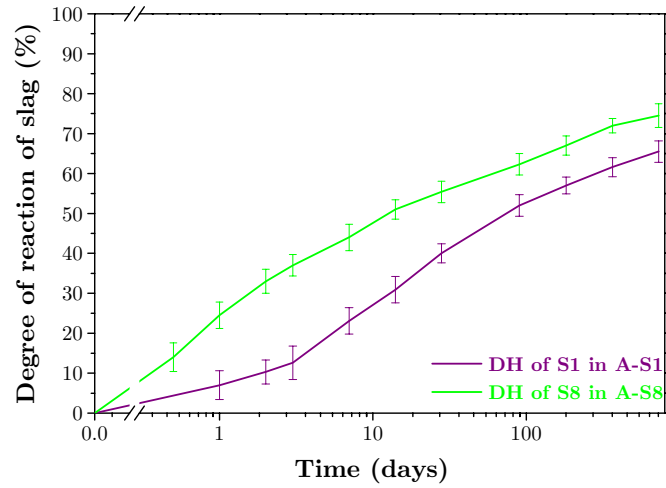


Figure V-15: degree of reaction of slag from SEM-IA-mapping in systems A

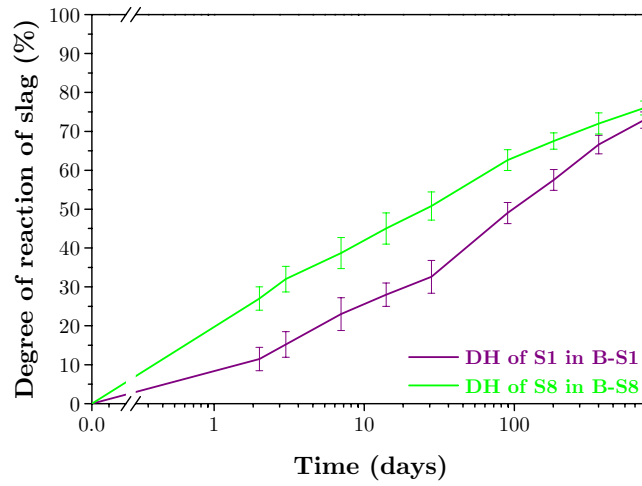


Figure V-16: degree of reaction of slag from SEM-IA-mapping in systems B

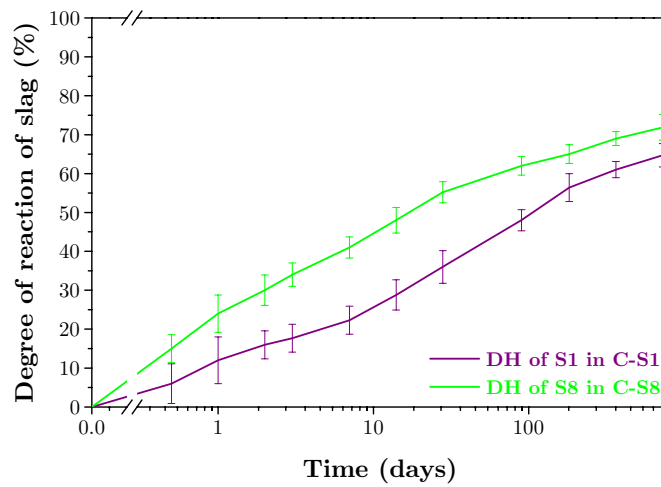


Figure V-17: degree of reaction of slag from SEM-IA-mapping in systems C

Figures V-18 and V-19 show the degree of reaction of slag per type of slag.

It seems that the reaction of slag is roughly affected by type of cement which is in blended pastes.

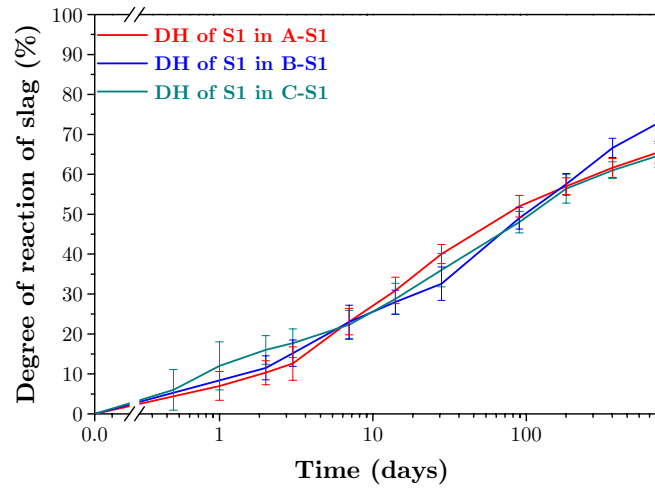


Figure V-18: degree of reaction of Slag 1 from SEM-IA-mapping in blended pastes

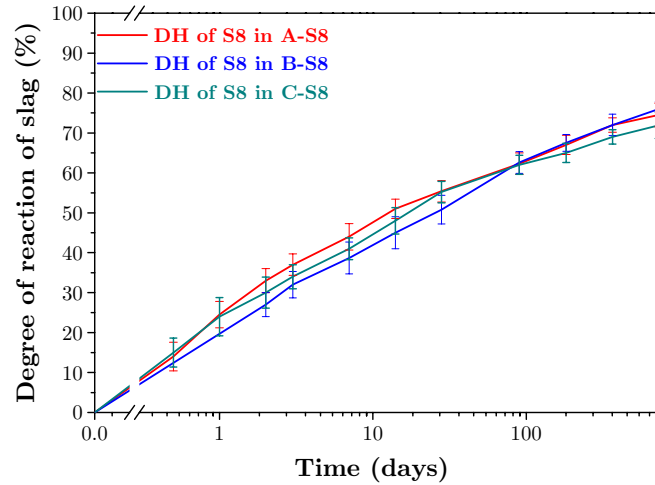


Figure V-19: degree of reaction of Slag 8 from SEM-IA-mapping in blended pastes

The results from SEM-IA-mapping were compared to the ones from selective dissolution in Figure V-20. As it was explained before, the degree of reaction of slag at 7 days is very overestimated by selective dissolution. However, the methods give similar results at 90 days.

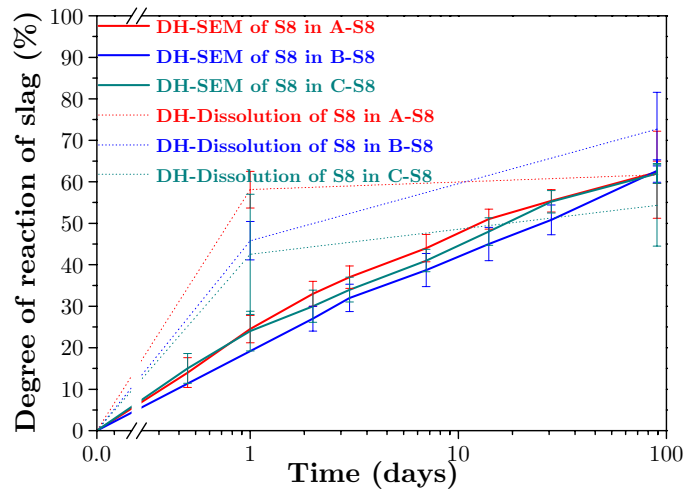


Figure V-20: degree of reaction of Slag 8 from selective dissolution and SEM-IA-mapping

For the A-S8 pastes, all the results from SEM-IA-mapping, DSC and selective dissolution were plotted in Figure V-21. The degree of reaction of slag from DSC at 7 days agreed with the results from SEM-IA-mapping but both these methods gave difference results at longer ages. Results from selective dissolution were in good agreement with SEM at 90 days.

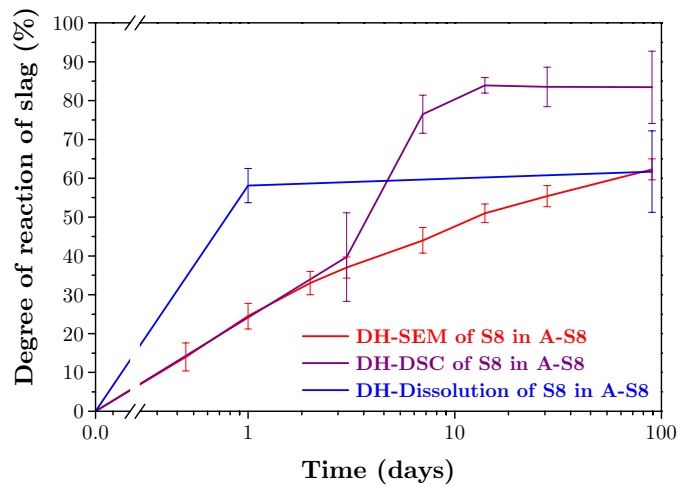


Figure V-21: degree of reaction of Slag 8 from SEM-IA-mapping, DSC and selective dissolution

V.5. CUMULATIVE HEAT EVOLUTION CURVES FROM ISOTHERMAL CALORIMETRY

V.5.1. WHY USE CUMULATIVE HEAT CURVES?

In previous studies [133,171] heat evolution was used for analysis and it was illustrated that cumulative heat liberated from neat and blended cements can be obtained (see Figure V-22).

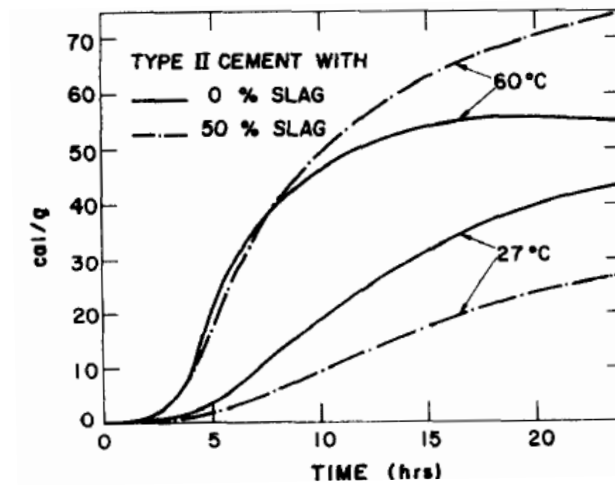


Figure V-22: cumulative heat liberation of cements at 27 and 60°C [133]

(this curve does not say if the unit corresponds to cal/g dry cement, dry cementitious, or paste)

The calorimetry measurement has the advantage of being continuous and having high precision if particular care is taken on base line stability and calibration to stabilise the equipment during long term acquisition.

As explained in Chapter III, particular care was taken to retain the stability of the calorimeter. Before each long term acquisition, a calibration was done and the stability of the baseline was carefully checked after acquisition.

As the conversion from the heat evolution curve to degree of reaction of slag is not well established, a special method needs to be developed.

V.5.2. RESULTS FROM ISOTHERMAL CALORIMETRY

Figure V-26 presents the cumulative heat evolution curves of pastes blended with Cement B over a period of 28 days and clearly shows the difference between cement pastes and blended pastes. Indeed, the heat evolved from hydration of blended pastes (normalised per gram of cement) rapidly surpasses that of the plain cement, to end up at 28 days with cumulated heat values considerably higher than the cement paste. This difference includes both the contribution from the reaction of the slag itself and the impact of the physical presence of slag on the rate of hydration of the clinker phases. To separate these effects, quartz was used as an inert filler with 40 wt% substitution as another reference sample. It was ground to have the same particle size range similar to that of slag (d_{50} of filler=10 μm and d_{50} of Slag 1=20 μm and d_{50} of Slag 8=15 μm).

Repeatability

For a given cementitious systems, all calorimetry experiments were run at the same time for 28 days. To insure a good accuracy of the results and verify the stability of the baseline, all the experiments were repeated twice.

Figures V-23 to V-25 show that the repeatability between two different batches was quite good even for long term acquisition.

In addition, these curves show the significant divergence of heat evolution for blended cements as compared to references samples and clearly establish the higher reactivity of Slag 8 compared to Slag 1.

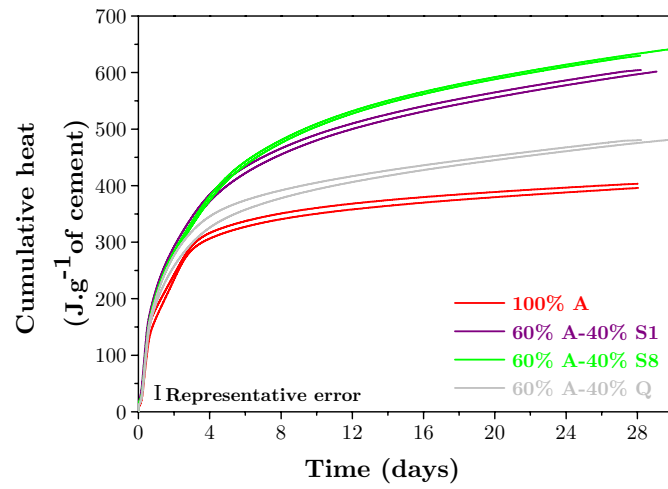


Figure V-23: normalised cumulative heat curves for systems A

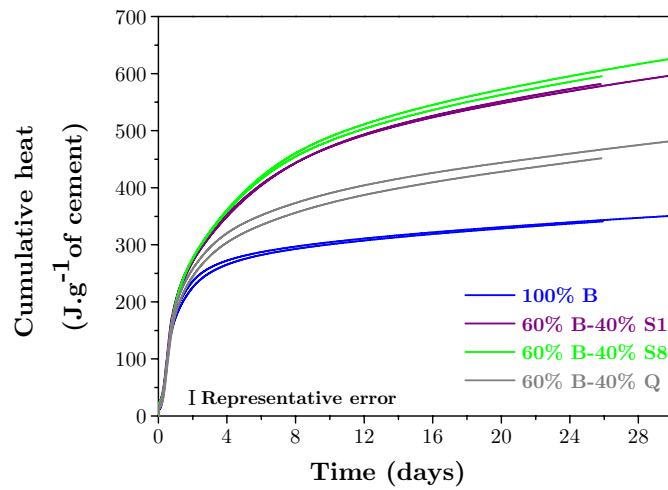


Figure V-24: normalised cumulative heat curves for systems B

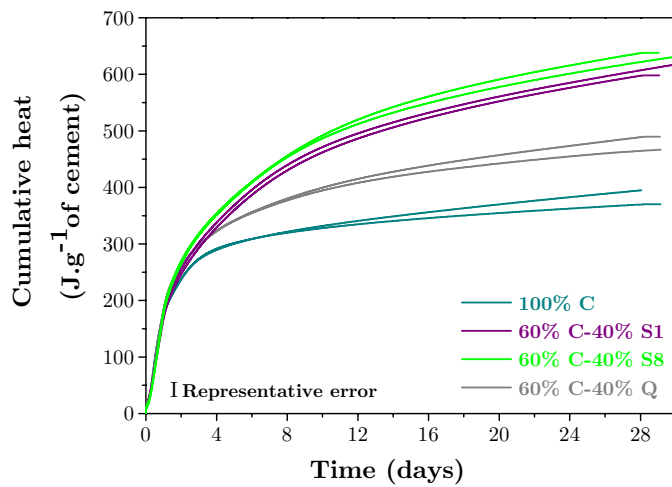


Figure V-25: normalised cumulative heat curves for systems C

Heat evolution profile of quartz is characteristically between that of cement and that of the blended systems. It was assumed that the filler was chemically inert and induced similar physical effect on the slags influencing the hydration of the clinker phases:

- At early age, the filler provides surface for the hydrates to nucleate and grow.
- In addition, there is an increased space for the hydrated phases to form, due to the dilution effect.

An enhancement of cement hydration compared to a pure system results from both phenomena. However, these results contradicted the first observations that we made in Chapter IV concerning the rate of alite consumption that this did not seem to be significantly affected by the slag (as filler). At present, the reasons for these discrepancies are not clear.

Because no reaction of quartz was observed in the SEM and it was assumed that its physical effect is similar to a system with both quartz and slag. The comparison of these two systems gives an indication of the chemical role of the slag and thus their reactivity.

By subtracting each cumulative heat curve of blended paste by the one of cement blended with quartz, the difference obtained can be attributed to the slag contribution (see illustration in Figure V-26).

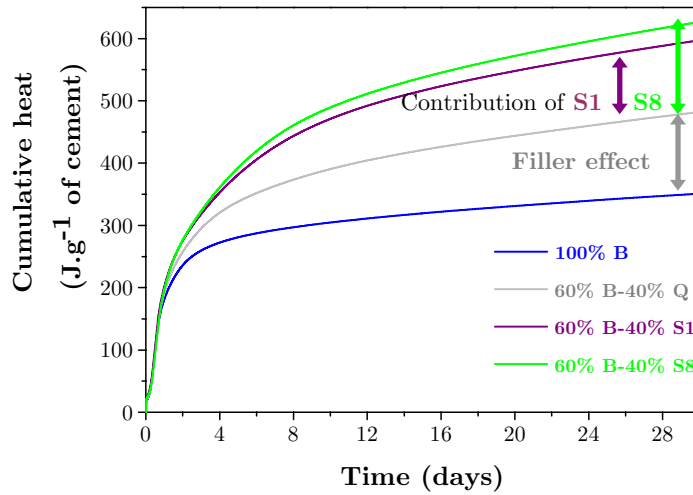


Figure V-26: illustration to isolate the contribution of slag from cumulative heat curves of blended and quartz pastes

In order to do this subtraction, curves had to be normalised by the amount of anhydrous material (cement + slag). After the subtraction, curves were normalized again by the amount of slag to present values in Joules per gram of slag (see illustration in Figure V-27):

$$(\text{Heat}_{\text{Blended slag}} - \text{Heat}_{\text{Blended quartz}}) [\text{J.g}^{-1} \text{ of anhydrous}] \times \frac{100\text{g of anhydrous}}{40\text{g of slag}} \longrightarrow \text{Heat}_{\text{slag}} [\text{J.g}^{-1} \text{ of slag}]$$

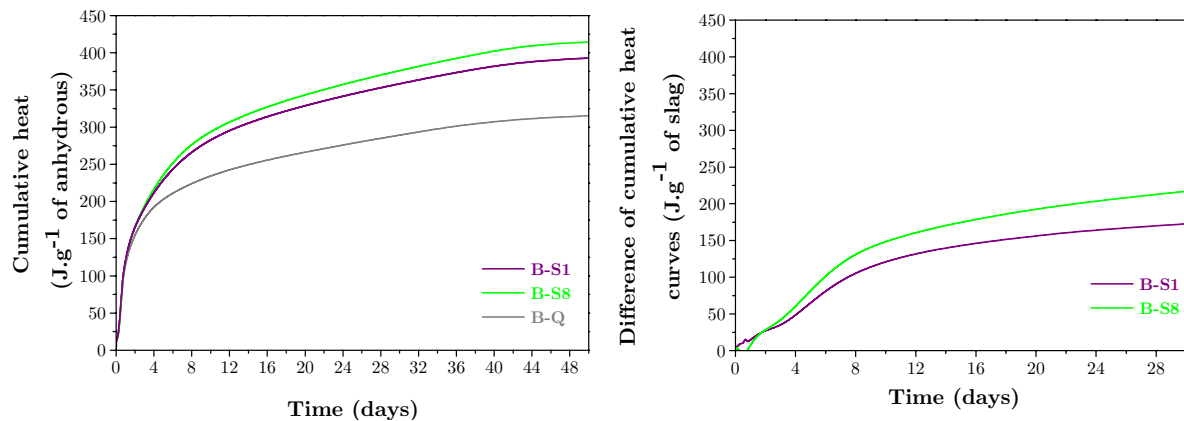


Figure V-27: cumulative heat per g of anhydrous and resulting difference curves which isolate the slag contribution

Calibration

In order to correlate the cumulative curves with degree of reaction of slag, a conversion factor needs to be established. To this end, different approaches were tried to estimate the enthalpy of slag hydration:

- A value from literature was initially used [180] (460 J.g^{-1} of slag) but it was found later that this value was based on adiabatic temperature measurements and was not measured in the regime where slag reacts.
- Some old papers suggested [181,182] to use the solubilities of hydroxides which form hydrates of slag to calculate the enthalpy of slag. This approach takes into account the composition of the slag and led to the following values: 1170 J.g^{-1} of slag and 1183 J.g^{-1} of slag respectively for Slag 1 and 8.
- From the experimental point of view, the heats of solution from both raw slag and slag burnt under different atmospheres allowed to calculate the enthalpy of slag. The procedure was adopted from EN 196-8, the European standard for heat of solution. The substance is dissolved in a mixture of nitric and hydro fluoric acid in a calibrated calorimeter. The temperature change is measured and the heat of solution is calculated from the increase of temperature.

	Slag 1	Slag 8
Heat of solution from raw slag (J/g)	2642	2644
Heat of solution from slag burnt under air (J/g)	2361	2212
Enthalpy of slag burnt under air (J/g)	281	432
Heat of solution from slag burnt under argon (J/g)	2417	2261
Enthalpy of slag burnt under argon (J/g)	225	383

Table V-4: enthalpy of slag under different atmospheres

When this difference is compared to the degree of reaction of slag from image analysis, it gives an indication of the behaviour of the slag itself.

As shown in the following figures (Figures V-28 to V-30), an independent calibration of each cumulative heat curve was made using degree of reaction of slag from SEM-IA-mapping.

Rather than fitting curves, we chose to use the 28 days values as reference for the calibration because we concluded that some discrepancies could be expected at early ages.

A calibration factor was established using the 28 days as the reference value (see Table V-5). At the minute, we did not have enough data to conclude if this calibration factor varies with time.

It could be noted that the calibration factor is a bit higher for systems B-S1.

	Degree of reaction of slag from SEM-IA-mapping (%)	Cumulative heat (J.g ⁻¹ of slag)	Calibration factor (J.g ⁻¹ of slag)
A-S1 at 28 days	40.0	182	4.56
A-S8 at 28 days	55.4	237	4.28
B-S1 at 28 days	32.6	170	5.21
B-S8 at 28 days	50.8	213	4.19
C-S1 at 28 days	36.0	165	4.58
C-S8 at 28 days	55.2	223	4.04

Table V-5: calibration factors to correlate cumulative heat and degree of reaction of slag

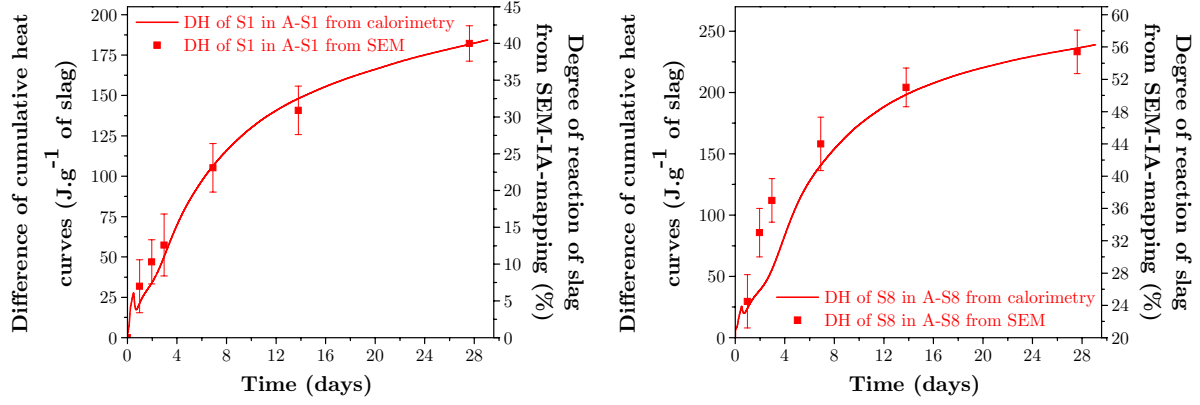


Figure V-28: calorimetry curves calibrated with SEM-IA-mapping in systems A

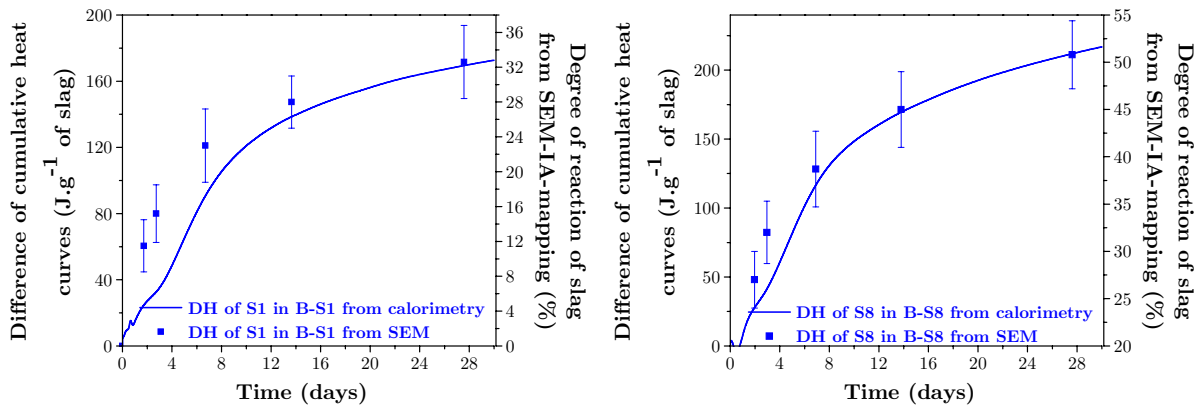


Figure V-29: calorimetry curves calibrated with SEM-IA-mapping in systems B

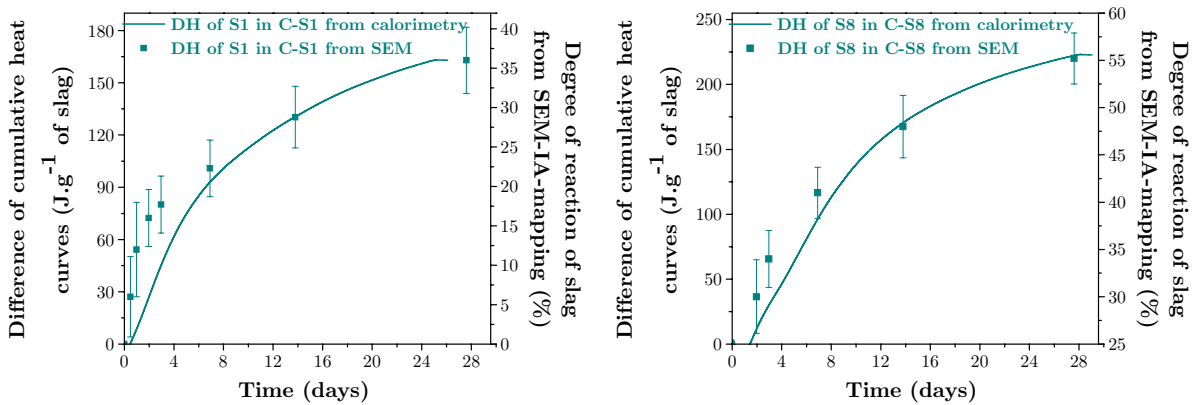


Figure V-30: calorimetry curves calibrated with SEM-IA-mapping in systems C

V.6. CHEMICAL SHRINKAGE

For chemical shrinkage, an approach identical to that described for calorimetry was used. For each given system, the curve of filler was subtracted from the blended one to isolate the contribution of the slag.

Figures V-31 to V-33 show a good repeatability between two different batches. Here again, the curves indicate the higher reactivity of Slag 8 compared to Slag 1 in all blended pastes.

Calibration with degree of reaction of slag from SEM

As shown in the part about a calorimetry, an independent calibration of each chemical shrinkage curve was made using degree of reaction of slag from SEM-IA-mapping (see Figures V-34 to V-36).

A calibration factor was established using the 28 days as the reference value (see Table V-6). As previously found for calorimetry, the calibration factor is a bit higher for systems B-S1.

	Degree of reaction of slag from SEM-IA-mapping (%)	Chemical shrinkage (mL.g ⁻¹ of slag)	Calibration factor (mL.g ⁻¹ of slag)
A-S1 at 28 days	40.0	0.128	3.2E-03
A-S8 at 28 days	55.4	0.163	2.9E-03
B-S1 at 28 days	32.6	0.154	4.7E-03
B-S8 at 28 days	50.8	0.018	3.5E-04
C-S1 at 28 days	36.0	0.013	3.6E-04
C-S8 at 28 days	55.2	0.206	3.7E-03

Table V-6: calibration factors to correlate chemical shrinkage and degree of reaction of slag

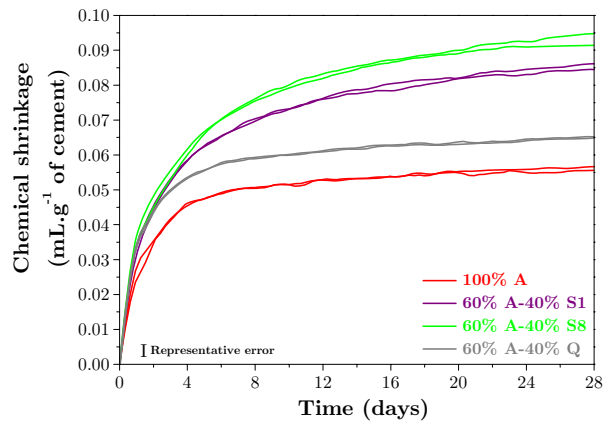


Figure V-31: evolution of chemical shrinkage for systems A

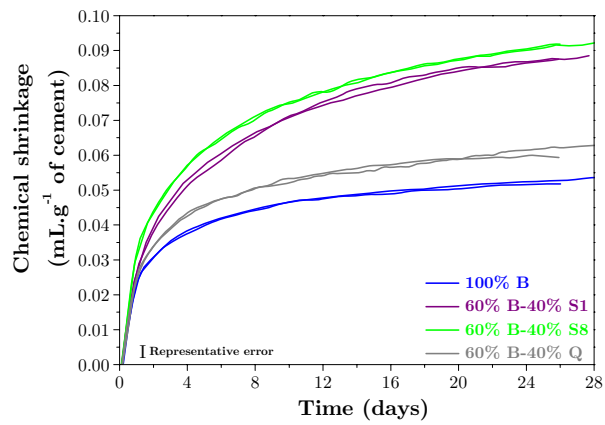


Figure V-32: evolution of chemical shrinkage for systems B

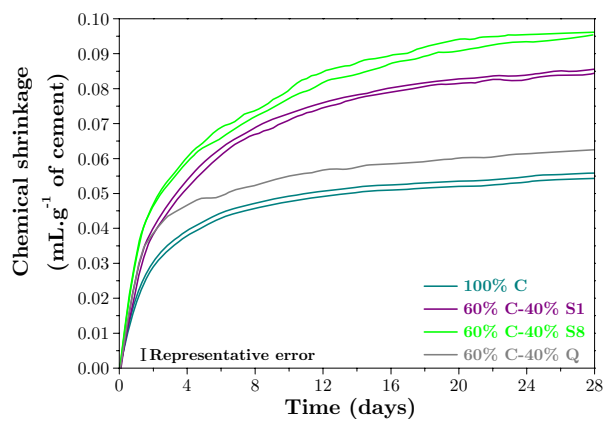


Figure V-33: evolution of chemical shrinkage for systems C

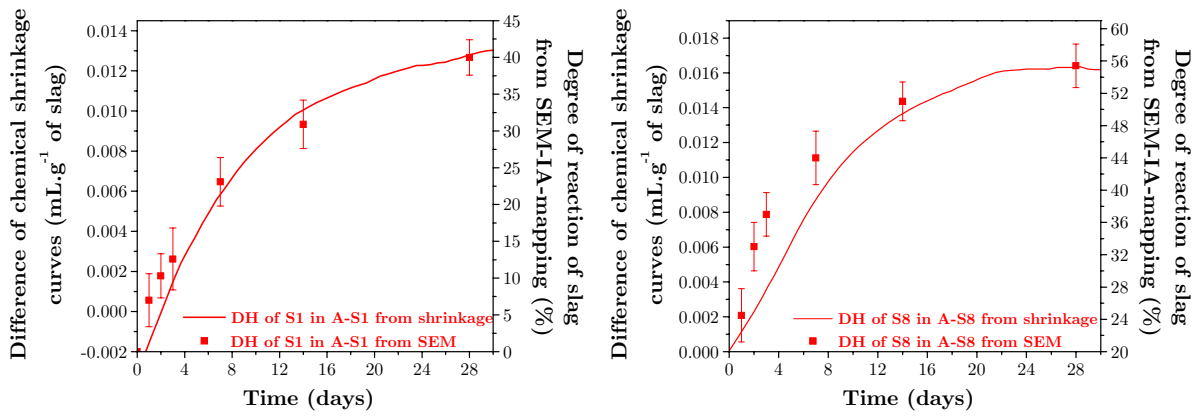


Figure V-34: chemical shrinkage calibrated SEM-IA-mapping for systems A

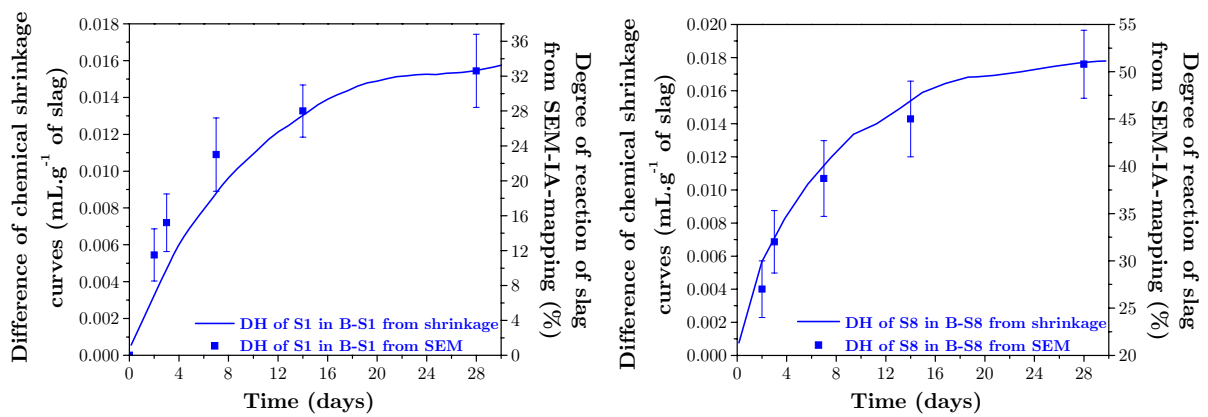


Figure V-35: chemical shrinkage calibrated SEM-IA-mapping for systems B

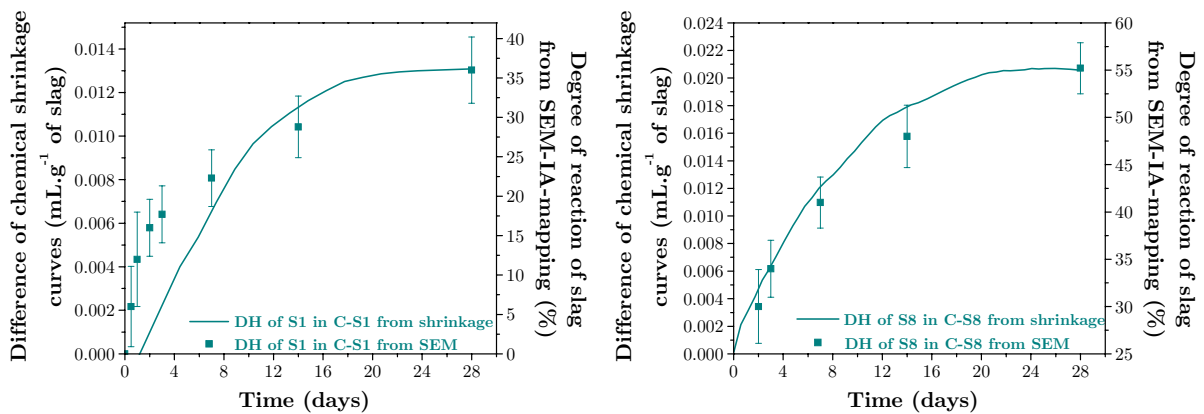


Figure V-36: chemical shrinkage calibrated SEM-IA-mapping for systems C

V.7. COMPARISON OF CALORIMETRY AND CHEMICAL SHRINKAGE RESULTS

The plot of calorimetry versus chemical shrinkage results shows a linear relation for pure and blended pastes (as illustrated in Figures V-37 to V-39). This is an indication to the measurement of the same overall reaction from both techniques.

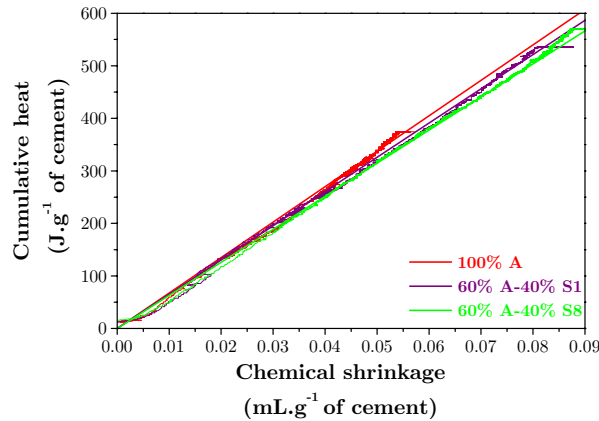


Figure V-37: calorimetry versus chemical shrinkage results for systems A

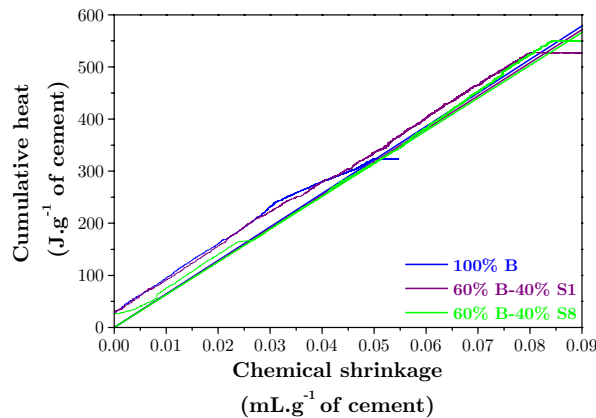


Figure V-38: calorimetry versus chemical shrinkage results for systems B

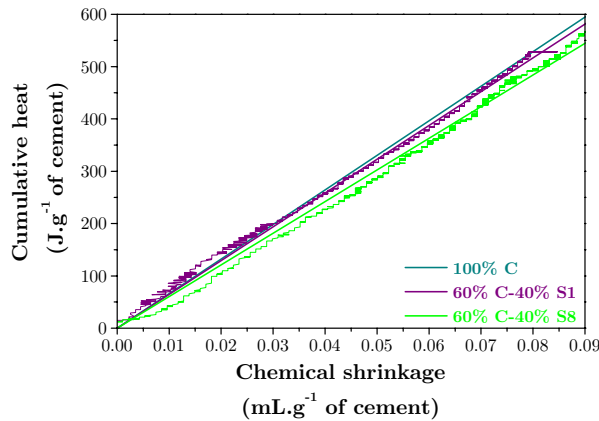


Figure V-39: calorimetry versus chemical shrinkage results for systems C

V.8. CONCLUSIONS AND DISCUSSION ON METHODS TO MEASURE THE DEGREE OF REACTION OF SLAG

For hydrated blended systems, a number of methods were tested to determine the amount of remaining slag and, thereby, the degree of hydration of slag in blended cements. It was found that two of these selective methods, dissolution and thermal analysis, are unsuitable.

- The idea of selective dissolution is to dissolve all unreacted cement and hydration products leaving the remaining slag. However, the study of the residues by XRD and SEM indicated that the selectivity of the dissolution procedure is far from that expected, because of the presence of both anhydrous cement and hydrated phases. The errors introduced by the remaining undissolved phases make it impossible to determine the degree of slag reaction with any degree of precision.
- By thermal method, the heat of recrystallization of the slag's glass content cannot be isolated because of the overlap with the crystallisation of belite in the same range of temperatures.

As selective dissolution and DSC were shown to be unreliable, other experimental methods were assessed to quantify the degree of reaction of the slag. For these three methods the results were relatively better than that obtained from selective dissolution and DSC.

- Backscattered electron image analysis coupled with Mg mapping gave results close to what we observed experimentally for the hydration of slag. However, this technique is time consuming, considering the sampling time and the time for image acquisition itself (around 12 hours per sample). The prerequisite is a well polished sample, which takes at least 5 hours and due to the differential hardness of the slag it is particularly difficult to obtain good sample preparation at young ages (up to 1 day). The image acquisition itself is now well automated in our laboratory and 150 images and Mg maps can be acquired in 10 hours overnight. In addition, the image

processing steps will mean that very small particles are not well measured, which increases the error at young ages. At late ages only large particles remained.

- It is shown that isothermal calorimetry, if performed in a well calibrated and stable instrument is a potentially powerful method to measure degree of slag reaction. The technique provides continuous and precise set of values. A good experimental calibration was established but it needs to be recalibrated for each system separately. The figures showed the contribution of combined filler effect and the individual reactivity of two slags (it is assumed the filler effect can be represented by the effect of ground quartz).

- Combination of SEM-IA-mapping and calorimetry provides a calibration for slag content in hydrated systems.

- Combination of SEM-IA-mapping and chemical shrinkage provides an alternate calibration method.

The following table (Table V-7) summarises the main parameters in different methods.

Method	Type of measurement	Time of acquisition per sample	Time to treat the results	Comments
Selective dissolution	Discrete	20 minutes	5 minutes	Remaining undissolved phases which induced large errors on the degree of reaction of slag
DSC	Discrete	2 hours	20 minutes	Overlap between peak of belite and the one of slag which does not allow to isolate the slag contribution
SEM-Image analysis-mapping	Discrete	10 hours	1 hour	Good accuracy but time consuming
Calorimetry	Continuous		1 hour	Needs to be calibrated with an external method
Chemical shrinkage	Continuous		1 hour	Needs to be calibrated with an external method

Table V-7: comparison between different methods used to calculate the degree of reaction of slag

The validity of our quantification of slag reaction was verified using comparison with results from ^{29}Si NMR given by Poulsen [22].

The following figures (Figures V-40 and V-41) show that the results from ^{29}Si NMR are a bit lower than the ones from SEM-IA-mapping. However, for A-S8, there was a good agreement with SEM-IA-mapping results.

At present the errors for the ^{29}Si NMR method are not well established. However, the ^{29}Si NMR results also showed that the Slag 8 was more reactive than Slag 1.

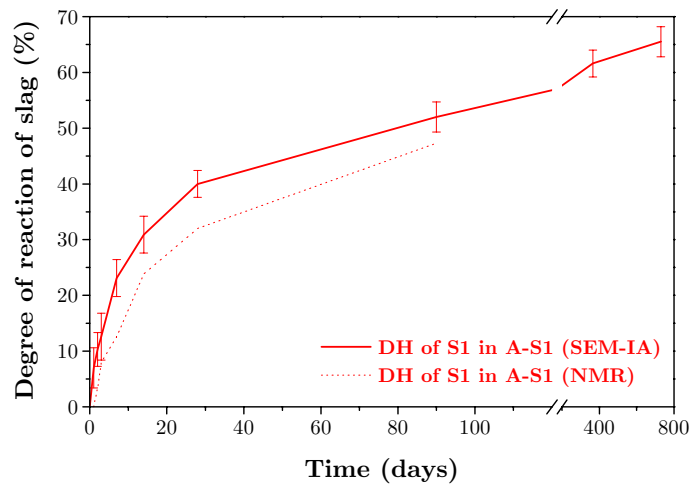


Figure V-40: comparison of degree of reaction of Slag 1 from ^{29}Si NMR and SEM-IA

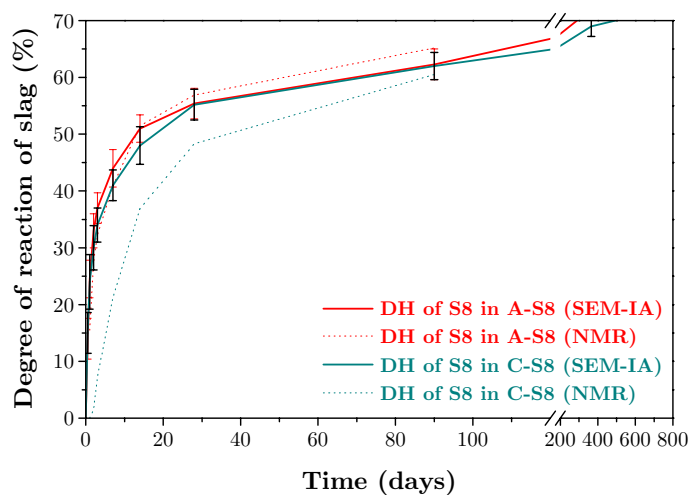


Figure V-41: comparison of degree of reaction of Slag 8 from ^{29}Si NMR and SEM-IA

Study shows clearly that Slag 8 reacted faster than Slag 1 which we can compare with different reactivity indices. For example, Figure V-42 plots $M1 = \text{CaO}/\text{SiO}_2$ and $M5 = (\text{CaO} + \text{MgO} + \text{Al}_2\text{O}_3)/\text{SiO}_2$ against degree of reaction of slag from SEM. However, no further conclusions can be made for the comparison of only two slag samples.

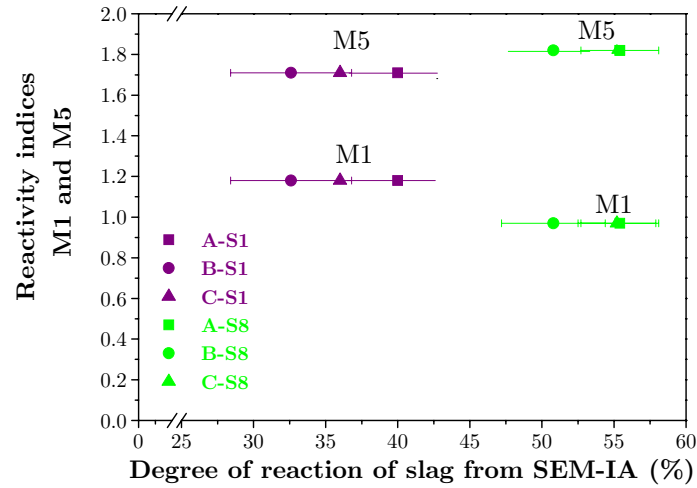


Figure V-42: reactivity indices M1 and M5 versus degree of reaction of slag from SEM-IA

CHAPTER VI: MECHANICAL PROPERTIES OF BLENDED SYSTEMS

Compressive strength is generally used as a reference for assessing the overall quality of construction materials. In this chapter, the changes in mechanical properties induced due to the substitution of cement by slag are presented for mortars. In addition, the correlation of strength with other properties such as porosity, degree of reaction of cement and slag and overall degree of reaction are studied.

VI.1. STATE OF THE ART

Many studies [62,89,150,156,183-190] have described the development of compressive strength in blended pastes. Most of these studies show that at later ages, up to a certain amount, slag improves the mechanical strength of the blends compared to plain Portland cement.

For example in Figure VI-1 from Hogan and Meusel [184], the blended mortar was stronger than OPC one at 28 days. However, the change in compressive strength with blending agent depends on the age and on dosage. As shown in Figure VI-1, at higher dosages the strengths are only equal to the control at 28 days.

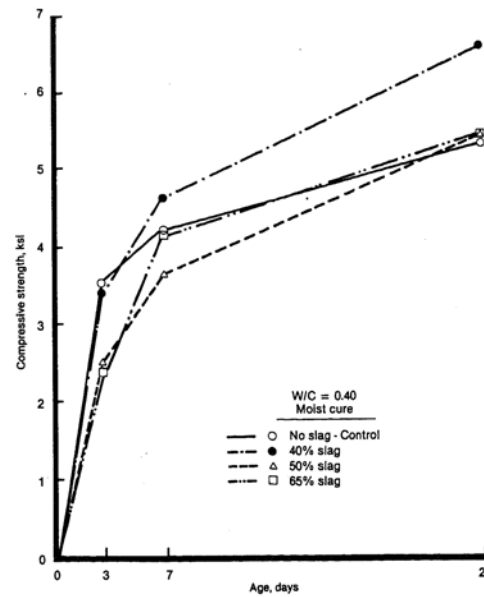


Figure VI-1: compressive strength evolution for air-entrained concrete [184]

Compressive strength is an indirect macroscopic parameter to evaluate the impact of slag and gives no direct information about the extent of its reaction.

Due to the difficulties in measuring the degree of reaction of slag, only limited literature is available that relates strength development to the reaction of the slag.

VI.2. EXPERIMENTAL PROCEDURE

Mortar samples of the plain cements were included as reference for each type of cement. As shown in Table VI-1, different batches were made:

- At the beginning of the project, a first batch of mortars was measured at 1, 3, 7 and 28 days of hydration;
- Two years later, a second batch was measured at 1, 7 and 28 days of hydration.

All the samples were redone in order to take into account possible ageing effect.

As for the study of pastes, quartz was used as a filler to separate the physical effect of the slag. Mortars with 40% quartz and 60% cement were studied at 1, 7 and 28 days.

As for the preparation of pastes, 60 wt% of cement and 40 wt% of substitution (slag or quartz) were premixed in a TURBULA shaker-mixer before the addition of sand to ensure a good initial homogenisation of the mixture.

Except for mortars blended with quartz, two different batches of mortars were done at two years interval (the effect of ageing is discussed in the following section).

All the mortars studied are summarised in the following table (Table VI-1).

Label of mortar samples	1 day	3 days	7 days	28 days
100%A (1 st batch)	X	X	X	X
100%A (2 nd batch)	X	-	X	X
100%B (1 st batch)	X	X	X	X
100%B (2 nd batch)	X	-	X	X
100%C (1 st batch)	X	X	X	X
100%C (2 nd batch)	X	-	X	X
60%A-40%Q	X	-	X	X
60%B-40%Q	X	-	X	X
60%C-40%Q	X	-	X	X
60%A-40%S1 (1 st batch)	X	X	X	X
60%A-40%S1 (2 nd batch)	X	-	X	X
60%B-40%S1 (1 st batch)	X	X	X	X
60%B-40%S1 (2 nd batch)	X	-	X	X
60%C-40%S1 (1 st batch)	X	X	X	X
60%C-40%S1 (2 nd batch)	X	-	X	X
60%A-40%S8 (1 st batch)	X	X	X	X
60%A-40%S8 (2 nd batch)	X	-	X	X
60%B-40%S8 (1 st batch)	X	X	X	X
60%B-40%S8 (2 nd batch)	X	-	X	X
60%C-40%S8 (1 st batch)	X	X	X	X
60%C-40%S8 (2 nd batch)	X	-	X	X

Table VI-1: list of mortars studied

The mortars were formulated and mixed following the protocol from the European norm EN 196-1. Each batch consisted of 1350 g of standardised sand, 450 g of binder and 225 g of water and allowed the casting of three 40 x 40 x 160 mm mortar bars.

The water to binder ratio of mortar was set to 0.5, which provides similar workability and hydration conditions as a paste with water to binder ratio of 0.4. In mortars, extra water is incorporated in the interfacial transition zone (ITZ) where there is less cement due to packing effects and, hence, unavailable for hydration [191].

The moulds were kept at relative humidity for 24 hours. Then, the mortar prisms were demoulded and submerged in a water bath at 20°C until the day of testing.

VI.2.1. RESULTS OF COMPRESSIVE STRENGTH

For all the mechanical tests, the results correspond to an average value from six different measurements (two per prism) and the corresponding standard deviation.

Flexural strengths were also measured but they were not included nor discussed here as they generally correlated to the compressive strength.

VI.2.1.a. Effect of ageing

Figures VI-2 to VI-4 show the evolution of compressive strength for the different batches of pure and blended mortars.

Special attention should be given to the 3 day-compressive strengths from the first batch because this value was not measured for the second batch.

While the effect of ageing seemed to affect significantly the compressive strength of neither the plain mortars nor mortars blended with Slag 8, it clearly reduced the strengths of mortars blended with Slag 1. This suggests that the Slag 1 (the less reactive and less alkali slag) was more sensitive to ageing effect compared to Slag 8 blends and reference cements. As final results, to avoid this ageing effect, all the compressive strength tests were redone on the reference mortars and blended mortars. In addition, the mortars with quartz were added to the initial selection.

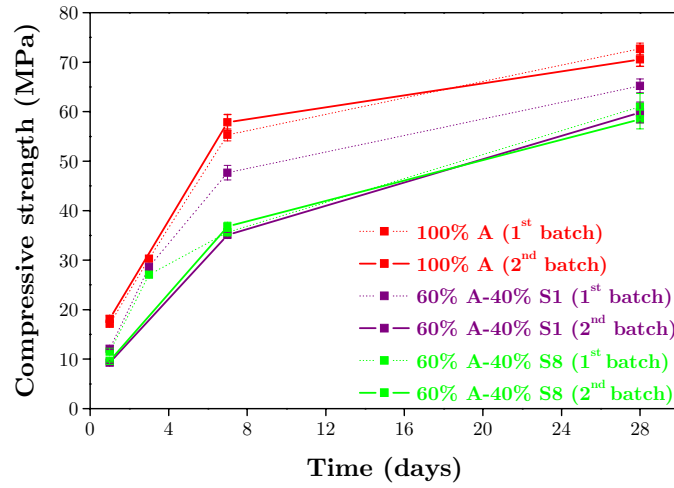


Figure VI-2: evolution of compressive strengths of all mortars with Cement A

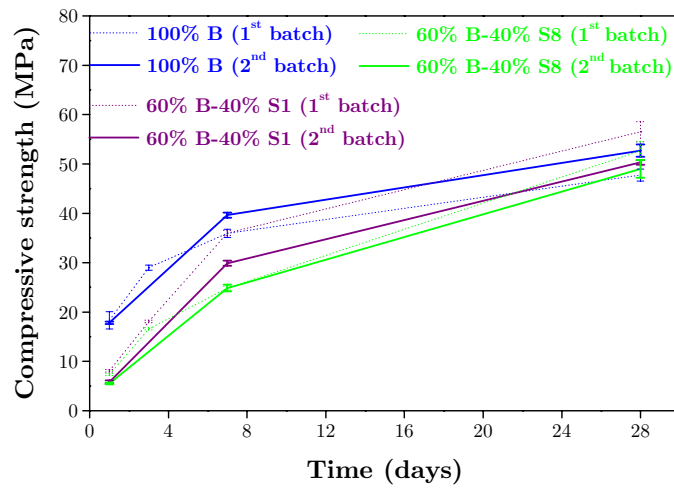


Figure VI-3: evolution of compressive strengths of all mortars with Cement B

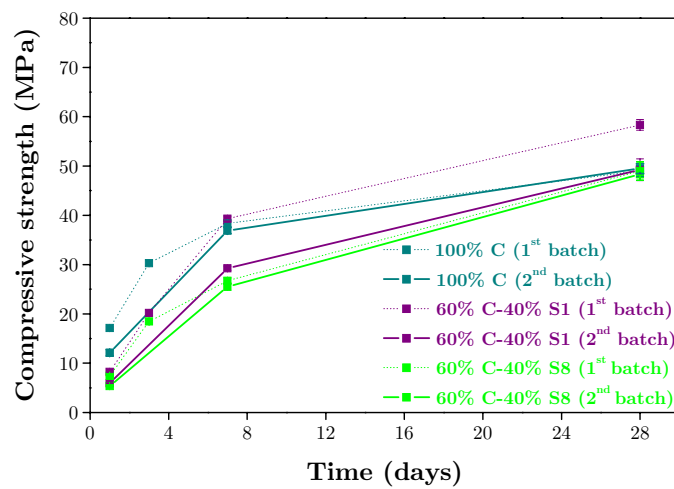


Figure VI-4: evolution of compressive strengths of all mortars with Cement C

VI.2.1.b. Effect of cement

Compressive strength is plotted as a function of time in Figures VI-5 to VI-7.

First, it can be noticed that pure mortars composed of 100%A have comprehensively higher strength up to 28 days compared to the 100%B and 100%C mortars. A difference of 20 MPa was observed even after 7 days of hydration. In addition, the blended mortar composed of 60%A also gave significantly higher strengths compared to mortars with 60%B and 60%C, but the difference was less. These differences can be attributed to the higher fineness of Cement A which leads to more rapid hydration.

For both blended and neat mortars, there was no significant difference between Cement B and Cement C despite having different mineralogies (particularly in terms of alkali contents).

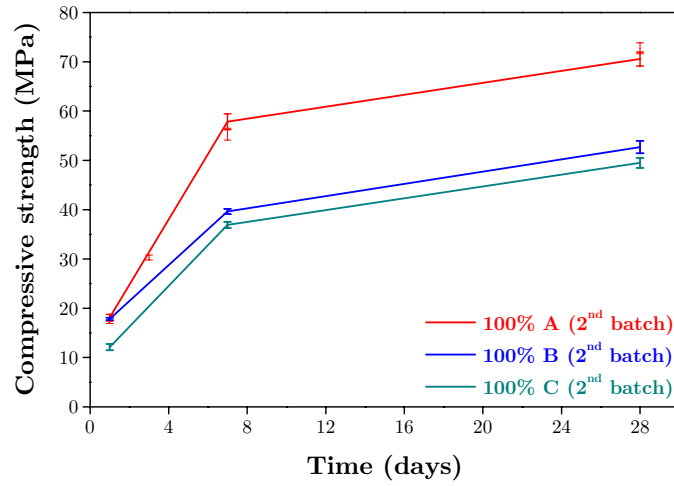


Figure VI-5: evolution of compressive strengths of pure mortars

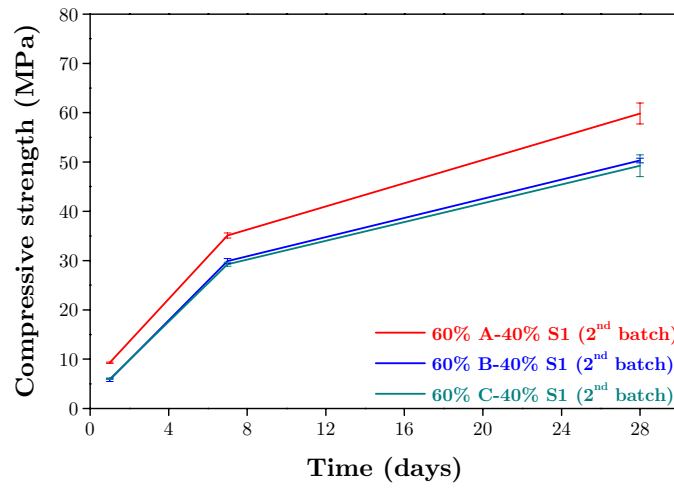


Figure VI-6: evolution of compressive strengths of mortars blended with Slag 1

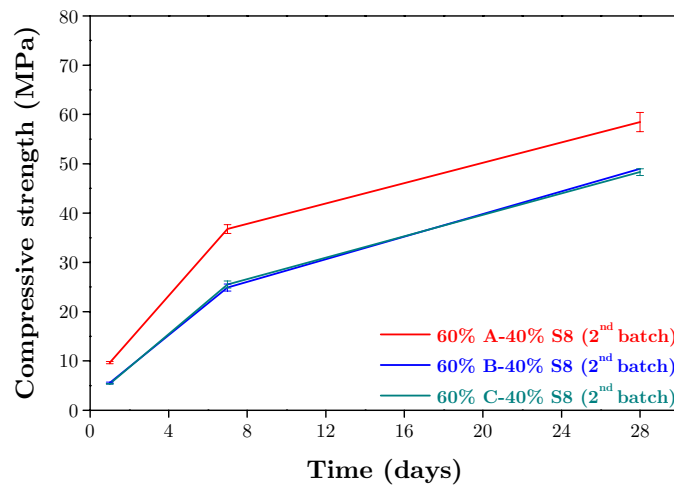


Figure VI-7: evolution of compressive strengths of mortars blended with Slag 8

VI.2.1.c. Effect of slag on each mortar systems

First, it can be noticed that all neat mortars developed the highest strength until 28 days. However, by 28 days, the strengths of the slag mortars approach those of the reference mortars. This can be explained by the difference of reaction kinetics between slag and cement. Figures VI-8 to VI-10 indicate that compared to the substitution by inert quartz, the contribution of slag was already significant at 7 days.

As shown in Chapters III and IV, the study of hydration degree shows that C_3S is virtually completely hydrated for 28 days whereas the degree of reaction of the slag continues to increase beyond 28 days. Therefore the strengths of the blended mortars are expected to increase more strongly than those of the plain mortars beyond 28 days.

Despite the clear difference in reactivity of the slags seen previously (Slag 8 more reactive than Slag 1) there appears to be little difference between them in terms of strength development. Indeed, at 7 days, the strength of the Slag 1 blends appears to be marginally higher than the Slag 8 blends.

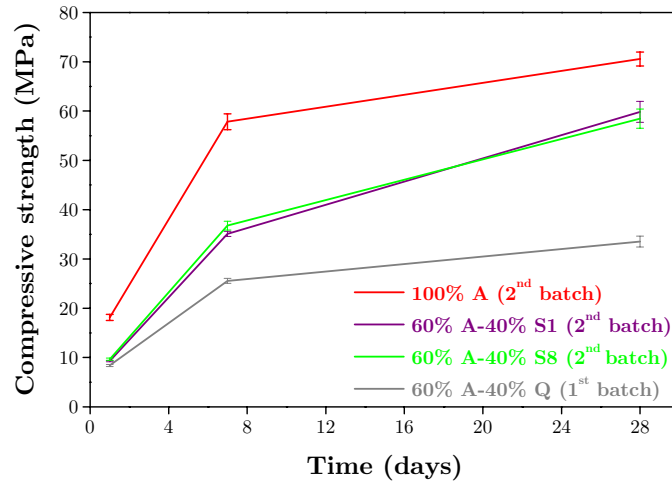


Figure VI-8: evolution of compressive strengths of selected mortars with Cement A

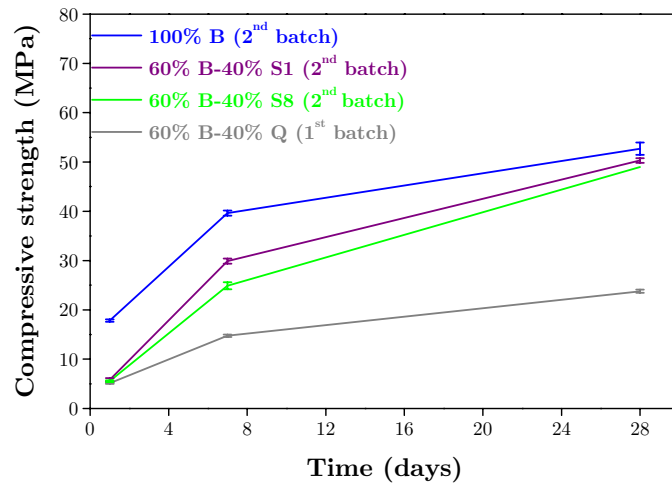


Figure VI-9: evolution of compressive strengths of selected mortars with Cement B

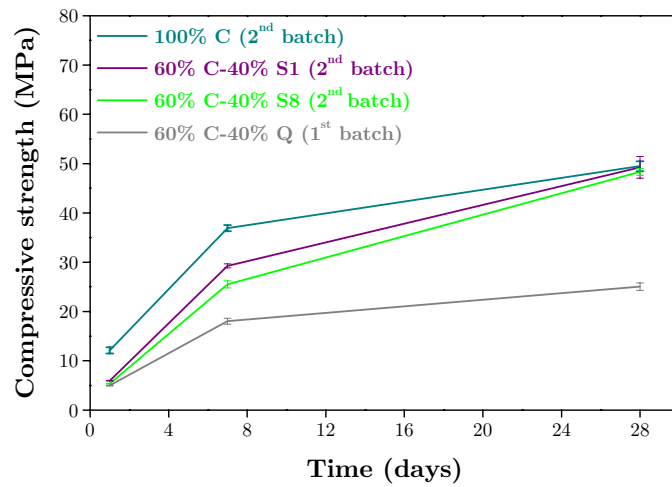


Figure VI-10: evolution of compressive strengths of selected mortars with Cement C

VI.2.2. COMPRESSIVE STRENGTH VERSUS REACTIVITY

In order to study the impact of the reactivity of cement on the mechanical properties, the compressive strengths of all mortars were plotted as a function of degree of reaction of cement from SEM-IA and XRD-Rietveld refinement which came from the measurements on equivalent pastes (see Figures VI-11 to VI-13). The errors on the degree of reaction of cement have been explained in Chapter III.

A linear relation can be established between strength and reactivity of cement for pure systems but not for blended ones. The lines for the blended pastes tend upwards at 7 and 28 days indicating that slag contributes to the strength. As it was established in the previous chapters, cement reacts almost 70% at 7 days whereas the slag just begins to react at that point (around 30% for Slag 8 and 20% for Slag 1).

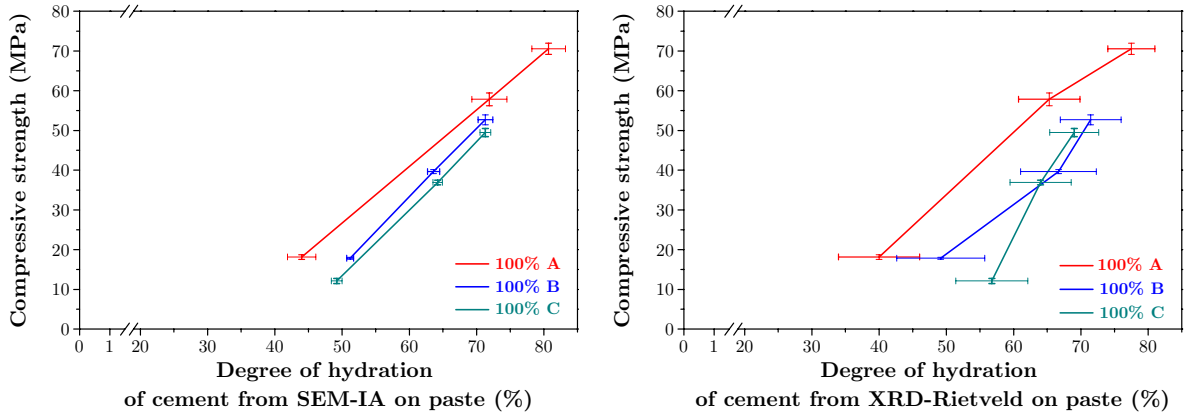


Figure VI-11: degree of hydration of cement from SEM-IA and XRD-Rietveld for 3 mortars containing 100% cement

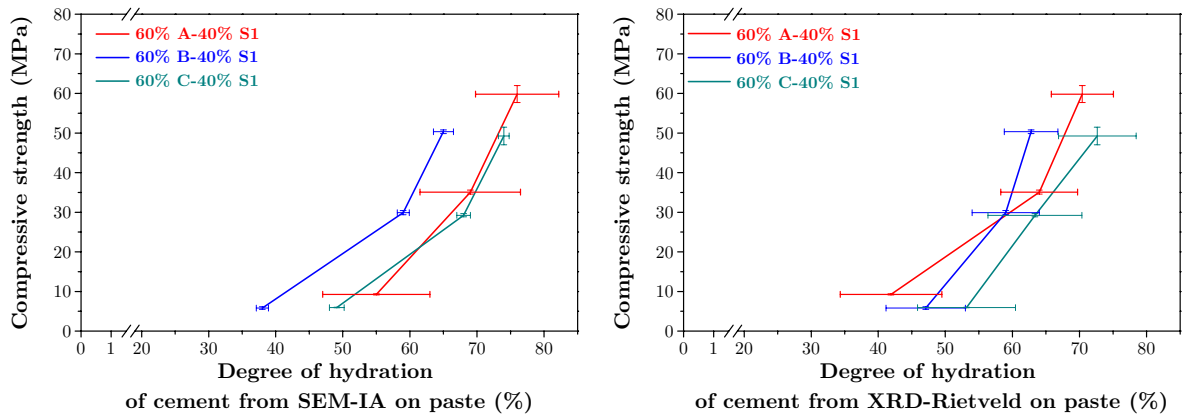


Figure VI-12: degree of hydration of cement from SEM-IA and XRD-Rietveld for 3 mortars containing 60% cement-40% Slag 1

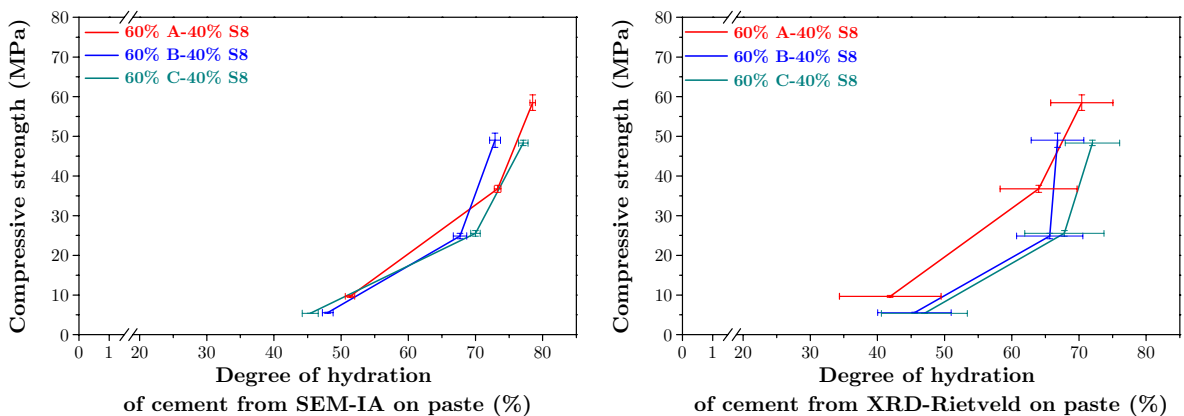


Figure VI-13: degree of hydration of cement from SEM-IA and XRD-Rietveld for 3 mortars containing 60% cement-40% Slag 8

A subtraction was made between the compressive strengths of slag and the ones of quartz for each given age because it makes more sense to compare the strength relative to the content of additional materials to the corresponding degree of slag reaction. So in Figure VI-14, the resulting differences of compressive strengths were plotted against degree of reaction of slag. It appeared that even if the compressive strength of blended mortars were not significantly different for a given age, the contribution of both slags were clearly different and did not seem to be significantly affected by the contribution of the cement. For same range of strengths, it appeared two different groups: in one hand for compressive strength with Slag 1 and on the other hand the one with Slag 8.

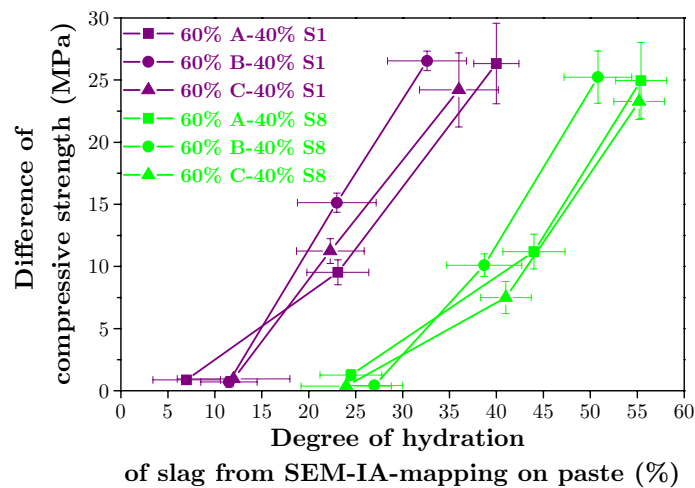


Figure VI-14: difference of compressive strength versus degree of hydration of slag from SEM-IA-mapping for 6 blended mortars

In order to take into account both contributions of cement and slag, overall degree of reaction in system was calculated as detailed in the following formula:

$$\alpha_{\text{OVERALL REACTION}}(t) = \frac{\%_{\text{cement}}(t=0) - \%_{\text{cement}}(t) + \%_{\text{slag}}(t=0) - \%_{\text{slag}}(t)}{\%_{\text{cement}}(t=0) + \%_{\text{slag}}(t=0)} \quad \text{Equation 36}$$

Where:

$\%_{\text{cement}}(t=0)$: percentage of the original cement;

$\%_{\text{cement}}(t)$: percentage of the remaining anhydrous cement from SEM-IA measurement;

$\%_{\text{slag}}(t=0)$: percentage of the original slag;

$\%_{\text{slag}}(t)$: percentage of the remaining anhydrous slag from SEM-IA-mapping measurement.

Figure VI-15 established the relation between compressive strength and overall degree of reaction in blended mortars (for pure mortars, the degree of reaction of cement is represented). It appeared that for a given strength, the overall degree of reaction was not significantly affected by the type of cement but was dependant on the slag used. Here again, for equivalent strength, Slag 8 contributed more than Slag 1 to hydration of mortars.

Except for strength of mortar A at 1 day, the benefit of pure cement was higher than the one of blends.

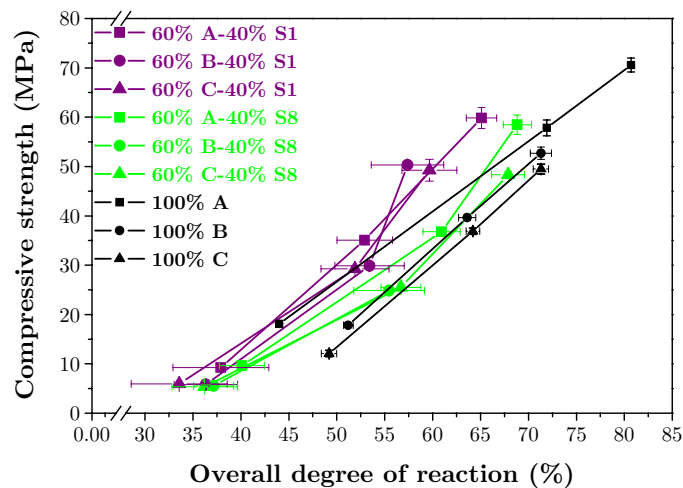


Figure VI-15: compressive strength versus overall degree of reaction in blended systems

VI.2.3. POROSITY AND COMPRESSIVE STRENGTH

As shown by the scheme in Chapter IV, considering the initial oxides present in slag, the main phases present in a hydrated blended paste are C-S-H, $\text{Ca}(\text{OH})_2$, sulfoaluminate phases AFt, AFm and hydrotalcite like phase.

To estimate the stoichiometry of slag hydration in blended paste, the calculation was similar to the one suggested by Taylor [5] with actual experimental input and not assumptions. The calculations were done using the steps outlined below:

- The hydrotalcite like phase contained all the Mg from the slag that had reacted. The measured Mg/Al ratio of hydrotalcite like phase is used from EDS measurements and the reaction of slag is taken into account the degree of slag reaction from SEM-IA-mapping measurements;

- all the Si from alite and belite (which composition come from XRD-Rietveld analysis) enters the C-S-H;

- using the above two steps, CH is deduced;

- slag SiO_2 (S) and Al_2O_3 (A) enter a C-S-H phase called $\text{C}_x\text{SH}_y\text{A}_z$ phase for which x and z are measured by EDS analysis and y is initially chosen;

- Ca, Al and S from ettringite calculated by XRD are removed;

- the remaining Al enters an AFm phase for which oxide composition is given by EDS measurements;

- the amount of CaO released from the slag is observed to be insufficient to account for that in the C-S-H and AFm phases. The deficiency is made by decreases in the content of CH formed from the Portland cement.

From the calculated content and knowledge of the density of the various phases (the density of C-S-H was chosen equal to 2242 kg.m⁻³ [192]) the total porosity can be calculated as followed:

$$\%_{\text{TOTAL POROSITY}}(t) = 1 - \frac{\sum \text{Dried volume of phases (t)}}{V_{\text{binder}}(t = 0) + V_{\text{water}}(t = 0)} \quad \text{Equation 37}$$

It is well know than the porosity is a major factor in controlling strength of cementitious systems.

Figures VI-16 to VI-18 show the evolution of calculated total porosity and the corresponding relation with compressive strength for the different systems. It is clear from the graphs that the reaction of the slag makes a contribution to strength beyond just the reduction in total porosity from its hydrates.

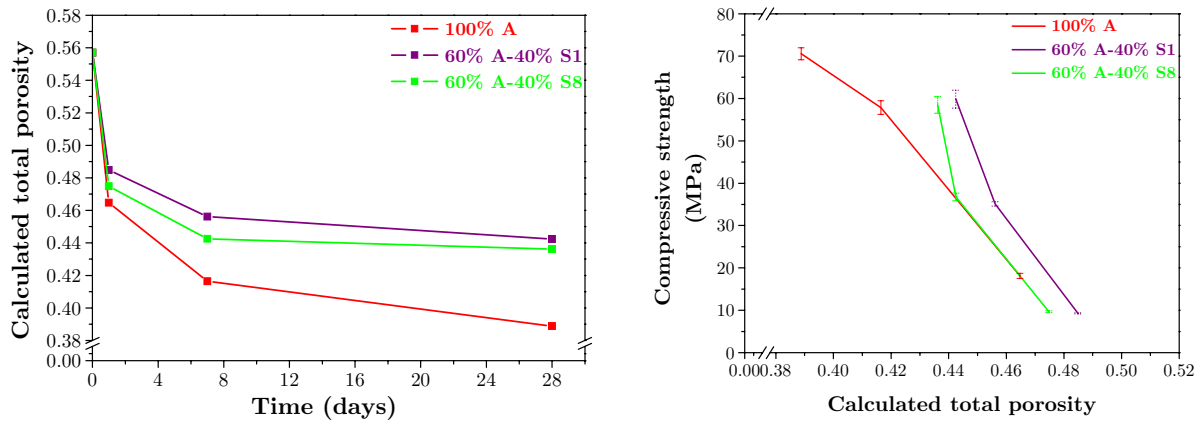


Figure VI-16: evolution of calculated total porosity and corresponding relation with compressive strength for systems A

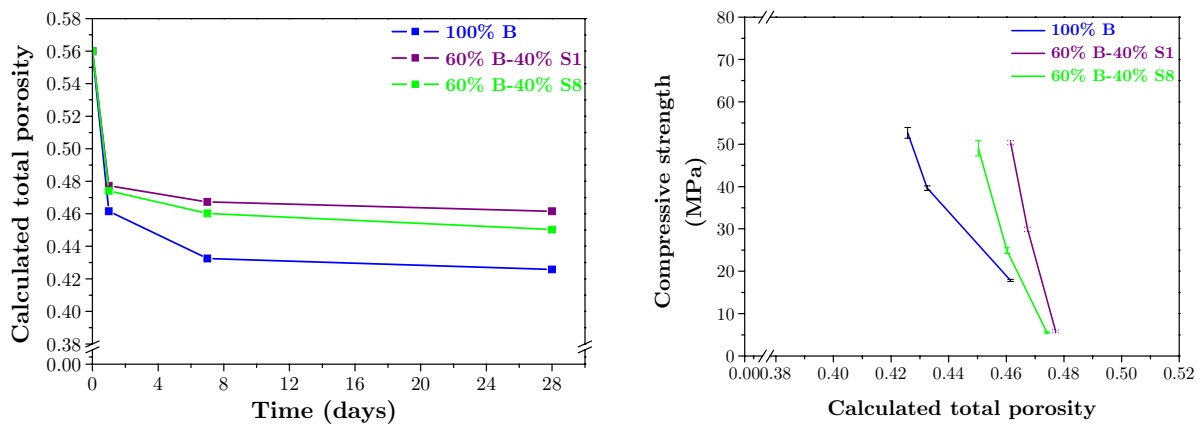


Figure VI-17: evolution of calculated total porosity and corresponding relation with compressive strength for systems B

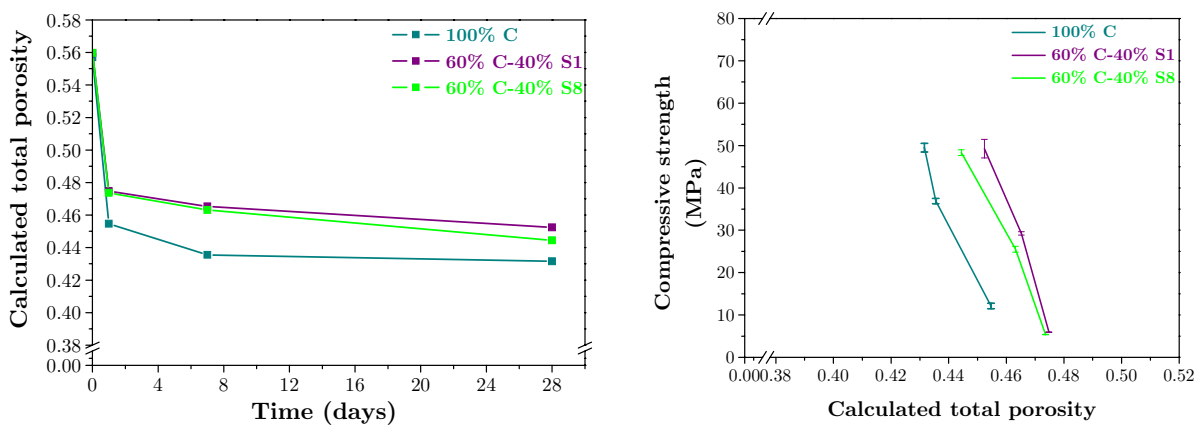


Figure VI-18: evolution of calculated total porosity and corresponding relation with compressive strength for systems C

VI.3. CONCLUSION ON MECHANICAL PROPERTIES

Compressive strength can be considered as an indirect macroscopic parameter to evaluate the impact of slag, but without any direct information regarding its extent of reactivity or influence on hydration of other phases. It should be noted that the reactivity indices (as described in Chapter II) had no relevance towards strength development.

It was established from our investigations that Slag 8 was the most reactive.

At 28 days the strength of the blends are comparable to those of the pure cements.

The contribution of slag started to be significant from 7 days when the strength development of the pure cements starts to level off. At longer ages, it would be expected that the blended cements would show higher strengths. Up to 28 days, there was no significant difference between strength from both slag blends despite the higher degree of reaction of Slag 8.

The compressive strengths of systems with Cement A were clearly influenced by the higher fineness of the cement itself. However, the different mineralogies of three cements appeared to have little impact on the strength at the same degree of hydration of cement.

Parameters such as overall degree of reaction and calculated total porosity clearly established that the impact of the slag on strength development is greater than what it would be expected just from the filling of space by the hydrates. The blended pastes have a higher calculated porosity at all ages. This poses important question regarding the impact of microstructural arrangement on the development of mechanical properties.

CHAPTER VII: DISCUSSION, CONCLUSIONS AND PERSPECTIVES

This work was divided in two main parts. In first part, investigations were done on anhydrous and hydrated materials to evaluate the characterisation methods and their accuracy. In the second part, a study of slags in blended paste was made developing methods to isolate and understand the contribution of slag itself.

VII.1. METHODS

It was clear than even for well established techniques, many details need to be taken into account to optimise the final results.

The **initial work done on anhydrous phases** mainly concentrated on XRD-Rietveld refinement with optimisation of its control files as a function of the different types of cements and slags. For anhydrous cements, the contents of clinker phases were compared with SEM-Point counting, Bogue and modified Bogue calculation. The alite/belite ratio from XRD-Rietveld agreed with SEM-Point counting investigation but there is some disagreement with results from ^{29}Si NMR, which could be related to the presence of some amorphous material on the surface of alite grains.

The oxides composition of the 4 main cements were estimated by reverse Bogue calculation using EDS measurements on clinker phases. The results agreed well with XRF data but all the Bogue techniques are mathematically only approximate, at best, considering that small variations in input data result in large variations in the output.

The improvement on characterisation of anhydrous materials provides the starting point for **the study of hydrated systems**, particularly concerning the XRD-Rietveld refinement and the corresponding control files.

To avoid a bias from sampling effect, one hydrated specimen from same mixing batch was analysed, each using different techniques: XRD, TGA, SEM, isothermal calorimetry and chemical shrinkage.

Independent repeatability tests allowed the limitations of different techniques to be identified and highlighted the interest to combine all the methods together.

So the techniques used in this study have been carefully selected in order to fully characterise the blended systems taking into account the pure systems as reference. No single technique provides all the data required to obtain a clear understanding of these systems. Each piece of data, therefore, contributes to the overall characterisation.

VII.2. STUDY OF SLAG

Using, the understanding of the methods and combining all information together, a special approach was developed to follow the influence of slag and isolate its contribution in blended systems.

Firstly, the **effect of slag on clinker phases** was identified:

- Concerning the aluminate phases, the separation treatment of calorimetry curves confirmed that there was no evidence for slag itself reacting. The “sharpening” of the aluminate peak is a “filler” effect due to the physical presence of slag.
- The presence of slag significantly retarded the hydration of belite and, consequently, the degree of reaction of cement.
- The slags favoured the hydration of the ferrite phase.

Secondly, the **slag modified the composition of hydrates**. The significant change in C/S ratio of the C-S-H between pure and blended paste is enough to account for the difference in overall C/S ratio of the blend, without taking into account the consumption of CH at early age. At longer ages, the C/S ratio continues to decrease slowly, but there is also a small decrease in the amount of portlandite in blended pastes. The decalcification of C-S-H can be explained by C-S-H acting as a source of calcium for slag hydrates.

Many studies have been conducted on the reactivity of slag in blended pastes, but the word “reactivity” is generally used in different contexts without much specification. In addition, there was a lack of good methods to quantify the degree of hydration of the slag. Almost no previous studies have provided proper considerations to precision and errors. Even if SEM-IA-mapping is time consuming, it appeared to be the only accurate method to quantify the degree of reaction of slag.

The computation of difference in cumulative calorimetry and chemical shrinkage curves of slag and its comparison to inert filler (quartz) allowed the reaction of the slag to be isolated. Their calibration using the SEM-IA-mapping results seems to be a promising method to understand and quantify the reactivity of slag. Further work should be done on a thermodynamic approach using the pure enthalpy of slag as a calibration factor for calorimetry and chemical shrinkage results to deduce the degree of reaction of slag.

All our investigations indicated that Slag 8 (high alumina and alkali contents) had a higher reactivity than Slag 1 (high amorphous content). This was in agreement with ^{29}Si NMR results. This difference in reactivity was confirmed for reaction of slag in pure NaOH solution as shown in Figure VII-1.

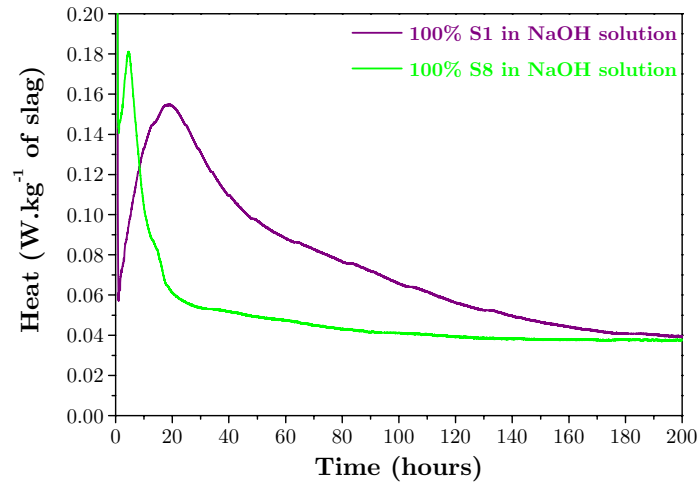


Figure VII-1: heat curves of both slags activated by NaOH solution

From our matrix of mortars, it was interesting to compare not only the performance and microstructure of blended systems but also the effect of using different kinds of cements.

The comparison of the effects of using low and high alkali cement (respectively Cement C and B) in combination with slag did not provide significant contrast in performance that was expected at early ages. In general, it was observed that the differences in cement clinker had very little impact on the reaction of the slags.

Using the overall degree of reaction, it was established that increasing reaction in the slag corresponds to an increasing strength in blended mortars. It is expected that the slag will make a more significant impact on strength at ages beyond 90 days.

Comparing the strength with calculated total porosity, the contribution of the slag seemed to be enhanced above that which might be expected from the filling of space by its hydration products.

In order to understand the microstructure better, the overall picture of the microstructural development of slag-pastes could be used as input for microstructural models such as the new modelling platform called μic [193].

In this study, other binary blended samples were also prepared with two fly ashes (FA1 and FA2 which is the one with high content of iron) and silica fume (SF which $d_{50} = 0.25 \mu\text{m}$) but in the available time, it was not possible to present all the results for these other SCMs. However, it was observed that both the fly ashes and the silica fume seemed to have quantifiable and reliable results by the calorimetry method as shown by Figure VII-2.

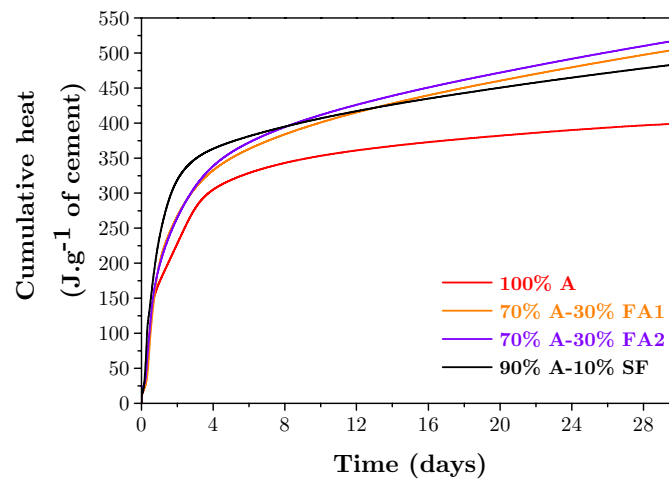


Figure VII-2: cumulative heat curves for fly ash and silica fume blended pastes compared to the reference paste

Furthermore, for fly ash, the SEM-IA-mapping method could be used to isolate its contribution. But compared to slag, the chemical composition of fly ashes is more heterogeneous and should require developing a special method with combination of multiple elemental mapping as it was recently investigated on pure fly ash by Chancey [194].

APPENDIX 2: MATLAB FILE FOR BACKGROUND REMOVAL OF DSC CURVES

The following code was developed in our laboratory at EPFL by Dunant:

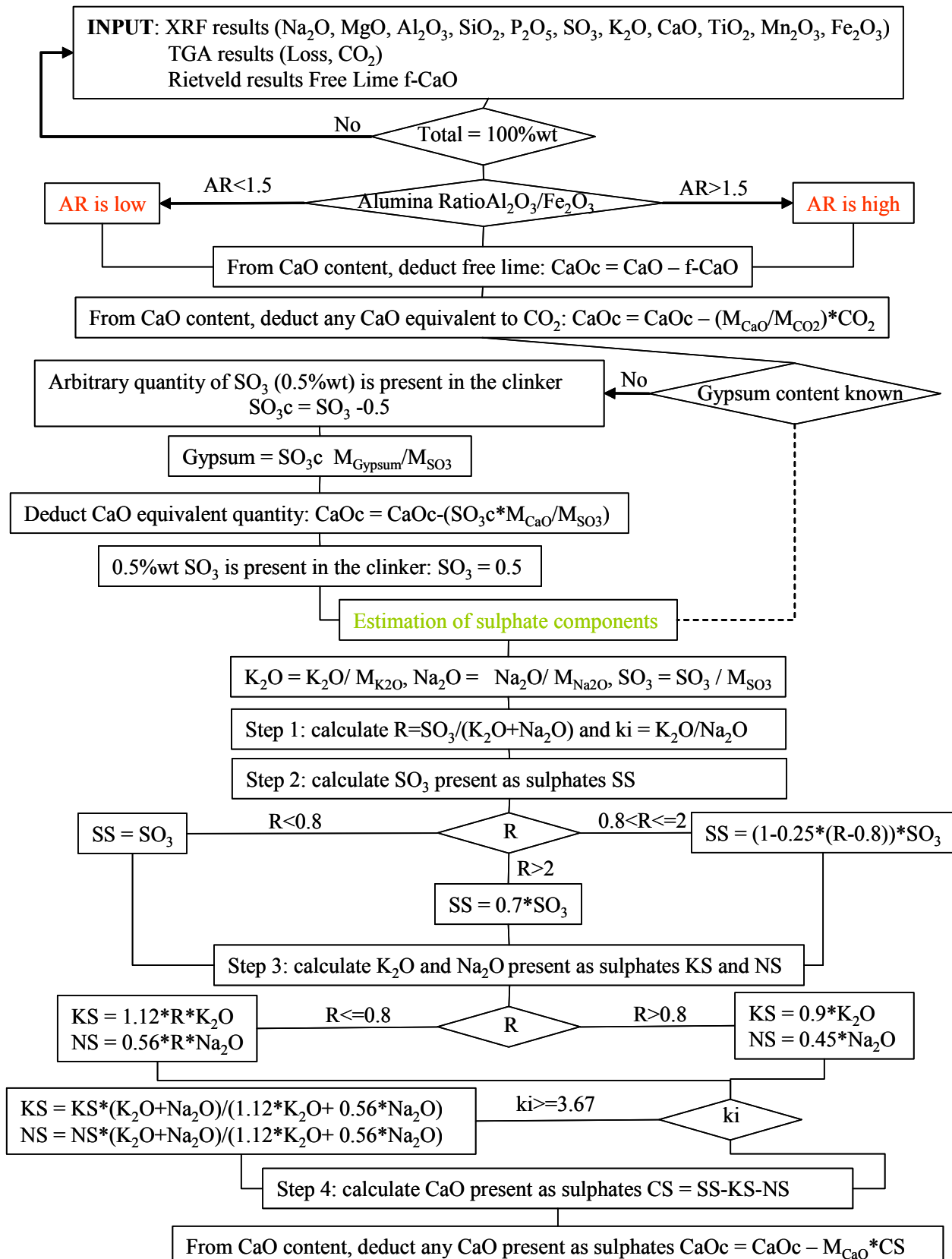
```
function b = xrdbbackground(a, sep, skip, delta)
% usage : b = xrdbbackground(a, sep, skip, delta)
% a: vector from which the background should be computed
% sep: index after which the peaks will be assumed to be exothermic
% skip: sub sampling interval
% delta: background curvature
b= a(1:skip:end) ;
b(end+1) = a(end) ;
if (sep > skip)
    for (i = 2:30 )
        for (j = 2:round(sep/skip)-1)
            avg = (b(j-1) + b(j+1))/2.;
            if ( (abs(b(j)) < abs(avg - delta) && b(j) < 0)
                || (abs(b(j)) > abs(avg - delta) && b(j) > 0)
                || b(j) == 0)
                b(j) = avg ;
            end
        end
        for (j = round(sep/skip):length(b)-1)
            avg = (b(j-1) + b(j+1))/2.;
            if ( (abs(b(j)) < abs(avg + delta) && b(j) < 0)
                || (abs(b(j)) > abs(avg + delta) && b(j) > 0)
                || b(j) == 0)
                b(j) = avg ;
            end
        end
    end
else
    for (i = 2:30 )
        for (j = 2:length(b)-1)
            avg = (b(j-1) + b(j+1))/2.;
            if ( (abs(b(j)) < abs(avg + delta) && b(j) < 0)
                || (abs(b(j)) > abs(avg + delta) && b(j) > 0)
                || b(j) == 0)
                b(j) = avg ;
            end
        end
    end
end

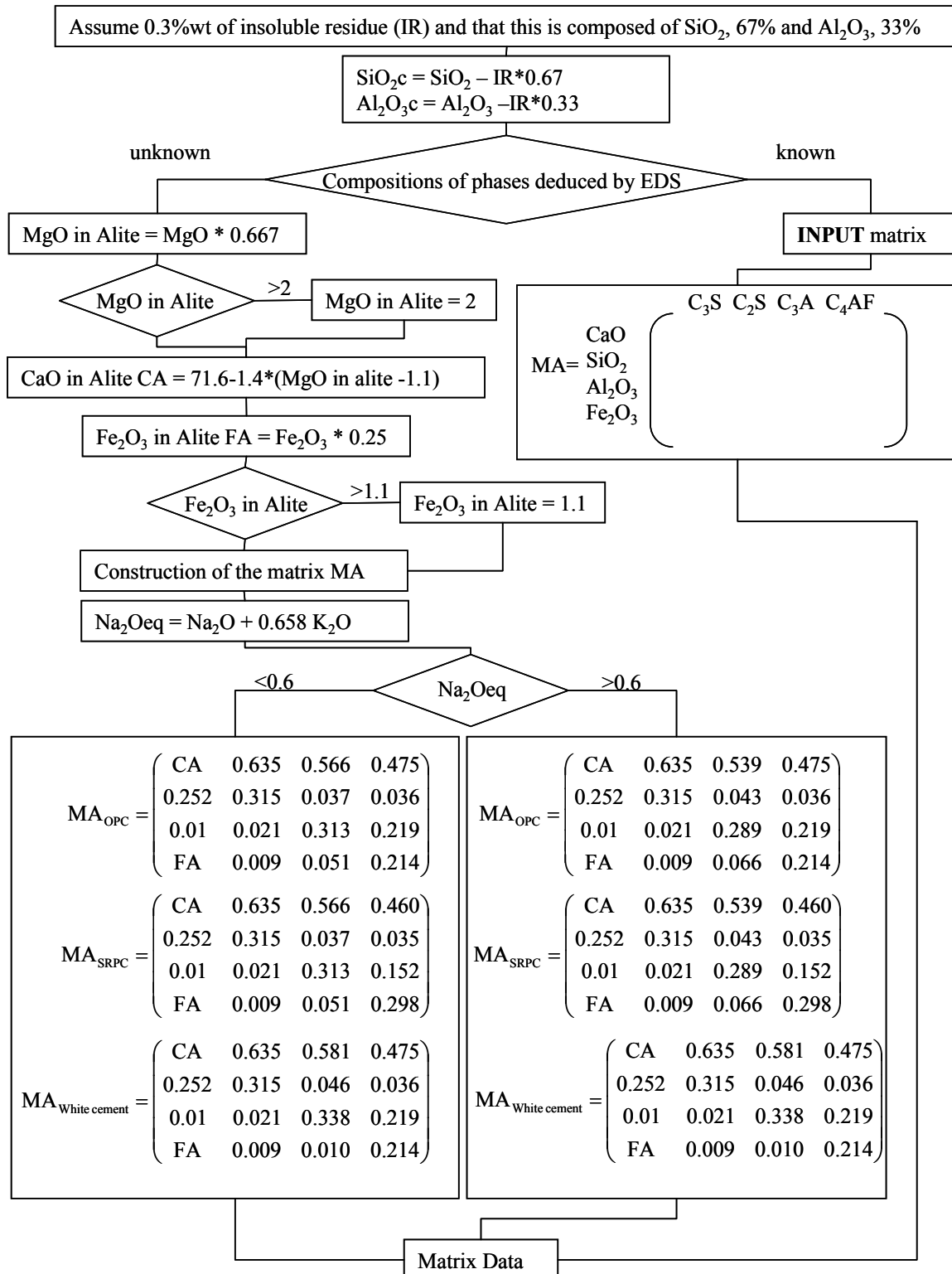
for (i = 1:length(b)-1)
    for (j = 1:skip)
        bg((i-1)*skip+j) = b(i)*(skip+1-j)/skip+b(i+1)*(j-1)/skip ;
    end
end
if length(bg) < length(a)
    for i = (length(bg)+1):length(a)
        bg(i) = b(length(b)) ;
    end
else
    bg = bg((length(bg)-length(a)+1):length(bg)) ;
end

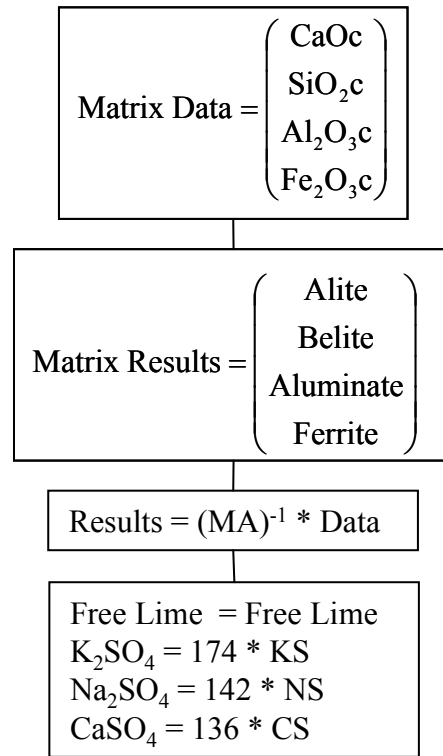
b = bg ;
return;
```

APPENDIX 3: SCHEMATIC REPRESENTATION OF PROGRAM FOR BOGUE CALCULATION

The following program was made in our laboratory at EPFL by Le Saoût:







REFERENCES

- [1] Oner M., Erdogdu K. and Gunlu A., Effect of components fineness on strength of blast furnace slag cement, *Cement and Concrete Research*, 33 (4), 463-469, 2003.
- [2] Bogue R. H., Calculation of the Compounds in Portland Cement, *Industrial and Engineering Chemistry*, 1, 192-197, 1929.
- [3] Taylor H. F. W., Modification of the Bogue calculation, *Advances in Cement Research*, 2 (6), 73-77, 1989.
- [4] Sorrentino D., Sorrentino F. and Gartner E., Prediction of a Portland Cement's Properties from its Chemical and Mineralogical Composition, in *Materials Science of Concrete VII*, J. Skalny F. Young (ed), The American Ceramic Society, 1-35, 2005.
- [5] Taylor H. F. W., Cement Chemistry, 2nd edition, in Thomas Telford Publishing, 1990.
- [6] Crumbie A., Walenta G. and Füllmann T., Where is the iron? Clinker microanalysis with XRD Rietveld, optical microscopy/point counting, Bogue and SEM-EDS techniques, *Cement and Concrete Research*, 36 (8), 1542-1547, 2006.
- [7] Aldridge L. P., Accuracy and precision of phase analysis in portland cement by Bogue, microscopic and X-ray diffraction methods, *Cement and Concrete Research*, 12 (3), 381-398, 1982.
- [8] Fullmann T., Pöllmann H., Walenta G., Gimenez M., Lauzon C., Hagopian-Babikian S., Dalrymple t. and Noon P., Analytical methods, *International cement review-Analysis and control*, 41-43, 2001.
- [9] Walenta G., Füllmann T. and Gimenez M., Quantitative Rietveld analysis of cement and clinker, *International cement review-Process control*, 2002.
- [10] Neubauer J., Pöllmann H. and Meyer H. W., Quantitative X-Ray analysis of OPC clinker by Rietveld refinement, *Proceedings of the 10th International Congress on the Chemistry of Cement, Gothenburg, Sweden*, 3, v007 012 pp, 1997.
- [11] Knudsen T., Quantitative analysis of the compound composition of cement and cement clinker by X-Ray Diffraction, *Bulletin of American Ceramic Society*, 55 (12), 1052-1054, 1976.
- [12] Campbell D. H. and Galehouse J. S., Quantitative Clinker Microscopy with the Light Microscope, *Cement and Concrete Aggregates*, 13, 94-96, 1991.
- [13] Märten A., Knöfel D. and Strunge J., Quantitative structure analysis via image analysis, *World Cement Technology*, 25 (8), 40-52, 1994.
- [14] Tabikh A. A. and Weht R. J., An X-ray diffraction analysis of portland cement, *Cement and Concrete Research*, 2 (1), 159-159, 1972.
- [15] Péter É., Die quantitative bestimmung der klinkermineralien mit dem diffraktometer, *Cement and Concrete Research*, 1 (1), 105-111, 1971.
- [16] Gutteridge W. A., Quantitative X-Ray powder diffraction in the study of some cementive materials, *British Ceramic Proceedings-The chemistry and chemically-related properties of cement*, 35, 11-23, 1984.
- [17] Madsen I. C., Scarlett N. V. Y., Cranswick L. M. D. and Lwin T., Outcomes of the International Union of Crystallography Commission on Powder Diffraction Round Robin on Quantitative Phase Analysis: samples 1a to 1h, In *Journal of Applied Crystallography*, 2001.
- [18] Roode-Gutzmer Q. I. and Ballim Y., Phase Composition and Quantitative X-Ray Powder Diffraction Analysis of Portland Cement and Clinker, Materials Science of Concrete VI, in *The American Ceramic Society*, J. Skalny (ed), 1-48, 2001.

- [19] Taylor J. C., Aldridge L. P., Matulis C. E. and Hinczak I., Chapter 18: X-ray powder diffraction analysis of cements, in *Structure and performance of cements*, 2nd edition, J. Bensted & P. Barnes (ed), Spon Press, 420-441, 2001.
- [20] Whestpal T., Walenta G., Füllmann T., Gimenez M., Bermejo E., Scrivener K. L. and Pöllmann H., Characterisation of cementitious materials, *International cement review-Process control*, 47-51, 2002.
- [21] Stutzman P., Powder diffraction analysis of hydraulic cements-ASTM Rietveld round-robin results on precision, *Powder Diffraction*, 20 (2), 97-100, 2005.
- [22] Poulsen S. L., Methodology to study the reactivity of blended materials using Nuclear Magnetic Resonance (pending), *PhD thesis*, 2009.
- [23] Poulsen S. L., Kocaba V., Le Saoût G., Jakobsen H. J., Scrivener K. L. and Skibsted J., Improved quantification of alite and belite in anhydrous Portland cements by ²⁹Si MAS NMR: Effects of paramagnetic ions, *Solid State Nuclear Magnetic Resonance*, 36 (1), 32-44, 2009.
- [24] Skibsted J., Jakobsen H. J. and Hall C., Quantification of calcium silicate phases in Portland cements by ²⁹Si MAS NMR spectroscopy, *Journal of the Chemical Society, Faraday Transactions*, 91 (24), 4423-4430, 1995.
- [25] Hjorth J., Skibsted J. and Jakobsen H. J., ²⁹Si MAS NMR studies of portland cement components and effects of microsilica on the hydration reaction, *Cement and Concrete Research*, 18 (5), 789-798, 1988.
- [26] Rietveld H. M., A profile refinement method for nuclear and magnetic structures, *Journal of Applied Crystallography*, 2, 65-71, 1969.
- [27] Nishi F., Takeuchi Y. and Maki I., Tricalcium silicate Ca₃O(SiO₄): The monoclinic superstructure, *Zeitschrift für Kristallographie*, 172 (297-314), 1985.
- [28] De La Torre Á. G., Bruque S., Campo J. and Aranda M. A. G., The superstructure of C₃S from synchrotron and neutron powder diffraction and its role in quantitative phase analyses, *Cement and Concrete Research*, 32 (9), 1347-1356, 2002.
- [29] De Noirfontaine M. N., Dunstetter F., Courtial M., Gasecki G. and Signes-Frehel M., Polymorphism of tricalcium silicate, the major compound of Portland cement clinker: 2. Modelling alite for Rietveld analysis, an industrial challenge, *Cement and Concrete Research*, 36 (1), 54-64, 2006.
- [30] Tsurumi T., Hirano Y., Kato H., Kamiya T. and Daimon M., Crystal structure and hydration of belite, *Ceramic Transactions*, 40, 19-25, 1994.
- [31] Mumme W. G., Hill R. J., Bushnell-Wye G. and Segnit E. R., Rietveld crystal structure refinements, crystal chemistry and calculated powder diffraction data for the polymorphs of dicalcium silicate and related phases, *Neues Jahrbuch für Mineralogie*, 169, 35-68, 1995.
- [32] Mondal P. and Jeffery J. W., The crystal structure of tricalcium aluminate, Ca₃Al₂O₆, *Acta Crystallographica*, B31, 689-697, 1975.
- [33] Nishi F. and Takéuchi Y., The Al₆O₁₈ rings of tetrahedra in the structure of Ca_{8.5}NaAl₆O₁₈, *Acta Crystallographica*, B31, 1169-1173, 1975.
- [34] Colville A. A. and Geller S., The crystal structure of Brownmillerite, Ca₂FeAlO₅, *Acta Crystallographica*, B27, 2311-2315, 1971.
- [35] Huang Q., Chmaissem O., Capponi J. J., Chaillout C., Marezio M., Tholence J. L. and Santoro A., Neutron powder diffraction study of the crystal structure of HgBa₂Ca₄Cu₅O₁₂⁺[delta] at room temperature and at 10 K, *Physica C: Superconductivity*, 227 (1-2), 1-9, 1994.

- [36] Petch H. E., The hydrogen positions in portlandite, $\text{Ca}(\text{OH})_2$, as indicated by the electron distribution, *Acta Crystallographica*, 14, 950-957, 1961.
- [37] Taylor D., Thermal expansion data. I. Binary oxides with the sodium chloride and wurtzite structure, *Transactions and Journal of the British Ceramic Society*, 83 5-9, 1984.
- [38] Wartchow R., Datensammlung nach der "Learnt profile"-Methode(LP) für Calcit und Vergleich mit der "Background peak background"-Methode (BPB), *Zeitschrift Fur Kristallographie*, 186, 300-302, 1989.
- [39] Cole W. F. and Lancucki C. J., A refinement of the crystal structure of gypsum $\text{CaSO}_4(\text{H}_2\text{O})_2$, *Acta Crystallographica*, 30, 921-929, 1974.
- [40] Abriel W. and Nesper R., Bestimmung der Kristallstruktur von $\text{CaSO}_4(\text{H}_2\text{O})_{0.5}$ mit Roentgenbeugungsmethoden und mit Potentialprofil-Rechnungen, *Zeitschrift Fur Kristallographie*, 205, 99-113, 1993.
- [41] Hawthorne F. C. and Ferguson R. B., Anhydrous Sulfates II. Refinement of the Crystal Structure of Anhydrite, *Canadian Mineralogist*, 13, 289-292, 1975.
- [42] McGinnety J. A., Redetermination of the structures of potassium sulphate and potassium chromate: the effect of electrostatic crystal forces upon observed bond lengths, *Acta Crystallographica*, 28, 2845-2852, 1972.
- [43] Courtial M., Noirfontaine M.-N. d., Dunstetter F., Gasecki G. and Signes-Frehel M., Polymorphism of tricalcium silicate in Portland cement: A fast visual identification of structure and superstructure, *Powder Diffraction*, 18, 7-15, 2003.
- [44] Poulsen S. L., Kocaba V., Le Saoût G., Jakobsen H. S., Scrivener K. L. and Skibsted J., Improved quantification of alite and belite in anhydrous Portland cements by ^{29}Si MAS NMR: Effects of paramagnetic ions *Solid-State Nuclear Magnetic Resonance*, 2009 (article in press).
- [45] Le Saoût G., Kocaba V. and Scrivener K. L., Application of the Rietveld method to the analysis of anhydrous cement, *To be published*, 2009.
- [46] Maki I. and Goto K., Factors influencing the phase constitution of alite in portland cement clinker, *Cement and Concrete Research*, 12 (3), 301-308, 1982.
- [47] Young R. A., Introduction to the Rietveld method, in *The Rietveld Method*, R.A. Young (ed), IUCr Monographs on crystallography 5, Oxford Univ. Press, 1-38, 2002.
- [48] Neubauer J., Kuzel H.-J. and Sieber R., Rietveld Quantitative XRD analysis of Portland cement: II. Quantification of synthetic and technical Portland cement clinkers, *Proceedings of the 18th International Conference on Cement Microscopy*, J. Bayles (Eds.), 100-111, 1996.
- [49] Caglioti G., Paoletti A. and Ricci F. P., Choice of collimators for a crystal spectrometer for neutron diffraction, *Nuclear Instruments*, 3, 223 – 228, 1958.
- [50] Dollase W. A., Correction of Intensities for preferred orientation in powder diffractometry-application of the March Model, *Journal of Applied Crystallography*, 19, 267-272, 1986.
- [51] Stutzman P. and Leigh S., Phase Analysis of Hydraulic Cements by X-Ray Powder Diffraction: Precision, Bias, and Qualification, *J. ASTM Int.*, 4 (5), 1-11, 2007.
- [52] Delesse M. A., Procédé mécanique pour déterminer la composition des roches, *Compte-Rendu de l'académie des Sciences de Paris* 25, 544-545, 1847.
- [53] Whitfield P. S. and Mitchell L. D., Quantitative Rietveld analysis of the amorphous content in cements and clinkers, *Journal of Materials Science*, 38, 4415-4421, 2003.

- [54] Jenkins R., Fawcett T. G., Smith D. K., Visser J. W., Morris M. C. and Frevel L. K., JCPDS- International Centre for Diffraction Data Sample Preparation Methods in X-Ray Powder Diffraction, *Powder Diffraction*, 1 51-63, 1986.
- [55] Taylor H. F. W., Cement Chemistry, 2nd edition, in Thomas Telford Publishing, 1997.
- [56] Taylor H. F. W., Chapter 9: Composite cements, in *Cement Chemistry*, 2nd edition, (ed), Thomas Telford Publishing, London, 261-294, 1990.
- [57] Euroslag, Granulated Blast Furnace, *Euroslag-Technical leaflet*, N°2, 2006.
- [58] Pietersen H. S., Reactivity of fly ash and slag in cement, *PhD thesis*, Technische Universiteit Delft, 1993.
- [59] Uchikawa H., Effect of blending components on hydration and structure formation, *Proceedings of the 8th International Congress on the Chemistry of Cement, Rio de Janeiro, Brasil*, I, III 250-280, 1986.
- [60] CEMEX, Capabilities in blast-furnace cements, CEMEX HOZ Seminar, Duisburg, Germany, *ZKG International*, 7, 27-31, 2007.
- [61] Smolczyk H. G., Slag structure and identification of slags, *Proceedings of the 7th International Congress on the Chemistry of Cement, Paris, France*, I, III 1/4-1/17, 1980.
- [62] Satarin V. I., Slag Portland cement, *Proceedings of the 6th International Congress on the Chemistry of cement, Moscow*, 1974.
- [63] Moranville-Regourd M., Chapter 11: Cements made from blastfurnace slag, in *LEA's chemistry of cement and concrete*, Peter C.Hewlett (ed), Arnold, London, 633-674, 1998.
- [64] Dron R., Structure et réactivité des laitiers vitreux, *PhD thesis*, Université de Paris VI et Laboratoire Central des Ponts et Chaussées, 1984.
- [65] Johansson M. E., Relation between strengths of slag cement and properties of slag, *Silicates Industriels*, 7-8, 139-143, 1978.
- [66] Itoh T., Rapid discrimination of the character of the water-cooled blast furnace slag used for Portland slag cement, *Journal of Materials Science*, 39, 2191-2193, 2004.
- [67] Krüger J. E. and Smit M. S., Endothermal DTA peak preceding exothermal devitrification peak for vitreous blast-furnace slag, *Cement and Lime Manufacture*, 42 (4), 77-80, 1969.
- [68] Lang E., Chapter 12: Blastfurnace cements, in *Structure and performance of cements*, 2nd edition, J. Bensted & P. Barnes (ed), Spon Press, 310-325, 2002.
- [69] Dron R., Structure and reactivity of glassy slags, *Proceedings of the 8th International Congress on the Chemistry of Cement, Rio de Janeiro, Brasil*, IV, 3 81-85, 1986.
- [70] Smolczyk H. G., Zum Einfluß der Chemie des Hüttensandes auf die Festigkeiten von Hochofenzementen, *Zement-Kalk-Gips*, 31 (6), 294-296, 1978.
- [71] Swainson I. P., Dove M. T., Schmahl W. W. and A. P., Neutron powder diffraction study of the akermanite-gehlenite solid solution series, *Physics and chemistry of minerals*, 19 (3), 185-195, 1992.
- [72] Demoulian E., Gourdin P., Hawthorn F. and Vernet C., Influence of slag chemical composition and texture on their hydraulicity, *Proceedings of the 7th International Congress on the Chemistry of Cement, Paris, France*, II, III 89-94, 1980.
- [73] Uchikawa H., Uchida S. and Hanehara S., *Proceedings of the 8th International Congress on the Chemistry of Cement, Rio de Janeiro, Brasil*, I, III 245, 1986.
- [74] Schrämli W., Characterisation of blastfurnace slags by means of differential thermal analysis, *Zement-Kalk-Gips*, 4, 140-147, 1963.

- [75] Regourd M., Mortureux B., Gautier E., Hornain H. and Volant J., Characterisation and thermal activation of slag cements, *Proceedings of the 7th International Congress on the Chemistry of Cement, Paris, France*, II, III 105-111, 1980.
- [76] Sersale R. and Frigione G., Microstructure and properties of hydrated cements with different slag content, *Proceedings of the 7th International Congress on the Chemistry of Cement, Paris, France*, II, III 63-68, 1980.
- [77] Hinrichs W. and Odler I., Investigation of hydration of Portland blastfurnace slag cement: hydration kinetics, *Advances in Cement Research*, 5 (2), 9-13, 1989.
- [78] Francis A. A., Non-isothermal crystallisation kinetics of a blast furnace slag glass, *Journal of American Ceramic Society*, 88 (7), 1859-1863, 2005.
- [79] Fredericci C., Zanutto E. D. and Ziemath E. C., Crystallization mechanism and properties of a blast furnace slag glass, *Journal of Non-Crystalline Solids*, 273 (1-3), 64-75, 2000.
- [80] Mazurin O. V., Problems of compatibility of the values of glass transition temperatures published in the world literature *Glass Physics and Chemistry* 33 (1), 22-36, 2007.
- [81] van Roode M., Douglas E. and Hemmings R. T., X-ray diffraction measurement of glass content in fly and slags, *Cement and Concrete Research*, 17 (2), 183-197, 1987.
- [82] Douglas E. and Zerbino R., Characterization of granulated and pelletized blast furnace slag, *Cement and Concrete Research*, 16 (5), 662-670, 1986.
- [83] Westphal T., Walenta G., Gimenez M., Bermejo E., Fullmann T., Scrivener K. L. and Pöllmann H., Characterisation of cementitious materials, *International cement review-Process control*, 2002.
- [84] Le Saoût G., Füllmann T., Kocaba V. and Scrivener K. L., Quantitative study of cementitious materials by X-ray diffraction/ Rietveld analysis using an external standard, *Proceedings of the 12th International Congress on the Chemistry of Cement, Montréal, Canada*, TH2-07.01, 2007.
- [85] Jenkins R. and Snyder R. L., Introduction to X-ray Powder Diffractometry, in *Chemical Analysis a series of monographs on chemistry and its applications*, J.D. Winefordner (ed), Wiley, 138, 1996.
- [86] Suherman P. M., van Riessen A., O'Connor B., Li D., Bolton D. and Fairhurst H., Determination of amorphous phase levels in Portland cement clinker, *Powder Diffraction*, 17 (3), 178-185, 2002.
- [87] Nassau K., Wang C. A. and Grasso M., Quenched metastable glassy and crystalline phases in the system lithium-sodium-potassium metaniobate-tantalate, *Journal of the American Ceramic Society*, 62 (9-10), 503-510, 1979.
- [88] Escalante J. I., Gomez L. Y., Johal K. K., Mendoza G., Mancha H. and Mendez J., Reactivity of blast-furnace slag in Portland cement blends hydrated under different conditions, *Cement and Concrete Research*, 31 (10), 1403-1409, 2001.
- [89] Battagin A. F., Influence of degree of hydration of slag on slag cements, *Proceedings of the 9th International Congress on the Chemistry of Cement, New Delhi, India*, III, II 166-172, 1992.
- [90] Köster H. and Odler I., Investigations on the structure of fully hydrated portland cement and tricalcium silicate pastes. I. Bound water, chemical shrinkage and density of hydrates, *Cement and Concrete Research*, 16 (2), 207-214, 1986.
- [91] Mouret M., Bascoul A. and Escadeillas G., Study of the degree of hydration of concrete by means of image analysis and chemically bound water, *Advanced Cement Based Materials*, 6 (3-4), 109-115, 1997.

- [92] Harris D. H. C., Free and bound water in cement pastes, *Magazine of Concrete Research*, 26 (87), 65-72, 1974.
- [93] Scrivener K. L., Fullmann T., Gallucci E., Walenta G. and Bermejo E., Quantitative study of Portland cement hydration by X-ray diffraction/Rietveld analysis and independent methods, *Cement and Concrete Research*, 34 (9), 1541-1547, 2004.
- [94] Scrivener K. L., Backscattered electron imaging of cementitious microstructures: understanding and quantification, *Cement and Concrete Composites*, 26 (8), 935-945, 2004.
- [95] Jennings H. M., Dalgleish B. J. and Pratt P. L., Morphological development of hydrating tricalcium silicate as examined by electron microscopy techniques, *Journal of the American Ceramic Society*, 64 (10), 567-572, 1981.
- [96] Moukwa M. and Aitcin P. C., The effect of drying on cement pastes pore structure as determined by mercury porosimetry, *Cement and Concrete Research*, 18 (5), 745-752, 1988.
- [97] Gallé C., Effect of drying on cement-based materials pore structure as identified by mercury intrusion porosimetry: A comparative study between oven-, vacuum-, and freeze-drying, *Cement and Concrete Research*, 31 (10), 1467-1477, 2001.
- [98] Taylor H. F. W. and Turner A. B., Reactions of tricalcium silicate paste with organic liquids, *Cement and Concrete Research*, 17 (4), 613-623, 1987.
- [99] Moore A. E. and Taylor H. F. W., Crystal structure of ettringite, In *Acta Crystallographica Section B*, 1970.
- [100] Goetz-Neunhoeffler F. and Neubauer J., Refined ettringite structure for quantitative XRD analysis, *Powder Diffraction*, 21, 4-11, 2006.
- [101] Francois M., Renaudin G. and Evrard O., A Cementitious Compound with Composition $3\text{CaO}\cdot\text{Al}_2\text{O}_3\cdot\text{CaCO}_3\cdot 11\text{H}_2\text{O}$, In *Acta Crystallographica Section C*, 1998.
- [102] Allmann R., Refinement of the hybrid layer structure $[\text{Ca}_2\text{Al}(\text{OH})_6]^+ \cdot [1/2\text{SO}_4\cdot 3\text{H}_2\text{O}]^-$, *Neues Jahrbuch für Mineralogie Monatshefte*, 136-144, 1977.
- [103] Pöllmann H., Kuzel H. J. and Wenda R., Compounds with ettringite structure, *Neues Jahrbuch für Mineralogie. Abhandlungen* 160, 133-158, 1989.
- [104] Fischer R. and Kuzel H. J., Reinvestigation of the system $\text{C}_4\text{A}\cdot n\text{H}_2\text{O} \text{ --- } \text{C}_4\text{A}\cdot\text{CO}_2\cdot n\text{H}_2\text{O}$, *Cement and Concrete Research*, 12 (4), 517-526, 1982.
- [105] Mohan K. and Taylor H. F. W., *University of Aberdeen, Old Aberdeen, Scotland, ICDD Grant-in-Aid*, 1980.
- [106] Bellotto M., Rebours B., Clause O., Lynch J., Bazin D. and Elkaim E., A Reexamination of Hydrotalcite Crystal Chemistry, *The Journal of Physical Chemistry*, 100 (20), 8527-8534, 1996.
- [107] Goetz-Neunhoeffler F. and Neubauer J., Refined ettringite ($\text{Ca}_6\text{Al}_2(\text{SO}_4)_3 (\text{OH})_{12} 26\text{H}_2\text{O}$) structure for quantitative X-ray diffraction analysis, *Powder Diffraction* 21, 4-11, 2006.
- [108] Sonneveld E. J. and Visser J. W., Automatic Collection of Powder Data from Photographs, *Journal of Applied Crystallography*, 8 (1), 1975.
- [109] Le Saout G., Lécolier E., Rivereau A. and Zanni H., Chemical structure of cement aged at normal and elevated temperatures and pressures: Part I. Class G oilwell cement, *Cement and Concrete Research*, 36 (1), 71-78, 2006.
- [110] Matschei T., Lothenbach B. and Glasser F. P., The AFm phase in Portland cement, *Cement and Concrete Research*, 37 (2), 118-130, 2007.
- [111] Skibsted J. and Jakobsen H. J., Characterization of the calcium silicate and aluminate phases in anhydrous and hydrated Portland cements, in *Nuclear Magnetic Resonance*

- Spectroscopy of Cement-Based Materials*, A.-R. Grimmer P.Colombet, H. Zanni, P. Soozzani (ed), Berlin, 3-45, 1998.
- [112] Dyson H. M., Early hydration in binary and ternary blended cement systems, *PhD thesis*, University of Leeds, 2005.
- [113] Gallucci E. and Scrivener K., Crystallisation of calcium hydroxide in early age model and ordinary cementitious systems, *Cement and Concrete Research*, 37 (4), 492-501, 2007.
- [114] Scrivener K. L., Development of the microstructure during the hydration of Portland cement, *PhD thesis*, University of London, 1984.
- [115] Jennings H. M. and Parrott L. J., Microstructural analysis of hydrated alite paste- Part 2: Microscopy and reaction products, *Journal of Materials Science*, 21, 4053-4059, 1986.
- [116] Scrivener K. L., Patel H. H., Pratt P. L. and Parrott L. J., Analysis of phases in cement paste using backscattered electron images, methanol adsorption and thermogravimetric analysis in microstructural development during the hydration of cement, *Proceedings of Material Research Society Symposium*, 85, 67-76, 1987.
- [117] Hadley D. W., Dolch W. L. and Diamond S., On the occurrence of hollow-shell hydration grains in hydrated cement paste, *Cement and Concrete Research*, 30 (1), 1-6, 2000.
- [118] Famy C., Scrivener K. L. and Crumbie A. K., What causes differences of C-S-H gel grey levels in backscattered electron images?, *Cement and Concrete Research*, 32 (9), 1465-1471, 2002.
- [119] Wadsö L., Notes from Nanocem Calorimetry Workshop, *Building Materials Lund University, Sweden*, October 2006.
- [120] Bentz D. P., Transient plane source measurements of the thermal properties of hydrating cement pastes, *Materials and structures*, 40 (10), 1073 -1080, 2007.
- [121] Holman J. P., Heat Transfer, in 1981.
- [122] Todd S. S., Low temperature heat capacities and entropies at 298.16°K of crystalline calcium orthosilicate zinc orthosilicate and tricalcium silicate, *Journal of American Chemistry Society*, 73, 3277-3278, 1951.
- [123] Geiker M., Studies of Portland cement hydration by measurements of chemical shrinkage, *PhD thesis*, 1983.
- [124] Costoya M., Effect of particle size on the hydration kinetics and microstructural development of tricalcium silicate, *PhD thesis*, Ecole Polytechnique Fédérale de Lausanne, 2008.
- [125] Odler I., Chapter 6: Hydration, setting and hardening of Portland cement, in *LEA's chemistry of cement and concrete*, Peter C.Hewlett (ed), Arnold, London, 241-298, 2001.
- [126] Nonat A., Calorimetry: a tool for studying early hydration of cement, *LMC-ICB Dijon seminar*, 2007.
- [127] Lothenbach B. and Winnefeld F., Thermodynamic modelling of the hydration of Portland cement, *Cement and Concrete Research*, 36 (2), 209-226, 2006.
- [128] Bland C. H. and Sharp J. H., A conduction calorimetric study of gasifier slag-Portland cement blends, *Cement and Concrete Research*, 21 (2-3), 359-367, 1991.
- [129] Escalante J. I. and Sharp J. H., Effect of temperature on the early hydration of the Portland cement and blended cements, *Advances in Cement Research*, 12 (3), 121-130, 2000.
- [130] Escalante-Garcia J. I. and Sharp J. H., Effect of temperature on the hydration of the main clinker phases in portland cements: part II, blended cements, *Cement and Concrete Research*, 28 (9), 1259-1274, 1998.

- [131] Richardson I. G., Wilding C. R. and Dickson M. J., The hydration of blast furnace slag cements, *Advances in Cement Research*, 2 (8), 147-157, 1989.
- [132] Utton C. A., Hayes M., Hill J., Milestone N. B. and Sharp J. H., Effect of Temperatures up to 90°C on the Early Hydration of Portland-Blastfurnace Slag Cements, *Journal of the American Ceramic Society*, 91 (3), 948-954, 2008.
- [133] Wu X., Roy D. M. and Langton C. A., Early hydration of slag-cement, *Cement and Concrete Research*, 13 (2), 277-286, 1983.
- [134] Hill J. and Sharp J. H., Heat evolution in composite cements with additions of Sn(II) and Sn(IV) chlorides, *Advances in Cement Research*, 15 (2), 57-66, 2003.
- [135] Bensted J., Some applications of conduction calorimetry to cement hydration, *Advanced in Cement Research*, 1 (1), 35-44, 1987.
- [136] Taylor H. F. W., Chapter 7: Hydration of Portland cement, in *Cement Chemistry*, 2nd edition, (ed), Thomas Telford Publishing, London, 187-226, 1990.
- [137] Gartner E. M., Young J. F., Damidot D. A. and Jawed I., Chapter 3: Hydration of Portland cement, in *Structure and performance of cements*, 2nd edition, J. Bensted & P. Barnes (ed), Spon Press, 57-113, 2002.
- [138] Le Saoût G. and Scrivener K. L., Early hydration of Portland cement with corundum addition, *Proceedings of the 16th Internationale Baustofftatung Universität Weimar*, pp. 1-0409 -0401-0415, 2006.
- [139] Fernandez Lopez R., Calcined clayed soils as a potential replacement for cement in developing countries, *PhD thesis*, Ecole Polytechnique Fédérale de Lausanne, 2009.
- [140] Abo-El-Enein S. A., Daimon M., Ohsawa S. and Kondo R., Hydration of low porosity slag-lime pastes, *Cement and Concrete Research*, 4 (2), 299-312, 1974.
- [141] Luke K. and Glasser F. P., Internal chemical evolution of the constitution of blended cements, *Cement and Concrete Research*, 18 (4), 495-502, 1988.
- [142] Ogawa K., Uchikawa H., Takemoto K. and Yasui I., The mechanism of the hydration in the system C₃S-pozzolana, *Cement and Concrete Research*, 10 (5), 683-696, 1980.
- [143] Taylor H. F. W. and Mohan K., Analytical study of pure and extended Portland cement pastes: II, fly-ash and slag cement pastes, *Journal of American Ceramic Society*, 68 (12), 685-690, 1985.
- [144] Harrisson A. M., Winter N. b. and Taylor H. F. W., Microstructure and microchemistry of slag cement pastes, *Materials Research Society Symposium Proceedings*, 85, 213-222, 1987.
- [145] Richardson I. G. and Groves G. W., The incorporation of minor and trace elements into calcium silicate hydrate (C-S-H) gel in hardened cement pastes, *Cement and Concrete Research*, 23, 131-138, 1993.
- [146] Harrisson A. M., Winter N. B. and Taylor H. F. W., *Proceedings of the 8th International Congress on the Chemistry of Cement*, 4, 170, 1986.
- [147] Faucon P., Delagrave A., Petit J. C., Richet C., Marchand J. M. and Zanni H., Aluminum incorporation in Calcium Silicate Hydrates (C-S-H) depending on their Ca/Si ratio, *Journal of Physics and Chemistry B*, 103 (37), 7796-7802, 1999.
- [148] Zhang X., Quantitative microstructural characterisation of concrete cured under realistic temperature conditions, *PhD thesis*, Ecole Polytechnique Fédérale de Lausanne, 2007.
- [149] Richardson I. G. and Groves G. W., Microstructure and microanalysis of hardened cement pastes involving ground granulated blast-furnace slag, *Journal of Materials Science*, 27, 6204-6212, 1992.

- [150] Doug Hooton R., Canadian use of ground granulated blast-furnace slag as a supplementary cementing material for enhanced performance of concrete, *Canadian Journal of Civil Engineering* 27, 754 -760, 2000.
- [151] Richardson I. G. and Cabrera J. G., The nature of C-S-H in model slag-cements, *Cement and Concrete Composites*, 22 (4), 259-266, 2000.
- [152] Escalante J.-I. and Sharp J. H., The chemical composition and microstructure of hydration product in blended cements, *Cement and Concrete Composites*, 26, 967-976, 2004.
- [153] Duchesne J. and Bérubét M. A., Effect of supplementary cementing materials on the composition of cement hydration products, *Advanced Cement Based Materials*, 2 (2), 43-52, 1995.
- [154] Richardson I. G., Brough A. R., Groves G. W. and Dobson C. M., The characterization of hardened alkali-activated blast-furnace slag pastes and the nature of the calcium silicate hydrate (C-S-H) phase, *Cement and Concrete Research*, 24 (5), 813-829, 1994.
- [155] Barker A. P., An electron optical examination of zoning in BFS-Part I-Slag cement pastes at early ages, *Advances in Cement Research*, 2 (8), 171-179, 1989.
- [156] Richardson J. M., Biernacki J. J., Stutzman P. E. and Bentz D. P., Stoichiometry of slag hydration with calcium hydroxide, *Journal of American Ceramic Society*, 85 (4), 947-953, 2002.
- [157] Regourd M., Structure and behaviour of slag Portland cement hydrates, *Proceedings of the 7th International Congress on the Chemistry of Cement, Paris, France*, I, III 2/10-12/26, 1980.
- [158] Daimon M., Mechanism and kinetics of slag Cement Hydration, *Proceedings of the 7th International Congress on the Chemistry of Cement, Paris, France*, I, III 2/1-2/9, 1980.
- [159] Song S., Sohn D., Jennings H. M. and Mason T. O., Hydration of alkali-activated ground granulated blast furnace slag, *Journal of Materials Science*, 35, 249– 257, 2000.
- [160] Tanaka H., Totani Y. and Saito Y., Structure of hydrated glassy blastfurnace in concrete, *Proceedings of the 1st International Congress on Fly ash, Silica fume, Slag and other Minerals By-products in Concrete, Montebello, Canada*, American Concrete Institute Special Publication, 79, 963-977, 1983.
- [161] Pane I. and Hansen W., Investigation of blended cement hydration by isothermal calorimetry and thermal analysis, *Cement and Concrete Research*, 35 (6), 1155-1164, 2005.
- [162] Marsh B. K. and Day R. L., Pozzolan and cementitious reactions of fly ash in blended cement pastes, *Cement and Concrete Research*, 18 (2), 301-310, 1988.
- [163] Raupp-Pereira F., Segadaes A. M., Silva A. S., Rocha J. and Labrincha J. A., ²⁷Al and ²⁹Si NMR and XRD characterisation of clinkers: standard phases and new waste based formulations, *Advances in Cement Research*, 107 (1), 37-45, 2008.
- [164] Brough A. R. and Atkinson A., Sodium silicate-based, alkali-activated slag mortars: Part I. Strength, hydration and microstructure, *Cement and Concrete Research*, 32 (6), 865-879, 2002.
- [165] Brough A. R. and Atkinson A., Automated identification of the aggregate-paste interfacial transition zone in mortars of silica sand with Portland or alkali-activated slag cement paste, *Cement and Concrete Research*, 30 (6), 849-854, 2000.
- [166] Demoulian E., Vernet C., Hawthorn F. and Gourdin P., Slag content determination in cements by selective dissolution, *Proceedings of the 7th International Congress on the Chemistry of Cement, Paris, France*, II, III 151-156, 1980.

- [167] Levelt V. F. J., Vriezen E. B. and Galen R. V., Determination of the slag content of BFS cements by means of a solution method, *Zement-Kalk-Gips*, 35 (2), 96-99, 1982.
- [168] Glasser F. P., Macphee D. E. and Lachowski E. E., Solubility modelling of cements: implications for radioactive waste immobilisation, *Materials Research Society Symposium Proceedings* 84, 331-341, 1987.
- [169] Luke K. and Glasser F. P., Selective dissolution of hydrated blast furnace slag cements, *Cement and Concrete Research*, 17 (2), 273-282, 1987.
- [170] Lumley J. S., Gollop R. S., Moir G. K. and Taylor H. F. W., Degrees of reaction of the slag in some blends with Portland cements, *Cement and Concrete Research*, 26 (1), 139-151, 1996.
- [171] Totani Y., Saito Y., Kageyama M. and Tanaka H., The hydration of blast furnace slag cement, *Proceedings of the 7th International Congress on the Chemistry of Cement, Paris, France*, II, III 95-98, 1980.
- [172] Taylor H. F. W. and Mohan K., Analytical study of pure and extended Portland cement pastes: I, pure Portland cement pastes, *Journal of American Ceramic Society*, 68 (12), 680-685, 1985.
- [173] Dyson H., Richardson I. and Brough A. R., A combined ²⁹Si MAS NMR and selective dissolution technique for the quantitative evaluation of hydrated blast furnace slag cement blends, *Journal of American Ceramic Society*, 90 (2), 598-602, 2007.
- [174] Goguel R., A new consecutive dissolution method for the analysis of slag cements, *Cement, Concrete and Aggregates*, 17 (1), 84-91, 1995.
- [175] Gutteridge W. A., On the dissolution of the interstitial phases in Portland cement, *Cement and Concrete Research*, 9 (3), 319-324, 1979.
- [176] Van Rompaey G., Etude de la réactivité des ciments riches en laitier, à basse température et à temps court, sans ajout chloruré, *PhD thesis*, Université Libre de Bruxelles, 2006.
- [177] Ramachandran V. S., Paroli R. M., Beaudoin J. J. and A.H. D., Handbook of thermal analysis of construction materials, in Noyes Publications, William Andrew publishing, Norwich, New York, U.S.A, 2002.
- [178] Sha W., O'Neill E. A. and Guo Z., Differential scanning calorimetry study of ordinary Portland cement, *Cement and Concrete Research*, 29 (9), 1487-1489, 1999.
- [179] Utton C. A., The encapsulation of a BaCO₃ waste in composite cement, *PhD thesis*, University of Sheffield, 2006.
- [180] Kishi T. and Maekawa K., Thermal and mechanical modelling of young concrete based on hydration process of multi-component cement minerals, *International RILEM Symposium*, 1994.
- [181] Grün R., K. T. and Kunze G., Messung der latenten Energie von Hochofenschlacken und von Einzelkomponenten des Dreistoffsystems Kieselsäure-Kalk-Tonerde-2, *Zement*, 1925.
- [182] Grün R., K. T. and Kunze G., Messung der latenten Energie von Hochofenschlacken und von Einzelkomponenten des Dreistoffsystems Kieselsäure-Kalk-Tonerde-1, *Zement*, 1925.
- [183] Fierens P. and Poswick P., New aspects of industrial slags hydration, *Proceedings of the 7th International Congress on the Chemistry of Cement, Paris, France*, II, III 112-116, 1980.
- [184] Hogan F. J. and Meusel J. W., Evaluation for durability and strength development of a ground granulated blast furnace slag, *Cement, Concrete and Aggregates*, 3 (1), 40-52, 1981.

-
- [185] Abo-El-Enain S. A., Ata A. A., Hassanien A. and Mikhail R. S., Kinetics and Mechanism of Slag Cement Hydration, *Journal of Chemical Technology and Biotechnology*, 32, 939-945, 1982.
- [186] Shi C. and Day R. L., Acceleration of strength gain of lime-pozzolan cements by thermal activation, *Cement and Concrete Research*, 23 (4), 824-832, 1993.
- [187] Lawrence P., Cyr M. and Ringot E., Mineral admixtures in mortars effect of type, amount and fineness of fine constituents on compressive strength, *Cement and Concrete Research*, 35 (6), 1092-1105, 2005.
- [188] Cyr M., Lawrence P. and Ringot E., Efficiency of mineral admixtures in mortars: Quantification of the physical and chemical effects of fine admixtures in relation with compressive strength, *Cement and Concrete Research*, 36 (2), 264-277, 2006.
- [189] Oner A. and Akyuz S., An experimental study on optimum usage of GGBS for the compressive strength of concrete, *Cement and Concrete Composites*, 29 (6), 505-514, 2007.
- [190] Chidiac S. E. and Panesar D. K., Evolution of mechanical properties of concrete containing ground granulated blast furnace slag and effects on the scaling resistance test at 28 days, *Cement and Concrete Composites*, 30 (2), 63-71, 2008.
- [191] Scrivener K. L. and Crumbie A. K., The Interfacial Transition Zone (ITZ) Between Cement Paste and Aggregate in Concrete, *Interface Science*, 12 (4), 411-421, 2004.
- [192] Taylor H. F. W., Chapter 5: Hydration of calcium silicate phases, in *Cement Chemistry*, 2nd edition, (ed), Thomas Telford Publishing, London, 113-156, 1990.
- [193] Bishnoi S. and Scrivener K. L., μ ic: A new platform for modelling the hydration of cements, *Cement and Concrete Research*, 39 (4), 266-274, 2009.
- [194] Chancey R. T., Characterization of crystalline and amorphous phases and respective reactivities in a class F fly ash, *PhD thesis*, The University of Texas at Austin, 2008.

CURRICULUM VITAE

Vanessa KOCABA
Chemin de Montelly, 70
1007 LAUSANNE
SWITZERLAND

E-mail: vanessa_kocaba@yahoo.fr
Marital status: Single
Date of birth: 18th July 1980

EDUCATION

PhD in Materials Science-EPFL (2005–2009) at Swiss Federal Institute of Technology, in the Laboratory of Construction Material, under the supervision of Prof. Karen L. Scrivener and supported by Nanocem (industrial-academic research network on cement and concrete). Development and evaluation of methods to follow the microstructural development of cementitious materials including slags.

Master in Materials and Multi-Materials-Claude Bernard University in Lyon, France (2004-2005).

Master in Materials engineering-ISTIL (Institut des Sciences et Techniques de l'Ingénieur de Lyon) in Lyon, France (2003-2005).

Diplôme d'Etudes Universitaires Générales, Licence, Maîtrise and Diplôme d'ingénieur maître in Materials-University of Evry, France (2000-2003): diplomas obtained after 2,3 and 4 years at the IUP (vocational university institute) specialized in Materials engineering passed with distinction (B).

Diplôme Universitaire de Technologie en Chimie-University of Orsay, France (1998-2000): Technical Diploma in Chemistry obtained after 2 years at technical college.

Baccalauréat Scientifique in Physics and Chemistry-Ambérieu-en-Bugey, France (1997-1998): diploma obtained at the end of high school.

PROFESSIONAL EXPERIENCE

2005-2009: Research assistant in Laboratory of Construction Materials, EPFL, Switzerland.

- Laboratory techniques: X-ray diffraction, scanning electron microscopy, isothermal calorimetry, thermal analysis, mechanical testing.

- Supervisory experience: Supervised 3 undergraduate students' projects (4 months each).

- Teaching experience:

 - Taught laboratory courses on thermal analyses methods.

 - Taught practical works on cement chemistry and initiation of scanning electron microscopy for undergraduate students.

 - Lecture in Nanocem Marie Curie Network Training about effect of SCMs on microstructure of cementitious systems.

- Outreach: Student representative to organise the doctoral day in February 2008 at EPFL.

March-August 2005: Intern at Lafarge Research Centre in St Quentin Fallavier, France.

- Influence of fines fractions of different ground sands on the rheological and mechanical performances of concrete.

May-July 2004: Intern at Forensic Sciences Laboratory in Lyon, France.

- Analysis of glass sample Glass Refractive Index Measurement.

February-June 2003: Intern at Saint-Gobain Materials Research Centre, in Aubervilliers, France.

- Influence of superplasticizers and mineral admixtures on properties of cement pastes.

January-February 2002: Intern at Forensic Sciences Laboratory in Lyon, France.

- X-ray fluorescence analysis of glass samples coming from car-windows-panes which can be found on the scene of different offences.

July 2001, summers 2002 and 2003: Chemical Receptionist (Substitute) in Société d'Aménagement Urbain et Rural in Maurepas, France.

- Metrologic measurements and management of chemical products.

May-June 2000: Intern at Northumbria University Laboratory in Newcastle, England.

- Synthesis and oxidation reactions of N-aryl-1,2,3,4-tetrahydroisoquinoline derivatives.

June-August 1999: Assistant Engineer at Bouygues Laboratory, in Coignières, France.

LANGUAGES

- French (mother tongue)
- English (fluent in both speaking and writing)
- Spanish (learning)

SPECIAL INTERESTS

- Athletics
- Equitation

PUBLICATIONS

Reviewed journal papers

▪ Poulsen S.L., Kocaba V., Le Saoût G., Jakobsen H.J., Scrivener K.L. and Skibsted J., Improved quantification of alite and belite in anhydrous Portland cements by ^{29}Si MAS NMR: Effects of paramagnetic ions, *Solid State Nuclear Magnetic Resonance*, 36 (1), 32-44, 2009.

Refereed conference papers with talks

▪ Le Saoût G., Füllmann T., Kocaba V. and Scrivener K.L., Quantitative study of cementitious materials by X-ray diffraction/Rietveld analysis using an external standard, *Proceedings of the 12th International Congress on the Chemistry of Cement*, Montréal, Canada, TH2-07.01, 2007.

Non-refereed conference papers with talks

▪ Kocaba V., Le Saoût G. and Scrivener K.L., Chemical structure and hydration kinetics of Portland cement with Supplementary Cementitious Materials, *27th Cement and Concrete Science Meeting*, Royal Holloway, London, September 2007.

▪ Kocaba V., Gallucci E. and Scrivener K.L., Measurement of slag reaction in blended cements, *28th Cement and Concrete Science Meeting*, University of Manchester, September 2008.

PRESENTATION OF THE PHD STUDY DURING EVENTS ORGANISED BY NANOCEM CONSORTIUM

- **26th April 2006:** Nanocem Spring Meeting in Copenhagen, Denmark.
- **24th October 2006:** Nanocem Fall Meeting in Bled, Slovenia.
- **8th November 2006:** Marie Curie Training Course in Aalborg, Denmark.
- **25th October 2007:** Nanocem Fall Meeting in Madrid, Spain.
- **26th February 2008:** Workshop on Hydration Kinetics in Morges, Switzerland.
- **4th November 2008:** Nanocem Fall Meeting in Dijon, France.
- **27th October 2009:** Nanocem Fall Meeting in Zurich, Switzerland.